MONASH University

Additively Manufactured TiTa Alloys for Improved Osseointegration of Bone Implants

Erin Grace Brodie

Bachelor of Engineering (BE(H1))

Bachelor of Arts (BA)

Supervisors:

A/Prof. Andrey Molotnikov

A/Prof. Jess Frith

A thesis submitted for the degree of *Doctor of Philosophy* at

Monash University in 2020

Department of Materials Science and Engineering

Copyright Notice

Abstract

Currently, bone implants are manufactured from Ti-6Al-4V, an alloy originally designed for use in aircraft. Hence, Ti-6Al-4V has short-comings in biological applications. This alloy contains toxic elements of Al and V and possesses a much higher elastic modulus than bone. The elastic modulus mis-match between bone implants and the natural bone surrounding the implant after implantation results in 'stress-shielding'. Stress-shielding causes the natural bone surrounding the implant to be resorbed by the body. Implant loosening and fracture of thinning bone surrounding the implant are, hence, common complications after surgery. Implant failure causes significant pain and reduction in quality of life of patients and leads to complicated revision surgeries with even further reduced success rates and increased surgical risk and cost.

Additive manufacturing is increasingly adopted by major implant manufacturers, aiming to improve surgical success rates by manufacturing bespoke implants. However, the suite of materials available for manufacture remains limited to Ti-6Al-4V. New alloys, specifically designed for bone implant applications, are required. Initial considerations such as removing toxic elements and reducing elastic modulus are a start. However, new understanding in the biological response to implant materials has encouraged design of new alloys which are 'bioactive', providing functionalities when implanted, such as anti-bacterial behaviour or enhanced osteogenesis. Bespoke additively manufactured bone implants made from new bioactive alloys have the potential to significantly reduce implant complications.

Tantalum (Ta) has a long history in biomedical applications and has recently been highlighted for its superior osteogenic response when compared with titanium (Ti). However, Ta is extremely dense at 16.7 g/cm^3, has a high elastic modulus of 186 GPa and is difficult to process and shape, due to its refractory nature. Ta acts as a β phase stabiliser in Ti and hence the TiTa system can reach low elastic moduli, whilst retaining a superior strength to pure Ti, due to solid solution strengthening. However, it is still unknown whether alloys of the TiTa system retain the improved osteogenic capabilities of pure Ta. In addition, due to the large difference in melting points between Ti and Ta, simultaneously holding these two metals in the molten state is extremely difficult. Preliminary studies of laser powder bed fusion (L-PBF) of TiTa alloys show remaining partially melted Ta particles embedded in the TiTa matrix, suggesting new processing methods are required to improve homogeneity.

This thesis addresses the gaps in the understanding of processing TiTa alloys using L-PBF and investigates the mechanical and biological response of these alloys. Two alloy compositions were chosen, as two minimum modulus points exist in the alloy system at Ti25Ta and Ti65Ta and were investigated through mixed powder L-PBF processing.

The thesis is divided into seven chapters. Chapter 1 provides the motivations for this thesis whilst Chapter 2 summaries the literature of biomedical alloys, additive manufacturing methods, the current

state of mechanical properties achieved in additively manufactured biomedical alloys and existing strategies to improve the biological response of implant materials.

Chapter 3 discusses the selection of Ti25Ta and Ti65Ta alloys and high throughput additive manufacturing is used to validate the alloy selection, by investigating the volume fractions of α and β phases present over a range of compositions. Laser directed energy deposition (L-DED) processing validated the expected crystal structures and highlighted the necessity of developing new processing strategies to ensure full melting and incorporation of the Ta. Processing parameter optimisation was then investigated for L-PBF of these alloys, the preferred AM method for implant manufacture. Improved melting of the refractory Ta was addressed by 'remelt scanning', a scanning strategy which has previously been investigated to improve surface finish and reduce residual stress, however, has not been investigated as a tool for improving alloy homogeneity. The density of the manufactured material was also used to validate parameter optimisation models. A normalised enthalpy model which includes chemical properties of the metals investigated, was applied to study the processing window. While this model highlighted benefits for parameter predictions over the traditional energy density model, some shortcomings, such as the lack of describing heat transfer between powder particles, were reported. Future work is suggested to further enhance the enthalpy model.

Chapter 4 investigates the microstructure and quasi-static mechanical properties of the L-PBF Ti25Ta and Ti65Ta alloys. The work furthers the disputed α'/α'' compositional boundary in the TiTa phase system, as the microstructure provides the unique opportunity of TEM crystal investigation across a variety of wt.% composition diffusion zones. In addition, this chapter highlights the non-columnar grain structure produced, which is unusual for Ti alloys produced via L-PBF. This is attributed to a combination of constitutional supercooling and remaining partially melted Ta particles acting as grain nucleation sites. The tensile and elastic modulus properties of the alloys are then related to their observed microstructure. The effect of the novel processing method of remelt scanning on disrupting grain structure and texture and increasing alloy strength is discussed. The developed alloys show similar strength to L-PBF produced pure titanium, with half the elastic modulus.

Chapter 5 investigates the performance of the TiTa alloys under cyclic loading, such as would be experienced by an implant. Fatigue testing was conducted for solid and lattice structures, neither of which have yet been explored in literature. The yield stress normalised fatigue behaviour of the solid material was shown to be superior to both pure Ti and Ti-6Al-4V, highlighting the applicability of the TiTa alloy system to low-stress loaded bone implant applications, such as maxillofacial implants. The remelt scanning strategy was found to decrease the fatigue life of the material due to increased internal stresses, however the remaining Ta particles in the single melt material were not seen to contribute to crack initiation and failure. Parameter optimisation for the creation of fine lattice structures is also explored, revealing the dependence of microstructure on the part geometry. The improved ductility of

the TiTa alloys was noted to be especially beneficial for lattice structures and their fatigue performance. By reducing notch sensitivity, the TiTa alloys show superior fatigue life to Ti-6Al-4V at an equal stress amplitude of 50 MPa. The fatigue behaviour of the TiTa alloy system provides a promising avenue for future development in new biologically designed lattice structures.

The biological performance of L-PBF Ti25Ta and Ti65Ta are compared to L-PBF Ti-6Al-4V in Chapter 6. The alloys are assessed *in vitro* through attachment, proliferation, morphology and osteogenesis assays with human bone marrow mesenchymal stromal cells (hBMSCs). The results showed that both the Ti25Ta and Ti65Ta compositions display an equal cell attachment and proliferation with an enhanced osteogenic response when compared with the standard Ti-6Al-4V alloy. However, no statistical difference in osteogenic behaviour is noted between the Ti25Ta and Ti65Ta alloys. This highlights that the Ti25Ta has sufficient Ta content to be 'bioactive' but also offers a reduced alloy cost and weight when compared with the Ti65Ta composition, making the Ti25Ta alloy the preferential material for bone implants.

Finally, Chapter 7 presents conclusions of the thesis and outlines recommendations for future work.

Overall, this thesis contributes to a better understanding of additive manufacturing methods for TiTa alloys, providing an improved material choice for bone implant applications to increase the success rate of implant surgeries. This thesis established an understanding of the microstructure formation and the corresponding mechanical properties of TiTa alloys. Furthermore, the biological response of these alloys is studied and osteogenic benefit over traditional Ti-6Al-4V highlights these alloys as promising candidates for the implant industry.

Declaration

This thesis is an original work of my research and contains no material which has been accepted for the award of any other degree or diploma at any university or equivalent institution and that, to the best of my knowledge and belief, this thesis contains no material previously published or written by another person, except where due reference is made in the text of the thesis.

Signature:

Print Name: Erin Brodie

Date: 28/09/2020

Communications

Publications

N. Soro, H. Attar, **E. Brodie**, M. Veidt, A. Molotnikov, M.S. Dargusch, Evaluation of the mechanical compatibility of additively manufactured porous Ti–25Ta alloy for load-bearing implant applications, J. Mech. Behav. Biomed. 97 (2019) 149-158.
(Award: The Anders Gustaf Ekeberg Tantalum Prize)

E.G. Brodie, A.E. Medvedev, J.E. Frith, M.S. Dargusch, H.L. Fraser, A. Molotnikov, Remelt processing and microstructure of selective laser melted Ti25Ta, J. Alloys Compd. 820 (2020) 153082.

E.G. Brodie, J. Richter, T. Wegener, T. Niendorf, A. Molotnikov, Low-cycle fatigue performance of remelted laser powder bed fusion (L-PBF) biomedical Ti25Ta, Mater. Sci. Eng., A 798 (2020) 140228.

E.G. Brodie, K.J. Robinson, E. Sigston, A. Molotnikov, J.E. Frith, Osteogenic potential of additively manufactured TiTa alloys, ACS Applied Bio Materials (Accepted)

E.G. Brodie, T. Wegener, J. Richter, T. Niendorf, A. Molotnikov, Low-cycle fatigue performance of L-PBF biomedical TiTa lattices, Additive Manufacturing (Manuscript in Preparation)

Conference Presentations

(2017) **Asia-Pacific International Conference on Additive Manufacturing**
Melbourne, Victoria, Australia.
Oral presentation: Mechanical properties, microstructure and biological response of additive manufactured TiTa alloys for medical implants.

(2018) **Materials Science and Engineering**
Darmstadt, Hesse, Germany.
Oral Presentation: Additive manufactured TiTa alloys for biomedical applications.

(2019) **Asia-Pacific International Conference on Additive Manufacturing,**
Melbourne, Victoria, Australia.
Oral Presentation: Mechanical properties, microstructure and osteogenesis of selective laser melted TiTa alloys.

(2019) **Powder Metallurgy and Additive Manufacturing of Titanium**
Salt Lake City, Utah, United States.
Oral Presentation: Additive manufactured TiTa alloys for biomedical applications.

(2019) **8th International Conference on Mechanics of Biomaterials and Tissues**
Waikoloa, Hawaii, United States.
Oral Presentation: Mechanical properties, microstructures and osteogenesis of selective laser melted TiTa alloys.

Acknowledgements

This research was funded by the Dr Marie-Faith Fiawoo Memorial Scholarship. Dr. Marie-Faith was tragically killed in a wall collapse in Carlton in late March 2013, whilst working as a postdoctoral researcher in the Materials Science and Engineering Department, on aluminium alloy characterisation. This thesis was conducted in her memory.

I would like to acknowledge the funding support from the ARC Research Hub for Transforming Australia's Manufacturing Industry through High Value Additive Manufacturing, led by Prof. Xinhua Wu, and the academic support and facilities provided by the Monash Centre for Additive Manufacturing (MCAM).

For further academic support and assistance throughout my PhD candidature, I would like to acknowledge;

- Dr. Elizabeth Sigston for her valuable insights into maxillofacial surgery.
- The Monash X-Ray Platform; in particular James Griffith and Jisheng Ma, for their guidance and support with X-ray analysis.
- The Monash Centre for Electron Microscopy; in particular Xi-Ya Fang for her assistance with imaging the stubborn L-PBF Ti25Ta.
- The Woodside Future Lab; in particular Dr. Lee Djumas for his guidance and excellent interfacing between business and research and Marten Jurg for his Mlab expertise.
- Collaborators at Universität Kassel, Karlsruhe Institute of Technology, RWTH Aachen, Ohio State University, University of Queensland and RMIT; in particular, Prof. Thomas Niendorf for his fantastic knowledge and assistance of testing the TiTa alloy system and Dr. Alex Medvedev, for his invaluable crystallography support.
- The amazing professional team in the Materials Science and Engineering Department, without whom the place would fall to pieces; Ms. Edna Tan, Ms. Kris Wirthensohn, Ms. Michelle Laing, Dr. Trina Majumdar and Mr. Ian Wheeler.

Finally, I am extremely thankful to my supervisors, Andrey and Jess, for their approachability and constant willingness to grow as supervisors. You are both fantastic additions to the academic world and I hope you can convey your approach to supervision to new and existing academics.

I would also like to acknowledge the non-academic support which I received, which cannot be underestimated. I would not have made it through without the amazing support of my teammates. Georgia and Ezgi, I cannot put into words how valuable your support has been. I am very lucky to have had you both as my team members and have thoroughly enjoyed eating a whole bunch of chocolate and delicious café food with you.

Furthermore, to the Frith group (including third wheels); I am extremely thankful for the kindness and patience you showed to the metallurgist infiltrating your ranks. To Carlos, Gabe, Ilze, Kaushik, James, Margeaux, Maria, Saab and Sura, I cannot thank you enough for your inclusivity and strong collaborative and supportive mentality.

I would also like to acknowledge my non-work supporters. Thank you to; Meg for your constant friendship and thesis related psychological support both of which have been invaluable, Chiara for our brief university catch-ups often with delicious baked goods, Megan for often feeding me and teaching me how to take care of myself with hugs and tea, Kathryn for your unique fun ability to take my mind very far away from anything work related and Nicole for endless beach and bike escapes and even coming to my conferences! And I would like to add a special mention to family dinners with Caz, Meg and Bibz which significantly brightened my week every Thursday.

To my family, my parents Carole and Garry, my brother Andrew and Spencer, thank you for supporting me in every way, for your never-ending encouragement and for your willingness to celebrate even the smallest accomplishments with a bottle of champagne.

And Kye, thank you for both your academic and personal support, reliability, positivity and your unique perspective on the world.

Contents

List of Figures

List of Tables

List of Abbreviations

ALP – Alkaline phosphatase

AM – Additive manufacture

ASTM – American Society for Testing and Materials

at. % – Atomic percent

BCC – Body centred cubic

BMP – Bone morphogenetic protein

BSI – Back scattered imaging

CAD – Computer aided design

CP Ti – Commercially pure titanium

DIC – Direct image correlation

DMEM – Dulbecco's modified eagle medium

EDX – Electron dispersive X-ray

EBSD – Electron back scattered diffraction

ELI – Extra-low interstitial

FBS – Foetal bovine serum

FCCZ – Face centred cubic lattice with vertical (z) struts

FDA – Food and drugs administration

FEA – Finite element analysis

Fn1 – Fibronectin 1

GM7373 – Bovine aortic endothelial cells

hBMSC – Human bone marrow mesenchymal stem or stromal cell

HCP – Hexagonal close packed

HIP – Hot-isostatic press

ITGα5 – Integrin α5

ITGβ1 – Integrin β1

ISO – International Organization for Standardization

L929 – Murine fibroblast cells

L-DED – Laser directed energy deposition

L-PBF – Laser powder bed fusion

MC3T3-E1 – Murine calvaria pre-osteoblast cells

MG63 – Human osteosarcoma cells

Micro-CT – Micro computed tomography

MSC – Mesenchymal stem or stromal cell

OCN – Osteocalcin

ON – Osteonectin

OP – Osteopontin

OPG – Osteoprotegerin

OPS – Oxide polishing suspension

PBS – Phosphate-buffered saline

PECS – Pulsed electric current sintering

p-FAK – Phosphor focal adhesion kinase

pNP – p-nitrophenol

R – fatigue load ratio

RANKL – Receptor activator of NF-κB ligand

RS – Remelt scanning strategy

SAD – Selected area diffraction

SaOS2 – Human osteosarcoma cells

SEM – Scanning electron microscopy

SS – Single melt scanning strategy

TEM – Transmission electron microscopy

Ti2448 – Ti-24Nb-4Zr-7.9Sn

TMZF – Ti-12Mo-6Zr-2Fe

TM – Trabecular Metal

TNTZ – Ti-29Nb-13Ta-4.6Zr

TPMS - Triply periodic minimal surfaces

UTS – Ultimate tensile strength

VCL – Vinculin

wt. % – Weight percent

XPS – X-ray photoelectron spectroscopy

XRD – X-ray diffraction

Chapter 1 Introduction

Head and neck squamous cell carcinoma is the 6th most common cancer worldwide, with alarming increasing rates in young people [1-3]. As the oral mucosa, where this cancer begins, is close to the mandible, the cancer often invades the mandibular bone and treatment involves radiotherapy coupled with removal of the tumour through bone resection. Large sections of the bone are removed, in attempt to remove all possible cancerous material, which results in chewing, speaking and swallowing difficulties and large facial deformities [4, 5].

Facial reconstruction following the resection surgery consists of acquiring suitable bone from a second site within the body, often the fibula or iliac crest (Figure 1-1(a)). This bone is then shaped and attached to the remaining mandible with a titanium plate, which is manually bent to the contour of the patient's face by hand during surgery and secured with multiple screws. Unfortunately, the success rate of this reconstructive surgery is low, with a high percentage of implant failures occurring in the first 6 months after surgery [6].

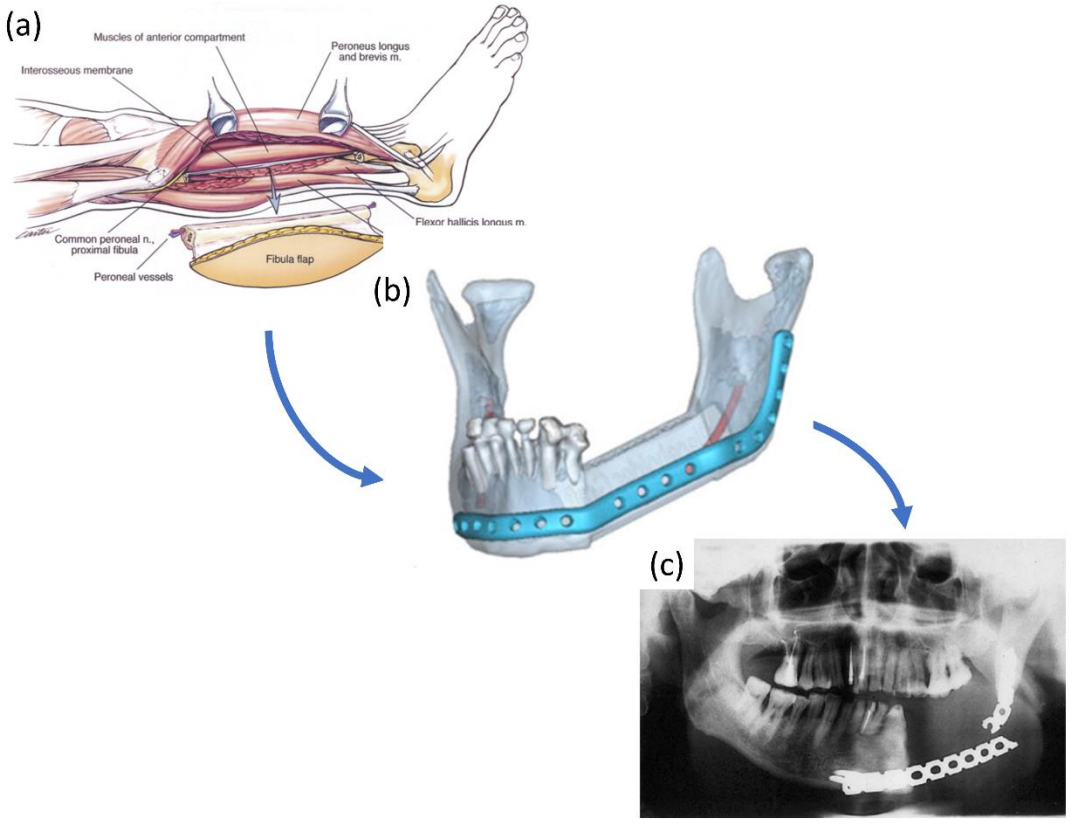

Figure 1-1: Components of mandible reconstruction. (a) Fibula free flap surgery provides the replacement bone which is attached (b) with a titanium plate and multiple screws. (c) Plate fracture is one of the causes of reconstruction failure. (a) (b) and (c) are reproduced with permission from [7] [8] [9], respectively.

10 – 20 % of failures occur due to screw loosening [6, 10-15], screw fracture [10, 12, 13] or plate fracture [6, 9-13, 15-18]. Due to bending of the plates during surgery, residual stresses are induced into the plate which can cause fatigue fracture [9, 12, 13], and contour mismatch between the plate and reconstructed bone can lead to micromotion which results in reduced bone bonding and plate and screw loosening [19]. Furthermore, the mechanical properties of the solid titanium plates and screws are much stronger and stiffer than the surrounding bone which can lead to bone resorption, also contributing to plate and screw loosening [15, 20].

To improve the success rate of mandible reconstructions and improve the quality of life for patients, new bespoke implants are considered in academia and industry. These designs can be enabled through an emerging manufacturing technique known as additive manufacturing (AM). AM can create implants which mimic a patient's individual bone shape [21], and open up an opportunity to explore new materials, which can improve the success of many types of stress-loaded bone implants.

Additive manufacturing (AM) is a layer-wise manufacturing process, capable of manufacturing complex geometries previously unattainable with conventional processing techniques. With the use of computer aided design (CAD), implants can be created which are based directly on CT scans of the patient's bone shape, and with the additional benefits of improved functional design, such as better fixation mechanisms. In the case of mandibular surgery, AM of mandible implants could remove the need for fibular surgery altogether, by producing a scaffold through which natural bone could grow to fill the resection defect. Many AM devices have already received approval from the Food and Drugs Administration (FDA) [22-25] and have facilitated surgeries that were previously impossible with conventional implants. One style of mandible reconstruction plate has already been designed [26], however, it is still manufactured using the conventional Ti-6Al-4V alloy, which was initially designed for use in aeroplanes, not implants.

Titanium (Ti) and its alloys have been widely used in medicine, due to their high strength to weight ratio and corrosion resistance. However, Ti-6Al-4V has many drawbacks as a biological alloy. It has a high elastic modulus, causing 'stress-shielding', a phenomenon that results in the resorption of natural bone in contact with the implant. Ti-6Al-4V also contains aluminium (Al) and vanadium (V), which are both toxic constituents, and is inert in the body, providing no benefit for the surrounding tissue. Additive manufacturing allows an exploration of new alloy systems which are specifically designed not only for use in the body, but for specific implant applications. For example, bone density and strength vary widely throughout the body, depending upon the magnitude of the forces applied to the bone by surrounding muscles and tendons. Furthermore, bone density and strength also vary significantly from one individual to another and is dependent upon age, gender and many other health factors. If all bone implants are manufactured from a single material, there will inevitably be mechanical property

mismatch between the implant and surrounding bone, leading to implant failure. Hence, a larger selection of materials is required to suit each bone implant application.

Materials which were previously difficult to manufacture, such as the refractory elements of niobium (Nb), tantalum (Ta) and zirconium (Zr), are useful β phase stabilisers in titanium. Pure Ti exists in the α phase at room temperature, which has a much denser atomic structure, and hence higher elastic modulus than the β phase, which exists at temperatures above 880 °C [27]. The addition of β stabilisers to pure Ti reduces the temperature at which the β phase is stable and with sufficient additions, the β phase becomes stable at room temperature. These β-type low modulus alloys have been highlighted over the last ten years as promising candidates for bone implants. Additive manufacturing is helping to realise these systems, due to the use of high input energy sources directed at small metallic powders, enabling the melting of refractory constituents on a much smaller scale.

One of the most promising refractory constituents is Ta. Ta not only has the ability to stabilise the β phase in Ti, but has also been highlighted in medicine for its superior bone integration properties [28-30]. Bone tends to form more quickly and strongly on Ta implants, compared with any other metal to date, and hence Trabecular Metal™, a porous Ta scaffold developed by ZimmerBiomet, has been used widely in a range of bone implants [31-35]. However, Ta on its own is very dense, four times as dense as titanium, and has a high elastic modulus of 186 GPa. The high weight of pure Ta limits its use to very small implant applications, whilst its high modulus is even further mis-matched from bone than Ti-6Al-4V, contributing to stress-shielding and implant failure. In addition, with a melting temperature of approximately 3000 °C Ta is extremely difficult to process, requiring special techniques such as chemical vapour deposition to create scaffolds.

Preliminary investigations into the TiTa system have shown that low elastic moduli of ~65 GPa can be achieved [36]. However, additive manufacturing may help to realise the full potential of this alloy system, by investigating a range of alloys and creating unique and complex geometries for implants. In addition, due to its difficulty of conventional manufacture, the TiTa systems has had little biological investigation and it is yet unknown whether any compositions of the TiTa alloy system show the improved osteogenic response of pure Ta when compared with pure Ti. Therefore, the following work investigates additively manufactured TiTa compositions, produced by laser direct energy deposition (L-DED) and laser powder bed fusion (L-PBF), for their microstructure, mechanical properties and biological response, in order to ascertain their suitability for stress-loaded bone implant manufacture.

1.1 Research Objectives

The primary objective of this research is to develop a more suitable TiTa alloy than Ti-6Al-4V for bone implants, which can be additively manufactured into the complex geometries required. In particular, the research aims to identify:

1. Favourable compositions in the TiTa alloy system for bone implants, considering both mechanical and biological response. The microstructure and mechanical properties of different alloy compositions will be explored and investigated *in vitro* for their biological suitability.

2. Improved processing techniques for AM TiTa alloys, focused on improving melting of the refractory Ta component. Parameter optimisation and new scanning strategies will be investigated to improve the homogeneity of as-built parts.

3. The static and dynamic mechanical response of L-PBF TiTa lattice structures. The suitability of the new TiTa alloys will be evaluated considering the complex geometric shapes and functional loading conditions experienced by implants.

4. The osteogenic response of the new TiTa alloys compared directly with the conventional Ti-6Al-4V alloy. The newly created AM TiTa alloys will be compared directly to Ti-6Al-4V *in vitro* to ascertain whether they elicit an improved bone response.

1.2 Thesis Scope

The scope of this research is as follows:

1. Identify favourable alloy compositions using thermodynamic modelling (ThermoCalc software) and high throughput L-DED manufacturing.

2. The favourable alloy composition and improved processing techniques will be investigated by assessing microstructure and mechanical properties. X-ray diffraction (XRD) , scanning electron microscopy (SEM), transmission electron microscopy (TEM) and electron back scattered diffraction (EBSD) will be used for microstructure characterisation, and supported with ultrasonic modulus testing, tensile testing and fractography.

3. The behaviour of the L-PBF alloys will be investigated under complex loading conditions of low-cycle fatigue (LCF), supported by Micro-CT analysis. Furthermore, the L-PBF TiTa alloys will be investigated in lattice form, identifying the changes to microstructure and mechanical properties resulting from the lattice geometry.

4. *In vitro* testing with human bone marrow stem cells will be used to identify and quantify any difference in osteogenic behaviour of the new AM TiTa alloys, compared directly with AM Ti-6Al-4V. Cell attachment and proliferation will be analysed, accompanied with cell morphology analysis and osteogenic assays.

Chapter 2 Literature Review

This literature review explores the range of biomedical alloys currently used in biomedical applications and their limitations. Titanium alloys are at the core of this review due to their significant use in orthopaedics. New developments in Ti based biomedical alloy systems are examined focusing on mechanical properties, such as their elastic modulus, toxicity, and bioactive response. Following this, additive manufacturing methods of metallic alloys are introduced and laser powder bed fusion (L-PBF) is highlighted as versatile manufacturing technique for implant manufacture. A brief introduction into L-PBF parameter optimisation is given and the limitations of current parameter modelling systems is highlighted. Furthermore, scanning strategies for *in situ* microstructural control are discussed and linked to control of part density and surface properties. The current state of mechanical properties achieved in additively manufactured biomedical alloys is then summarised, particularly highlighting the recent studies in L-PBF of the pure Ti, pure Ta and TiTa systems. To contextualise the mechanical research for implant applications, the current understanding of fatigue behaviour of AM materials is summarised and new research investigating promising lattice geometries for tissue integration are presented. Finally, the developing definition of 'biocompatible' for orthopaedic materials is discussed and experimental techniques for determining 'biocompatibility' critically analysed. To date *in vitro* and *in vivo* comparative testing of Ti and Ta studies are reviewed, confirming the improved osteogenic response of Ta over Ti, but also highlighting the limitations of the *in vitro* experimental techniques used. Finally, the current hypotheses for the mechanisms contributing to Ta improved osteogenic response compared to Ti is discussed. The literature review is concluded with a summary of the existing gaps and a formulation of critical research questions to be answered in this thesis.

2.1 Biomedical Alloys

Metals have been used in the body as surgical aids for the past 100 years, with the first total metallic hip replacement implanted in 1938 [37]. Metals are employed to replace or stabilise bone, due to their high strength, for electrical devices like pacemakers and electrodes, due to their conductivity, and for antibacterial coatings. In orthopaedics, metals are generally employed as fixation plates and screws to stabilise fractures and reconstructions, and as large structural members, such as artificial joints. The mostly commonly used biomedical metals today include stainless steels, cobalt-chrome alloys and titanium alloys, whilst magnesium alloys and pure tantalum are growing in use.

Stainless steels tend to show a high ductility, good corrosion resistance and twist strength and are generally used in short-term fracture plates due to their wide availability and low cost. Cobalt-chrome alloys show a high resistance to fatigue and wear and hence are heavily used in joint prostheses [27, 37]. Magnesium occurs as a vital trace metal in the body and hence magnesium alloys are investigated for possible *in vivo* degradation applications [38]. On the other hand, tantalum (Ta) is of interest due to opposite reasoning; Ta is biologically inert and forms strong oxide layers that inhibit corrosion and hence is deemed to create very safe implants [39]. Titanium alloys exhibit high strength, low density and high corrosion resistance, making them the ideal candidate for bone replacement applications.

Matching the mechanical properties of metal exactly to the mechanical properties of bone is critical to create a well-functioning implant. For example, the metal must display a strength equal to that of bone, so that the implant does not fail under loading. In addition, the metal must possess a good fracture toughness, so that the implant has a similar resistance to impact like bone. But most crucially and most difficult to achieve, the metal must show a similar stiffness or elastic modulus to bone as an implant with a high stiffness will preferentially absorb stress and lead to a phenomenon called ‘stress-shielding’. This phenomenon results in bone resorption surrounding the implant, which ultimately leads to implant loosening and failure [20, 40, 41]. Even though stress-shielding caused by metallic implants was first observed in the 1970s, it is still a recurring issue today. With increasing global life expectancy, the need for increased implant lifetime, particularly in osteoporotic patients, is growing [42]. Exactly replicating the mechanical properties of bone is difficult. Bone is a complex hierarchical structure made of ceramic and organic components, resulting in its light weight, strength and flexibility. Among metallic materials, titanium alloys, particularly if designed to possess a low elastic modulus and manufactured into bone-mimicking shapes, are the closest replicate available.

The most common medical titanium alloys include commercially pure (CP) titanium and Ti-6Al-4V. There has been significant research into new titanium alloys since the 1980s, but only a handful have achieved approval for use in medical devices, subject to standards produced by ASTM International and International Organization for Standardization (ISO) standards [43, 44]. A review of the materials

used to produce commercially available mandible plates and screws showed that only CP Ti, Ti-6Al-4V and one case of Ti-6Al-7Nb are used for this system to date (see Table 2-1).

Table 2-1: Materials used for current medical devices.

Company	Medical Device Material	Reference
BioUre	Plates: CP Ti (no grade specified) Screws: Ti-6Al-4V	*
DePuySynthes	Plates: CP Ti (no grade specified) Screws: Ti-6Al-7Nb	[45, 46]
GlobalD	Plates: Grade II, Grade IV and Ti-6Al-4V	[47]
Medartis	Plates: CP Ti (no grade specified) and Ti-6Al-4V	[48]
ZimmerBiomet	Plates: Grade II, Grade IV	[49]

CP Ti is available in four different grades, depending on oxygen content (0.18 – 0.45 wt.%), which adjusts the yield strength from 170 - 520 MPa [50]. Despite this increase in strength, CP Ti is still the lowest strength biomedical alloy, which makes it suitable for implant materials which must be customised by bending during surgery, such as mandible plates [19]. Whilst the tensile strength of CP Ti is adequate when compared with bone, the elastic modulus of CP Ti is still three times that of the strongest form of bone, cortical bone (see Table 2-2).

Ti-6Al-4V was initially developed for use in the aerospace industry in the 1960s, but has since been employed in orthopaedics due to its superior tensile and cyclic properties in comparison with CP Ti [50]. Whilst CP Ti seems to provide adequate tensile strength, the complex forces of the body and cyclic loading conditions can result in mechanical situations where the strength of CP Ti is inadequate. The higher static and fatigue strength of Ti-6Al-4V is required for structural implants, such as hip stems, which undergo millions of stress cycles per patient per year [51] at forces 4 to 6 times that of the body weight of the patient simply by walking up and down stairs [52]. Small changes have been made to the Ti-6Al-4V alloy to increase its ductility and fracture toughness for biomedical applications. Ti-6Al-4V ELI (extra low interstitial) is most commonly used in biomedical applications and has reduced levels of carbon, nitrogen, iron and oxygen. However, it possesses an even higher elastic modulus than CP Ti, accentuating stress-shielding. A further variant of Ti-6Al-4V was developed replacing the toxic vanadium (V) with niobium (Nb), Ti-6Al-7Nb, however the aim was to produce an alloy with similar mechanical properties to Ti-6Al-4V, not bone [53].

* Written correspondence with the company representative

Table 2-2: Mechanical properties of commonly used biological metals in comparison to bone.

Bone/Alloy	Yield Strength/UTS (MPa)	Elongation (%)	Elastic Modulus (GPa)	ASTM Standard [44]	Reference
Cortical Bone	85 ± 10 /68 - 150	1 - 3	13 - 35	-	[54-56]
Cancellous Bone[†]	25 / 0.9 - 10	2 - 9	0.02 - 2	-	[54, 57, 58]
Stainless Steel	190 - 690 / 490 - 1350	-	200 - 210	F139	[59]
Cobalt-chrome	310 - 1586 / 655 - 1793	-	210 - 253	F75	[59]
Ta	165 - 220 / 200 - 390	20 - 50	186	F560	[60]
CP Ti (Gr I – IV)	170 - 586 / 240 - 662	20 - 30	103 - 104	F67	[60]
Ti-6Al-4V	795 - 875 / 960 - 965	10 - 15	101 - 110	F136	[54]
Ti-6Al-7Nb	795 / 860	10	105	F1295	[54]

The use of Ti-6Al-4V is widespread in the biomedical industry, however this alloy only became popular in medicine because it was deemed suitable for the body due to its high corrosion resistance. It was not purposefully designed for use in the body and therefore there exists an opportunity to design an alloy which is specifically tailored for use in orthopaedic implants. As new research from collaborations between materials scientists and biologists evolves, new requirements for improved implant materials are discovered. For orthopaedics, these requirements have centred around three major themes;

- Reducing the elastic modulus mismatch between the implant and the host tissue.
- Reducing toxicity concerns around implant alloy constituents.
- Controlling the interaction between the implant material and host tissue.

2.1.1 Achieving Low Elastic Modulus

In orthopaedics, metals are required which possess an elastic modulus close to bone to avoid stress-shielding. Cortical bone, the dense bone found on the outside of most bones, has an elastic modulus of 13 – 35 GPa, whereas cancellous bone, the porous bone constituting the inside of the bone has a much lower elastic modulus of 0.02 - 2 GPa [61] (Figure 2-1). If an implant made of Ti-6Al-4V, with an elastic modulus of ~110 GPa, is put into direct contact with bone, the implant absorbs the functional stresses, the bone is unstimulated by stresses and resorbed by the body. Bone is remodelled and created

[†] Properties listed for cancellous bone are from compression testing

in areas of high stress, and less so in areas of low stress [62]. This ultimately results in implant failure as the implant will come loose or the surrounding bone will become thin and break.

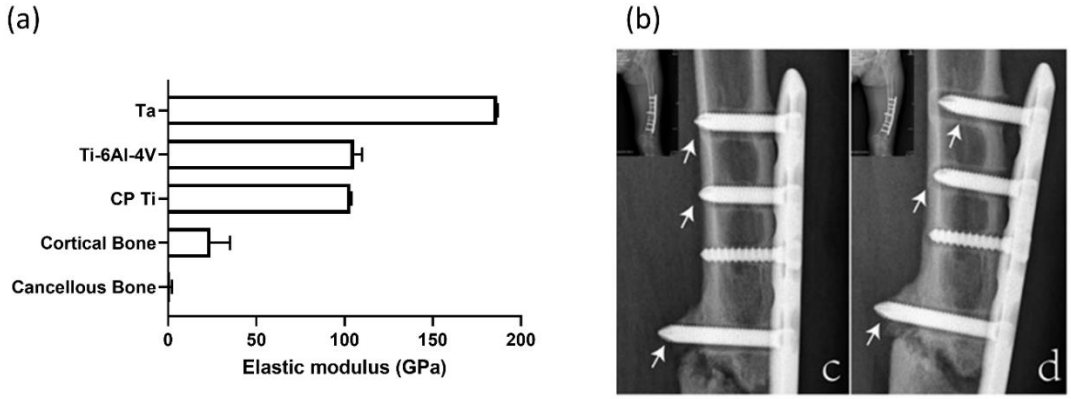

Figure 2-1: (a) Elastic modulus of biomedical metals compared to bone (b) Comparitive X-rays showing screw loosening as a result of stress-shielding. Reproduced with permission from [40].

β-type titanium alloys were first investigated in the 1980s to address the elastic modulus problem. CP Ti exists in an α hexagonal close packed (HCP) crystal structure below 882.5 °C, and as a β body centred cubic (BCC) structure above this temperature. Elements such as aluminium (Al), oxygen (O), nitrogen (N) and carbon (C) stabilise the α phase, whilst molybdenum (Mo), vanadium (V), tungsten (W), tantalum (Ta), niobium (Nb), iron (Fe), chromium (Cr), copper (Cu), nickel (Ni), cobalt (Co), manganese (Mn) and silicon (Si) stabilise the β phase [63]. The β phase can achieve a much lower elastic modulus compared with the α phase, attributed to the lower packing density of the BCC crystal structure [27]. The elastic moduli of β-type Ti alloys generally lie between 60 – 80 GPa, which is a reduction of 25 – 50% compared with pure titanium. Generally, these alloys possess a lower strength coupled with their lower elastic modulus (see Table 2-5), and strengthening methods such as solid solution strengthening, cold working and ceramic additives are often employed.

β-type titanium alloys are either classed as stable or metastable. Stable β-type alloys have sufficient β-phase stabilising element content that the β phase is retained entirely upon ageing. Metastable β-type alloys contain enough β stabilising elements to suppress the martensite start temperature to below room temperature, however can precipitate α phase upon ageing. Even lower concentrations of β stabilisers result in the martensite start temperature occurring above room temperature, and upon quenching, fractions of the β phase may turn into α′ or α″ martensite. α′ martensite possesses the same crystal HCP crustal structure as α Ti whilst α″ martensite exists in an orthorhombic structure (see Figure 2-2). The final phase identified in this alloy class is the ω phase, which can occur on β phase decomposition and can result in strengthening but also severe embrittlement. Whilst not technically classed as β-type alloys, some of the α + β and ω microstructures can still retain low elastic modulus values and acceptable mechanical properties for biomedical applications.

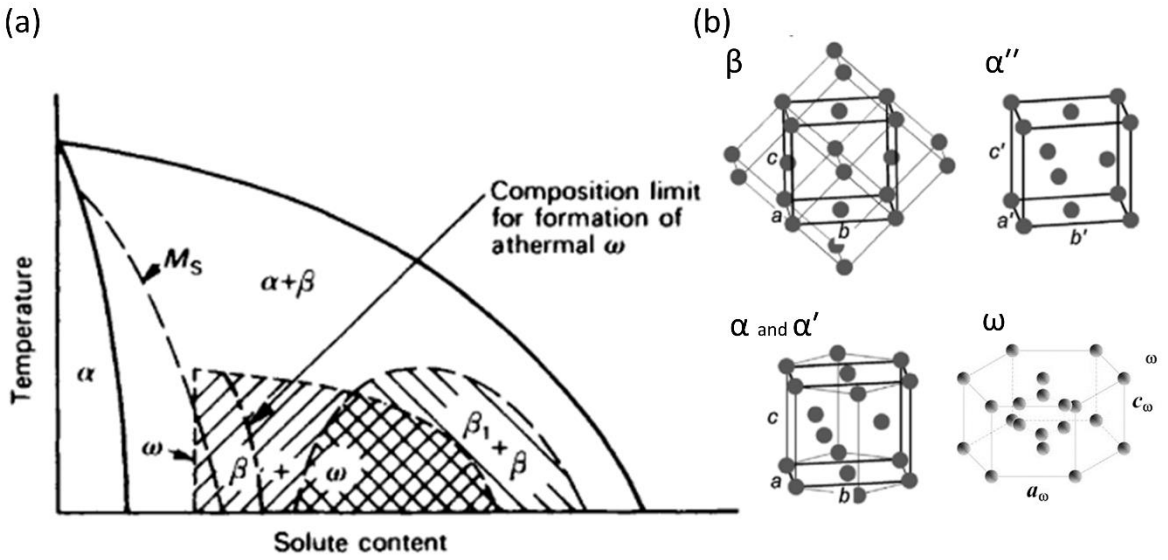

Figure 2-2: (a) Schematic of β isomorphous alloy phase diagram. (b) Crystal structures present in β Ti alloys. Reproduced in part with permission from [63].

The β phase stabilising elements are classed as isomorphic (Mo, V, W, Nb, Ta) or eutectoid stabilisers (Fe, Cr, Cu, Ni, Co, Mn, Si). The isomorphic stabilisers result in a binary system, whilst the eutectoid stabilisers can show a eutectoid reaction, resulting in a third intermetallic phase. Increasing solute content of the isomorphic stabilisers results in a decrease in the β transition temperature, whilst increasing solute content of the eutectoid stabilisers can either increase or decrease the β transition temperature. For this reason, isomorphic stabilisers are often favoured as the β phase can be retained at lower solute contents.

Molybdenum is well-known as the most potent isomorphic β phase stabilising element. Only 10 wt.% of Mo is required to retain 100 % beta phase on water quenching [63]. Of the Ti-Mo compositions the Ti-15Mo alloy has been highlighted for biomedical applications due to its high strength, high strain hardening and good cold forming ability [64] and is one of the few β-type Ti alloys which has received an ASTM standard (see Table 2-5). However, despite the full β phase microstructure, the alloy still displays an elastic modulus of 100 GPa, as well as a reduced corrosion resistance compared with Ti-6Al-4V [65]. Attempts have been made to further reduce the elastic modulus and increase the corrosion resistance of the Ti-15Mo alloy through alloying with niobium. The Ti-15Mo-20Nb alloy displayed an elastic modulus reduction down to 80 GPa, but no improvement in corrosion resistance was noted [66]. By using the theoretical approach of reducing the electron-atom ratio, a Ti-15-Mo-5Zr-3Al alloy was produced which exhibited an elastic modulus as low as 43 GPa in single crystal condition, by suppressing the formation of the ω phase [67]. However, single crystal formation provides little benefit to complex shaped implants. Ti-12Mo-6Zr-2Fe (TMZF) has proven to be the most promising alloy in the TiMo system with reduced elastic modulus of 74 – 85 GPa and yield strengths to 1000 MPa upon

ageing. The success of this system is evident in its inclusion in ASTM standards [68]. Interestingly, it was commented that the alloy increased in modulus due to the dissolution of the ω precipitates, disagreeing with the findings in [67] which suggest larger amounts of ω phase increases elastic modulus.

Ti-Fe alloys are also under investigation due to Fe being a relatively low cost β stabiliser which also occurs naturally in trace amounts in the body [69]. Fe is a very potent β stabilizer with only 3.5 wt.% required to retain 100% β upon water quenching, however it falls into the eutectoid category and high contents of Fe can lead to an intermetallic phase of TiFe, resulting in modulus values > 175 GPa [70]. The Ti-31Fe alloy can reach very high yield strengths of 2028 ± 20 MPa [71], but its high elastic modulus makes it unsuitable for orthopaedic applications. Additions of Ta and Nb to this system can stabilise the β phase and reduce the martensite transition temperature, but low contents of Fe are required to supress the TiFe intermetallic phase [69]. A modulus of 92 GPa was obtained by cold crucial levitation melting in the Ti-10Fe-10Ta system [69], whilst 84 GPa was reported in the Ti-7Fe-11Nb study [72], both showing no intermetallic phase. Compressive yield strengths of 1000 MPa were retained for both alloys, with plastic strain from 35 – 38%. These alloys were not investigated under tension.

The Ti-Fe-Cu system is also of interest due to the reported antibacterial properties of Cu. Whilst the Ti-3.5Fe-3.9Cu alloy showed acceptable electrochemical behaviour compared to Ti-6Al-4V [73], the low Fe content results in lower strengths and complex manufacturing of dual-axial hot forging repeated 20 times was required to create a nanostructured alloy to achieve an ultimate tensile strength of 1100 MPa [74]. The as-cast material showed a strength of 900 MPa with a small elongation of < 2%. The elastic modulus is quoted for the Ti-3.5Fe-3.9Cu alloy to be at 70 GPa [75].

Titanium alloys with Nb and Ta additions form the bulk of newly developed β-type alloys, despite their higher cost. These metals are both classed as refractory, due to their high melting temperatures (see Table 2-3), and are very electronically similar, notoriously being recorded as the same element until 1884 when they were finally chemically distinguished [76].

Table 2-3: Metal densities and melting temperatures of β phase stabilising elements [77].

	Ti	**V**	**Cr**	**Fe**	**Co**	**Ni**	**Cu**	**Nb**	**Mo**	**Ta**	**W**
Density (g/cm^3)	4.54	6.11	7.19	7.87	8.90	8.9	8.96	8.57	10.2	16.7	19.3
Melting Point (°C)	1660	1890	1860	1530	1490	1450	1080	2470	2620	3000	3410

The ability of both these metals to form strong oxides results in a strongly inert status in the body, supported by the long positive clinical history of Ta. Both Nb and Ta are isomorphic β phase stabilisers, and due to their similar atomic properties, the TiNb and TiTa systems form similar crystal structures at similar at. % compositions (see Table 2-4). The crystal structure changes through α′ → α″ → β as more solute content is added, however the TiNb system retains a full β phase at a slightly lower at.% composition. The TiNb investigated was arc melted under vacuum and then cooled to room temperature by dropping in a graphite crucible [78], whilst the TiTa study investigated was cast, solution treated above the β transus and then rapidly quenched in ice water [36]. This may result in vastly different cooling rates for each system and hence differing ability to retain β phase upon quenching. However, it can be reliably concluded that a lower atomic percentage of Nb is required to form a β phase alloy.

Table 2-4: Crystal structures of TiNb and TiTa compositions after arc melting and quenching.

	Nb [78]	**Ta [36]**
α′	< 15 wt.% = < 8 at.%	10 – 20 wt.% = 3 – 6 at.%
α″	17.5 – 25 wt.% = 10 – 15 at.%	30 – 50 wt.% = 10 – 21 at.%
β	> 30 wt.% = > 18 at.%	70 – 80 wt.% = 38 – 51 at.%

The TiNb system shows two points of minimum elastic modulus values of 58 – 65 GPa at compositions of 16 – 17.5 wt. % and 26 – 40 wt.% Nb [78-82]. The elastic modulus of Ti initially decreases as Nb is added and reaches a minimum value at the beginning of the α″ crystal structure compositional region (16 – 17.5 wt.% Nb). The elastic modulus then increases with increasing Nb content, first due to Nb saturation of the α″ crystal structure, and then decreases with increasing Nb content as the β phase forms. The second modulus minimum occurs in the full β phase, however the compositional range at which this minimum occurs (26 – 40 wt.%) is much wider across literature studies. This is most likely due to the occurrence of the ω phase as studies show ω phase is possible in as-cast material at compositions of 18.5 wt.% Nb, but absent in homogenised and water quenched material of similar and higher Nb concentrations [82]. The volume fraction of ω was seen to increase upon ageing [80] and larger volumes of ω phase were noted to cause higher strength and elastic modulus [79, 80]. The as-cast yield strength of the TiNb system ranges from 600 – 900 MPa with strength initially increasing with Nb content, due to solid solution strengthening and ω phase formation. The strength begins to decrease above 30 wt.% Nb [78, 82]. Due to this mechanical profile, compositions between 30 – 40 wt.% Nb show the best strength-to-modulus ratio for biomedical applications. Ramarolahy et al. [83] also showed that oxygen additions to Ti-41 wt.% Nb could improve the alloy strength from 445 – 810 MPa whilst only slightly increasing the elastic modulus from 50 – 54 GPa. This was attributed to the

oxygen providing solid solution strengthening in the β phase and fully suppressing the formation of the α″ phase.

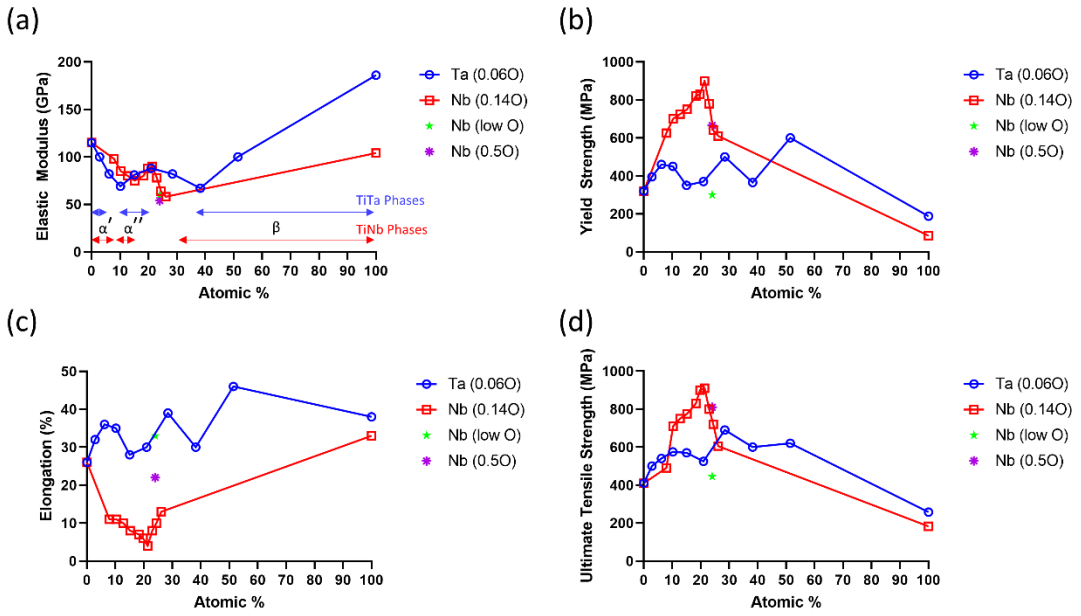

Figure 2-3: Mechanical properties of TiNb and TiTa systems based on atomic % of Ta or Nb. (a) Elastic modulus, (b) yield strength, (c) elongation and (d) ultimate tensile strength. Data reused with permission from; Ta (0.06O) [36], Nb (0.14O) [79], Nb (low O) and Nb (0.5O) from [83].

The TiTa system shows similar compositional and mechanical properties to the TiNb system, also showing two minimum elastic modulus points of 64 - 67 GPa at approximately 25 wt. % and 65 wt. % Ta [36]. The first minimum modulus point occurs on the α′/α″ phase boundary and the second in the β phase. The transition in elastic modulus is explained by the unit cell volume of the phases present. As the α′ phase increases in lattice volume with Ta content, the modulus decreases up to the α′/α″ phase boundary, whereas the α″ phase decreases in lattice volume with Ta content, and hence the modulus increases beyond the α′/α″ phase boundary. The β phase also decreases in lattice volume with Ta content, and hence the minimum modulus point occurs at the full β phase composition with the lowest Ta amount. The yield strength of the as-cast TiTa system ranges from 400 – 700 MPa [36]. A gradual increase in yield strength is noted as the Ta content increases from 0 – 25 wt.%, due to solid solution strengthening. However, a following decrease in strength is noted between 30 - 50 wt.% Ta, which is still unexplained. An increase in strength is then again seen > 60 wt.% Ta as solid solution strengthen in the β phase dominates.

The two main alloy compositions investigated in literature are the 25 wt.% Ta and the 50 wt.% Ta compositions, due to their high ratio of strength-to-modulus. The Ti25Ta was highlighted by Zhou et al. [84] to show the best ratio of yield strength (480 MPa) to elastic modulus (64 GPa). The lower concentration of Ta in Ti25Ta, compared with the Ti50Ta alloy, makes the alloy less dense and hence

preferable for bone applications. Studies show either complete α′ phase [85, 86], complete α″ [84] or a combination of α″ and β [87] phases existing at this composition upon quenching, hence the compositional phase boundaries, particularly the α′/α″ boundary, remain disputed. Where β phase was noted, heat treatments in the range between 700 – 1000 °C for 30 mins followed by quenching retained higher amounts of β phase at higher temperatures, which increased the alloy strength [87]. However, no elastic modulus values were measured for this study, but it is likely the modulus would have increased with the increasing strength. Despite the promising strength to ratio that this composition presents, few studies have investigated this alloy, likely because it is not classed as a stable β phase alloy.

The Ti50Ta composition has been much more heavily investigated, likely as it is well known that at least 45 wt.% of Ta is required to form a fully β phase alloy on quenching [63] and in addition, it can display shape memory effects [88, 89]. Shape memory is a phenomenon where a material can return to its trained shape, generally induced by temperature changes. The TiTa system can show this phenomenon due to the crystal structure change between α″ and the β phase. This phenomenon can be used in medical devices, such as cardiovascular stents which inflate once inside the body but is yet to find uses in orthopaedics and hence will not be further discussed here. The as-cast Ti50Ta alloy shows a yield strength of 380 MPa and elastic modulus of 90 GPa, inferior in strength-to-modulus ratio to the Ti25Ta composition [36]. However, Zhou et al. [90] showed that heat treatments at 600 °C could double the yield strength from 380 MPa to 877 MPa, due to the formation of the ω phase. The ability to form ω phase has not yet been noted in the Ti25Ta system. However, a reduction in ductility from 25 – 2.6% accompanied the formation of ω phase seen by Zhou et al. [90] and has been seen in many studies as a result of ω phase formation [88, 89, 91], reducing the efficacy of ω formation as a strengthening mechanism. The formation of the ω phase also inhibits the shape memory effect [88, 89].

Many ternary and quaternary titanium alloys, using combinations of these β stabilising elements have also been investigated, with the aim of achieving the lowest elastic modulus possible. Many compositions have been determined theoretically using the d-electron alloy design method [27]. The ternary alloy Ti-13Nb-13Zr (wt.%) has achieved an ASTM standard [44] and shows good tribological properties for its low modulus of 80 GPa [65]. Its low Nb content also results in the lack of ω phase upon ageing [92, 93], retaining a good ductility of 28% with a yield strength of 515 MPa. Additions of 13 (at.%) Ta to the Ti-30Nb (at.%) system showed the creation of a novel face centred cubic (FCC) γ phase in Ti rich regions and the original β phase in Ti poor regions [94]. This novel microstructure, created by fine microstructure milled powders and pulsed electric current sintering (PECS), resulted in a very low elastic modulus of 49 GPa and outstanding compressive yield strength of > 1860 MPa. However, PECS is difficult to be scaled up and is unable to produce complex geometries, such as lattice structures, which are required in orthopaedics.

The most heavily investigated quaternary alloys are Ti-29Nb-13Ta-4.6Zr (TNTZ) and Ti-24Nb-4Zr-7.9Sn (Ti2448). TNTZ was developed by Akahori and Niinomi [95] using the d-electron alloy design method, which successfully produced a β phase alloy with low elastic modulus of 62 GPa and yield strength of 650 MPa. A single crystal of TNTZ was found to exhibit an extremely low modulus of 35 GPa in the <1 0 0> direction, which was directly comparable to the elastic modulus of bone [96]. Severe cold working and ageing was required to give the alloy similar strengths to Ti-6Al-4V ELI (1050 Mpa and 1000 MPa respectively) [95], however comparable fatigue performance could not be achieved through this strengthening method as introduced strains resulted in reduced fatigue life. Liu et al. [97] was also able to mimic the strengths of Ti-6Al-4V ELI and also reported an increase in fatigue life of TNTZ, due to the use of small oxygen additions of 0.1-0.7 wt.%. This method was much more effective at retaining the low elastic modulus, whilst increasing strength. The oxygen addition aids work hardening and induces fine densely arranged α″ twins, enhancing resistance to fatigue crack initiation and propagation.

Ti-24Nb-4Zr-7.9Sn (Ti2448) was developed as the additions of Zr and Sn were found to suppress the formation of athermal ω and α″, which removed the two minimum modulus points in the TiNb system and replaced them with one even lower modulus point in the metastable β phase [98, 99]. An extremely low elastic modulus of 42 GPa was obtained in this alloy, with an accompanying ultimate tensile strength of 850 MPa. The strength can also be increased with ageing at 500 °C to 1150 MPa, whilst only increasing the elastic modulus to 70 GPa, achieving the best strength-to-modulus ratio to date. Additions of oxygen to the alloy to improve strength and fatigue performance have not yet been investigated. The complexity of the alloy however makes it hard to manufacture, with multiple arc melting and homogenisation steps required, using a mix of elemental powders and TiNb master alloys. Sintering of elemental powders resulted in a two-phase microstructure with α phase precipitated upon β grain boundaries and a reduced ductility due to restricted diffusion caused by oxygen pick up. However, an elastic modulus of 57 GPa was still achieved, with a UTS of 760 MPa [100].

Overall, Table 2-5 shows that low modulus β Ti alloys have been created which range in elastic modulus from as low as 35 – 100 GPa. The lowest achieved elastic modulus of 35 GPa is similar to the upper range of cortical bone, however no alloy has been designed which can bridge the breadth of the elastic modulus of natural bone (0.02 – 35 GPa). Strengthening these alloys to be comparable to the strength of the current industry standard material, Ti-6Al-4V ELI, is also challenging as many strengthening mechanisms also raise the elastic modulus of the material. The most promising strengthening mechanisms for β Ti alloys include solid solution strengthening with small oxygen concentrations and suppressing α″ and ω phase formation with ternary and quaternary elemental additions, such as Zr and Sn. In addition, due to the refractory nature of the Ta and Nb often employed in these alloys, conventional manufacturing methods require multiple melting and homogenisation steps. Complex mechanical treatments to produce novel microstructures and exceptional mechanical properties cannot

be applied to complex shaped implants, so low elastic moduli achieved by single crystal formation or high mechanical strength achieved by severe cold working are not applicable to implant manufacture.

Conventional manufacturing methods and alloy design have slowly reached the limits of mechanical properties obtainable from the β Ti alloy systems. Additive manufacturing provides new ways of manipulating microstructures to achieve similar strengths in the β Ti alloys to conventional Ti-6Al-4V. In addition, to further reduce the elastic modulus of implants, new geometries can be designed based on complex lattice structures, which better mimic bone porosity and reduce the implant structural elastic modulus to within the range of the bone.

Table 2-5: Phases and mechanical properties of β-type Ti alloys.

Alloy	**Manufacturing conditions**	**Phase**	**Yield Strength/ UTS (MPa)**	**Elongation (%)**	**Elastic Modulus (GPa)**	**ASTM Standard [44]**	**Ref.**
Ti-15Mo	Cold rolled and annealed	β	451 / 752	37	100	F2066	[64, 65]
Ti-12Mo-6Zr-2Fe (TMZF)	Annealed	β	1000 - 1060 / 1060 - 1100	18 - 22	74 - 85	F1813	[54]
Ti-31Fe	Conventional	B	2028 / 2627	7.5	-		[71]
Ti-10Fe-10Ta	Cold crucible levitation melting	α + β	- / 1005	-	92		[69]
Ti-3Fe-3Cu	Dual-axial forging, 20 times	α + β	1050 / 1200	8	70 - 100		[73, 75]
TiNb (16 - 40 wt.%)	Conventional and aged	α′, α″, β	290 - 900 / 420 - 900	0.5 - 33	50 - 115		[78-83]
TiTa (10 - 80 wt.%)	Conventional and aged	α′, α″, β	350 - 877 / 500 - 700	3 - 25	67 - 100		[36, 90]
Ti-13Nb-13Zr	Conventional	α, α′, β	515 / 680	28	80	F1713	[65, 92, 93]
Ti-30Nb-13Ta (at.%)	PECS	β, γ	> 1860‡	-	49		[94]
Ti-29Nb-13Ta-4.6Zr (TNTZ)	Conventional, cold rolled, aged, single crystal	α, α″, β	300 - 1350 / 500 - 1450	1 - 26	(35§) 59 - 110		[95, 97]
Ti-24Nb-4Zr-7.9Sn (Ti2448)	Conventional, cold rolled	α, β	350 - 1100 / 700 - 1600	2 - 20	42 - 105		[98-101]

‡ Tested in compression
§ Single crystal

2.1.2 Elemental Biocompatibility

Another important requirement for the development of new biomedical alloys is a consideration of the biocompatibility of their constituents. Already 40 years ago, the biocompatibility of V in Ti-6Al-4V became a concern as toxicology studies showed many of the compounds formed by vanadium in the body were highly toxic [76]. Despite this, the majority of Ti-6Al-4V implants, implanted since the 1950s, have shown no serious toxic effects as they have strong corrosion resistance [53]. Nonetheless, Ti-6Al-7Nb and Ti-5Al2.5Fe were developed in response to the vanadium toxicity concerns, only to have Al recently classed as a neurotoxin [102-104].

As the population ages, orthopaedic implants are expected to last for longer in the body and hence implant degradation becomes an even greater concern. Studies show metal ions and oxide nanoparticles in hard and soft tissues surrounding implants [105-109], even in the absence of wear and when the metal particles are considered virtually insoluble [110]. In addition, titanium particles from hip, knee and mandible implants have been found in the liver, spleen, lungs and lymph nodes of patients [111, 112] and in regenerated bone surrounding implants in animals [113, 114]. So far, concentrations of vanadium found in surrounding tissues have been below toxic level [115], however this highlights the need for strict assessment of the biocompatibility of Ti alloy constituents in new orthopaedic alloys.

There has been an effort to comparatively study the *in vitro* biocompatibility of the commonly used β phase stabilising elements, however no consensus has been reached concerning biocompatibility rankings [116-121]. This is a reflection of the large variability in the types of biocompatibility testing conducted, due to the flexible definition of 'biocompatible'. The definition of 'biocompatible' and the difficulties surrounding consistent biocompatibility testing will be discussed further in Section 2.5. Here, the studies focus on the cytotoxicity of these elements using viability and haemolysis assays to assess toxicity, however some studies accompany this data with cell morphology and protein activity. This range of analysis techniques, in conjunction with the use of different cell types and material preparation (particles of various sizes or solid surfaces) lead to conflicting results.

Eisenbarth et al. [116] conclude that Ta, Nb, Ti and Zr show the highest biocompatibility, by assessing cytotoxicity, cell proliferation and cell morphology, using two different cell types (MC3T3-E1 and GM7373), in direct contact with the polished metals. This comparatively robust study found molybdenum and 316L stainless steel to be cytotoxic in comparison to Ti, whilst Al was not classed as cytotoxic but showed a reduced corrosion performance, which would release ions into the body. Hence, the biocompatibility of the metals was ranked from Ta, Nb, Ti, Zr > Al > 316L > Mo. This highlights the limitations of *in vitro* cytotoxicity testing as systemic effects of these metals are not considered and Al, which is known to cause systemic neurotoxicity, is rated as relatively 'biocompatible'.

Ti, Nb, Ta and Zr are concluded as most biocompatible by the majority of studies [117-119], however contention still exists concerning other elements. For example, Zhang et al. [117] assessed 17 elemental metals for cytotoxicity, cell proliferation, cell morphology and cell protein activity with osteoblast-like cells (SaOS2) and found Cr to be part of the biocompatible elements, whilst Song et al. [118] assessed just cytotoxicity with mouse fibroblast cells (L-929) and found Cr to be highly cytotoxic. Zhang et al. [117] also found that V, Mn, Fe, Co, Ni, Cu and Zn caused severe cytotoxicity, whilst Rae et al. [119], studying the effects of elemental particulates, agrees that Ni and Co were cytotoxic but Cr, Fe and Mo were only mildly cytotoxic. Sakai et al. [120] also investigated the cytotoxicity of elemental particulates and found even Ti, Nb, Ta and Zr to be highly cytotoxic to MG-63 osteoblast-like cells. However, Kuroda et al. [121] concludes that the size of the metal particulates has a strong effect on results, and found Al, Ti and Zr to by cytotoxic, whilst Ta, Nb and Cr were not. This makes the studies very difficult to compare as Rae et al. [119] do not quote the particulate size used, Sakai et al. [120] use a range of particle sizes from 1 – 150 µm and the lowest particle range Kuroda et al. could practically use for their study was 5 – 23 µm [121].

Comparing biocompatibility studies is fraught with variation in experimental methods. Different cell lines [122], different material preparation such as particulate size [121] and different biocompatibility measures, all contribute to varying conclusions. In addition, *in vitro* biocompatibility testing is very limited as, when implanted in the body, the material will come into contact with much more than one cell type, and any ions or particulates which are released from the metal can cause systemic effects in other areas of the body. A set of testing regimes must be developed for AM materials including both *in vitro* and *in vivo* testing of materials in preparation states which reflect AM implants in the body. This should include particulate cytotoxicity testing of particles representing the size of the stock material used in processing, as well as direct contact testing across a range of cell types.

In conclusion, the majority of studies find Ti, Ta, Nb and Zr to be most biocompatible, whilst Co, Cu, Mo, Ni and V seem to be least biocompatible (see Table 2-6). This is supported by a recent literature review which investigated the cytotoxicity of a range of β Ti alloys and concluded Nb, Ta and Zr were most prevalent in the least cytotoxic titanium alloys [123]. As toxicology studies further develop, it is likely that the definition of biocompatible constituents will develop further, and it is important to be flexible in alloy design to accommodate these future changes.

Table 2-6: Ranked cytotoxicity of β phase stabilising elements based on in vitro *investigations.*

Ranking of cytotoxicity	**β phase stabilising elements**	**References**
Lowest cytotoxicity	Ti, Ta, Nb, Zr	[116-120]
Medium cytotoxicity	Fe, Cr, Mn, Zn, Sn	[119, 120]
Highest cytotoxicity	Co, Cu, Mo, Ni, V	[116-118]

2.1.3 Bioactive Metals

The need to reassess the use of Ti-6Al-4V due to toxicity concerns of Al and V provides an excellent opportunity to design Ti alloys for implants which have constituents that not only improve the mechanical properties of the material but are also beneficial to their surrounding biological environment. Some metals have been classed as 'bioactive' due to their ability to encourage healing or because they display antibacterial properties. These metals are not just inert in the body, like Ti-6Al-4V, but actively provoke a beneficial biological effect. Examples include Ag and Cu, which exhibit antibacterial properties and could reduce the failure of implants due to infection, Mg, which already exists as a trace element in the body and degrades leaving porous structures to be filled by bone and Ta, which shows an enhanced osteogenic response, improving implant stability.

Recently, additions of Cu and Ag to implant alloys have been investigated due to the antibacterial effect of these elements. Studies of 1 – 6 wt.% Cu additions to Ti-6Al-4V have shown antibacterial effects for Cu contents greater than 4 wt.% [124, 125], however Krakhmalev et al. [126] found only 1.38 wt.% Cu was effective to reduce bacterial growth in a Ti-6Al-4V additively manufactured alloy [126]. Cu additions also strengthened the alloy and increased corrosion resistance. A 4.5 wt.% addition of Cu to 316L also showed good antimicrobial behaviour but resulted in lower corrosion resistance [127], suggesting antimicrobial Ti alloys are the more promising alloy class. Ag additions have also been investigated in Ti-6Al-4V, however 0.5 wt.% additions were found to reduce the strength of the alloy [125]. Cu was deemed the more effective additive as it had a stronger antibacterial effect, increased alloy strength and decreased the elastic modulus of Ti-6Al-4V slightly from 114 GPa to 110 GPa. The anti-bacterial mechanism of Cu and Ag additions in alloys is still disputed, however two possible mechanisms dominate discussion; metal ion sterilisation, which relies on metal ion release from the alloy, and contact sterilisation, which suggests some metal compositions disrupt membrane proteins and ion channels in the bacteria, causing death. A recent investigation by Shi et al. [128] suggested that for Ti-Ag alloys antibacterial activity was caused mainly by contact sterilisation with Ti_2Ag particles, though ion sterilisation was also still present. A new anti-bacterial mechanism has also been reported for Ti-Mg composites which suggested the formation of a microscale electric field between the galvanically different Ti and Mg which inhibits bacterial attachment [129].

Mg alloys are also of interest as bioactive implant materials due to their ability to safely biodegrade in the body. The recommended daily intake of Mg is 4.43-6.00 mg/kg/day for an average 70kg human [130], as Mg is essential to maintain bone health and lower the risk of cardiovascular disease. A bone scaffold made of Mg could provide this requirement for Mg intake, whilst degrading and being replaced entirely by natural bone tissue, removing the need for revision surgeries or the possibility of stress-shielding complications in the future. However, degradation of Mg in the body results in the creation of hydrogen gas, which can cause problems for biological systems if not carefully controlled.

Controlling the degradation rate is crucial and is a balance between the need for sufficient mechanical properties with the correct surface area to degrade at the desired rate. One approach to maintaining this balance is the creation of Ti-Mg composites which leaves porosity on the surface of the titanium matrix as the Mg degrades [131-134]. This leaves an interconnected porous network to encourage bone regeneration but also retains sufficient mechanical properties during degradation. More recently, Li et al. [135] have shown that careful topological design of scaffolds using additive manufacturing can control scaffold degradation rate *in vitro*, removing the need for the Ti component and allowing complete regeneration of bone.

Ta has been highlighted in literature as a bioactive metal which encourages bone growth and healing when in direct contact with bone [136]. Originally employed in wire form as a skin suture material, Ta showed such promising bioinert behaviour that it was heavily used in applications from nerve repair to cranioplasty to radiopaque markers. However, studies during the 1980s and 1990s which highlighted the osteogenic capability of Ta brought this metal forward for bone applications [137-140]. Due to its physical characteristics (e.g. high density, hardness and melting point) Ta remained restricted in its use in medical devices until the early 2000s when Trabecular Metal™ (TM) (Figure 2-4) was introduced by ZimmerBiomet. A new manufacturing method of chemical vapour deposition (CVD) was introduced, where thin layers of Ta (approximately 50 µm) were deposited onto a carbon scaffold [140]. The 75 – 80% porous scaffold possessed similar strength to cortical bone (60 MPa), similar elongation to cancellous bone (5%) and an elastic modulus between that of both types of bone, at 8 GPa [141]. The interconnected porous network also allowed for fluid flow, which is critical for bone ingrowth [142]. Since its introduction, TM has been used in over 800,000 surgeries [143], mainly in hip [144-148], knee [149-152], spinal [153, 154] and dental applications [155-159]. The clinical results highlight the good osteogenic and non-toxic behaviour of the TM material [160] however there has been no direct comparison to Ti or Ti-6Al-4V implants manufactured using the same method. Only recently have there been investigations directly comparing the osteogenic capability of Ta and Ti which show an improved bone response on Ta, though the attributed mechanism is still unknown and will be discussed in Section 2.4.3.

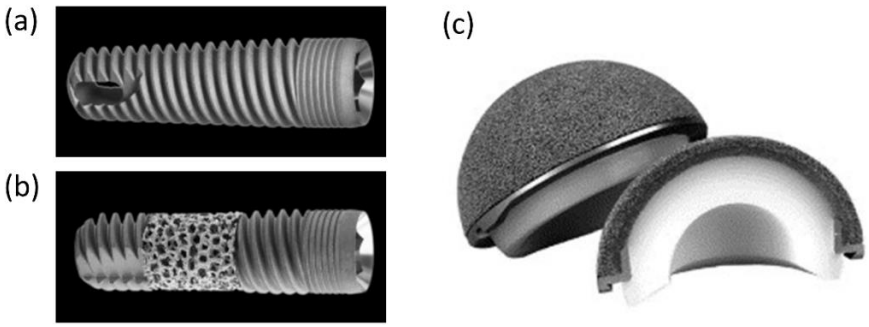

Figure 2-4: Biomedical devices made from pure titanium and Trabecular Metal™ (pure tantalum). (a) Pure titanium tooth implant and (b) pure titanium tooth implant with improved Trabecular Metal™, adapted with permission from [31] (c)Trabecular Metal™ acetabular cup, reproduced with permission from [150].

Nb has also been recently highlighted as a possible bioactive osteogenic metal [28]. Nb and Ta are very similar and were only chemically distinguished from one another in 1864 [76]. The largest difference between the two metals is their density (see Table 2-3). Ta is almost twice as dense as Nb, and hence less suitable for large implants. However, Ta has been used clinically since 1940 [30] and Nb only began to appear in the medical field in 1977 as an additive to Ti alloys [53]. As a result, the toxicology information on niobium is much more limited than Ta [76]. In addition, direct comparisons of the osteogenic capability of Ta and Nb are even more rare than Ta and Ti. One *in vivo* study found Nb was less effective at osteogenesis compared to Ta and Ti when coated on a polycarbonate scaffold and inserted into a rat tibia [138], however a second *in vivo* study found that Nb was more effective at osteogenesis compared with Ta and Ti when wires were implanted in rat bone marrow [28]. More direct comparative studies between these metals are required to ascertain the magnitude of osteogenic benefit for each metal and the mechanisms behind this benefit. Due to its thorough medical history and more accessible toxicology information, tantalum was chosen over niobium as the osteogenic bioactive material for this study.

When Ta is added to Ti, the resulting alloys can display a low elastic modulus, are likely biocompatible proven by the thorough medical history of both Ti and Ta, and may display bioactive qualities, due to the enhanced osteogenic response of Ta [136]. In addition, these alloys possess a lower density than pure Ta, better mimicking the lightweight characteristic of bone than TM. The TiTa alloy system is hence a very promising new biomedical alloy for orthopaedic devices. However, combining Ti and Ta is not easy. Titanium begins to boil and evaporates intensely at the temperature that Ta begins to melt (3000 ° C) [77]. A homogeneous solid solution of TiTa alloys can only be produced with multiple arc melting steps, which are inverted between melting steps to mixing the widely different density metals [36, 87, 91, 161]. The resulting ingot is difficult to machine into the complex shapes required for implants, as the material has high strength and hardness. In addition, machining results in waste material which becomes a major factor when using higher cost constituents.

Additive manufacturing (AM) is an emerging manufacturing method capable of exploring new alloy systems, by mixing elemental powders, and capable of producing complex geometries, impossible to produce with conventional machining. AM provides a new method for investigating TiTa alloys, avoiding large scale batch homogeneities, by beginning with a micron sized powder and melting with a laser on a micron scale. It remains to be shown whether these alloys, when produce by AM, retain their biocompatible status and the improved osteogenic qualities of pure Ta.

2.2 Additive Manufacturing

Additive manufacturing (AM) is a viable manufacturing method for bespoke implants, benefiting patients through exact matching and replication of their bone shape, which leads to better implant stability and performance [21, 162]. Complex geometric features, such as hollow structures and lattice work, can also be added to implants to improve their performance and expensive materials can be explored, due to less material waste than conventional manufacturing processes, such as computer numerical control milling. AM differs from conventional manufacturing as it is an additive as opposed to a subtractive process. Material is added to a part in layers, as opposed to a subtractive machining from a large ingot. AM is also possible over a wide range and combination of materials through different AM techniques; binder jetting, directed energy deposition, material extrusion, material jetting, powder bed fusion, sheet lamination and vat photopolymerisation. Each method requires an energy source (e.g. laser, electron beam or heated nozzle) and a material stock (e.g. metal/ceramic powder, liquid polymer resin, thermoplastic filament) which can be formed, melted or cured in a sequential layer-by-layer manner.

2.2.1 Types of Metal AM

For metal powder processing, the two main methods are directed energy deposition (DED) and powder bed fusion (PBF). An E or L preceding the naming acronym indicates an electron beam or laser power source [163]. L-DED systems, Figure 2-5(a), comprise of a nozzle which can move in three axes and carries feedstock wire or powder in a stream of gas into the path of a laser beam, where it is melted directly onto a substrate or existing part. Due to the free moving nozzle, DED systems can build and repair parts up to meters in scale and is considered ‘high throughput’ due to the high rate of material deposition. Large laser spot sizes on the mm scale are used with large feed powders of up to 100 µm in particle diameter [164]. As DED is a ‘high throughput’ system, it is well-suited to alloy development as many different alloy compositions can be produced in a short amount of time. In addition, multiple powder feeders can be connected to the nozzle and their feeding rates altered, to instantaneously create new alloy compositions and gradient structures. However, due to the large laser spot size and large particle diameter, DED systems cannot achieve the high dimensional tolerances needed for implant applications.

L-PBF systems, Figure 2-5(b), comprise of a chamber of metal powder and build plate arranged sequentially. The powder is spread layer-wise onto the build plate via a powder spreader and the laser, controlled by a series of mirrors, follows a scan path dictated by the computer-generated slice file. The powder delivery system is then raised, the build plate lowered, and another layer of powder is spread over the solidified material. The laser spot size is generally less than 100 µm and powders between 10

– 50 µm in particle diameter are used. This configuration facilitates dimensional tolerances and features of < 200 µm [164]. The downside here remains that, due to the small powder size and powder spreading mechanism, the deposition rate is much lower than DED. In addition, as the metal powder needs to be inside the working chamber before the process begins, premixing of powders is required before the printing process.

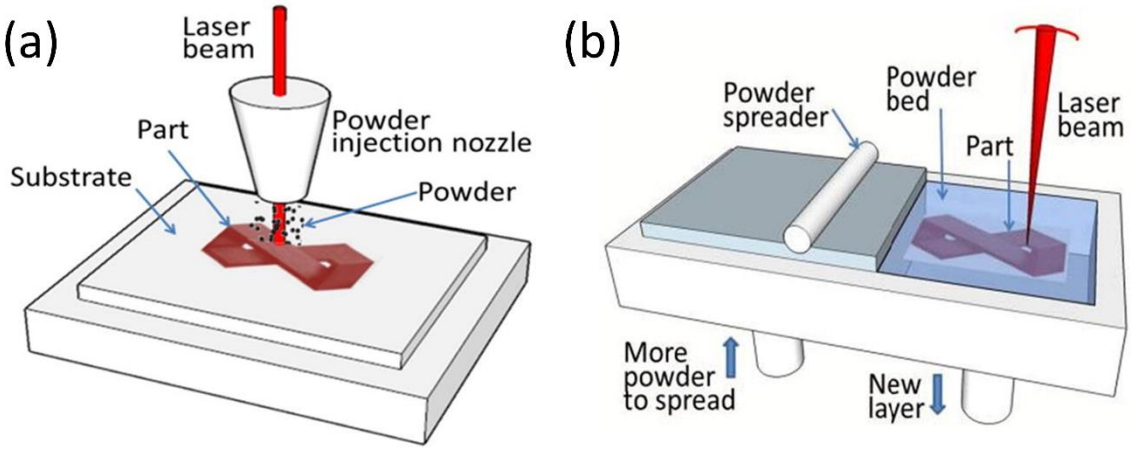

Figure 2-5: (a) L-DED and (b) L-PBF schematic. Reproduced in part with permission from [164].

To investigate new alloys in metal AM processing, the feedstock powders can be in either pre-alloyed or pre-mixed form. Pre-alloyed powders are created from gas atomisation of a pre-alloyed ingot, whilst pre-mixed powders consist of mechanically mixed elemental powders. Pre-alloyed powders have the benefit of producing more homogeneous material [165-167], as homogenisation occurs during ingot fabrication. However, pre-alloyed powders are difficult to acquire for all but a few common alloy compositions, e.g. Ti-6Al-4V, 316SS, IN718, AA6061 and H13 steel. Therefore, pre-mixed powders are more suitable for investigating new alloy systems.

Refractory elements, such as Nb, Mo, Ta and W which act as β stabilizers in Ti alloys, are difficult to form into powder due to their high melting temperatures. New methods of plasma atomisation are required to produce spherical powders from these materials [168]. This leads to high powder costs, with the Ta powder for this study costing $2000 AUD/kg.

2.2.2 Parameter Optimisation in L-PBF

The initial aim in additive manufacturing of a new material is to find adequate process parameters to achieve high quality material. For L-PBF systems, laser scanning speed (*v*), laser power (*P*), hatch distance (*h*) and layer thickness (*t*) are the most frequent parameters adjusted. The hatch distance is the distance between two adjacent laser passes, as shown in Figure 2-6. The layer thickness is dependent upon the vertical distance moved by the build plate, the surface roughness and shrinkage of the previously processed layer and is integral in ensuring the connectivity between the solidified layers. Many AM studies use 'energy density', Eq. 1, to model the combined effect of these parameters on material density as a single variable [164, 169, 170]. Generally, a low energy density causes insufficient melting of the material, resulting in 'lack of fusion' defects. Too high energy density can cause material vaporisation which leads to 'keyhole' defects. These defects can be differentiated by their shape, as 'lack of fusion' defects tend to be irregular and often between layers, whilst 'keyhole' defects show round or conical formation, mimicking the shape of a gas bubble at the bottom of the melt pool [164, 171, 172].

$$E = \frac{P}{vht} \tag{1}$$

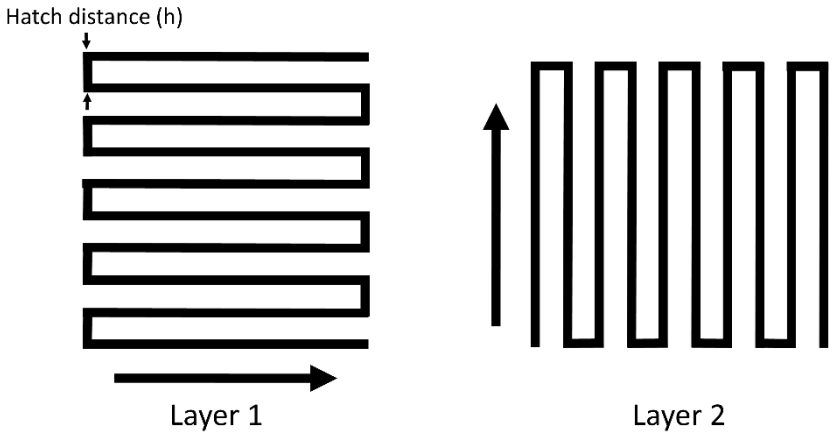

Figure 2-6: A typical scanning pattern used in L-PBF and L-DED processes. The hatch distance (h) is the distance between two adjacent laser scans.

The energy density equation, however, is limited, when used to model L-PBF processes, particularly in the case of mixed powders. The equation does not include variables which represent elemental specific variables such as thermal conductivity, elemental diffusivity and absorption of laser radiation by the powder and hence does not allow a quantitative comparison between processing of different alloys. Furthermore, alloys which contain elements with significantly different chemical properties often experience preferential vaporisation of the lower melting point constituent [171, 173, 174] and the

energy density model has no capacity to address this processing difficulty. As Ti melts at approximately 1600 °C whilst Ta melts at approximately 3000 °C, close to the temperature at which Ti boils and evaporates intensely [77], the energy density equation is unlikely to be a representative parameter optimisation model for this alloy system.

The normalised enthalpy model, Eq. 2, proposed by King et al. [175], incorporates powder specific variables, such as absorption of the laser radiation by the powder (A) and thermal diffusivity (D), as well as chemical specific variables incorporated in the enthalpy term h_s, Eq. 3, such as melting temperature (T_m) and thermal conductivity (κ). Additionally, the model includes the laser spot size (∅), critical to the powder-laser interaction. The normalised enthalpy model predicts a region at which material vaporisation is likely to occur, called the 'keyhole zone'. This zone occurs at normalised enthalpy values of 30 ± 4. There has yet been no investigation as to whether this model is appropriate for modelling mixed powder alloys such as TiTa.

$$\frac{\Delta H}{h_s} = \frac{AP}{h_s\sqrt{\pi D v \emptyset^3}} \quad (2)$$

$$h_s = \frac{T_m \kappa}{D} \quad (3)$$

2.2.3 L-PBF Scanning Strategies

In addition to achieving dense material, it is important for many applications to obtain homogeneous material. This is more difficult for powders with refractory components and more difficult for pre-mixed powders than pre-alloyed powders. Generally, heat treatments such as hot isostatic pressing (HIP) are used to improve the quality of AM material post-processing. However, this incurs more time and cost for part production. By making adjustments to parameters and scanning strategies, *in situ* heat treatments can be achieved improving material density, surface finish, alloy homogeneity microstructure and mechanical properties [168, 176, 177].

One strategy which can be used to increase the homogeneity of an AM produced alloy is 'remelt' scanning. This consists of two passes of the laser per powder layer, providing a second opportunity for element melting and mixing and could prove an essential processing method for the TiTa system to increase material homogeneity.

The remelt scan has been investigated as a tool to increase part density, by allowing gas release from previously formed pores [168, 177-181], as well as to increase surface quality, by allowing a second liquid metal flow to fill surface unevenness [182-184]. However, applying a second laser scan per layer also alters the thermal history of the part and results in microstructural changes. The most noted change is that the remelt scan can cause a finer grain structure [180, 185, 186]. It is hypothesised that as the

laser interacts with a pre-solidified metal surface, instead of a layer of powder, there is a decrease in laser absorption and hence a shallower melt pool is formed. No thermodynamic and microstructural modelling has yet been completed to assess this hypothesis.

The remelt scan has also been assessed as a tool to reduce residual stress in AM parts. Due to the high cooling rates experienced in PBF, parts often retain a high level of residual stress. Literature studies show that remelt scanning can be employed to reduce residual stress, however the efficiency depends on the scanning parameters used [178, 187-190]. Studies exploring remelt scans, using different scanning parameters for the single and the remelt scan, show that the remelt parameter set can be optimised to decrease residual stress [187-189]. However, studies using identical scanning parameters for the remelt scan show an initial increase in residual stress in the range of 22 – 68 % upon the application of one remelt scan [178, 187, 190]. It is suggested that this is due to a slight increase in cooling rate upon the first remelt scan, due to the lower laser absorption and subsequent smaller melt pools. With subsequent remelt scans, the residual stress begins to decrease, eventually reaching values below that of the single melt sample. Upon subsequent remelt scans, it is hypothesised that the part begins to accumulate heat, hence reducing thermal gradients and lowering the cooling rate.

Remelt scanning has shown to both increase and decrease the tensile strength of L-PBF Ti-6Al-4V [178, 187]. Xiao et al. [178] found that applying one to three remelt scans successively increased the strength and decreased the ductility of the material. This was attributed to strain hardening induced by multiple rapid heating and cooling cycles. Upon the fourth remelt scan, however, it was found that the strength once again decreased and this was attributed to retained heat in the material causing annealing. Strain hardening strengthening caused by the remelt scan is supported by the findings of Wei et al. [190] who noted no increase in strength in remelt material after the samples had been stress relieved. Ali et al. [187] also found that a single remelt scan would slightly increase material strength and decrease ductility, however when the energy density of the remelt scan was reduced, a drop in material strength and increase in ductility was observed. It was hypothesised that the remelt scan changed material density, induced phase transformation from α' to $\alpha + \beta$ and increased the oxide layer thickness, which all contributed complexly to mechanical property changes. An increase in oxide thickness on the surface of remelted parts [184] and phase transformations [191] have been observed in other studies investigating the effects of remelt scanning.

Remelt scanning can be used to alter the microstructure and mechanical properties of L-PBF produced alloys and optimising the remelt scan parameters is complex when considering not just porosity, but residual stresses and oxide complications. A small number of studies have been performed investigating the remelt strategy as a homogenisation tool [126, 167] and no study has been done investigating this tool for use in the TiTa alloy system. Remelt scanning is a promising new strategy for the increase in

homogenisation of alloys with refractory constituents, however the effects of this strategy on microstructure and mechanical properties is so far limited.

2.3 Mechanical Properties of Additively Manufactured Titanium Alloys

Implants under lower stresses, such as mandible reconstruction plates, require less static strength than implants under high stresses, such as hip stems. Currently only two alloys are used to represent all implants within this stress scale; CP Ti is used for low stress applications whilst Ti-6Al-4V is used for high stress applications. As a result, the strength of the Ti-6Al-4V alloy often overshoots the mechanical properties required for the application. As high strength is often linked to high elastic modulus, high strength implants are more likely to cause stress-shielding. AM of new biomedical Ti alloys introduces the prospect of tailoring specific alloys for specific implant applications. Coupled with advances in mechanical modelling of physiological forces, implants could be designed which much more closely represent their mechanical environment. As accurate physiological models are still under development, the mechanical properties of new L-PBF produced Ti alloys must be compared to conventionally produced CP Ti or Ti-6Al-4V.

2.3.1 Quasi-Static Mechanical Properties of AM Ti Alloys

Due to the high cooling rates in L-PBF processing, microstructures possess high dislocation densities, resulting in higher strengths but lower ductilities than their conventionally cast counterparts. In addition, unique metastable microstructures can be formed, as well as fine grain microstructures which contribute to higher strengths. L-PBF Ti alloys generally consist of plate-like α or α′ acicular grains, which nucleate out of columnar prior-β grains oriented in the building direction [192, 193]. This is due to the strong thermal gradient between the melt pool and the cold build plate. The columnar grain structure, however, leads to anisotropic mechanical properties, as the lack of grain boundaries in the build direction provide less boundaries for dislocation slip. Methods to tackle the columnar grain structure include the inclusion of grain refinement particles such as boron, and heating of the build plate. Studies of L-PBF produced CP Ti also highlight the need for oxygen level testing [60, 193-195]. Most studies begin with a Grade 1 or Grade 2 powder, however depending on the L-PBF process, different levels of oxygen can be picked up during printing, resulting in higher strengths [194]. To accurately assess the strength of L-PBF produced Ti, it is important to assess the oxygen content after printing.

Ti-6Al-4V is one of the most investigated additive manufacturing alloys, due to its use in the biomedical and aerospace industries, and significant data is available for the mechanical properties of this material produced by L-PBF [174, 178, 192, 196, 197]. As can be seen from Table 2-7, the tensile strength of

L-PBF Ti-6Al-4V can reach as high as 1400 MPa in the as-built condition, 400 – 500 MPa higher in strength than conventionally wrought or cast Ti-6Al-4V. However, the ductility of the material is severely reduced to 1.6%, which severely impacts the applicability of the material for fatigue applications. The lower strength but improved ductility and lower elastic modulus of β type alloys benefit from L-PBF processing as fine grain structures can increase strength in as-built materials, without increasing elastic modulus and whilst retaining a much higher intrinsic ductility than Ti-6Al-4V.

Table 2-7: Mechanical properties of additively manufactured biomedical Ti and Ta alloys.

	Manufacturing Method	**Elastic Modulus (GPa)**	**Yield Strength (MPa)**	**Tensile Strength (MPa)**	**Elongation (%)**	**Reference**
CP Ti (Gr I – IV)	Conventional	103 - 104	170 - 586	240 - 662	20 - 30	[60]
Ta	Conventional	186	165 - 220	200 - 390	20 - 50	[60]
Ti-6Al-4V	Conventional	101 - 110	795 - 875	960 - 965	10 - 15	[54]
CP Ti (Grade I,II)	L-PBF	91 - 104	353 - 587	413 - 800	7 - 25	[60, 193, 194, 198-201]
Ti-6Al-4V	L-PBF	94 - 118	910 - 1330	1035 - 1400	1.6 - 11	[196]
Ti-15Mo	L-DED	73	-	-	-	[202]
Ti-15Mo-5Zr-3Al	L-PBF	69	-	-	-	[203]
Ti-20Mg-5Ta	L-PBF	43 - 72	747 - 989	763 - 1089	13 - 20	[204]
TiNb (26 - 45 wt.%)	L-PBF/L-DED	61 - 85	768	683 - 799	11 - 22	[166, 167, 205-210]
Ti-Nb-Zr (TNZ)	L-PBF	65 - 85	756 - 874	916 - 1155	2 - 7	[211-213]
Ti-Nb-Ta-Zr (TNTZ)	L-PBF	64	520	680	15	[214, 215]
Ti-24Nb-4Zr-8Sn (Ti2448)	L-PBF/EBM	53	563	665 - 950	14 - 28	[173, 216, 217]
Ta	L-PBF	-	450 - 654	739	2	[60, 218]
Ti10Ta	L-PBF	110	730	780	11	[219]
Ti25Ta	L-PBF	89	1029	1186	5	[220]
Ti30Ta	L-PBF	72	920	950	10	[219]
Ti50Ta	L-PBF	76	883	925	12	[221]

Only a few of β Ti alloys have been thus far explored using additive manufacturing. As with Ti-6Al-4V, the literature shows that the mechanical properties of the L-PBF material exhibit slightly higher strengths than conventional processing methods, but with retained low elastic modulus and reasonable ductility [166, 173, 211, 213, 214, 217, 220]. A few L-PBF studies record significantly higher strengths than conventionally processed material [211, 220]. One example of the L-PBF processing of the TNZ alloy showed a maximum strength of 1155 MPa [211], almost double the strength achieved through conventional processing. However, the increase in strength was attributed to the formation of the ω phase which also significantly decreased the material ductility to 2%. The most promising mechanical properties achieved to date are by Yan et al. [204] in a very recent study which showed how a novel cross-scanning strategy could produce nano sized grains in a Ti-20Mg-5Ta alloy. The alloy showed strengths similar to conventionally produced Ti-6Al-4V, whilst retaining elongations of up to 20% and the lowest elastic modulus yet achieved by L-PBF, 43 GPa. The novel cross-scanning strategy shows promise for improving the mechanical properties of L-PBF materials and possibly for increasing the melting of refractory constituents, as almost all the other studies highlight the difficulty of fully melting components such as Nb and Ta [204, 210, 221-223].

Despite its refractory nature and high cost, pure Ta has been successfully printed using L-PBF to densities of > 99.8% [218, 224-226]. High laser powers of 200 – 400 W are often required to prevent inter-layer porosity due to insufficient melting, and mechanical failure is often attributed to crack initiation at these defects [218, 226]. Studies of mechanical properties show yield strengths two to three times larger than that of cast material, attributed to grain refinement [218, 224], Table 2-7. Unfortunately, the ductility is also reduced from 40% to 2%, for solid material, however a compressive ductility of 35% was observed when lattice structures of 80% porosity were created [225]. This may be due to the microstructural differences between solid and lattice material. Ta forms a β phase microstructure and shows a strong crystallographic texture when printed, resulting in mechanical property anisotropy [224]. The porosity of lattice structures likely disrupts the strong thermal gradients in the building direction. The Ta lattices were considered more applicable to cyclic loaded implants than pure Ti, due to its higher normalised fatigue strength [60].

L-PBF provides a new unique manufacturing method to combine Ti and Ta by melting them on a micron scale. The two most investigated compositions in literature are Ti25wt%Ta [220] and Ti50wt%Ta [219, 221, 227, 228]. The Ti25Ta composition reportedly has the best strength-to-modulus ratio of the TiTa system [84], whilst the Ti50Ta composition has the lowest Ta content to produce a fully β phase microstructure in conventional manufacturing [63]. Sing et al. [221] were the first to successfully fabricate Ti50Ta by L-PBF, using pre-mixed CP Ti (Grade 2) and pure Ta powders. It was shown that a fully β microstructure was obtained, formed of equiaxed grains, however some partially melted Ta particles remained within the matrix. The volume of unmelted Ta particles was not quantified, making predictions, concerning how these particles will affect mechanical behaviour, difficult. The mechanical

properties of this composition were promising, showing an improved yield strength (883 ± 20 MPa) compared to L-PBF CP Ti (620 ± 20 MPa) and improved ductility (11 ± 1%) compared with L-PBF CP Ti and L-PBF Ti-6Al-4V (5 ± 1% and 6 ± 3%, respectively). The improved ductility was linked to the absence of strain hardening due to the lack of the α′ phase. Parameter optimisation studies also showed that a higher input energy improved the melting of Ta, however full incorporation of Ta was not achieved [228]. Optimal parameters for Ti50Ta were found to be P = 460 W, v = 500 mm/s, h = 0.125 mm and t = 0.05 mm, with an 80 µm laser spot size. These parameters result in an energy density of 147 J/mm^3.

Zhao et al. [220] more recently investigated Ti-xTa (x = 6, 12, 18, 25 wt.%) which showed a gradual increase in yield strength with increasing Ta content from CP Ti at 560 ± 13 MPa to Ti-18Ta at 668 ± 20 MPa. However, at the Ti25Ta alloy, a significant jump in strength to 1029 ± 8 MPa was noted. This jump in strength was attributed to the fine grain size and quantities of the β phase, as the Ta content supressed the α′ formation, however no other literature studies have noted β phase at this composition. This study used ball milled spherical CP Ti Grade 1 powder with an average particle size of 30 µm, and smaller irregular Ta powders with an average particle size of 3.66 µm, which may have contributed to enhanced solid solution strengthening, however also led to low relative densities achieved, below 95%, due to the irregular particle flow. In addition, despite the small Ta particle size, remaining partially melted Ta particles were still noted in the matrix, and were hypothesised to act as heterogeneous nucleation sites for small grain formation. The optimal parameters for the Ti25Ta alloy were found to be P = 340 W, v = 1200 mm/s, h = 0.07 mm and t = 0.05 mm, with an 80 µm laser spot size. These parameters result in an energy density of 81 J/mm^3.

Huang et al. [219] investigated Ti-xTa (x = 10, 30, 50 wt.%) and found the Ti30Ta alloy to be most favourable for biological applications due to its highest yield strength (925 ± 10 MPa) and lowest elastic modulus (72 ± 10 GPa). The strength was seen to increase with increasing Ta content as the lath/acicular phase refined but strength decreased at 50 wt.% Ta when the coarse β phase was retained. The Ti30Ta alloy showed a combination of α″ and α′ phases, with partially melted Ta particles present in the matrix, which caused reduction in elongation. The same process parameters were used for each composition and the porosity was found to increase with Ta content from 0.04 to 0.47 % due to insufficient melting.

The L-PBF TiTa alloy system requires further investigation to address the inconsistencies in tensile behaviour and microstructure reported in these few papers. In particular, the α′, α″ and β phase boundaries in L-PBF TiTa alloy system remain disputed. Differences are possibly due to the different printing systems and parameters used and a thorough database of material properties and quality must be made to understand how these materials will behave and pinpoint their optimal processing parameters. The difference in ‘optimal’ energy density, 147 J/mm^3 [221] and 81 J/mm^3 [220] for Ti25Ta and Ti50Ta respectively, highlights that the energy density equation is not particularly suitable for

modelling the optimal process parameters for the L-PBF TiTa system. As higher energy density is required to melt higher Ta contents, it is inconsistent that the optimal energy density for the Ti50Ta is lower than that of the Ti25Ta alloy.

2.3.2 Fatigue of L-PBF Materials

Understanding the fatigue performance of biomaterials is critical for reliability of cyclically loaded implants. AM materials are known to be inferior in fatigue performance to conventionally produced materials due to the presence of internal defects, stresses and rough surfaces [229-231]. Whilst post-processing methods such as milling, micro-machining and HIP are known to increase fatigue life, many AM parts are created in complex geometries which cannot by fully processed. Hence, it is important to understand the as-built fatigue response of AM parts.

The high residual stresses present in as-built AM parts results in less damage resistant parts [232-234]. Residual stresses are relieved when the part is removed from the build plate [188], however depending on part material and size, further stress relieving treatment is required. Chastand et al. [235] found 4 hr of heat treatment at 640 °C was sufficient to relieve stress in L-PBF Ti-6Al-4V parts and return comparable fatigue behaviour to EBM Ti-6Al-4V parts, which were deemed to not have residual stress, due to the heating the build platform and chamber during the printing process. Other methods to reduce residual stress in building is to use scanning strategies such as, island scanning, where each large surface area scanned by the laser is broken down into smaller segments [187, 236, 237], or remelt scanning [187, 189, 190]. In addition, heated build plates can be used to lower the thermal gradients between the melt pool and built platform [188, 189], however not all L-PBF systems have this functionality. Samples which are electro-discharge machined (EDM) from a bulk printed sample are also believed to be somewhat stress relieved, though the exact quantification of remaining stress is still debated [238-240]. In conclusion, it is important when comparing fatigue properties of L-PBF materials to estimate their residual stress state by considering their manufacturing history.

Process-induced porosity, particularly at the surface of AM specimens where stresses are highest, leads to premature fatigue failure [197, 232, 241-243]. Defects act as stress concentration points, resulting in earlier crack formation. Whilst hot isostatic pressing (HIP) can be used to decrease the final defect concentration, investigations into real time print monitoring systems [164, 244] and modelling of defect dependant mechanical properties [245-247] are addressing the reliance on post-processing treatments. Rough surfaces are also detrimental to fatigue life [197, 229, 230, 248], and can be removed by post-process machining for simple shapes, but is not possible for complex geometries such as lattices. Remelt scanning has been shown to effectively reduce surface roughness [182-184], however, for implant applications, surface roughness is seen as crucial to successful implant integration. Rougher surfaces

provide better mechanical interlocking between the bone and the sample, as well as encouraging superior osseointegration [249-251]. Hence, it is important to investigate both as-built and machined surface conditions, to find a balance between fatigue life and biological behaviour.

The fatigue behaviour of Ti-6Al-4V is the most widely studied of L-PBF Ti alloys, with fatigue strengths at 10^6 cycles of 100 – 250 MPa [60, 242], superior to that achieved in L-PBF CP Ti and Ta (see Table 2-8). This is attributed to the higher strength of Ti-6Al-4V obtained on precipitation strengthening. However, when normalised by yield strength, CP Ti and Ta both outperform Ti-6Al-4V. Due to their superior ductility [60], CP Ti and Ta perform particularly well in the high-cycle fatigue regime (> 10^6 cycles) where crack propagation dominates fatigue failure. Porous Ta structures even showed a higher absolute value of fatigue strength when compared with porous Ti-6Al-4V structures (7.35MPa to 4.18 MPa, respectively) [252]. This was attributed to increased ductility lowering the notch sensitivity in a structure which has a high surface area. Ti-6Al-4V, which has a high notch sensitivity [253], does not perform particularly well in lattice configurations as early crack formation occurs at multiple sites within the lattice. More ductile metals, such as CP Ti and Ta are more suitable for implant applications which include complex geometries and undergo lower bodily stresses, such as maxillofacial implants.

Table 2-8: Fatigue life of L-PBF Ti alloys.

	Elastic Modulus (GPa)	**Yield Strength (MPa)**	**Tensile Strength (MPa)**	**Elongation (%)**	**Fatigue Strength at 10^6 cycles (MPa)**	**References**
TNTZ	64	550	680	15	225	[214]
Ti-6Al-4V	94 - 118	910 - 1330	1035 -1400	1.6 - 11	100 - 250	[60, 196, 242]
Ta	-	450 - 654	739	2	120	[60, 218]
CP Ti (Grade I,II)	91 - 104	420 - 555	500 - 800	8 - 25	82	[60, 193, 194, 198-200]

There is little literature investigating the fatigue behaviour of new β-type Ti alloys. However, one study by Luo et al. [214] shows promising fatigue properties for the low modulus TNTZ alloy. Despite a much lower yield strength than Ti-6Al-4V (TNTZ = 500MPa and Ti-6Al-4V = 900-1300 MPa, see Table 2-8), the heat-treated TNTZ samples showed a similar fatigue strength at 10^6 cycles of 225 MPa. No explanation was given for this impressive fatigue behaviour. It was, however, noted that the fatigue limit of the L-PBF TNTZ was much lower than conventionally produced material, due to the inherent processing shortfalls of AM on fatigue life noted earlier. However a promising study investigating the fatigue behaviour of conventionally produced TNTZ showed that small (0.1 - 0.7 wt.%) additions of

oxygen to the TNTZ alloy increased the fatigue performance of this alloy, without significantly raising the elastic modulus of the alloy [97]. Oxygen additions have not yet been investigated in L-PBF TNTZ alloys, however, provide a likely mechanism for further improving fatigue behaviour. As yet, there have been no investigations into the fatigue life of the AM TiTa alloy system.

2.3.3 Mechanical Properties of Lattice Structures for Implants

One of the main benefits of AM implants is that complex geometries, such as lattice structures, can be incorporated in the implant design to improve their mechanical and biological functionality. Therefore, it is important to understand how the new β type Ti alloys function when formed in these complex structures. Beam-based lattice structures, triply periodic minimal surfaces and graded designs are all made possible with AM and open a new avenue of mechanical response which is not dependent simply upon the mechanics of the material, but a combination of the mechanics of the material and the structure. The designs are referred to as 'meta-materials' and are critical in bridging the mechanical property gap between synthetic materials and natural bone [254].

Most investigations into the mechanical response of lattice structures have focused on beam-based structures, which consist of a repeating unit cell, such as cubic, diamond, and dodecahedron structures [61, 171, 255-258]. Lattices can be classified into stretch-dominated and bending-dominated unit cells, which determines their failure mechanisms. Stretch-dominated structures tend to shower higher stiffness and strength at low weight, whilst bending-dominated structures show a lower stiffness and strength but accommodate much larger strains [259]. Cubic lattices with vertical struts, such as FCCZ design, tend to show stretch-dominated behaviour whilst lattices lacking vertical struts, such as BCC, show bending-dominated behaviour [255, 258]. In both cases, stress concentrations are highest at the lattice nodes, which undergo plastic deformation under compression [61]. The porosity of these lattice structures is used to lower their elastic modulus similar to human bone, as the elastic modulus of the structure follows the power-law relationship, Eq. 4, where ρ represents the lattice relative density and the power law exponent b is close to 1 for stretch-dominated unit cells and equal to 2 for bending-dominated unit cells [259, 260].

$$E = \sigma_y \, \rho^b \tag{4}$$

Using this design ideology, lattice structures have been created by L-PBF in both conventional and new β-type biomedical alloys which show elastic modulus levels that mimic the range of natural bone (see Table 2-9). However, there is still a large range of fields to be investigated considering the manufacturing and mechanical response of these lattices. For example, the strongest Ti-6Al-4V lattices still cannot mimic the strength of the strongest bone found in the body (usually found in the long bones

of the tibia and femur) and the ductility of these structures, even in compression, is limited to 3.5 – 5.0% [61]. In conjunction with the limited surface finishing techniques available, fatigue life of these structures is unreliable. Further research is also required for parameter optimisation for lattice struts, as most studies show a large variation between CAD and the final printed geometry [61, 222, 254, 261-264], as well as porosities within the struts acting as critical points of failure [265]. In addition, the microstructure has been found to be dependent on the geometry used and can be markedly inhomogeneous across the structures [255, 265]. Finally, whilst the structural elastic modulus has been reduced to levels similar to natural bone, a single cell will only experience the elastic modulus of the surface it is attached to, and not the entire structure. The elastic modulus of a substrate is known to effect cell fate [266], and it is not understood how the difference in material modulus from conventional alloys to new β-type alloys can affect cell behaviour on a much smaller scale.

Table 2-9: Mechanical properties of L-PBF lattice structures with different geometries.

	Elastic Modulus (GPa)	**Yield Strength (MPa)**	**Porosity (Designed/Actual)**	**Structure Type**	**References**
Cortical Bone	13 - 35	85 ± 10	-	-	[54-56]
Cancellous Bone	0.02 - 2	25	-	-	[54, 57, 58]
Ti-6Al-4V	22 - 58	160 - 520	25 - 64% (12 - 51%)	Schwartz (TPMS)	[267]
	0.6 - 13	10 - 250	15 - 50% (18 - 58%)	Diamond	[268]
	0.9 - 7	14 - 200	15 - 50% (22 - 53%)	Neovius	[268]
	1.1 - 4	27 - 130	15 - 50% (21 - 51%)	Gyroid	[268]
	0.6 - 3.5	16 - 92	(69 - 84%)	Dodecahedron	[252]
	3.2 - 6.4	92 - 276	43 - 77% (35 - 71%)	Primitive, gyroid, diamond (TPMS)	[269]
CP Ti	0.6 - 2.6	9 - 37	(66 - 82 %)	Dodecahedron	[60]
	1.5 - 2.7	45 - 57	(68 - 73 %)	Gyroid (TPMS)	[270]
Ta	1.2	12.7	(80%)	Dodecahedron	[225]

Elastic modulus is not the only important feature to investigate in lattice structures for implants. The size and shape of the pores in the structure, as well as their interconnectivity, also has a strong effect on tissue formation. It has been shown that bone is more likely to regenerate in concave shaped pores, and the higher the curvature, the faster the tissue regeneration [271-273]. This has led to investigations into new structures called triply periodic minimal surfaces (TPMS) (see Figure 2-7). TPMS locally minimise surface energy, which results in an equivalent mean curvature of zero, a structure frequently seen in nature which leads to a unique combination of topological, mechanical and mass transport properties [269]. Studies investigate the balance between sufficient mechanical properties and increased permeability of the scaffold to allow nutrient flow and cell migration [269, 274, 275] and recent investigations into L-PBF of these structures have shown promising biological and mechanical results, with improved strength-to-modulus ratio [269] and excellent fatigue endurance of 60% of their yield strength [269]. Comparatively, beam-based unit cells tend to show a fatigue endurance limit of 20 – 30% of their yield strength [256, 276]. This improvement is attributed to TPMS structures being less affected by processing defects than beam-based structures [277].

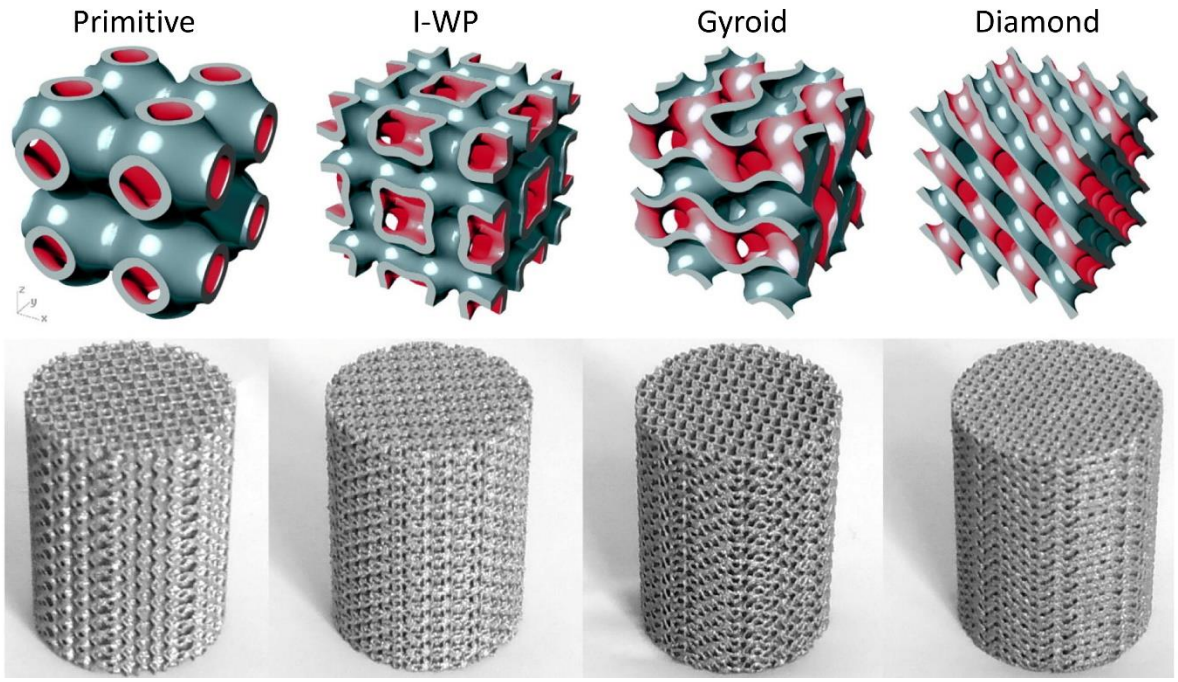

Figure 2-7: Functional scaffolds designed for biological applications. Reproduced with permission from [269].

2.4 Biological Response of TiTa Alloys

New alloys have been developed and manufactured by AM that can simulate similar mechanical properties when tested *in vitro*. However, the human body is a dynamic and complex environment, raising many more requirements to a suitable new alloy, than mechanical properties. It was previously mentioned that the design of new biological alloys includes considerations of 'biocompatibility' and 'bioactivity' of the alloy and its constituents. The following section explores the definitions of these words and the experimental methods used to determine their properties. The section will then explore the literature investigating the bioactivity of pure tantalum, pure titanium and TiTa alloys, and how the presence of Ta may lead to a superior orthopaedic alloy to Ti-6Al-4V. The hypothesised mechanisms causing the improved osteogenic capability are then discussed.

2.4.1 Biocompatibility: from bio-inert to smart materials

Determining the 'biocompatibility' of materials is a complex field. It requires collaboration of materials engineers and scientists, cell biologists and clinicians, and is a constantly developing area of research. Since the synthetic materials were first used as implant materials, the definition of 'biocompatible' has developed significantly.

For first generation biomaterials, biocompatibility was generally defined as materials which did not cause an adverse systemic reaction in the body or trigger an immune response [278]. These materials are classed as 'bio-inert', although they may still trigger a 'foreign body' response from the body's immune system which results in fibrous capsule formation (Figure 2-8). The fibrous capsule separates the material from the surrounding tissue and systemic environment of the body. For metallic implant materials, achieving first generation biocompatibility comes down to the systemic toxicity and cytotoxicity of the metal in its solid or corroded state. Hence, first generation biocompatible metals are generally highly corrosion resistant; e.g. stainless steels, CoCrMo and Ti alloys. This stops metallic leachables or particles from entering surrounding tissues and interfering with biological processes. However, fibrous capsule formation effectively separates the implant material from surrounding tissue, which is problematic when trying to create a strong implant-tissue interface, such as is required for orthopaedic implants.

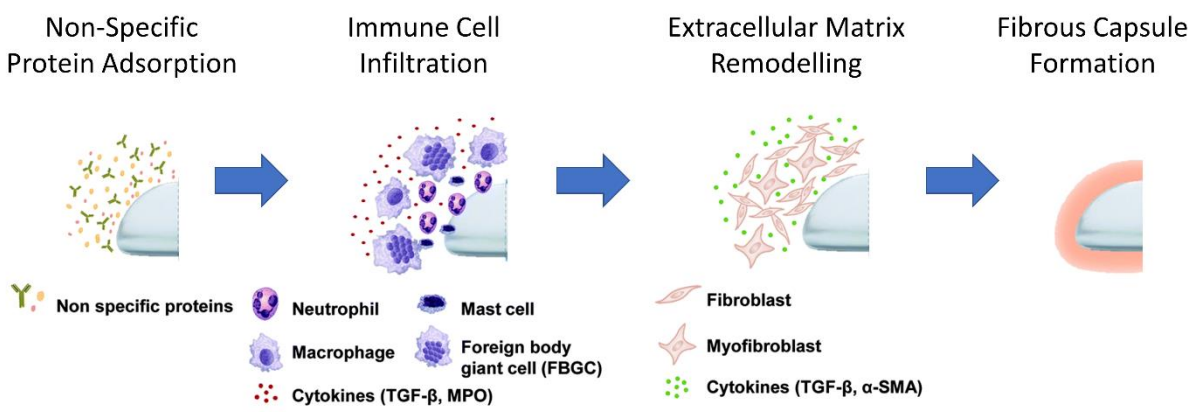

Figure 2-8: Mechanisms of fibrous capsule formation. Adapted with permission from [279].

Second generation biomaterials attempt to elicit a positive and controlled reaction from surrounding tissues, critical for implant osseointegration [280]. TiTa alloys may provide a benefit over the current industry standard material of Ti-6Al-4V because Ta is highlighted as a bioactive metal, due to its increased ability for osseointegration [136]. This class also includes resorbable materials, such as Mg alloys [131-134], which are designed to be resorbed by the body and replaced by local tissue, and anti-bacterial alloys, such as Ti-Ag and Ti-Cu [124-129], which are designed to reduce infection rates upon implantation.

Third generation biomaterials attempt to stimulate and regenerate functional tissue. Here, the freedom of design in AM allows for the creation of scaffolds which can be penetrated by regenerating bone. Hence, the bioactivity of the base material is aided by the implant structure to encourage the body to regenerate tissue. If TiTa alloys provide enhanced bone formation, scaffolds of this material may further improve bone regeneration throughout an implant, leading to improved stability. Other investigations of third generation biomaterials include coatings which include biological molecules that stimulate bone growth [281, 282] and fully degradable magnesium bone scaffolds. Whereas Ti implants will always remain in the body and hence not allow for complete tissue regeneration, fully degradable magnesium scaffolds could eventually be completely replaced by regenerated tissue.

Finally, fourth generation biomaterials are often termed ‘smart biomaterials’ [283]. These materials aim to replicate the complex structural hierarchy of natural materials. For bone, that consists of re-creating the structure of bone from nano sized hydroxyapatite crystals, to micro scale fibril bundles and finally the macro scale porous and dense transition of cancellous to cortical bone, Figure 2-9. Whilst AM has advanced to printing with multi-material feedstocks, printing with complex materials, such as live cells, to create live tissues is still in its infancy [38]. Bioprinting uses ‘bio-inks’ which generally consist of hydrogels, live cells and sometimes growth factors, however limitations still exist in that cells are often damaged due to heat or shear stresses during printing and creating vascularised tissue remains a large

challenge [38, 284-286]. It is likely that bulk non-degradable metals will have little future in this area as stock material as printing with living cells, ceramics and collagen, the natural building blocks of bone tissue, will become more possible.

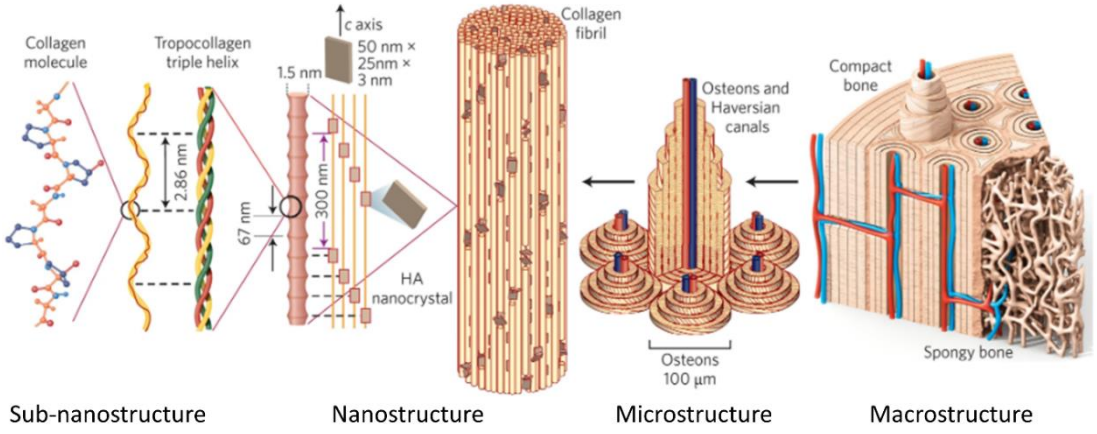

Figure 2-9: Hierarchical structure of bone. Adapted with permission from [287].

In conclusion, 'biocompatible' materials have developed, and continue to develop, from 'bio-inert' to 'bioactive' to 'regenerative' to 'smart'. As more materials are developed in the 'bioactive', 'regenerative' and 'smart' categories, it is likely that simple 'bio-inert' behaviour will no longer be considered biocompatible. Hence, the days of Ti-6Al-4V as a biocompatible material are likely numbered, and new materials which help tissue regeneration will replace it. A first step to this could be additively manufactured TiTa alloys, which offer the bioactive nature of tantalum and complex scaffold structures to encourage local bone tissue regeneration. This solution could significantly increase the success rate of bone implant devices, allowing time for research into new 'smart' materials and manufacturing methods, which is still in its infancy, but could eventually replace the need for metallic implants altogether.

2.4.2 Experimental Techniques for Determining 'Biocompatibility' and Osteogenesis

As the definition of 'biocompatible' materials develops, so do the experimental methods used to evaluate a material's suitability to be used in the body. Whilst some standards exist for *in vitro* testing of biomedical materials, such as ISO 10993-5 Tests for *in vitro* cytotoxicity and ISO 10993-4 Selection of tests for interactions with blood, there is often still great variability in results due to cell line, type or passage used [122]. Sometimes where the cell type is specified, the cell type is unrepresentative of the material's future environment, such as using fibroblasts (connective tissue cells) for a cytotoxicity study of an orthopaedic material, and hence studies choose a more preferable cell type, such as osteoblast precursors [54, 123, 288] or osteosarcoma cells [87, 219, 289]. There is no chapter within the ISO 10993 standard for *in vitro* osteogenic testing. This is likely why many *in vitro* test results do

not agree with the results of subsequent *in vivo* studies. For example, Zadpoor et al. [290] found that lower porosities in bone scaffolds were superior to bone formation when tested *in vitro*, however higher porosities produced better bone formation *in vivo*. This highlights the need for development of new biocompatibility standards, particularly when considering new AM scaffold materials. In addition, care must be taken when comparing literature studies which investigate the different biological behaviour of Ti and Ta metals.

Cytotoxicity is the most common *in vitro* testing method used to determine a material's 'biocompatibility'. The standard ISO 10993-5 [291] describes procedures for testing in direct contact to or with liquid extracts from biomaterials using a colorimetric MTS or MTT assay, which relies on the cells to metabolize a yellow water-soluble reagent into a blue-violet insoluble formazan product. The optical density of the solution in contact with the cell-seeded test material (OD_s) is compared with the optical density of a cell-seeded positive control solution (OD_c), Eq. 5. This value represents the 'cell viability' and is interpreted as a comparative representation of how many cells are left alive after contact with the test material. Measurements are generally taken over a period of 7 days to assess whether the cells proliferate normally over that time period. A viability of < 70% is generally used to indicate that the material has cytotoxic potential, whilst the shape of proliferation curves can indicate if cells are proliferating similarly on each sample.

$$Viab.\% = \frac{100 \times OD_s}{OD_c} \tag{5}$$

The amount of reagent metabolized on each sample, and hence the optical density of the solution, is affected by more factors than just the *cytotoxic* behaviour of the material. For example, how many cells attach to each sample, how quickly the cells proliferate on each sample and the speed of cell metabolism can all affect viability readings [122]. Hence, care should be taken when observing 'viability' data and further experimental techniques, such as individual cell counting and normalisation of proliferation data by cell attachment number, should be used to verify viability data. In addition, a control curve should be used for each cell type, line and passage to give an indication of the metabolic rate. For AM produced scaffolds, cell attachment often plays a key factor in affecting viability data, as scaffolds with larger surface areas tend to have more cells attach, and hence show false higher viability readings.

Investigating the osteogenic potential of new biomaterials *in vitro* is often explored through cell morphology and chemical markers. The study of mechanotransduction investigates how mechanical cues from the external microenvironment are sensed by a cell and how these forces alter biochemical signalling within the cell, which in turn alters cell fate [292]. Cells attach to a substrate via transmembrane receptors called integrins and cluster together to form focal adhesions, which link the external substrate to the internal actin cytoskeleton of the cell, Figure 2-10. This network of proteins is

essential for the cellular sensing of the mechanical properties of the substrate to which the cell is attached, and results in conformational changes in the proteins. These structural changes activate the intracellular signalling cascades which determine cell fate [293, 294].

Cell attachment is a highly complex system, combining both mechanical and biochemical cues and hence there can be multiple mechanisms to activate a particular signalling pathway and cell fate. In the context of bone formation and osseointegration, high tension in the actin filaments activates pathways which lead to osteogenic behaviour, but this can be achieved through starkly different cell morphologies. For example, topographical grooves directed osteogenic differentiation in stem cells by elongating the cell, increasing its aspect ratio and inducing higher tensile forces [295]. However, simply measuring a higher aspect ratio does not always mean improved osteogenic differentiation. Lee et al. [296] found a lower aspect ratio (2:1) but complex concave shaped pit was more effective for osteogenic differentiation than a high aspect ratio (12:1) oval. Generally, more spread cells have higher tension which is seen as a good sign for osteogenesis, as well as suggesting a strong interaction between the cell and the material [288, 294, 295]. Hence, measures of cell area and cell shape can be useful in determining osteogenic capability of a substrate material.

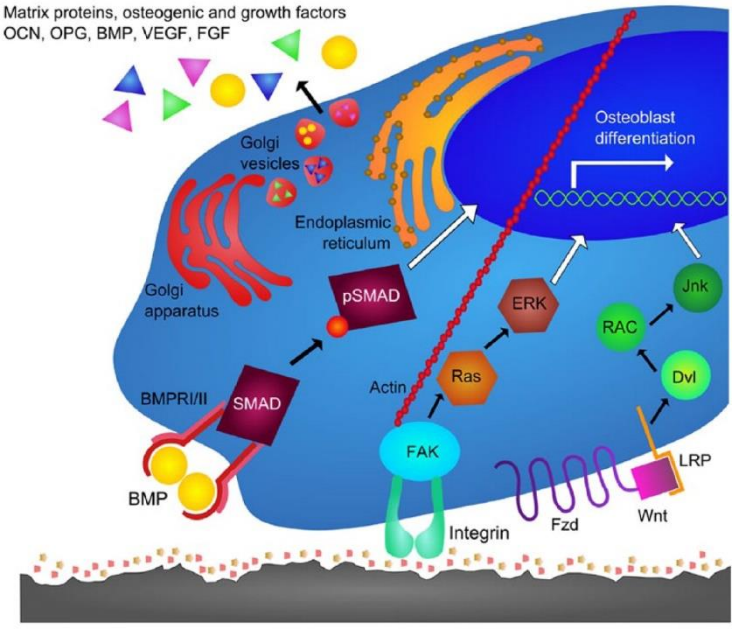

Figure 2-10: Cell attachment mechanisms. Reproduced with permission from [293].

The biochemical markers induced by the attachment mechanics of the cell can also be measured to indicate osteogenic behaviour. However, the genetic markers are dependent upon the cell type used in the experiment. The most common cell types used to study osteogenic behaviour are osteoblasts (mature bone cells), pre-osteoblasts (stem cells which have already committed to the osteogenic pathway) and mesenchymal stromal or stem cells (MSCs) (cells with differentiation capacity to bone, fat and cartilage

cells). An MSC differentiating into a pre-osteoblast and then an osteoblast expresses different levels of genes at different stages of its differentiation. The earliest markers for osteogenesis noted in MSCs and pre-ostoblasts include RUNX-2, osterix and alkaline phosphatase (ALP). RUNX-2 is the master transcription factor which upregulates many of the following markers, whilst osterix (OSX) is trigged after RUNX-2 and ALP is present throughout the early stages of osteogenesis. Later chemical markers for osteogenesis which are produced by pre-osteoblasts and mature osteoblasts are osteonectin (ON), osteocalcin (OCN) and osteopontin (OP). These late chemical markers lead to the formation of mineral deposits on the substrate surface [297].

Genetic markers can be measured through reverse transfection polymerase chain reaction (qRT-PCR) assays, whilst Western Blotting is used to measure protein markers [295, 296, 298-301]. Furthermore, colorimetric p-nitrophenol (pNP) assays investigate ALP activity, whilst late mineral formation can be detected by Ca or phosphate staining and imaging [29, 288, 295, 302, 303]. Early markers are assessed within one week of cell seeding whilst late markers are assessed after three to seven weeks. Increased levels of early and late osteogenic markers generally indicate enhanced osteogenic behaviour, however, like the viability measure, quantitative gene expression and mineral formation is affected by the number of cells present and hence these measures should be normalised to DNA content where possible. Furthermore, the validity of these *in vitro* measures of osteogenesis are disputed. A study from Hulsart-Billström et al. [304] investigated 93 different biomaterials over 36 *in vivo* and 47 *in vitro* studies. The *in vitro* studies measured osteogenic capability through ALP activity, RUNX2 expression and mineral formation, whilst the *in vivo* studies assessed bone regeneration in animal models. A poor correlation was found between the *in vitro* and *in vivo* osteogenic capabilities, highlighting the inadequacies of current *in vitro* assessments and the importance of *in vivo* validation. Despite this lack of correlation, *in vitro* testing is critical to reduce the burden on animal testing and for rapid clinical translation of new materials.

In vivo testing requires scaffold implantation in animals, followed by animal sacrifice and measurement of regenerated bone within the implant. Due to the high financial and ethical cost of animal testing, few *in vivo* studies exist for AM metallic scaffolds [225, 250, 305-308]. Histology is often used to assess bone formation, through sectioning and staining of the sliced implant, however this requires sacrifice of the test animal. Wauthle et al. [225] were the first to show successful bone integration into a porous Ta AM implant, with histology analysis showing regenerated bone almost completely bridging the 6 mm bone defect after 12 weeks. However, no CP Ti or Ti-6Al-4V implant was used in comparison to show relative osteogenic behaviour. More recently, Micro Computed Tomography (Micro-CT) has been used to provide an accurate ratio of bone volume within the scaffold after implantation [305]. Guo et al. [305] showed increase bone volume in L-PBF produced Ti-Ta-Nb-Zr scaffolds when compared directly with identical Ti-6Al-4V scaffolds. This remains the only *in vivo* study to directly compare

bone formation in a new AM β Ti alloy with identical scaffolds in either Ti-6Al-4V or CP Ti and is a promising sign for increased osteogenesis and improved implant stability from new β Ti alloys.

In conclusion, *in vitro* testing is important for basic cytotoxicity testing and can provide crucial insights into cell behaviour, through analysing cell morphology. However, *in vivo* experiments rarely mimic the positive osteogenic results found *in vitro*. This highlights the need for further research into methods of *in vitro* osteogenic assessment and improvements in the *in vitro* testing pipeline, to more effectively translate newly developed possible osteogenic materials to clinical applications.

2.4.3 Review of Biological Comparison Studies of Ti, Ta and TiTa Alloys

Since the introduction of Trabecular Metal™ by ZimmerBiomet, it is been claimed in many studies that Ta shows superior osteogenic properties to pure Ti or Ti-6Al-4V. Both *in vitro* and *in vivo* studies have been conducted to investigate this claim, however, due to the inconsistencies and unreliability of osteogenic testing mentioned above, it is important to evaluate the experimental methods of these studies critically. In addition, pinpointing the cellular mechanisms which differ for cells and tissues in contact with Ti and Ta should indicate the fundamental mechanisms that govern the osteogenic behaviour of Ta, allowing this to be applied to other biomaterials.

A review of *in vitro* studies which directly compare the osteogenic capability of Ti and Ta substrates showed that the majority (12 out of 16) conclude that Ta shows improved osteogenic properties related to either higher cellular area or volume, higher expression of bone markers and/or higher mineralisation [116, 288, 300, 309-317], Table 2-10. The remaining 4 out of 16 studies conclude that there was no statistical difference observed between Ta and Ti for the majority of these measures [29, 117, 318, 319], however each of these studies does note at least one difference in behaviour between Ta and Ti substrates. 12 out of 16 of the studies also highlight an improved adhesion and/or proliferation of cells to Ta substrates. This could suggest that the improved osteogenic response on Ta surfaces is simply due to the presence of more cells colonising the implant surface, rather than a direct pro-osteogenic effect. However, 6 out of 9 studies also noted a higher cellular area or volume on Ta surfaces. Cell area and volume cannot be affected by attachment numbers, whilst higher proliferation is more likely to lead to smaller cell areas, as less space is left available for the cells to spread when arranged in higher density. The higher cellular area and volume may suggest a stronger interaction between the cell and the Ta substrate, allowing the cell to form more anchor points on the surface. The result of this higher spreading is increased internal tension, which causes osteogenic differentiation [288, 294, 295]. This is supported by the 12 out of 14 studies which noted chemical changes through a higher expression of at least one genetic marker for osteogenesis, or in another cellular mechanistic area (e.g. mitochondrial activity or immuno-profile). 9 out of 11 studies note higher mineralisation on Ta surfaces, including 4 studies

which investigated increase bone volume *in vivo*. These results strongly support the improved osteogenic behaviour of Ta, and suggest the mechanism is due to the increased attachment and spreading of cells.

Table 2-10: Review of studies directly comparing the osteogenic response of Ti and Ta surfaces.

Ta Improved Osteogenic Behaviour? (Y/N)	**Cell Type**	**Increased attachment?**	**Increased proliferation?**	**Increased cell area?**	**Increased marker expression?**	**Increased mineral?**	**Ref.**
12/16		**12/16**		**6/9**	**12/14**	**9/11**	
Y	Pre-osteoblast (MC3T3-E1)	-	Y	Y	Mitochondrial activity	-	[116]
Y	Human MSC	N	N	Y	ALP	Y	[309]
Y	Osteoblast (hFOB)	Y (not differentiated)		Y	-	Y	[315]
Y	Osteoblast (hFOB)	Y (not differentiated)		Y	ALP	-	[314]
Y	Osteoblast (HOB)	Y	Y	-	OCN	Y	[320]
Y	Human BMSC	Y (not differentiated)		Y	ALP, RUNX2	Y (*in vivo*)	[310]
Y	Goat BMSC	N	Y	-	-	Y (*in vivo*)	[312]
Y	Rabbit Osteoblast	Y (not differentiated)		Y	ALP, Mitochondrial activity	Y (*in vivo*)	[317]
Y	Pre-osteoblast (MC3T3-E1)	Y (not differentiated)		-	ALP	Y (*in vivo*)	[316]
Y	Rat BMSC	Y	-	-	VCL, ITGα5, ITGβ1, Fn1, p-FAK-	-	[311]
Y	Rat BMSC	-	N	N	ALP, ITGα5, ITGβ1, RUNX2	Y	[300]
Y	Pre-osteoblast (MC3T3-E1)	Y	N		ALP, BMP-2, OCN, OPN	N	[288]
N	Osteoblast (NHBC)	N	N	N	RANKL, OPG	Y	[29]
N	Human MSC	Y	-	N	N	N	[319]
N	Human BMSC	N	-	-	Immuno-profile	-	[318]
N	Osteosarcoma (SaOS2)	Y	N	-	N	-	[117]

Due to the difficulty of conventionally manufacturing TiTa alloys, few *in vitro* and no *in vivo* studies exist for the TiTa alloy system. Furthermore, the *in vitro* studies aim to prove basic biocompatibility of the alloy system through cytotoxicity testing, without assessing improved osteogenic behaviour. Compositions ranging from 5 wt.% to 70 wt.% Ta have been investigated with colorimetric assays and it is concluded that there is no increase in cytotoxicity compared with CP Ti [139], no difference in cytotoxicity between different alloy compositions [321] and no increase in cytotoxicity when the alloys are heat treated [87]. Only one study investigated cell morphology and found no qualitative difference in cell morphology between cells cultured on the Ti5Ta alloy and the CP Ti control [139]. The low amount of Ta in the alloy studied is likely a contributing factor as to why no difference was observed. Each study claims that the TiTa alloys studied are 'biocompatible' as they do not show significant cytotoxic effects. However, this does not help to answer the question as to whether the TiTa alloys retain improved osteogenic behaviour compared with CP Ti, or what levels of Ta are required to induce this capability.

Additive manufacturing has significantly enhanced the capability of manufacturing TiTa alloys and studies investigating the biological behaviour of the TiTa alloy system are beginning to emerge. Taking advantage of the design freedoms capable in additive manufacturing, Huang et al. [219] used L-PBF processing to manufacture scaffolds using a basic cubic unit cell in Ti10Ta, Ti30Ta and Ti50Ta compositions. The biological investigation was conducted on the Ti50Ta alloy, in comparison to CP Ti and Ti-6Al-4V scaffolds, although the Ti30Ta alloy was deemed as most mechanically suitable for implant applications. Cytotoxicity testing through an MTT assay and live/dead staining showed no statistical difference in cell attachment at the 24 hr timepoint, or cell proliferation at the 7 day timepoint. The stronger adhesion and proliferation noted on pure Ta may be reduced by the lower content of Ta present, or the geometry of the scaffold interrupting the improved cell spreading capability. However, a second study which investigated Ta and Ti30Ta cold spray coatings on EBM manufactured Ti-6Al-4V substrates showed a significant increase in cell number on the Ti30Ta coating compared with Ti-6Al-4V and pure Ta [322]. As only image analysis is used to manually count cells, the study may have been biased by preferential imaging of regions with larger cell densities. In addition, mouse fibroblast cells were used, a very different cell type to those reviewed in Table 2-10. No indication is given as to why the Ti30Ta coating showed a 2.5-fold increase in cell attachment, compared with both Ti-6Al-4V and pure Ta, after only 6hrs of culture. In this study the Ta coating also showed equal cell attachment to the Ti-6Al-4V material, disagreeing with the previously surveyed literature.

In conclusion, it has been well established that the cytotoxicity of the TiTa alloy system is no worse than CP Ti or Ti-6Al-4V, and hence achieves a basic level of 'biocompatibility'. Studies which investigate the osteogenic behaviour of these metals have made little attempt to separate the initial number of cells attached with the following cell proliferation. This makes it difficult to assess whether the improved osteogenic capability of Ta surfaces is due simply to a higher number of attached cells.

However, supporting data of cell area and morphology, as well as expression of a variety of markers, indicate higher tension in the Ta-contacting cells which is leading to chemical responses within the cells. No studies have yet investigated whether the TiTa alloy system retains an osteogenic benefit compared with CP Ti or Ti-6Al-4V. Significant research is required to determine what level of Ta is required for an improved osteogenic response whilst balancing the composition with the changing mechanical properties.

2.4.4 Mechanisms for Improved Osteogenesis on Ta Compared with Ti

The mechanism by which Ta leads to improved osteogenesis is still unknown. Both material properties and cellular processes likely contribute and hence answering this question requires strong knowledge from both material science and biology. However, determining the mechanism could allow a mechanistic approach to improving osteogenic behaviour of other biomaterials. Current investigations by materials scientist explore the specific oxide surface energy of Ta which allows cells to wet surfaces to differing degrees, whilst biologists tend to highlight the chemical ability of Ta to up-regulate adhesion related genes through the specific cell-substrate attachment points.

The measure of wettability is often used to determine the comparative area of cell-substrate contact. A higher surface energy or hydrophilicity generally results in improved wettability. Surface energy can be increased by increasing surface roughness [323] or by changing the surface chemistry [315]. Ta surfaces generally show a more hydrophilic nature than Ti surfaces, often measured through contact angle testing [315, 319, 324] however various surface treatments can change this by altering topography [282, 325]. Contrary to other studies, Lu et al. [300] showed a lower hydrophilicity of Ta than Ti when testing polished surfaces of equal roughness cut from conventionally manufactured plate, suggesting the material manufacturing method may also contribute to surface oxide chemistry, altering the surface energy. Unfortunately, increased surface energy does not directly correlate to increased cell attachment [282]. Cell attachment is a combination of cell wetting and protein attachment, and hydrophobic materials attract more proteins. Hence, a complex balance is required between hydrophilic and hydrophobic nature to maximise cell attachment [326]. Hemmersam et al. [324] showed that Ti and Ta surfaces adsorbed different levels of fibrinogen protein depending on the concentration of protein in the solution applied. In addition, the adsorbed fibrinogen layer on each surface showed different affinities for antibodies, suggesting that the fibrinogen layer is likely oriented and/or denatured differently on each surface. Further understanding of the chemical and physical nature of oxide layers and their protein attached layers is required to elucidate the mechanism of improved osteogenesis.

The effect that the substrate surface has on the internal cell signalling may also provide the clue to improved osteogenic capability. Lu et al. [300] found that Ta surfaces up-regulated the α5 and β1

integrin expression and when α5 and β1 integrin expression was intentionally down-regulated, osteoblastic differentiation was severely impaired. This suggests that the ability of Ta to more strongly activate integrin production may be the cause of increased osteogenesis. Zhu et al. [311] made a similar conclusion finding thin film Ta surfaces up-regulated fibronectin, vinculin, integrin α5, integrin β1 and β-actin expression, all adhesion-related genes. Lu et al. [300] hypothesised that the surface metallic oxide and the integrins act as semiconductors. As the electronic band gap between titanium oxide and the integrins is more similar than that between tantalum oxide and the integrins, electron transfer is more likely to occur between titanium oxide and the integrins. This electron transfer may disrupt the integrin behaviour, and hence cause less integrin signalling leading to osteogenesis.

In conclusion, literature suggests that Ta has a superior interaction with cells compared with Ti. The increased interaction, possibly due to the surface energy of Ta oxide or increased integrin production and signalling, or a combination of both, may be the key to improved osteogenic behaviour. Increased cell and substrate interaction provides promising outlooks for improving implant behaviour by causing enhanced bone formation and minimizing bone implant interface micro-motion [327]. Future research into the interactions of cells and biomaterials can lead to more tailored surface modification strategies for implant materials to improve implant integration. However, with current knowledge, Ta shows promise as a bone implant alloy constituent and promises to further bioinert implant alloys such as Ti-6Al-4V to a more bioactive status. Additive manufacturing is now allowing Ta to be processed more easily and produced in alloys with Ti, making this alloy system more available for *in vitro* and *in vivo* testing. It is yet to be shown, either *in vitro* or *in vivo*, that the TiTa alloy system can provide the beneficial osteogenic capabilities of pure Ta, or whether certain levels of Ta are required to elicit this bioactive benefit.

2.5 Literature Review Summary

The current literature highlights the need to replace Ti-6Al-4V with more mechanically and biologically suitable alloys for implant use. The following gaps in theoretical understanding were identified:

- Wider biomedical alloy selection: Natural bone covers a range of strengths and elastic moduli. New alloys with a range of mechanical properties are required to suit the specific mechanical properties of bone for the required bone implant application.

- Bioactive alloys: Simply corrosion resistant alloys are no longer acceptable for implant alloys. The material must be able to interact in a positive way to its biological environment, for example, by aiding bone regeneration or reducing infection by inhibiting bacterial colonisation.

- Improved predictive capabilities for L-PBF modelling of parameter optimisation: Parameter optimisation for L-PBF is a costly process in both time and material. The energy density equation is not sufficient to describe a suitable parameter space for alloys comprised of components with very different melting characteristics. Parameter optimisation modelling must be further developed to include thermal characteristics of the elemental components of the alloy, particularly in the case of mixed powder alloy processing.

- New scanning strategies for processing of alloys with refractory components: Most L-PBF mixed powder alloys which contain a refractory component struggle to fully incorporate the refractory component into the material matrix. New scanning strategies are required to produce homogeneous material and the wider implications of remaining partially melted particles on mechanical performance must be investigated.

- Effect of new scanning strategies on microstructural formation and mechanical behaviour: New L-PBF scanning strategies will inevitably lead to new microstructures and hence mechanical behaviours. The microstructure and mechanical property relationship of the TiTa alloy system must be well understood for its reliable use in implant applications.

- Performance of L-PBF lattice structures: The surface roughness of L-PBF structures is known to decrease their fatigue performance. This is accentuated in lattice structures due to the large increase in surface area. In addition, L-PBF Ti-6Al-4V shows a low ductility which leads to high notch sensitivity and poor fatigue performance. More ductile β Ti alloys must be investigated to achieve an improved fatigue performance of lattice structures.

- Osteogenic potential of L-PBF TiTa alloys: Ta has been observed in multiple studies to enhance osteogenesis, however it is yet unknown whether L-PBF TiTa alloys will benefit from the improved osteogenic capabilities of its Ta component, or possibly what concentration of Ta is required to induce improved osteogenesis. Furthermore, the biochemical and mechanic mechanisms behind improved osteogenic performance on Ta surfaces remain unexplained.

This thesis aims to address the above gaps in current knowledge by investigating the TiTa alloy system as a possible new low modulus and bioactive alloy replacement for Ti-6Al-4V. AM processing of the TiTa alloy system will be investigated with a focus on the ability to process the refractory Ta component in conjunction with identifying the optimal alloy composition for bone replacements. L-DED and L-PBF TiTa alloys will be characterised for their microstructure and mechanical properties, and manufactured in lattice structures, the most applicable geometry for future AM implants. Finally, the alloys will be tested *in vitro* for their biocompatibility and osteogenic nature.

Chapter 3 Additive Manufacturing of the TiTa Alloy System

In order to identify new alloys which can be used for additively manufactured bone implants, the TiTa alloy system is explored to determine the most suitable compositions. This includes a theoretical exploration, using the ThermoCalc software, to determine possible phases at different compositions in conjunction with an assessment of the mechanical properties and phase fractions quoted in literature for the conventionally manufactured compositions. The TiTa system is then explored through the high throughput AM method of L-DED to manufacture a range of compositions, which can be analysed for their phase volume, microstructure and hardness. Whilst the thermodynamic conditions of L-DED and L-PBF processing, the AM method most suitable for implant application, are significantly different due their difference in physical scale, L-DED can still be used to give a unique insight into the laser-powder interactions and can be used to quickly create a range of alloys which can be screened for biocompatibility. From L-DED and ThermoCalc investigations, the Ti25Ta and Ti65Ta compositions are highlighted as most suitable for implant applications and are then explored through L-PBF processing. Parameter optimisation using single laser scan tracks and metallographically assessed porosity is conducted. A remelt scan strategy, consisting of a second laser pass identical to that of the first laser pass per layer, was investigated as a homogenisation tool and the volume of remaining unmelted Ta quantified for each sample to determine total homogeneity. Finally, predictions using the normalised enthalpy model are compared with the experimental results, to determine the applicability of the model for mixed powder TiTa alloy processing.

3.1 Theory of Alloy Selection

A low elastic modulus is possible in the TiTa system due to the β phase stabilising effect of Ta. Figure 3-1 displays the phase diagram of the TiTa system, as calculated by ThermoCalc software. As Ta atoms are added to Ti, the β phase is stabilised at lower temperatures. The β phase generally results in a lower elastic modulus than the α phase as the crystal structure has a lower atomic density [328]. Experimentally, it has been shown that the β phase can be entirely retained at room temperature by water quenching of alloys containing greater than 45 wt.% Ta [63]. AM techniques generally show very fast cooling rates, similar to quenching, however, the layer-by-layer process also generates repeated heating cycles through the already solidified material, which could lead to decomposition of the β phase.

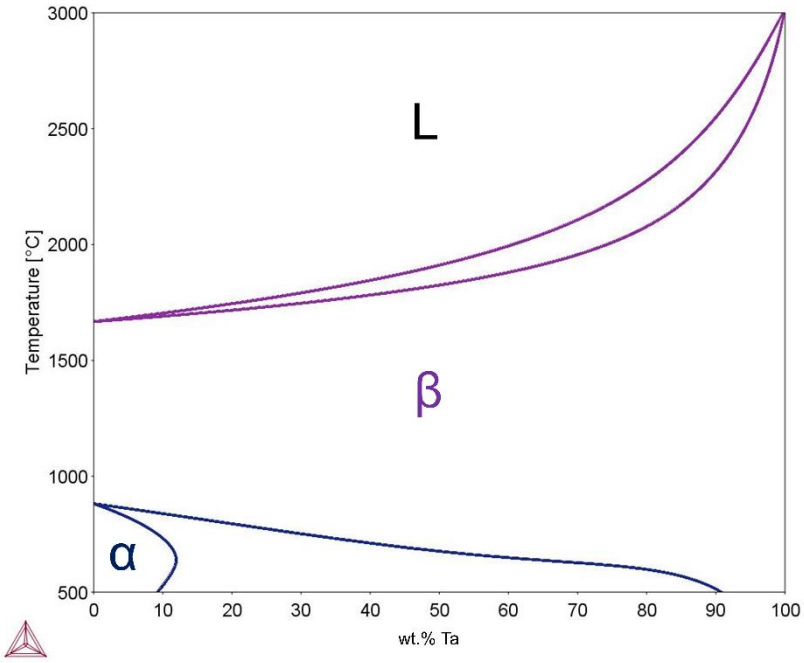

Figure 3-1: Phase diagram of TiTa system in wt.% calculated using ThermoCalc software.

In addition, the α phase exists in three different morphologies and structures. Equiaxed α grains can be formed by working and annealing of Ti in the α phase field. However, when quenched from the β phase field, an α′ martensitic phase forms, comprising of dislocation dense, parallel-sided laths. As the crystal structure does not alter between α and α′, there is little hardening effect caused by α′ martensite formation. Increasing the Ta content of the alloy will first result in the laths becoming smaller and cause degeneration of the ordered structure into individually oriented α′ laths [63]. With further additions of Ta of between 22 – 25 wt.% Ta [84-86], a phase change to α″ laths occurs, which have an orthorhombic crystal structure. This phase is responsible for the shape memory behaviour observed in many β Ti alloys.

These crystal structure changes result in changes in elastic modulus. Two minimum modulus points have been noted; at the boundary between the α′/α″ phases (~ 25 wt.% Ta) and in the fully β phase microstructure at (~70 wt.% Ta) [36], Figure 3-2. Zhou et al. [36] also noted that increasing solute content in the α′ phase increased tensile strength and reduced elastic modulus, whilst the opposite trend is noted in the α″ phase, shown earlier in Figure 2-3. Similar to the α″ phase, the β phase increases in modulus with increasing Ta content.

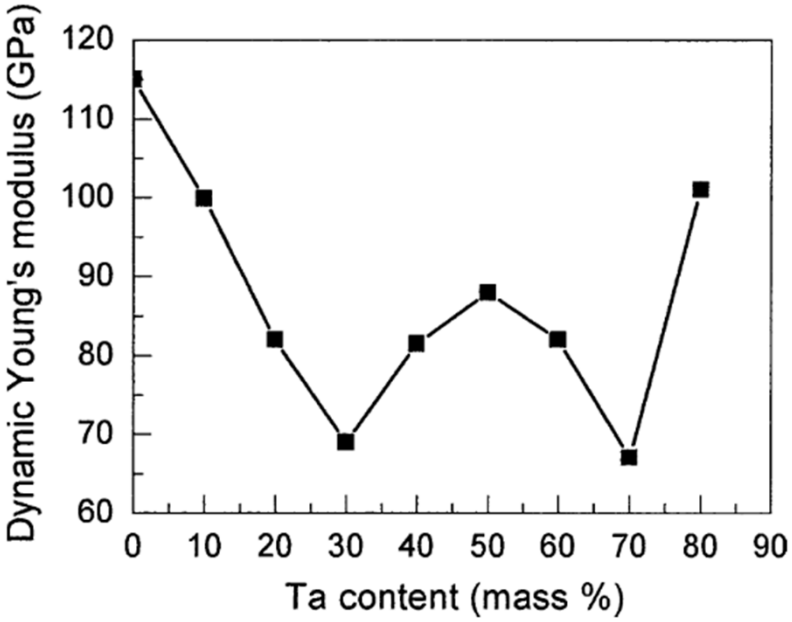

Figure 3-2: Variation of Young's (elastic) modulus with Ta content. Reproduced with permission from [36].

Therefore, it was concluded that the composition range from 30 – 70 wt.% should be investigated through AM processing techniques, beginning with L-DED high throughput processing.

3.2 Validation of Alloy Selection via L-DED High Throughput Screening

L-DED was used as a high throughput screening method to create a range of TiTa compositions, whilst investigating the process of laser melting of mixed powders. Whilst it is understood that the microstructures produced by L-DED are different from those produced by L-PBF processing, due to the different cooling rates and different laser spot sizes, L-DED processing can give a unique initial insight into laser-powder interactions and can quickly manufacture a range of TiTa alloy compositions which are suitable for preliminary biological testing. A similar L-DED approach was used by Nag et al. [329] who demonstrated that a gradient of Ta could be added to Ti through L-DED processing and presented the phase composition of the created alloys after β solutionising, followed by furnace or air

cooling. The as-built phase compositions of L-DED processed TiTa alloys have not been recorded in literature. Hence, in this study, a range of TiTa compositions will be created and their as-built phases investigated, and compared to the results of Nag et al. [329]. In this study, Ta and Ti powders were loaded into separate powder feeders, and the powder feedrate and carrier gas flow altered to create sample cubes in pure Ta, pure Ti and a range of TiTa compositions. The layer height, the vertical distance moved by the nozzle between each layer (z), and the laser power were also altered in order to maximise the height of the solidified sample during printing. Further parameter optimisation was not undertaken as L-DED processing experiences very different thermal conditions to L-PBF, which will ultimately be used for implant manufacture.

Samples were manufactured using a TruLaser Cell 7040 (Trumpf, Ditzingen, Germany). The TruLaser Cell 7040 consists of a nozzle, moveable in x, y and z directions, which is used to print directly onto an appropriate substrate, secured to a table within the printing chamber, Figure 3-3. Powders are fed from the powder hoppers to the nozzle, through tubing carrying helium gas streams. The powders are fed evenly into the tubing using a groove on a rotating disc, and hence powder feedrate is measured in revolutions per minute (rpm). The flow rate of the helium gas stream, measured in litres per minute (L/min), can also be adjusted to increase or decrease powder fed into the path of the laser, and hence alter deposition rates. The powder feedrate and carrier gas flow are used to alter the ratio between deposition of Ti and Ta, and hence create TiTa alloy compositions.

Due to the reactive nature of Ti and the 3 beam nozzle available, printing was conducted in an argon filled bag. A plastic bag was attached to a circular plate around the nozzle head, Figure 3-3 (a), and printing conducted once the bag was inflated, Figure 3-3 (b). An O_2 monitor was used to ensure the oxygen content within the bag remained below 50 ppm and was attached to the circular plate around the nozzle head. New coaxial nozzles available have additional capabilities of feeding a separate shield gas to the print area through a separate gas stream, however the argon bag set-up used in this study provided better atmosphere protection to the entire build plate during extended part cooling. The 4 kW disk laser used was a 1064 nm Nd:YAG with a 2 mm spot size.

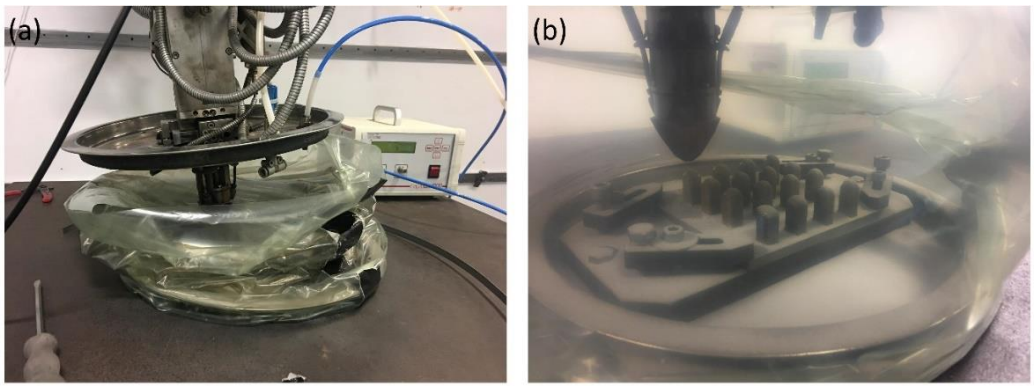

Figure 3-3: L-DED reactive material set-up showing (a) nozzle head with O_2 monitor attached and (b) printing conducted in argon inflated bag.

Parameter optimisation of L-DED processing to achieve fully dense material also involves adjusting the laser power, laser scan speed, layer thickness, and hatch spacing. However, as L-DED was utilised in this study in order to quickly create multiple TiTa compositions, which likely all have their own individual optimised parameters, these parameters were not widely investigated here. Laser powers from 600 – 1200 W were investigated, in conjunction with layer heights from 0.2 – 0.4 mm, in order to achieve the highest deposition rate possible, assessed by the final build height of the samples. Laser scan speed and hatch spacing were kept constant 800 mm/min and 2 mm (50 %), respectively. A bi-directional scan pattern, with a 90 ° rotation of the scan pattern between layers, as shown in Figure 2-6, was used to create 15 mm sample cubes.

Ta powder from American Elements and grade 1 CP Ti powder from Advanced Powders & Coatings was used, Figure 3-4. The Ta powder was irregular in shape and had a 10 – 75 µm particle size distribution. The CP Ti powder was spherical with a 45 – 150 µm particle size distribution.

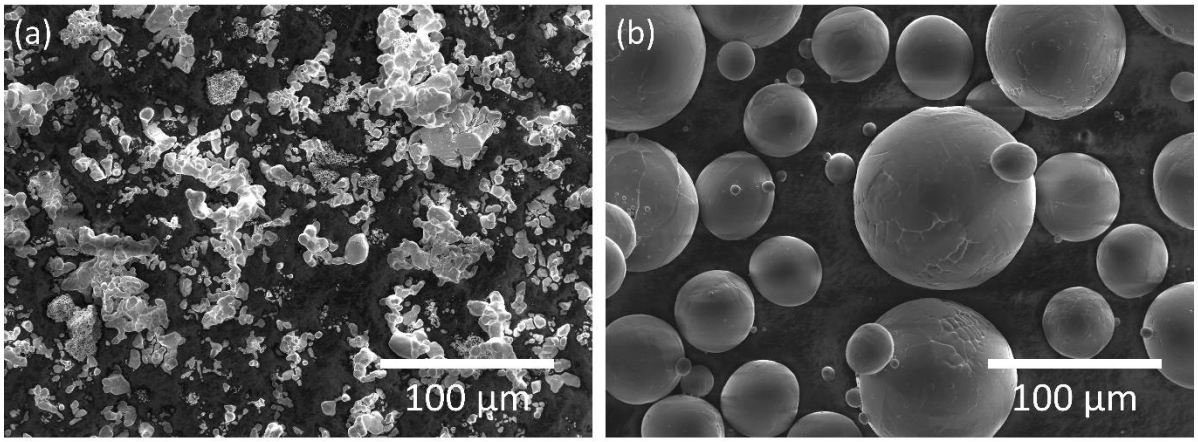

Figure 3-4: (a) American Elements Ta powder, (b) Advanced Powders & Coatings Ti powder.

The samples were removed from the titanium substrate by electro-discharge machining (EDM) and prepared for microstructure analysis by cross-sectioning, grinding using grades 180 – 4000 SiC paper and polishing using oxide polishing suspension (OPS). The porosity (%) of each sample was determined using optical images obtained with a GX51 Optical Microscope, each image covering a sample area of 35 mm^2 and analysed using ImageJ software. In addition, energy dispersive spectroscopy (EDX) was conducted on samples 9-13, to determine the alloy composition. Vickers hardness measurements were taken using a Duramin A-300 hardness tester with a 600 gf load applied for 10 s. An average of 9 points were taken in a grid pattern over the available surface.

Table 3-1: Process parameters, resulting porosity and chemical composition for L-DED manufactured cubes.

Sample Number	Power (W)	Layer Height (mm)	Powder Feedrate (rpm)	Carrier Gas Flow (L/min)	wt.% Ta	Porosity (%)	Hardness (HV)
1	1000	0.4	3 (Ta)	4	100	13.5	-
2	1000	0.4	6 (Ta)	4	100	9.7	-
3	1000	0.3	6 (Ta)	4	100	11.1	-
4	1000	0.2	6 (Ta)	4	100	10.0	240 ± 40
5	1000	0.4	3 (Ti)	4	0	1.8	171 ± 16
6	800	0.4	3 (Ti)	4	0	6.0	-
7	1200	0.4	3 (Ti)	4	0	1.9	-
8	600	0.4	3 (Ti)	4	0	2.8	-
9	1000	0.4	3 (Ti) / 3 (Ta)	4/4	33 ± 2	2.4	274 ± 22
10	800	0.4	3 (Ti) / 3 (Ta)	4/4	34 ± 2	4.6	-
11	1000	0.4	3 (Ti) / 6 (Ta)	4/6	48 ± 2	6.6	274 ± 15
12	1000	0.4	3 (Ti) / 9 (Ta)	4/10	58 ± 2	7.7	-
13	1000	0.4	3 (Ti) / 10 (Ta)	4/15	55 ± 2	2.8	259 ± 15

Table 3-1 displays the process parameters and resulting porosity, hardness and Ta content of the L-DED material. EDX analysis revealed that the compositions of the TiTa mixed samples ranged from 33 – 58 wt.% Ta, showing the powder feed rate and carrier gas flow to be the dominant variables for creating compositional change. The porosity of the samples ranged between 1.8 – 13.5 %, with the highest porosity occurring in the solid Ta samples. The pure Ti samples showed much lower porosity values from 1.8 – 6.0 %, suggesting that the high porosity in the Ta samples was caused by a combination of insufficient energy to induce full melting of the Ta powder and the irregular shape of the Ta powder. The cross-sectional optical micrographs showed large gaps between the powder layers in the Ta samples, Figure 3-5(a), and no gaps between layers in the Ti samples, Figure 3-5(b). As the Ta content increases in the TiTa compositions, the gaps between layers become more visible, Figure 3-5(c) and (d).

The porosity of the samples also led to a large standard deviation in the material hardness and caused the pure Ti sample (171 ± 16 HV) to display a slightly lower hardness than conventionally wrought CP Ti (210 HV) [330]. However, all three TiTa compositions showed a higher hardness than both the pure Ti and pure Ta samples, indicating that the Ta atoms have led to solid solution strengthening in the Ti. The Ti33Ta and Ti48Ta compositions also showed a similar hardness to L-PBF Ti50Ta, reported by Sing et al. [221] (284.5 ± 11.06 HV) and cast and quenched Ti50Ta reported by Trillo et al. [331] (265

HV). The Ti55Ta composition however showed a decreased in hardness, likely reflecting a decrease in strength due to a higher retained content of β phase.

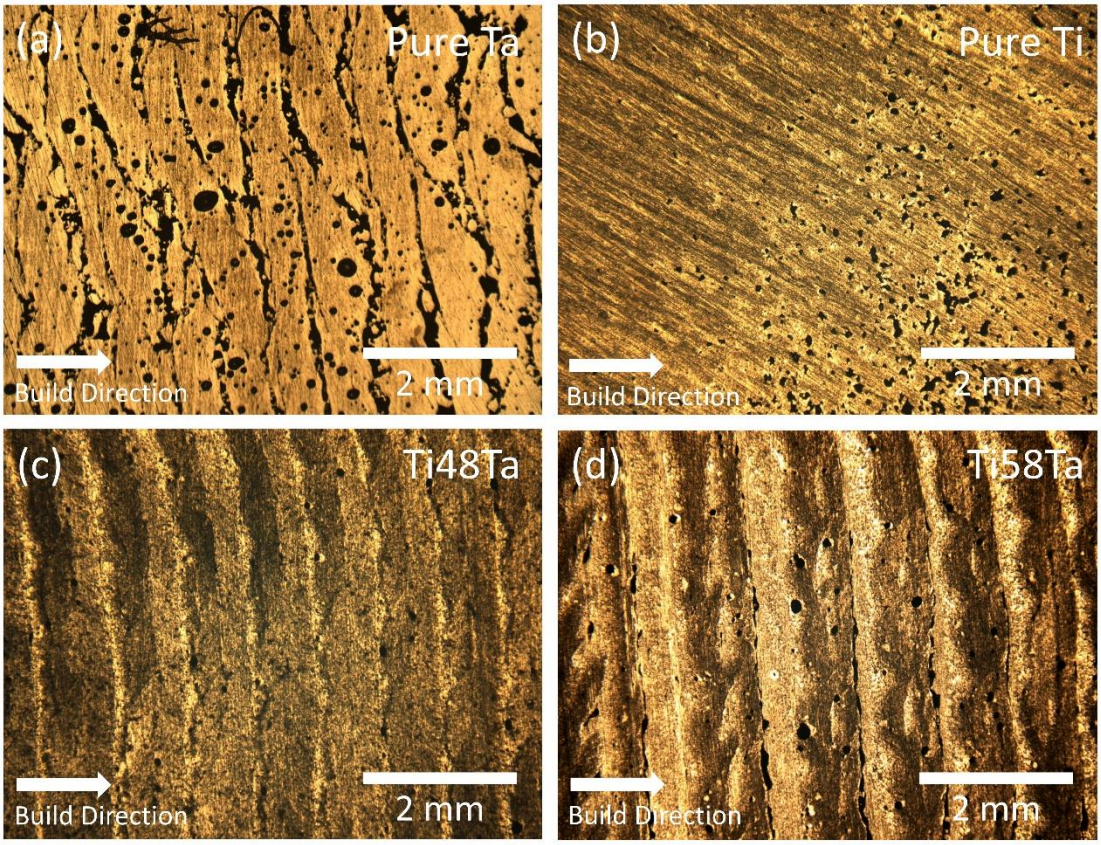

Figure 3-5: Optical micrographs of L-DED cross-sections for (a) pure Ta (sample 2), (b) pure Ti (sample 8), (c) Ti48Ta (sample 11) and (d) Ti58Ta (sample 12).

To investigate the melting of the Ta particles, back scattered imaging using a JOEL 7001F FEG SEM of two adjacent scan tracks from the Ti48Ta sample was conducted, Figure 3-6. The scan tracks were approximately 400 µm in height, and showed a microstructure peppered with bright partially melted Ta particles and dark pores. Clearly, the Ta has not been fully incorporated into the matrix, highlight the difficulty of creating a homogeneous alloy from mixed powders with refractory constituents, such as Ta. The upper scan track, running in the y-direction, shows dendritic solidification at the front of the melt pool, highlighted in Figure 3-6(a). These images confirm that solidification is mainly initiated at the front laser scanning direction of the melt pool, as seen in previous L-DED studies [191, 332, 333]. The lower scan track, running in the x-direction, shows a less noticeable grain structure as the dendrites appear perpendicular to the reader.

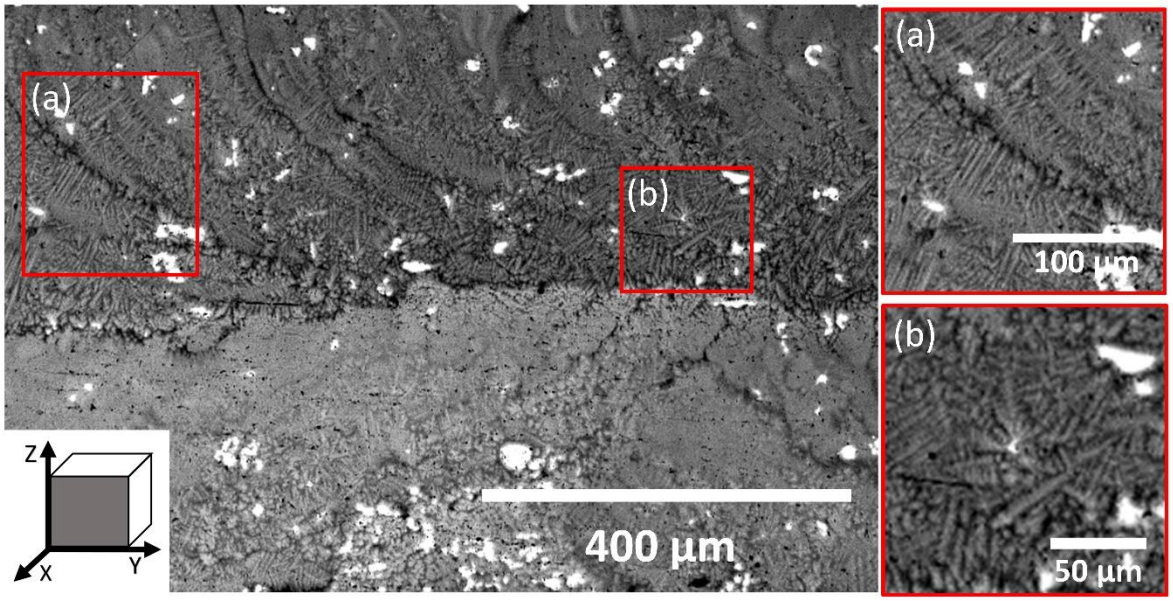

Figure 3-6: Back-scattered image of Ti48Ta showing two adjoining scan tracks, partially melted Ta particles and dark pores. (a) Strong dendritic solidification is seen at the front of the melt pool and (b) partially melted Ta particles act as heterogeneous nucleation sites.

However, in addition to the edge of the melt pool, radial dendrites can be seen to form around the partially melted Ta particles, Figure 3-6(b), suggesting that the partially melted Ta particles are acting as heterogeneous nucleation sites. Tedman-Jones et al. [334] also observed refractory particles of Mo, Nb and W acting as nucleation sites during wire arc additive manufacturing of Ti alloys. It was hypothesised that the partial melting of refractory elements in Ti creates a saturated zone around the particle leading to 'dissolutional supercooling' and nucleation. An increased number of heterogeneous nucleation sites during solidification can lead to a finer and more equiaxed grain structure, which could prove to be a useful grain refinement technique for additively manufactured TiTa alloys.

Finally, to complete the L-DED sample characterisation X-ray diffraction (XRD) analysis was undertaken, to identify the phases present in each alloy. A Bruker D8 Advance X-ray diffractometer with a Cu Kα X-ray source was used. Scans were conducted from 30 – 110 ° at 0.02 ° increments with a speed of 1s per step. The XRD patterns for the Ti33Ta and Ti48Ta samples showed peaks for both the α and β phases, Figure 3-7, confirmed with powder diffraction file (PDF) cards 00-044-1294 and 00-004-0788, respectively. The Ti55Ta sample showed dominant β peaks with only minor indications of α. To quantify the volume of each phase present, Rietveld refinement was undertaken using TOPAS software, and the volume percentages displayed in Table 3-2, in comparison to the phases seen in the TiTa alloy system in literature.

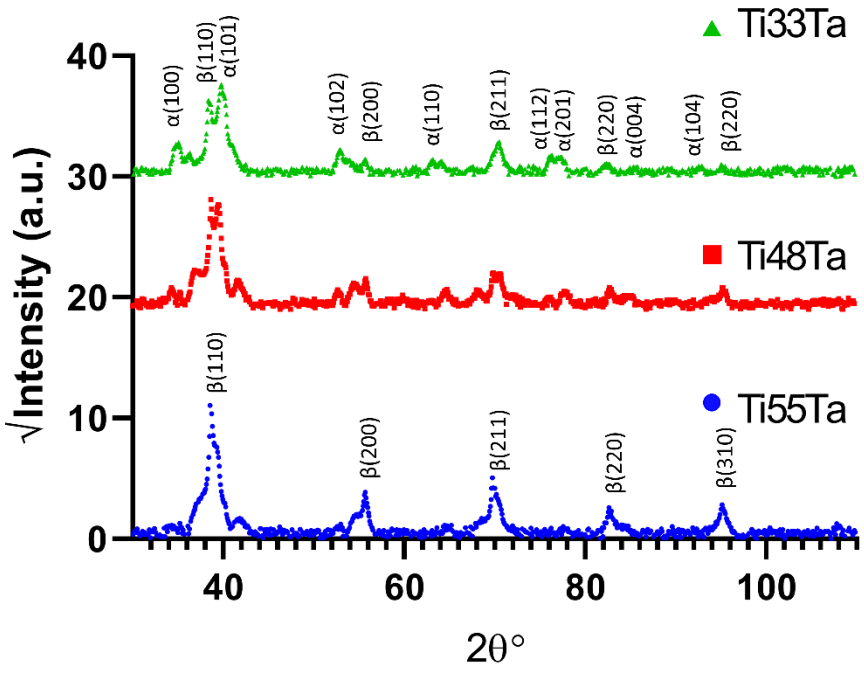

Figure 3-7: XRD spectra of L-DED produced TiTa compositions.

Table 3-2: Phase fractions of α and β measured in L-DED TiTa compositions.

Wt.% Ta	**Volume % β Phase**	**Volume % α Phase**	**Volume % α observed in [329]**	**Qualitative phases observed in [36]**
Processing	L-DED as-built [this study]	L-DED as-built [this study]	L-DED, solution treated in β phase field and furnace cooled	Cast, rolled, solution treated in β phase field and quenched in ice water
33 ± 2	27 ± 5	73 ± 5	83.33 (Ti32Ta)	α″ (Ti30Ta)
48 ± 2	89 ± 5	11 ± 5	65.97 (Ti49Ta)	α″ (Ti50Ta)
55 ± 2	97 ± 5	3 ± 5	57.98 (Ti51Ta)	α″ + β (Ti60Ta)

As the Ta content increases in the L-DED as-built material, the volume % of the retained β phase also increases, reflecting the β phase stabilising effect of Ta in Ti. The β phase is almost entirely retained in the Ti55Ta alloy, which supports the softening observed in the hardness testing. When compared to L-DED solutionised and furnace cooled TiTa alloys, investigated by Nag et al. [329], a higher volume % of α phase is noted in similar compositions when the samples are furnace cooled. The furnace cooling likely gives the opportunity for α nucleation and growth, as the samples are held for longer in the α + β phase region. The difference in volume of α phase increases with the increasing Ta content, likely as the α + β phase region increases in size at higher Ta contents.

Zhou et al. [36], on the other hand, investigated conventionally produced arc-melted TiTa alloys, which were cast, rolled into 3 mm thick plates, solutionised above the β transus temperature and quenched in ice water. These samples showed no β phase present until the Ti60Ta composition was reached. It was first suggested by Bania et al. [335] that a fully β microstructure could be obtained at Ti45Ta upon water quenching, however no experimental data was given to support this claim. Hence, there still exists disagreement in literature as to the composition at which a fully β microstructure can be obtained. The current work supports that a fully β alloy can be obtained through L-DED processing at a Ti55Ta composition. Whilst the single layer cooling rates of L-DED likely sit between air cooling and water quenching rates, the multiple layer application of the laser, likely results in some heat treatment of the pre-solidified material. Hence, it is unlikely that a L-DED processed alloy would retain a higher percentage of β phase than a cast and water quenched alloy simply due to cooling rate. As the L-DED produced material is inhomogeneous, as seen in Figure 3-6, it is possible that a portion of the β XRD peaks are attributed to the remaining Ta particles. A powder mixture of Ti55Ta, would show approximately 25% volume β phase, contributing a significant volume of β phase to an inhomogeneous L-DED alloy.

In conclusion, pure Ti, pure Ta and TiTa compositions of Ti33Ta to Ti58Ta were manufactured using L-DED. Hardness measurements suggested the TiTa alloys display a superior strength to L-DED CP Ti and hence are a promising replacement material for CP Ti implants. Microstructure analysis highlighted the difficulty of fully incorporating the refractory Ta into the Ti matrix, highlighting that further *in situ* methods of homogenisation should be explored, such as new scanning strategies. However, the partially melted Ta particles also acted as heterogeneous nucleation sites and may act as grain refiners, reducing the columnar grain structure often seen in L-PBF Ti alloys. With a narrowed compositional window, L-PBF investigations for mixed powder TiTa alloys could begin.

3.3 L-PBF Single Tracks for Narrowing the Parameter Space

L-PBF is better suited to implant manufacture than L-DED due to its higher achievable tolerances facilitated by the smaller laser spot size. Finer features can be manufactured, which due to their smaller volume, experience higher cooling rates, resulting in finer microstructures and hence different mechanical properties to L-DED produced material. The L-PBF process is also capable of fabricating fine and complex features such as lattice structures, which can facilitate bone ingrowth in implants.

To determine the best parameters for L-PBF processing of the TiTa alloys, earlier studies of L-PBF CP Ti, Ti50Ta and pure tantalum were consulted, Table 3-3. According to the energy density model, a higher energy density is required to process pure Ta when compared with pure Ti as Ta possesses a much higher melting temperature (Ta; 3000 °C to Ti; 1660 °C [77]). However, the difference in energy

density required to process pure Ti and Ti50Ta (~21 at.% Ta) is relatively small, suggesting the energy density does not increase linearly with increasing Ta content. The limitations of the energy density model for predicting optimal processing parameters, discussed in Section 2.2.2, are clearly highlighted.

Table 3-3: L-PBF process parameters for CP Ti, Ti50Ta and Ta from literature.

Material	**CP Ti (Grade II)**	**Ti50Ta**	**Ta**
Power (W)	165	360	300
Scan speed (mm/s)	138	400	100
Thickness (mm)	0.1	0.05	0.03
Hatch Distance (mm)	0.1	0.125	0.230
Energy Density (J/mm^3)	120	144	435
Reference	[193]	[221]	[218]

A recognised method for narrowing the parameter space in L-PBF processing is the analysis of single and multi-scan tracks [336-339]. The single scan track method uses minimal material and time, as only a single laser path up to a centimetre in length can be used to analyse the lateral stability of the scan track, as well as the dimensions of the melt pool. Track stability and melt pool dimensions can indicate the susceptibility of a part to processing-induced porosity or lack of fusion defects [164]. In this study, 20 parameter sets were explored for single and multi-scan tracks, using a laser power of 95 W, and scan speeds from 100 - 480 mm/s, at 20 mm/s increments.

An Mlab Cusing R (Concept Laser GmbH, Germany), with a small build chamber (90 mm × 90 mm × 80 mm) suited for the processing of expensive powders, such as Ta, was used. The laser system is a 100 W Nd:YAG fibre laser with a 1070 nm wavelength and a 50 µm spot size. The maximum laser power in this study was limited to 95 W to maximise the repeatability of the print jobs, as it was noted that using the laser at its maximum capacity could lead to fluctuations in laser intensity. Printing was conducted under an argon atmosphere with oxygen content below 0.2 %. Residual powder from the L-DED process was used, at an approximate composition of Ti50Ta. This powder was deemed suitable for narrowing the parameter space for L-PBF of the TiTa alloy system, as the composition lay between the Ti25Ta and Ti65Ta alloys, and the laser Ta particle interactions could be investigated. The Ti and Ta elemental powders are described in Section 3.2. A single 25 µm layer of powder was spread over the build plate to create the single scan tracks, 10 mm in length. The multi-scan tracks consisted of ten powder layers, with the laser applied per layer. The single scan and multi-scan tracks were imaged laterally and through their cross-section by optical (GX51 Optical Microscope) and SEM (JEOL 7001F FEG SEM) microscopes. The SEM was fitted with back scattered electron and electron dispersive X-ray detectors.

Figure 3-8 displays an example of a laterally stable (a) and an unstable (b) melt track. A laterally stable melt track should appear similar to a truncated cylinder on the substrate whilst unstable melt tracks often show variation in diameter. Preliminary observations of the single scan track stability, showed a decrease in scan track width with increasing scan speed, Figure 3-8(c). All the investigated parameter combinations showed a linearly consistent melt track, without balling or scan track breaks. BSI of the scan track produced at 220 mm/s scan speed, Figure 3-8, showed unmelted Ta particles dispersed randomly throughout the track, as well as swirling patterns within the track matrix, indicating the Marangoni flow characteristics caused by temperature gradients in the melt pool [340].

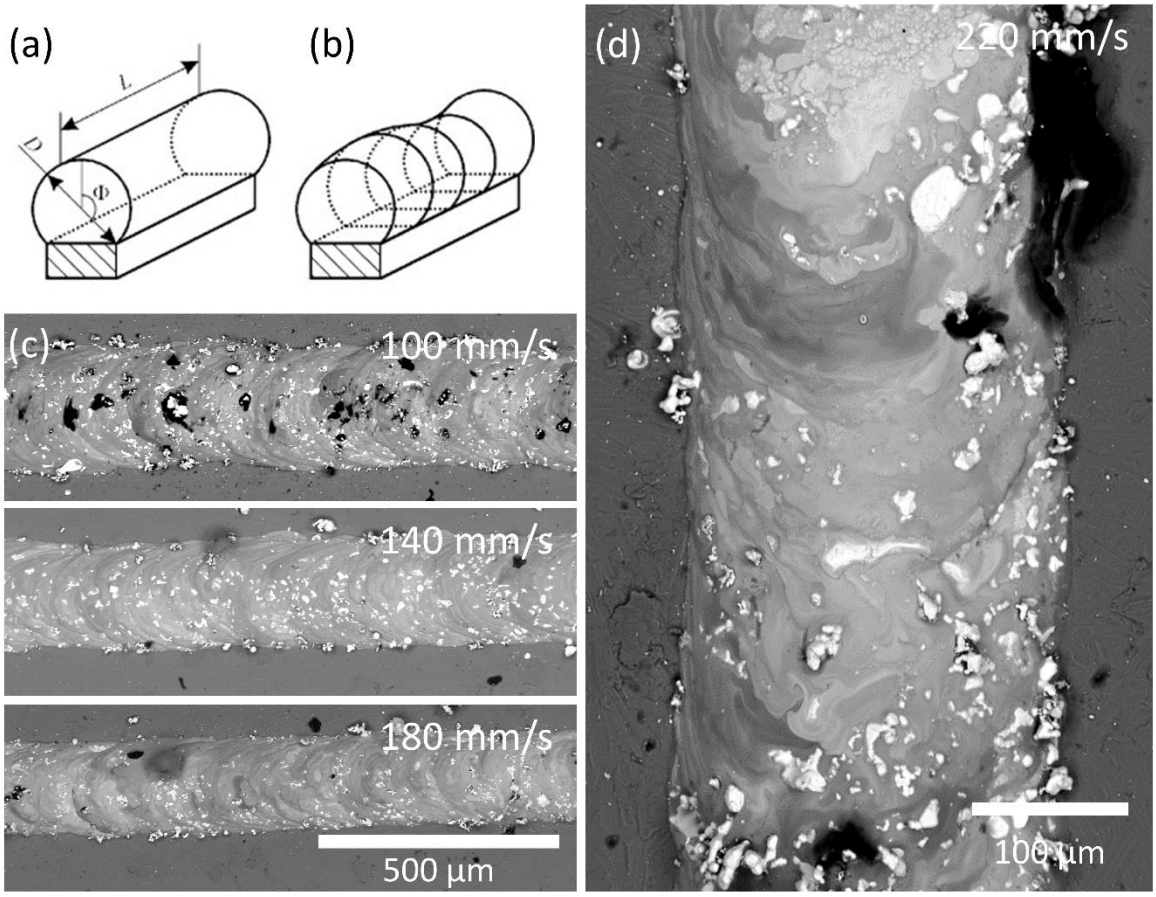

Figure 3-8: Schematic of a (a) stable and (b) unstable melt track, reproduced with permission from [338]. (c) and (d) Electron back scattered images of single scan tracks of mixed TiTa powders produced at different scanning speeds.

To further understand the parameter space for L-PBF of TiTa alloys, the single scan and multi-scan tracks were cross-sectioned, and the melt pool dimensions analysed, Table 3-4. The width (W) and depth (D) of the melt pools decreased with increasing scan speed, Figure 3-9(a) and (b). The melt pool width and depth decreased with scan speed from 232 to 125 µm and 215 to 52 µm, respectively. The ratio of melt pool depth (D) to width (W) has been used as an indicator for keyhole formation. Keyhole pores are formed as a result of excessive energy and material vaporisation, which results in melt pool

collapse and defects at the bottom of the melt pool, where the temperature is highest [175, 341]. A D/W ratio greater than 1.5 indicates likely keyhole formation [339, 342]. The maximum D/W ratio observed in the TiTa melt pools was 0.92 at the slowest scan speed of 100 mm/s and decreased with increasing scan speed. Hence, none of the selected parameter sets are likely to cause keyhole vaporisation.

Table 3-4: TiTa single layer melt pool dimensions across scan speeds of 100 – 480 mm/s.

Melt Pool Dimensions	**Maximum (at 100 mm/s)**	**Minimum (at 480 mm/s)**
Melt pool width (µm)	232 ± 11	125 ± 17
Melt pool depth (µm)	215 ± 21	52 ± 4
D/W	0.92	0.42
D/t	9	2

The ratio of melt pool depth (D) to layer thickness (t) is also used to consider whether lack of fusion defects will occur between layers [343, 344]. A D/t ratio less than 1 suggests that the laser energy provided by the chosen parameters is not sufficient to penetrate through a single powder layer and hence fuse the powder to the pre-solidified material, resulting in lack of fusion defects. The D/t melt pool ratios in the current study ranged from 9 – 2, suggesting that the investigated parameters created deep melt pools which would penetrate through multiple layers. Such a deep melt pool may cause inconsistencies in geometries, particularly at overhangs, but could also assist in further melting the refractory Ta particles remaining in previous layers.

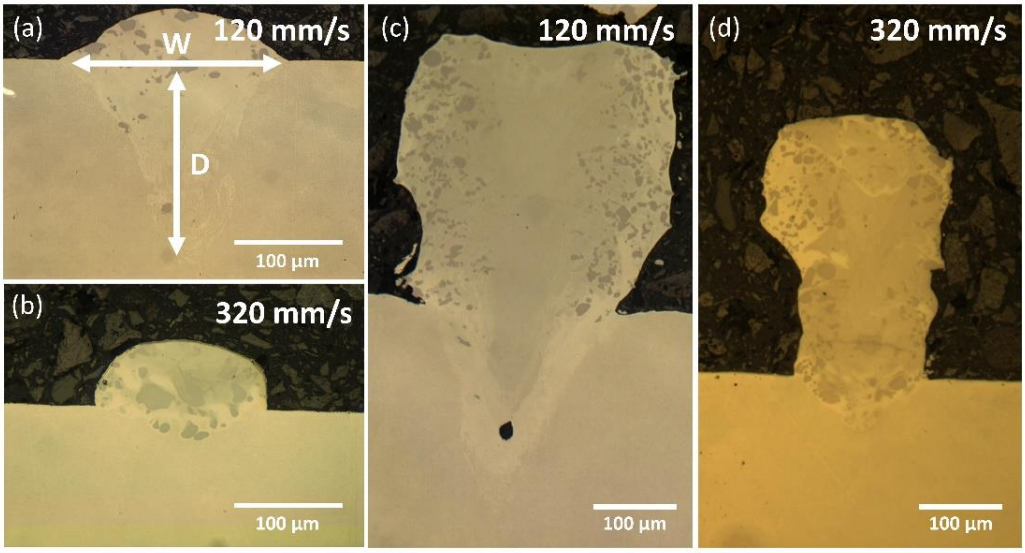

Figure 3-9: Single and multi-scan tracks produced in mixed powder Ti50Ta. Single melt tracks (a) and (b) and ten-layer multi-scan tracks (c) and (d).

The multi-scan tracks, Figure 3-9(c) and (d), clearly display the effect of the high D/t ratio. The multi-scan track produced at 120 mm/s, with an associated D/t ratio of 8, showed good homogeneity at the centre of the scan track. Each melt pool is deep enough to penetrate 8 previous layers of material, and hence provide sufficient energy to fully incorporate the Ta. However, a pore is also observed at the bottom of the melt pool which, due to its round form and position, can be identified as a keyhole defect. Hence, despite the low D/W ratio indicating unlikely keyhole formation, keyhole vaporisation can still occur in the case of high D/t ratios. The multi-scan track printed at 320 mm/s, with an associated D/t ratio of 5, had a smaller homogeneous zone at the centre, but showed no keyhole formation. Hence, scanning speeds around 100 mm/s are likely to cause keyhole vaporisation in the TiTa alloys, due to the large melt pool depth. Laser scan speeds of 300 mm/s are likely to be more suitable and will be used as the median scan speed for investigating the optimal process parameters for the Ti25Ta and Ti65Ta mixed powder alloys.

In conclusion, single and multi-scan tracks confirm that the parameter space encompassing scan speeds of 100 – 500 mm/s is suitable for processing TiTa mixed powder alloys. It must be noted that the observations of homogeneity are only preliminary, as during the L-PBF process, the overlapping hatch distance between adjacent scan tracks will contribute to further Ta melting and mixing. However, it can clearly be seen that a deep melt pool which penetrates multiple powder layers is effective at increasing material homogeneity, though a tipping point will likely be encountered between creating homogeneous and pore free material.

3.4 L-PBF Parameter Optimisation for High Density and Homogeneous Parts

Spherical powders ensure optimal powder layer packing and aid in the formation of dense parts for L-PBF processing. Hence, spherical tantalum (TEKNA, Canada) and titanium (Grade 1 ASTM B861, TLS Technik Spezialpulver, Germany) powders were acquired for TiTa part manufacture. Both powders showed a similar particle size distribution from 5 – 45 µm, Figure 3-10, though the titanium powder also showed a bimodal distribution, which is optimal for high density packing [345]. The chemical compositions, as measured by the suppliers, are displayed in Table 3-5, showing that the oxygen content of the Ti powder is below 0.18 wt.% and hence conforms to the CP Ti Grade 1 specification. The powders were combined in 25 wt.% Ta and 65 wt.% Ta compositions and tumble mixed for 12 hr at 15 rpm.

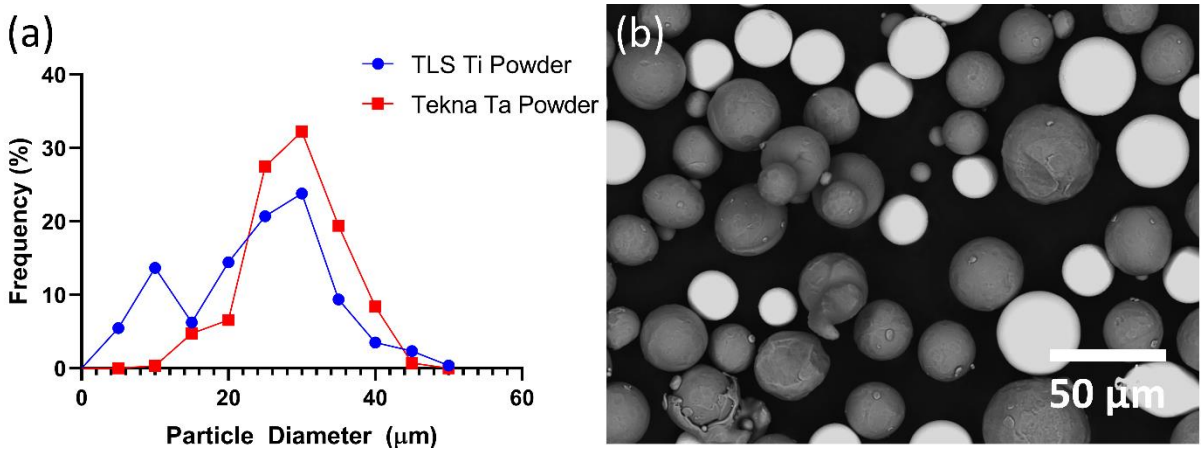

Figure 3-10: The high quality mixed TiTa powder used for L-PBF part processing. (a) Particle size distribution for the Ti and Ta powders. (b) A back-scattered electron image showing the mixed Ti (dark) and Ta (light) particles, reproduced from [346].

Table 3-5: Chemical composition of as-received powders in wt.%, measured by suppliers. Reproduced from [346].

	Ta	**Ti**	**O**	**Fe**	**N**	**C**
Ta	> 99.95%	-	0.033	≤ 0.001	≤ 0.001	≤ 0.001
Ti	-	Bal.	0.11	0.012	0.009	0.006

Cuboid samples (15 mm × 15 mm × 10 mm) were printed at 95 W with varying scan speeds within the identified parameter space of 100 – 700 mm/s. The hatch distance was set to 35 µm, to ensure good overlap between scan tracks (laser spot size = 50 µm) and the layer thickness was kept constant at 25 µm. The scanning strategy applied per layer was a single continuous laser path running at 45 ° to the y-axis and between layers there was a 90 ° rotation to the scanning strategy. However, due to the remnant partially melted particles noted in the single track study, in addition to those noted in the study of Ti50Ta by Sing et al. [221], a remelt scanning strategy was attempted (denoted as RS) and compared to the single melt material (denoted as SS). The remelt scan consisted of a second laser pass per layer to allow a second opportunity for melting. The laser parameters of the remelt scan were kept identical to the laser parameters of the initial laser scan, and the remelt scan followed an identical laser path to the previous scan. Although it has been previously noted in literature that investigating different parameters for the remelt scan can alter material properties such as residual stress and surface roughness [178, 187-190], the rescan parameters were kept identical to the original scan parameters in this study as only preliminary investigations of the remelt scan as a homogenisation tool have yet been undertaken and initial results comparing the single melt to the remelt conditions are required in literature. Future work will investigate optimising the remelt scan laser parameters to improve homogeneity, residual stress and mechanical properties.

The density of the printed samples was assessed through cross-sectioning, metallographic grinding and polishing, and optical analysis. The samples were cross-sectioned through the y-z plane and polished with 0.04 µm OPS colloidal silica. Optical images were taken using a GX51 Optical Microscope at 10X magnification and the images analysed using thresholding techniques in ImageJ analysis software. The density of the samples was calculated as the average area fraction of pores taken across five images spread over the cross-sectional surface of each sample.

Figure 3-11(a) and (b) show that high densities > 99.7 % were achieved in both the Ti25Ta and Ti65Ta compositions, with similar laser scan speeds. The Ti25Ta composition showed the highest density of 99.9 % at a scan speed of 300 mm/s Figure 3-11(d), with a slight decrease in density at higher scan speeds and a larger decrease in density at lower scan speeds, Figure 3-11(c). At the low scan speeds, pores are likely created due to keyhole vaporisation, as observed in the multi-track scans in Section 3.3, where excessive laser energy leads to material vaporisation [175, 341, 347]. The slight increase in porosity at higher scan speeds could be due to lack of fusion, where there has been insufficient energy to cause full melting and densification of the powder particles. However, the depth of the melt pools observed in Section 3.3, suggest lack of fusion defects are unlikely. In addition, the part density at 200 mm/s is lower than that at 100 mm/s, suggesting other mechanisms contributing to pore formation, such as spatter particles passing through the laser beam and diffracting or blocking the incident energy. Spatter particles often also have a much higher oxygen content and irregular shape, which reduces particle wetting and can lead to subsequent defects if they land in the laser path [179, 244, 348]. Porosity caused by spatter particles may be amplified at lower scan speeds as the spatter particles have more time to pass through the incident laser beam or settle in the laser path.

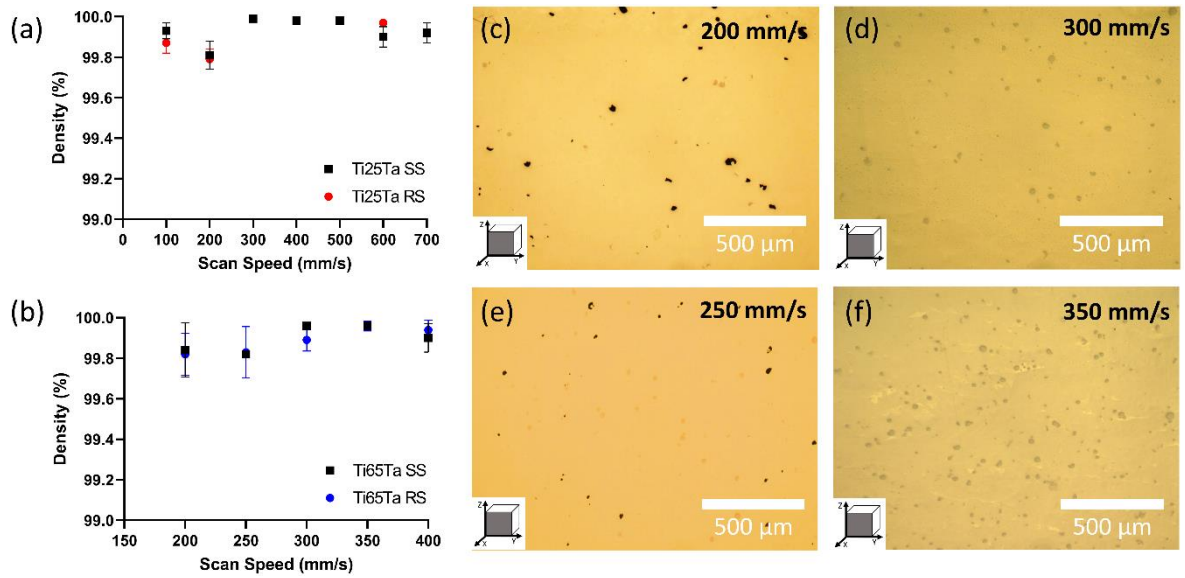

Figure 3-11: Parameter optimisation for high density Ti25Ta (a)(c)(d) and Ti65Ta (b)(e)(f) material. (a) and (b) show the density of parts at difference scan speeds, for the single melt and remelt scan strategies. (c)(d)(e)(f) Optical micrographs of porosity, showing the highest (c)(e) and lowest porosity (d)(f) achieved in each composition. Ti25Ta data reproduced from [346].

Similar trends in porosity were observed in the Ti65Ta composition, however the optimal scan speed was found to be 350 mm/s, Figure 3-11(b). Due to the higher content of Ta in this composition, it was expected that lower scan speeds and hence higher energy densities would be required to adequately melt the higher concentration of Ta. However, the optimal parameter sets produce an energy density of 361 J/mm^3 and 310 J/mm^3 for the Ti25Ta and Ti65Ta compositions respectively. Hence, the limitations of the energy density equation as a parameter prediction tool are clearly seen. The disparity in energy density is even greater when considering previous literature works which found the optimal energy density for Ti25Ta to be 81 J/mm^3 [220] and Ti50Ta to be 147 J/mm^3 [221]. It is clear that parameter optimisation is also heavily influenced by mechanistic and morphological processes, such as the interactions between the laser spot size and individual powder particles. Hence, considering parameters such as laser focal spot size is much more applicable for L-PBF processing than the energy density number.

The observation that porosity at higher scan speeds is caused by a mechanism other than insufficient melting is supported by the findings of porosity levels after the application of the remelt scan. The remelt scanning strategy slightly decreased material density at low scan speeds, whilst having negligible effect on porosity at the optimal scan speed for each alloy. This supports that keyhole vaporisation is caused by the lower scan speeds, and hence the remelt scan may fill in existing pores, but also compound the pore volume upon the second melting. At the higher scan speeds, however, the remelt scan causes a minor increase in material density, likely by filling in pre-existing pores created by the initial scan. This suggests that the mechanism of pore formation at these higher scan speeds, is not replicated during the remelt scan. Hence, the mechanism for pore formation at the higher scan speeds is likely associated with the powder layer and thermal transfer between individual powder particles. A hypothesised mechanism will be discussed further in Section 3.5.

The optical micrographs in Figure 3-11(d) and (f) also clearly show particles incorporated in the TiTa matrix. Back scattered electron imaging (BSI) and X-ray dispersive spectroscopy (EDX) were used to confirm that these particles were remaining partially melted Ta. Further optimisation of the processing parameters for material homogeneity was conducted by quantifying the area fraction of partially melted Ta particles by image analysis for all parameter combinations.

The area percent of partially melted Ta particles decreased with decreasing scan speed, suggesting increasing the melt pool depth does enhance Ta melting, Figure 3-12(a) and (b). It is possible that the remaining area percent of partially melted Ta would decrease further at even lower scan speeds however, as porosity was seen to increase at lower scan speeds, this is an inadequate solution. The remelt scan, on the other hand, successfully further decreased the remaining partially melted particles at all scan speeds on average 40 % for the Ti25Ta alloy and 36 % for the Ti65Ta alloy. Hence, the material produced at the optimal scan speed for density could be improved in homogeneity without

increasing porosity. This resulted in a small area percent of Ta particles of 0.3 % and 0.8 % at the optimal porosity processing parameters for the Ti25Ta and Ti65Ta alloys respectively. A third remelt scan could potentially further solutionise the Ta however, the effect of the remelt scan on the microstructure and mechanical properties should first be understood.

It was also hypothesised that the area percent of remaining Ta particles indicated that the matrix Ta composition deviated from the desired nominal compositions. However, simple volume calculations showed that a 1 % or 2 % area of unmelted Ta particles in the Ti25Ta and Ti65Ta alloys respectively, would only adjust the matrix composition to 23.3 wt.% Ta and 64.0 wt.% Ta. This variation of 1 – 2 % Ta content in the matrix was confirmed using point EDX analysis (Appendix Figure 8-1).

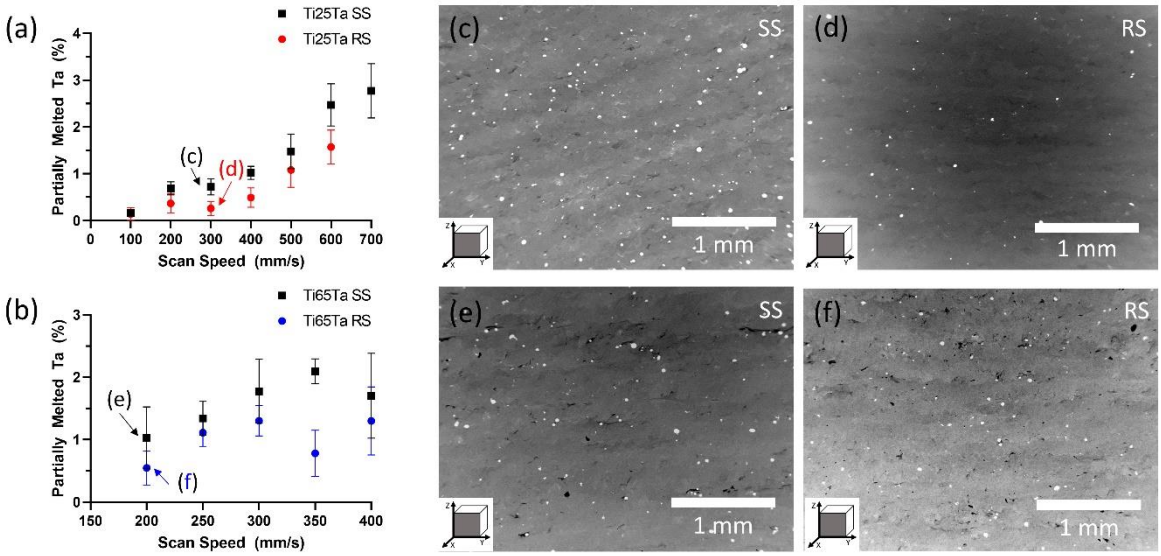

Figure 3-12: Increase in homogeneity caused by the remelt scan. Partially melted Ta particle percentage decreases with decreasing scan speed in (a) the Ti25Ta alloy and (b) the Ti65Ta alloy. (c),(d) Optical micrographs show the Ti25Ta and Ti65Ta single melt material and (e),(f) show the reduction in partially melted Ta particles after the remelt scan was applied. Ti25Ta data reproduced from [346].

In conclusion, the optimal scanning speeds for high density in the Ti25Ta and Ti65Ta compositions were found to be 300 mm/s and 350 mm/s respectively, however, the compositions still retain partially melted Ta particles. The designed remelt scan successfully decreased the remaining portion of partially melted particles, however further understanding of the melting enthalpy of the mixed powder TiTa alloys is required to determine whether parameter optimisation can indeed achieve a fully homogeneous material.

3.5 Normalised Enthalpy Model for L-PBF

Decreasing laser scan speed increased the melting of Ta but began to induce keyhole porosity. Using the energy density equation, it is suggested that keyhole formation begins at energy densities between 361 - 542 J/mm^3 and 310 – 361 J/mm^3 for the Ti25Ta and Ti65Ta alloys, respectively. Note that the range is larger for the Ti25Ta as 100 mm/s increments of laser scan speed were investigated, whilst the increments were refined for the Ti65Ta alloy. The lower energy density for the Ti65Ta alloy is contradictory to earlier findings which suggest that compositions with high contents of refractory constituents, such as Ta, require higher energy densities to produce optimal processing conditions.

To improve upon the predictions of the energy density model, the normalised enthalpy of melting was considered. Eq. (2), developed by King et al. [175], utilises chemical properties of the feedstock powders, including the absorption of the laser radiation by the powder, melting temperature, thermal conductivity and thermal diffusivity to predict the enthalpy of melting at different laser scan speeds. King et al. [175] found experimentally that a normalised enthalpy region existed where keyhole formation begins, at 30 ± 4.

The chemical data for pure Ti, pure Ta, Ti25Ta and Ti65Ta alloys was used to calculate the normalised enthalpy of melting using Eq. (2). Where literature values did not exist for thermal properties of the Ti25Ta and Ti65Ta alloys, the rule of mixtures was used to predict likely values (Appendix Table 8-2). The normalised enthalpy curves of pure Ti and Ti25Ta intersect the keyhole formation zone identified by King et al., whilst the curves for Ti65Ta and pure Ta do not, Figure 3-13. The enthalpy model suggests that the normalised enthalpy for the Ti25Ta alloy is approximately 44 % higher than that for the Ti65Ta alloy, and that for keyhole vaporisation to occur in the Ti65Ta composition, scanning speeds below 100 mm/s are required. However, in this study it was found experimentally that pore formation began in both the Ti25Ta and Ti65Ta alloys between scan speeds of 200 – 300 mm/s. Furthermore, the Ti65Ta alloy optimal scan speed was found to be 350 mm/s, slightly higher than the Ti25Ta composition, indicating that the processing of both the Ti25Ta and Ti65Ta is likely limited more by mechanistic processes, rather than chemical ones. For example, as the laser spot size for the Mlab system (50 µm) is very similar to the powder particle size (15 – 45 µm), at any instant in time one powder particle may be irradiated by the laser. If this one particle were a Ti particle, the chemical nature of pure Ti would suggest vaporisation at scan speeds of ~ 200 mm/s. Hence, it is likely that the processing of mixed powder alloys are limited by the melting and vaporisation characteristics of the lowest melting point constituent.

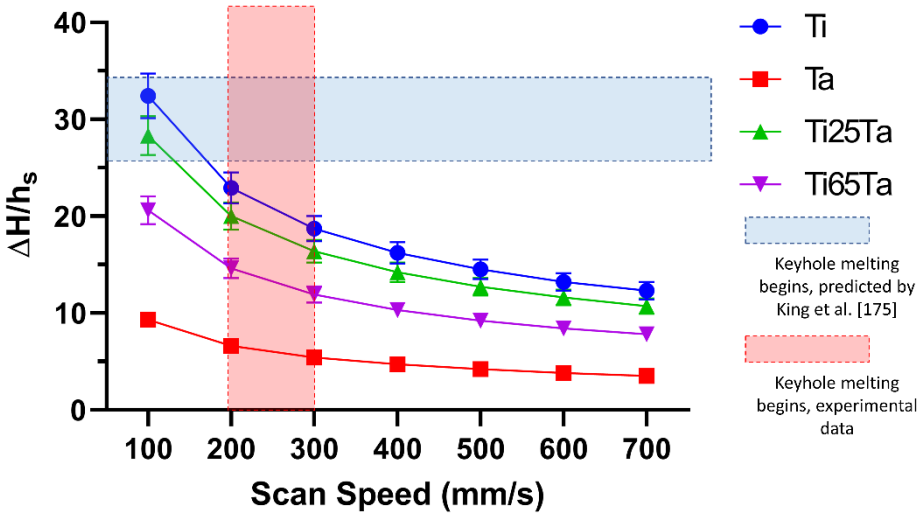

Figure 3-13: Normalised enthalpy as calculated by King et al. [175] for L-PBF of pure Ti, pure Ta, Ti25Ta and Ti65Ta. Keyhole formation is expected by King et al. at 30 ± 4 however, for the Ti25Ta and Ti65Ta alloys, this region is not reached until scan speeds below 200 mm/s. Despite this, keyhole pores were recognised at speeds > 200 mm/s in the experimental data. Adapted from [346].

The normalised enthalpy model provides slightly improved predications when compared to the energy density model as it considers the thermal properties of the alloy printed. However, the normalised enthalpy model is very limited for mixed powder alloys, as it does not consider the interaction between the laser and individual powder particles of a single element. Measurements of the thermal diffusivity and conductivity of the mixed powder, to better show energy transfer between single powder particles, may improve the predictive capabilities of the model. The normalised enthalpy model is much more suited to pre-alloyed powders and cannot be used to address the material inhomogeneity seen in Section 3.4.

3.6 Chapter 3 Summary

TiTa mixed powder alloys were investigated in both L-DED and L-PBF processing. The following conclusions can be drawn from Chapter 3:

- The composition range from 30 – 70 wt.% Ta is the most promising for TiTa AM implants. L-DED produced Ti33Ta, Ti48Ta and Ti55Ta alloys displayed a superior strength to L-DED CP Ti and hence are promising replacement materials for CP Ti implants.

- L-PBF parameter optimisation must find a balance between pore free and homogeneous material. Scan speeds between 100 – 500 mm/s with 95 W laser power were found suitable for stable track and melt pool formation, however low scan speeds induced keyhole formation in

multi-scan tracks and high scan speeds produced inhomogeneous material. The designed remelt scanning strategy successfully increased material homogeneity, without increasing material porosity, and is likely an applicable tool for processing of refractory component alloys.

- Partially melted Ta particles were observed to act as heterogeneous grain nucleation sites. These particles may be employed as grain refiners and could reduce the columnar grain structure often seen in L-PBF Ti alloys, and will be investigated in Section 4.2.2.

- Optimal scanning speeds for high density Ti25Ta and Ti65Ta compositions were found to be 300 mm/s and 350 mm/s respectively, with 95 W laser power. This finding disagrees with predictions from both the energy density and normalised enthalpy models. The energy density model is limited as it does not consider the differences in chemical nature between the Ti25Ta and Ti65Ta alloys, whilst the normalised enthalpy model is limited as it does not consider the laser and individual powder particle interactions, which play a significant role in mixed powder L-PBF.

Chapter 4 Microstructure and Mechanical Properties of L-PBF Ti25Ta and Ti65Ta

For the Ti25Ta and Ti65Ta L-PBF alloys to be considered as implant materials, a thorough understanding of their microstructure and mechanical properties must be determined. The mechanical properties of each alloy must be determined to assist in tailoring these new alloys to specific implant applications. Further understanding of microstructure formation during L-PBF processing will assist with adapting this new manufacturing method to achieve the required properties. Hence, the Ti25Ta and Ti65Ta alloys, produced at the optimal parameters determined in Chapter 3 were assessed for their volume phase structure using ThermoCalc and X-ray diffraction analyses, and the morphology of the microstructure further investigated using SEM and TEM imaging methods. The mechanical properties of each alloy were then analysed by tensile testing, with fractography used to investigate the effect of remaining Ta particles on failure mechanisms. Ultrasonic modulus testing was used in addition to tensile testing to validate the elastic modulus of the alloys, due to the higher accuracy possible with this method. Furthermore, two different tensile geometries were used, due to the high cost of the Ti65Ta alloy, however both geometries were designed according to the ASTM E8 standard. Finally, the microstructure is linked to the observed mechanical properties and the strengthening contributions discussed.

4.1 Phase Analysis

Early sources investigating the TiTa alloy system claim that a 100 % β phase alloy can be created in the Ti45Ta composition upon water quenching, based on the Molybdenum equivalency equation (see Bania et al. [335]). However, as L-PBF processing introduces a new kind of thermodynamic treatment, the phases which are present directly after printing must be investigated. To understand the initial equilibrium phases in the TiTa alloy system, ThermoCalc investigations were undertaken.

4.1.1 Thermodynamic and Oxygen Assessment

The ThermoCalc software was used to calculate equilibrium phase diagrams of both the Ti25Ta and Ti65Ta systems. The results in Figure 4-1, showed that both the Ti25Ta and Ti65Ta alloy systems fall into the 'meta-stable' category, with both α and β phases present at equilibrium at room temperature, which facilities precipitation strengthening on ageing. The Ti65Ta alloy shows a much higher molar percent of β phase stable at room temperature, due to the higher Ta concentration. However, it should be noted that the existing ThermoCalc database (TTTI3 v. 3.1) is not able to distinguish the effect of Ta composition on the formation of α′ or α″ phases.

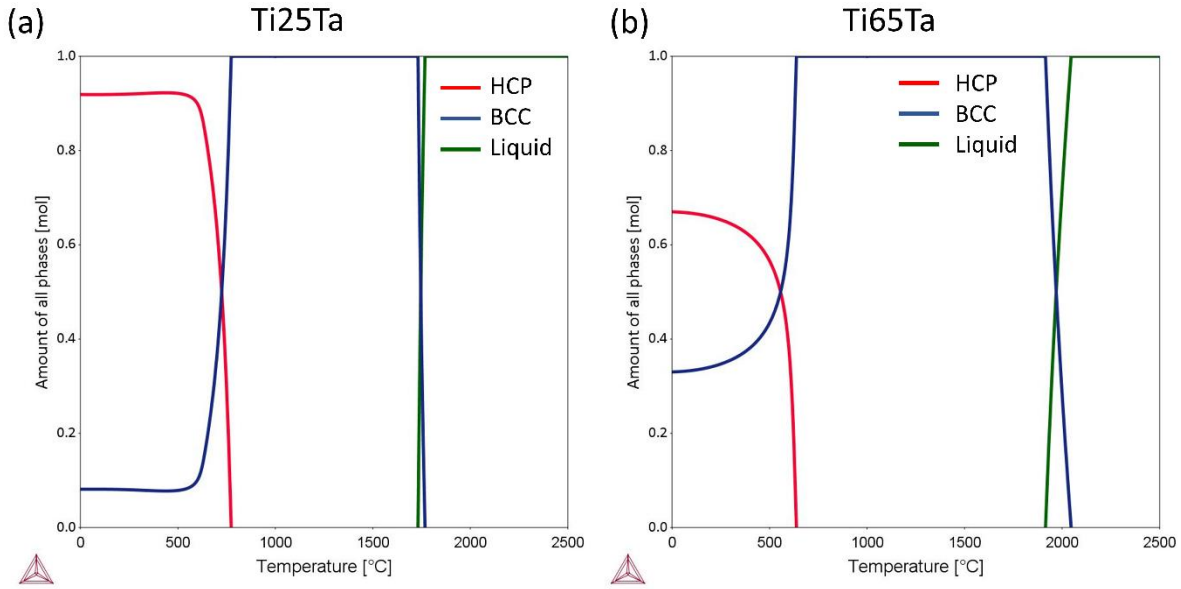

Figure 4-1: ThermoCalc simulations of equilibrium phases in (a) Ti25Ta and (b) Ti65Ta.

It is known that Ti alloy strength and phase volume fraction is dependent upon oxygen content [349]. While the L-PBF process is conducted under an argon atmosphere, several studies reported that the reactive materials such as Ti can experience oxygen pick-up during the printing process, powder storage and powder reuse [350-353]. Furthermore, as the remelt scanning strategy, investigated in Chapter 3,

effectively doubles the time molten material is in contact with the argon atmosphere, an increase in oxygen could be possible. Higher oxygen content powders have been linked to defect formation through the amalgamation of oxide particles, with reduced melting capabilities [179]. It is also known that oxygen is an α phase stabiliser in the TiTa system, and leads to solid solution strengthening, particularly in the α phase. Therefore, the oxygen content of the virgin and reused Ti25Ta powders, Table 4-1, was analysed and compared with samples of the single melt and remelt solid material, Table 4-2. The reused powder analysed had been used for 15 build jobs and stored, sealed, in an oxygen atmosphere.

Table 4-1: Chemical analysis of virgin and reused powders in wt.%.

	Ti	**Ta**	**N**	**C**	**O**	**H**	**Fe**	**Al**	**V**
Virgin Powder	Bal.	25.1	0.01	0.01	0.07	<0.005	0.06	0.03	<0.01
Reused Powder	Bal.	24.9	0.01	0.01	0.07	<0.005	0.08	0.04	<0.01

The chemical analysis of the virgin and reused powders revealed no oxygen pick-up, but a slight increase in other impurities, such as Fe and Al, was observed. This is understandable since the printer utilised in this project is used by multiple users to print different material classes and despite following the manufacturer prescribed cleaning processes, some residue may remain. Also note that the Ta composition stayed relatively stable in the reused powder, supporting the assumption that a stable nominal composition was retained between builds.

The oxygen content of the final printed material was also investigated, to assess whether the remelt scan caused an increase in oxygen content. When the remelt scan was applied, particularly to tall samples, colouration was seen on the sample surface, suggesting higher oxidation, Figure 4-2. A colour gradient was observed, from gold to blue, which increased with build height, but then disappeared abruptly at specific build layers. This was attributed to gradual blocking of the gas flow filter, which resulted in decreased argon flow during printing. When the filter became full, the print was paused, the filter replaced, and hence good argon flow resumed. This design flaw is inherent to the Mlab Cusing R and requires improvement in future designs of the machine but is beyond the scope of this thesis. To assess the oxygen content of the coloured surfaces in comparison to the material bulk, both samples from the inner and surface of the printed block were analysed for oxygen content, Table 4-2.

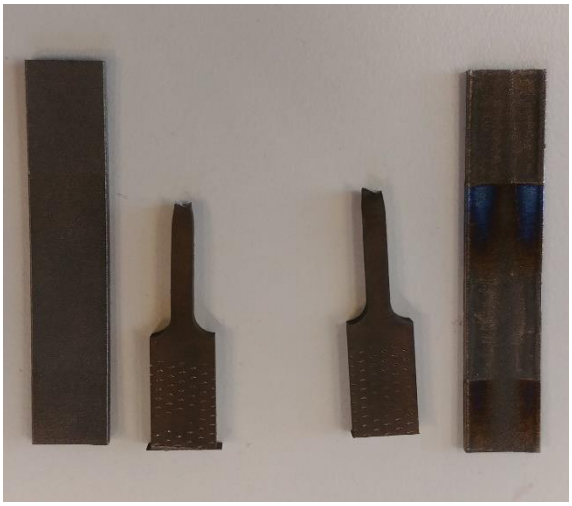

Figure 4-2: Example of oxidised surface caused by the remelt scan. Single melt samples on left and remelt samples on right. The tensile samples were cut from the centre of the block corresponding to the adjacent surface specimen.

Table 4-2: Chemical analysis of single melt and remelt material in wt. %.

	Ti	**Ta**	**N**	**C**	**O**	**H**	**Fe**	**Al**	**V**
SS (bulk)	Bal.	25.2	0.02	0.02	0.09	<0.005	0.02	<0.01	<0.01
RS (bulk)	Bal.	25.9	0.02	0.02	0.11	<0.005	0.02	<0.01	<0.01
SS (surface)	Bal.	25.9	0.01	0.02	0.09	<0.005	0.03	<0.01	<0.01
RS (surface)	Bal.	25.1	0.05	0.02	0.16	<0.005	0.03	<0.01	<0.01

The remelt scan increased the oxygen content by 0.02 % in the bulk and by a 0.07 % at the sample surface. The increased oxygen levels for both the bulk and surface material still fall within the range of oxygen required for ASTM grade 1 CP Ti, 0 – 0.18 wt.% oxygen [349], however even small additions of 0.1 wt.% of oxygen can increase material strength up to 100 MPa in CP Ti. Previous studies investigating the oxygen content after remelt scanning concluded that any oxygen increase in printed material caused by the remelt scan had negligible effects on the final material [177, 184, 185, 187]. It is hypothesised that the remelt scan increases the depth that oxygen can penetrate into the surface [187], however as the remelt scan is acting on a pre-solidified surface, with a much lower surface area than a powder layer, the bulk increase in oxygen content is negligible [177]. However, none of these studies were investigating the mechanical properties of titanium where minor increases in oxygen can have large mechanical effects. To confirm the increased oxygen content on phase volume is also negligible, ThermoCalc analysis of the Ti25Ta and Ti65Ta compositions including 0.16 wt.% oxygen was conducted, Figure 4-3.

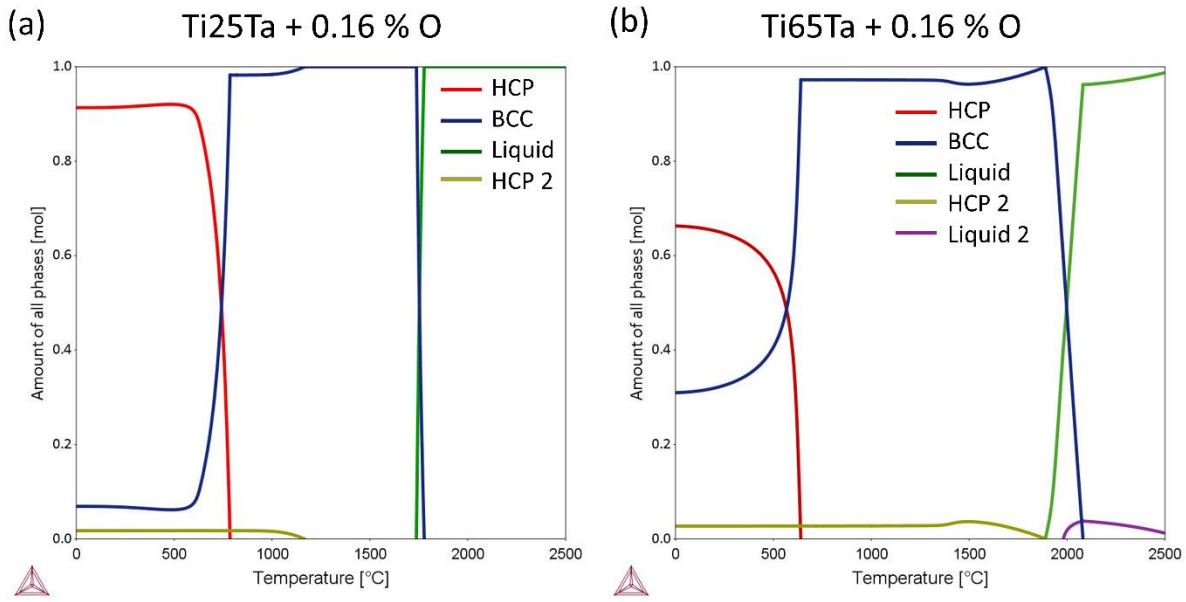

Figure 4-3: ThermoCalc simulations of equilibrium phases with 0.16 wt.% oxygen additions in (a) Ti25Ta and (b) Ti65Ta.

The ThermoCalc simulation suggested that the increased oxygen content of 0.16 wt.% could cause an approximate increase of 1 % in the molar volume of α phase, in the form of a second α phase which begins to form at higher temperatures, Figure 4-3 (HCP 2). The ThermoCalc TTTI3 v. 3.1 database does not provide further details of the second α phase which alloy the phase to be differentiated from the initial HCP phase in the following analysis. It should be noted that the HCP and HCP 2 phases do not represent the α′ and α″ phases, as the α″ phase is orthorhombic, as opposed to HCP, and occurs with increasing Ta content, as opposed to increasing O content.

In conclusion, the oxygen content changes negligibly during L-PBF processing and is unlikely to change the phase fractions or mechanical properties of the material.

4.1.2 X-Ray Diffraction Phase Analysis

The phases present in the as-built single melt and remelt L-PBF TiTa alloys were investigated using XRD on the cubic samples produced at the determined optimal parameters. A Bruker D8 Advance X-ray diffractometer with a Cu Kα X-ray source was used. Scans were conducted from 30 – 100 ° at 0.02 increments at a speed of 1s per step, on the polished cross-sections of both the Ti25Ta and Ti65Ta samples. In addition, samples of the CP Ti and Ta virgin powders were analysed for comparison.

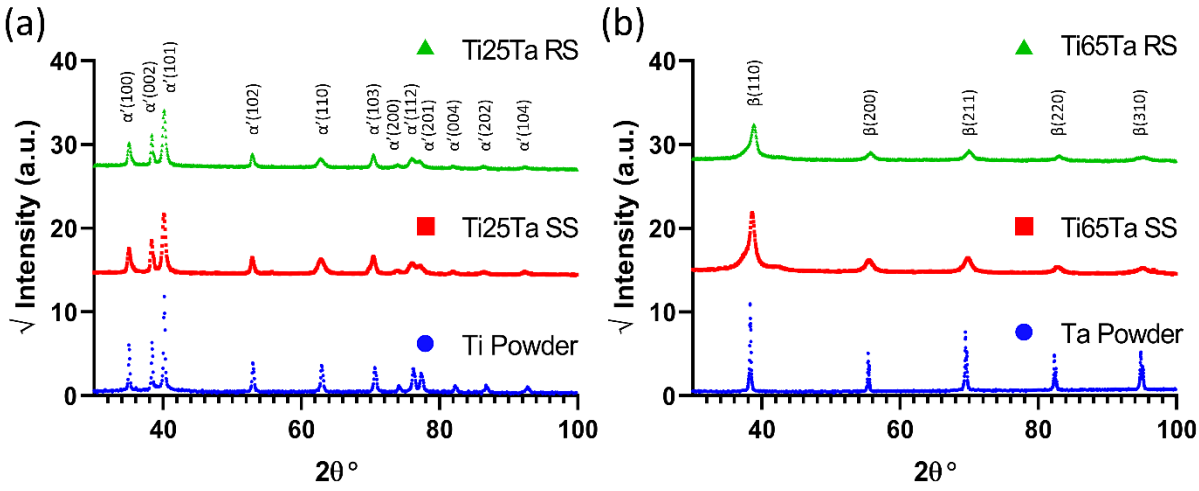

Figure 4-4: The XRD phases observed in (a) L-PBF Ti25Ta with CP Ti powder for comparison and (b) L-PBF Ti65Ta with Ta powder for comparison. Adapted from [346].

The XRD analysis revealed that the Ti25Ta material showed a similar crystal structure to the pure Ti powder, Figure 4-4(a). Both the Ti25Ta material and CP Ti powder displayed an HCP phase structure, confirmed by PDF card 00-044-1294. The peaks in Figure 4-4(a) are labelled as α′ as this is the metastable, martensitic form of the stable α phase, which possesses the same crystal structure and is consistently observed in L-PBF CP Ti and conventional quenched TiTa alloys [36, 193]. The Ti65Ta material showed the same crystal structure as the Ta powder, Figure 4-4(b). Both displayed a BCC phase structure, confirmed by PDF card 00-004-0788.

Upon higher resolution analysis, Figure 4-5, peak shifts and peak broadening were recognised in the L-PBF material. The peak shift indicates a change in lattice parameter size. For the Ti25Ta material, Figure 4-5(a), the L-PBF material peak is shifted to the left, suggesting an increase in lattice parameter size and supports the drop in elastic modulus compared to CP Ti, due to a decrease in lattice atomic density. There is negligible peak shift between the single melt and remelt scan peaks, suggesting the remelt scan does not significantly alter the material crystal structure. For the Ti65Ta L-PBF material, Figure 4-5(b), the peak is shifted slightly to the right, indicating a decrease in lattice parameter. The peak broadening can be explained by increased dislocation density and residual stress in the L-PBF material. This is a common result of the rapid solidification occurring during solidification in L-PBF processing [354].

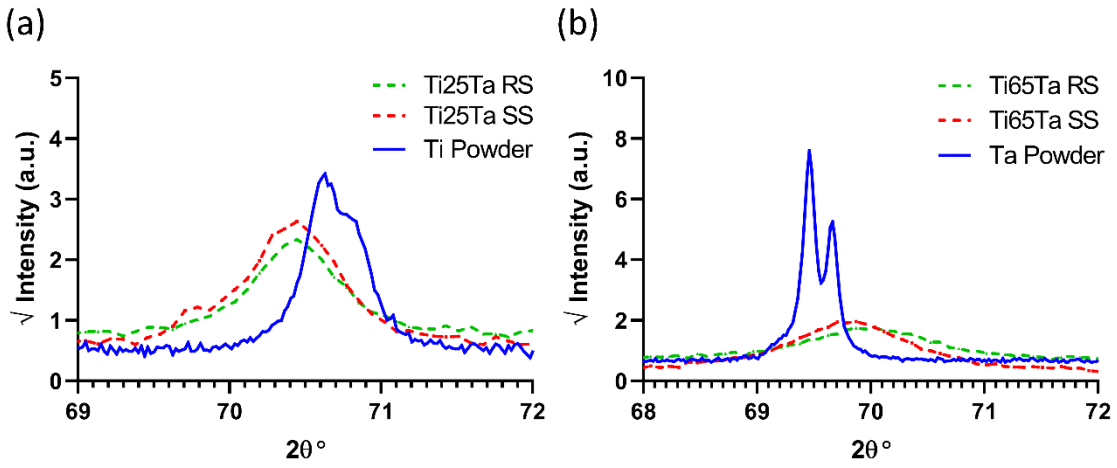

Figure 4-5: Magnified analysis of the (a) Ti and (b) Ta powder XRD analysis, overlayed with the L-PBF material, showing peak shifts and broadening. Adapted from [346].

Contrary to the equilibrium calculations in Figure 4-1, the L-PBF Ti25Ta and Ti65Ta both show single phase microstructures. The 9 % retained β phase in the equilibrium Ti25Ta alloy is likely undetectable in the XRD analysis due to its low volume fraction, whilst the 67 % α phase in the equilibrium Ti65Ta alloy is supressed by the rapid solidification of the L-PBF process.

4.2 Microstructure Morphology and Formation

To further understand the crystal and grain structure of the L-PBF Ti25Ta and Ti65Ta alloys, SEM and TEM analysis was used. SEM sample preparation for the Ti25Ta alloy included ion beam polishing at 300 µA and 7kV for 10 min followed by 100 µA and 3kV for 15min, to provide an adequate surface for high indexing in EBSD analysis. The L-PBF Ti25Ta was difficult to image due to the high dislocation concentration of the martensitic α′ laths. The Ti65Ta samples underwent the same preparation for consistency. A JEOL 7001F FEG SEM equipped with back scattered image (BSI), electron dispersive X-ray (EDX) and electron back scattered diffraction (EBSD) detectors, was used to assess the elemental homogeneity and microstructure morphology of the samples. TEM samples were prepared using focused ion beam milling and lifted out from the bulk sample with a FEI Scios Dual-beam FEGSEM. A JEOL 2100F FEGTEM, with an Oxford X-MaxN EDX detector, was used to conduct brightfield imaging, selected area electron diffraction (SAED) and EDX analysis. An accelerating voltage of 200 kW was used.

4.2.1 BSI and EDX Analysis

BSI revealed the overlapping melt pool structure in the y-z plane, Figure 4-6. The inhomogeneity of the Ti25Ta single melt material is clearly observed in Figure 4-6(a). The melt pool shows swirl patterns indicating the Marangoni flow, which occurs due to temperature gradients in the melt pool [340]. This adds a physical mixing characteristic to the melt pool, in addition to the Ta diffusion caused by high temperatures. The swirl patterns were not observed in the melt pool after the remelt scan was applied indicating increased homogeneity, Figure 4-6(b). Swirl patterns were noted to a lower degree in the single melt Ti65Ta material, due to the higher weight percent of Ta in the composition, Figure 4-6(c). To quantify the melt pool homogeneity, EDX point analysis was used. Ten points were analysed across the melt pool cross-section and the standard deviation in composition calculated, Table 4-3. For both the Ti25Ta and Ti65Ta alloys, the remelt scan showed a significant decrease in the standard deviation, highlighting an increase in homogeneity.

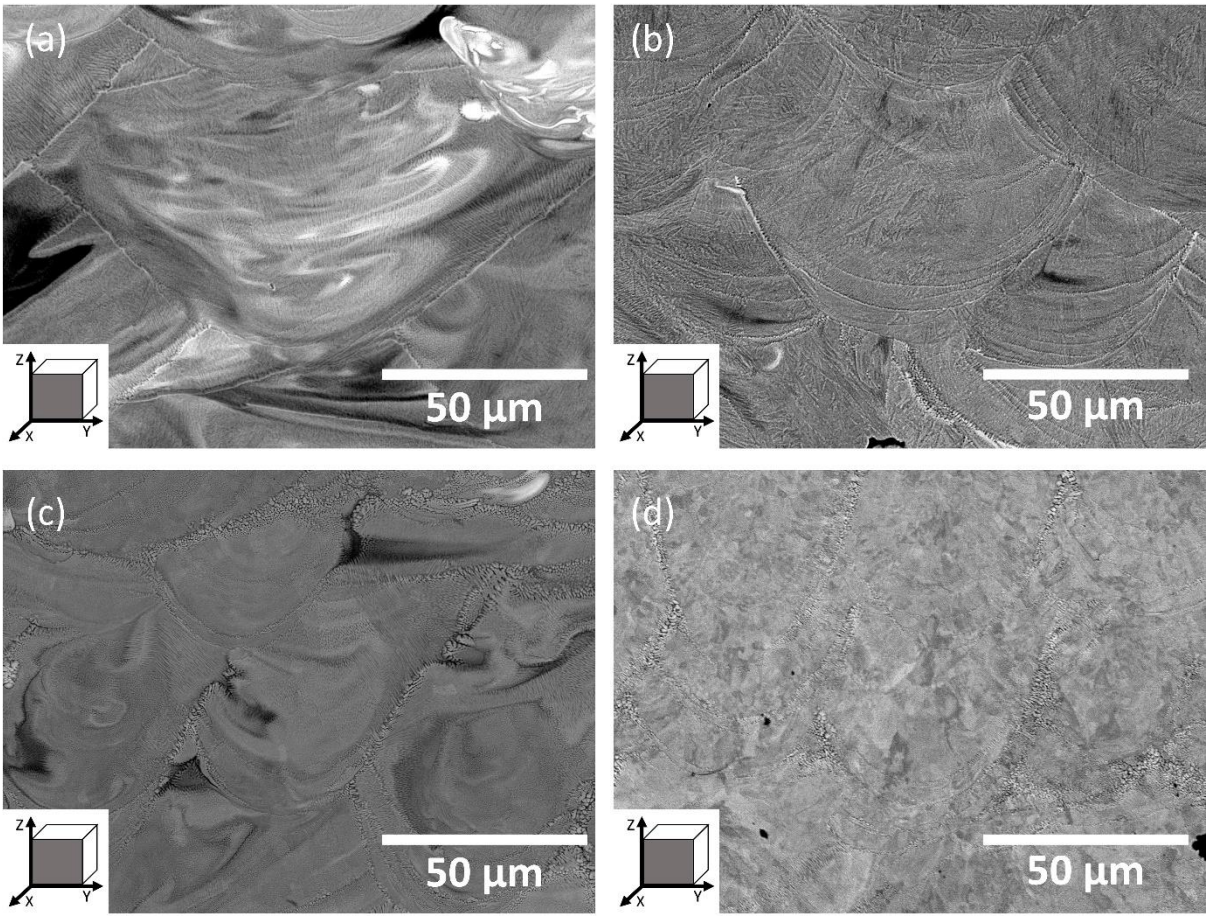

Figure 4-6: Melt pools observed with BSI in Ti25Ta (a) single melt and (b) remelt and in Ti65Ta (c) single melt and (d) remelt. Adapted from [346].

Table 4-3: Standard deviation in Ta elemental wt.% across a single melt pool.

	Single Melt	Remelt
Ti25Ta (wt.% Ta)	± 2.66	± 0.26
Ti65Ta (wt.% Ta)	± 1.34	± 0.69

In addition, a change in melt pool size and shape between the single melt and remelt conditions can be observed in Figure 4-6. The single melt condition, in both alloys, produced a wider and deeper melt pool than the remelt condition, Table 4-4. Furthermore, a lower melt pool width (W) and depth (D) was noted in the Ti65Ta composition when compared with the Ti25Ta composition. These differences are likely linked to the applied energy density and enthalpy of melting for each condition. For the single melt condition, the wider melt pool is created by a higher incident energy [337], likely due to the morphology of the absorbing surface. In the single melt condition, the laser is absorbed by a layer of powder. King et al. [345] showed using finite element simulation that a layer of Ti powder absorbs twice as much energy as a flat surface, due to multiple scattering of the laser between powder particles. Furthermore, the melt pool is larger in the Ti25Ta alloy, as the normalised enthalpy of melting is lower, due to the lower content of Ta. As a result, the melt pool penetrates a larger number of pre-formed layers in the Ti25Ta composition, enhancing the Ta melting. This explains why the remelt scan was more effective at reducing the area % of remaining Ta particles in the Ti25Ta alloy as opposed to the Ti65Ta alloy, noted in Section 3.4.

Table 4-4: Melt pool dimensions in L-PBF Ti25Ta and Ti65Ta

	Width (µm)	Depth (µm)	D/W Range	Layers Melted
Ti25Ta SS	135 ± 5	65 ± 5	0.43 – 0.54	2.6
Ti25Ta RS	85 ± 5	55 ± 5	0.55 – 0.75	2.2
Ti65Ta SS	90 ± 5	45 ± 5	0.42 – 0.58	1.8
Ti65Ta RS	60 ± 5	40 ± 5	0.54 – 0.82	1.6

The melt pool D/W ratio was also higher for the remelt condition for both alloys. As discussed in Section 3.3, a D/W ratio greater than 1.5 has been observed in literature to cause keyhole formation, as a tall narrow melt pool, is more likely to undergo collapse. The D/W ratio for both alloys is much less than 1.5 for both scanning conditions, however it can be concluded that the remelt scan is more likely to result in keyhole formation than the single melt condition, due to the melt pool morphology.

4.2.2 EBSD

The increased homogeneity and decreased melt pool size of the remelt samples observed likely influences the microstructure morphology. To observe the microstructure, EBSD analysis was conducted both in the x-y and y-z planes and inverse pole figure (IPF) maps created. The x-y plane tends to show a microstructure based on the laser scan pattern, whilst the y-z plane tends to show columnar grains formed due to the strong temperature gradient between the melt pool and cold build platform. The EBSD analysis was undertaken using α phase indexing for the Ti25Ta alloy and β phase indexing for the Ti65Ta alloy.

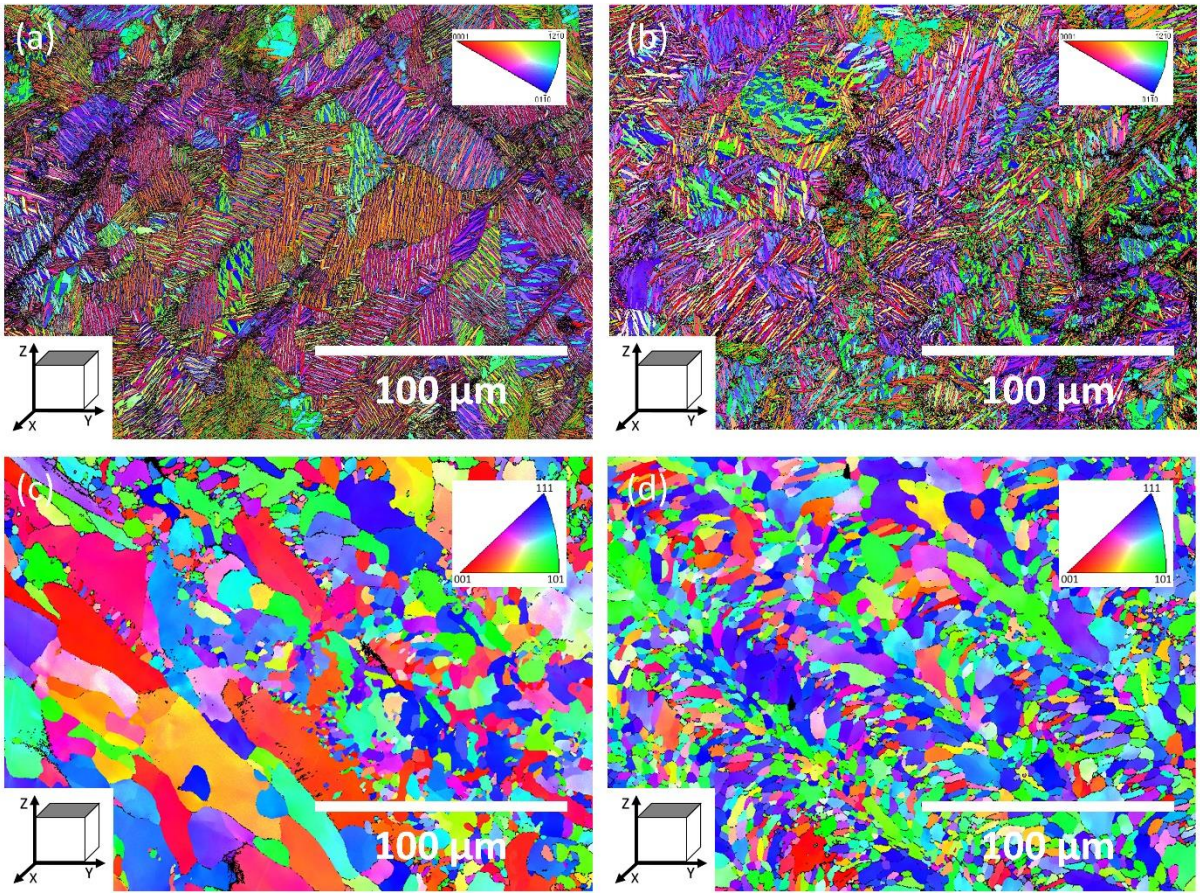

Figure 4-7: EBSD IPF of top surface of Ti25Ta (a) single melt and (b) remelt and of Ti65Ta (c) single melt and (d) remelt. Adapted from [346].

The x-y plane for both alloys, Figure 4-7, showed grain structures which reveal the scanning track of the laser, approximately 35 µm wide and running at 45 ° to the parallel. The Ti25Ta single melt sample, Figure 4-7(a), showed regions of prior β grains, filled with aligned martensite, due to the crystallographic link between martensite and the prior β grains from which it forms [63, 355]. The prior β grain structure is less defined in the remelt condition and the martensite arrangement appears to be more random, Figure 4-7(b). The loss of martensite alignment may be caused by a combination of more

homogeneous Ta atom distribution and the changed thermodynamics of the remelt scan. It has been previously shown that increasing substitutional atom additions to the Ti lattice decreases the size of the martensite colonies and can eventually lead to the nucleation of randomly oriented plates [63]. In addition, the remelt material is formed with smaller melt pools and hence there may be refinement in the prior β grains, which is difficult to discern in the α′ microstructure. Ti25Ta α′ laths were measured manually through a selection of 100 laths from different prior β grain regions. The average lath length was found to be 6.1 ± 3.4 µm and the average lath width was 0.45 ± 0.28 µm for the single melt material, and 5.7 ± 4.1 µm and 0.30 ± 0.11 µm for the remelt material, Table 4-5. There was no statistical difference in lath size between the single melt and remelt conditions when analysed with a paired t-test at a confidence level of 95 %. Future work investigating prior β grain reconstruction could assist with determining exact values of grain refinement in the Ti25Ta alloy, however the β grains of the Ti65Ta sample, provide a good indication.

A fully β grain microstructure was observed in the Ti65Ta alloy. The single melt material displayed both regions of elongated grains in the scanning direction and regions of much finer grains, likely where scan tracks overlap, Figure 4-7(c). Fine grains at scan track overlaps are attributed to recrystallisation of the solidified adjacent scan track [332]. The average grain size determined using the line intercept method was 4.8 ± 5.6 µm for the single melt sample and was reduced to 3.3 ± 2.9 µm for the remelt sample, Figure 4-7(d). This reduction in grain size was significant when tested with an unpaired t-test at a confidence level of 95 %. The reduction in grain size in the Ti65Ta remelt sample is likely caused by the smaller melt pools which physically restrict the possible grain size area. In addition, the cooling rate experienced by the remelt scan is possibly faster than that experienced in the single melt condition, as discussed in Section 2.2.3. Hence, grain growth is further restricted than in the single melt condition.

Table 4-5: Grain sizes measured from EBSD analysis in Ti25Ta and Ti65Ta single melt and remelt material

	Single Melt		**Remelt**	
Ti25Ta	**α′ Width (µm)**	**α′ Length (µm)**	**α′ Width (µm)**	**α′ Length (µm)**
	0.45 ± 0.28	6.1 ± 3.4	0.30 ± 0.11	5.7 ± 4.1
Ti65Ta	**Average β Diameter (µm)**		**Average β Diameter (µm)**	
	4.8 ± 5.6		3.3 ± 2.9	

Analysis of the y-z plane of the Ti25Ta, Figure 4-8, and Ti65Ta, Figure 4-9, alloys showed a lack of columnar grain structure in each composition, which is usually found in L-PBF produced Ti alloys [354]. The strong thermal gradient between the melt pool and the build platform in L-PBF processing usually results in epitaxial grain growth. When the solidification front caused by thermal gradients is faster than solid nucleation within the liquid, grains take the same orientation as the previous layer and

form long columnar grains over multiple layers [354]. Columnar grains can lead to anisotropic mechanical properties and hence, altering the alloy solidification rate through composition and the use of grain refiners, such as boron, are used to hinder columnar grain growth [356].

The y-z plane of the Ti25Ta alloy, Figure 4-8, showed equiaxed prior β grains, indicated by aligned and colour matching martensite laths. The region displayed in Figure 4-8 covers approximately 10 powder layers. As the martensite transformation can make it difficult to discern the prior β grain structure, an etched sample was also analysed to confirm this conclusion (Appendix Figure 8-2). Despite the equiaxed grain regions, a slight texture was noted in the Ti25Ta single melt sample, with a maximum MUD (multiples of uniform density) of 5.85. The remelt condition, which displayed randomly aligned martensite, decreased the MUD value to 3.86. Whether the lath randomisation is due to a more homogeneous distribution of Ta atoms, or the different thermodynamic conditions of the remelt scan, it appears that the opportunity for a second nucleation step resulted in a reduction in anisotropy. Hence, it is possible that the remelt scan could be used as a strategy in other alloy compositions to reduce anisotropy.

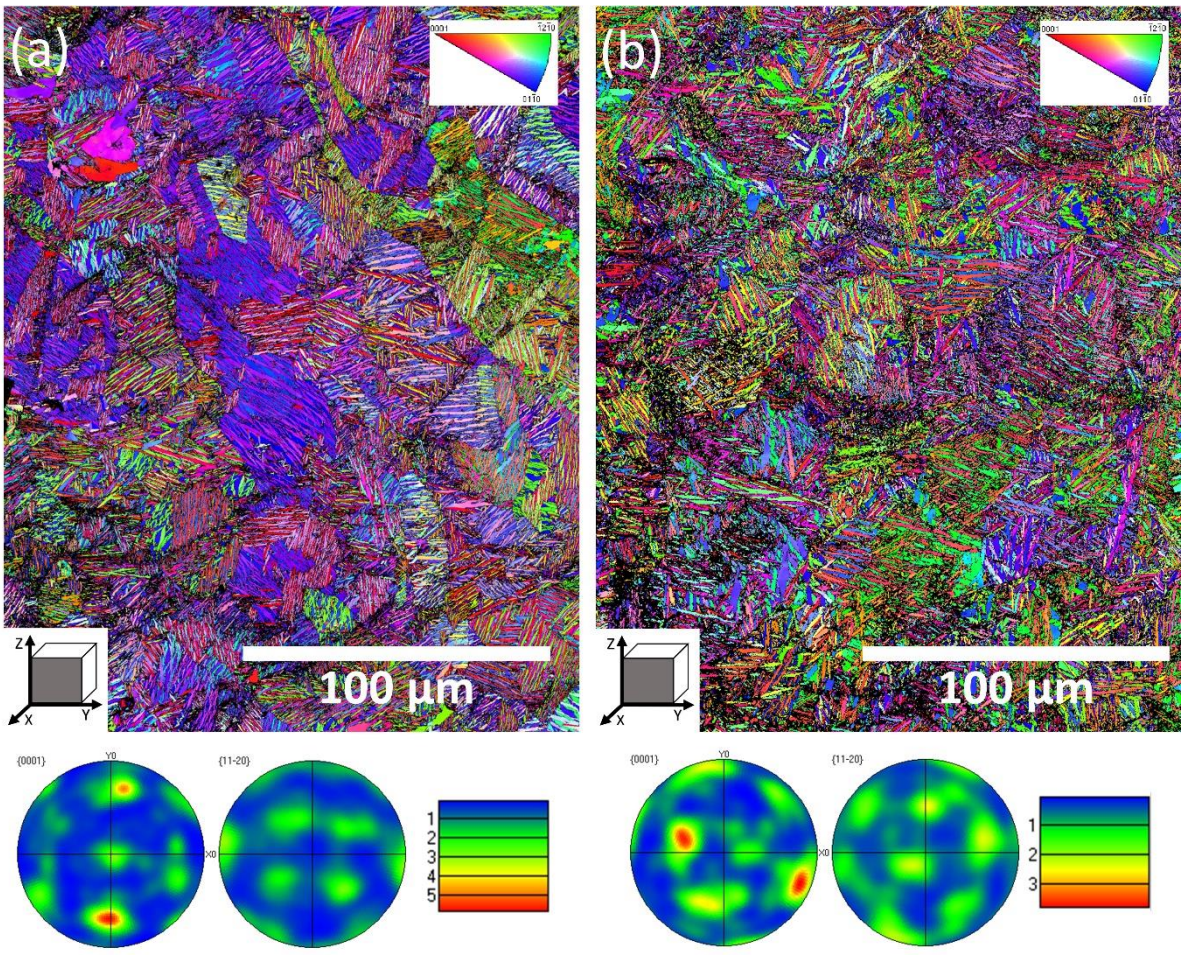

Figure 4-8: EBSD IPF of side surface of Ti25Ta (a) single melt and (b) remelt. Adapted from [346].

Epitaxial growth is avoided here due to the high compositional solidification rate of the Ti25Ta alloy, which is likely aided by partially melted Ta particles acting as nucleation sites. Compared to other commonly L-PBF produced Ti alloys, such as CP Ti and Ti-6Al-4V, the Ti25Ta alloy has an increased solidification rate. The formation of the Ta rich solid phase from the liquid leads to constitutional supercooling, facilitating nucleation ahead of the epitaxial solidification front. This was also seen in the Ti50Ta composition produced by Sing et al. [221] where only equiaxed grains were observed. According to the phase diagram, Figure 3-1, the liquid + β phase region is smaller for the Ti25Ta alloy compared with the Ti50Ta alloy (36 ° - 91 ° respectively), however the undercooling occurring is still sufficient to cause equiaxed grain growth in front of the epitaxial solidification front. In addition, the partially melted Ta particles are likely acting as heterogeneous nucleation sites. Tedman-Jones et al. [334] investigated using refractory particles such as W and Nb as grain refiners in Ti wire arc melted alloys and found that partially melted particles created an enriched zone around them, raising the equilibrium liquid temperature which facilitated grain nucleation. This phenomenon was termed ‘dissolutional supercooling’.

Similarly, the y-z plane of the Ti65Ta alloy showed no columnar grains and an equiaxed grain structure, Figure 4-9. In contrast to the Ti25Ta alloy, the Ti65Ta displayed no texture in the single melt or remelt conditions, suggesting stronger composition driven solidification. The grain refinement noted in the x-y plane was also observed in the y-z plane. Regions of thin, elongated β grains were observed, often radiating in a curve mimicking the melt pool shape. These grains likely indicate the different thermodynamic conditions of the remelt scan, as the smaller melt pool and faster cooling rates, lead to small areas of epitaxial grain growth, forming in the direction of the greatest thermal gradient.

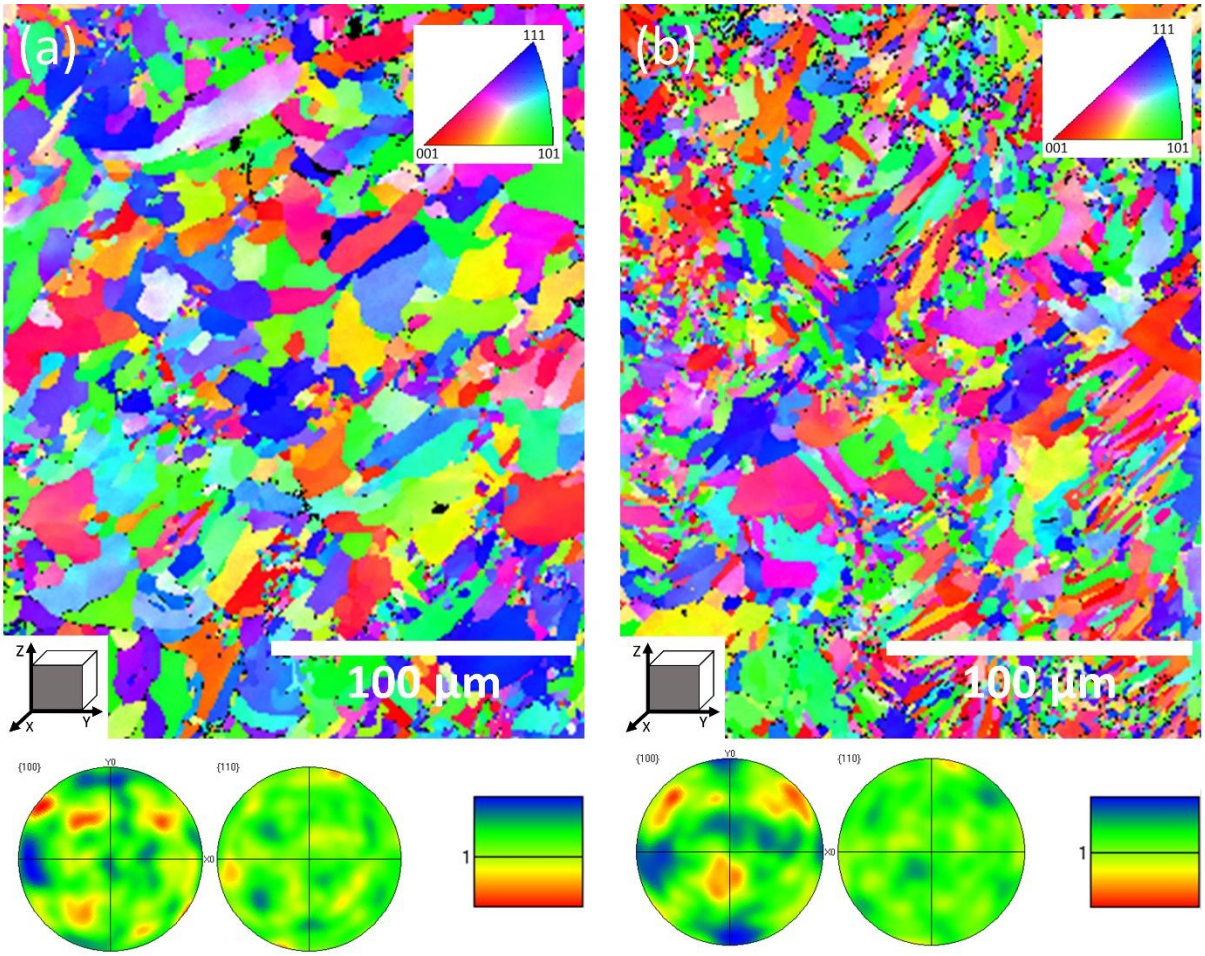

Figure 4-9: EBSD IPF of side surface of Ti65Ta (a) single melt and (b) remelt.

To confirm a lack of columnar grains in the Ti65Ta material, EBSD was conducted over an area covering approximately 60 powder layers, Figure 4-10. This could not be replicated in the Ti25Ta alloy as the fine and dislocation dense martensite laths could not be indexed at a lower magnification. However, the Ti65Ta microstructure confirmed an equiaxed grain structure over a large area, with a higher percentage of elongated radial grains in the remelt material. The lack of columnar grains was also attributed to constitutional supercooling and remaining Ta particles acting as nucleation sites. Due to the even higher weight percent of Ta in the Ti65Ta composition, larger compositional gradients lead to an even stronger nucleation in front of the temperature driven solidification front. The Ti25Ta and Ti65Ta L-PBF consist of starkly different crystal structures, however, due to the solidification mechanism from β to α grains, the overall grain structure for each alloy is relatively similar.

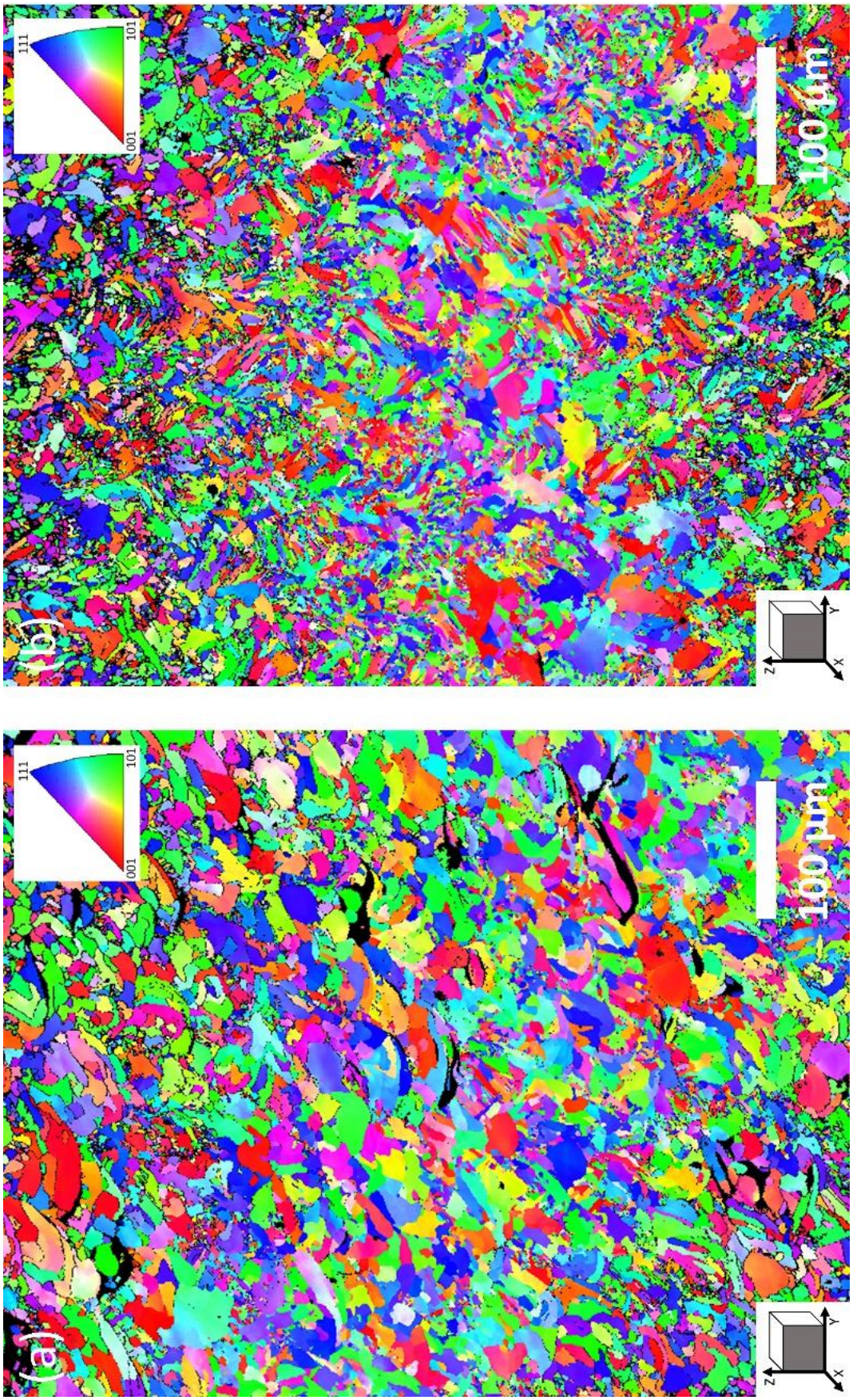

Figure 4-10: Large area EBSD IPF of x-y plane of Ti65Ta (a) single melt and (b) remelt conditions.

4.2.3 TEM

As the Ti25Ta alloy sits on the boundary between the α′ and α″ phase regions, an in-depth TEM analysis was undertaken in an attempt to identify any small volume fractions of the α″ phase, as only the α′ phase was observed in XRD analysis. Early investigations of the TiTa alloy system assert that the α′/α″ phase boundary exists between 22 – 23 wt.% Ta [85] and most studies confirm α″ formation at 25 wt.% Ta [84, 87, 219]. However, only one of these studies [84] used TEM analysis to confirm the α″ phase. The other studies rely on previous literature and XRD scans. The XRD peaks between α′ and α″ are difficult to differentiate, as only a few peaks undergo slight peak splitting when transforming from the α′ to α″ phase [357]. One study concluded that peak broadening is noted when both the α′ and α″ phase exist simultaneously [219], however this is very difficult to differentiate from peak broadening due to residual stresses and lattice strains in L-PBF material.

Due to the inhomogeneity of the L-PBF samples, TEM analysis also provided a unique opportunity to investigate the α′/α″ compositional boundary by assessing crystal structures in different compositional areas. Hence, a region with nominal composition was analysed for both the single melt and remelt conditions, alongside a Ta rich region. Selected area diffraction (SAD) patterns were used to identify the crystal phases.

The SAD patterns of the nominal composition region of the Ti25Ta single melt and remelt samples both indicated only lattice structures corresponding to the hexagonal α′ phase, Figure 4-11. The lattice parameters calculated from the SAD patterns are displayed in Table 4-6. The ‘a’ lattice parameter for the HCP lattice increased when compared to that of L-PBF CP Ti (a = 0.27 nm) [194, 358], confirming the lattice size increase noted in the peak shift of the XRD data (Section 4.1.2).

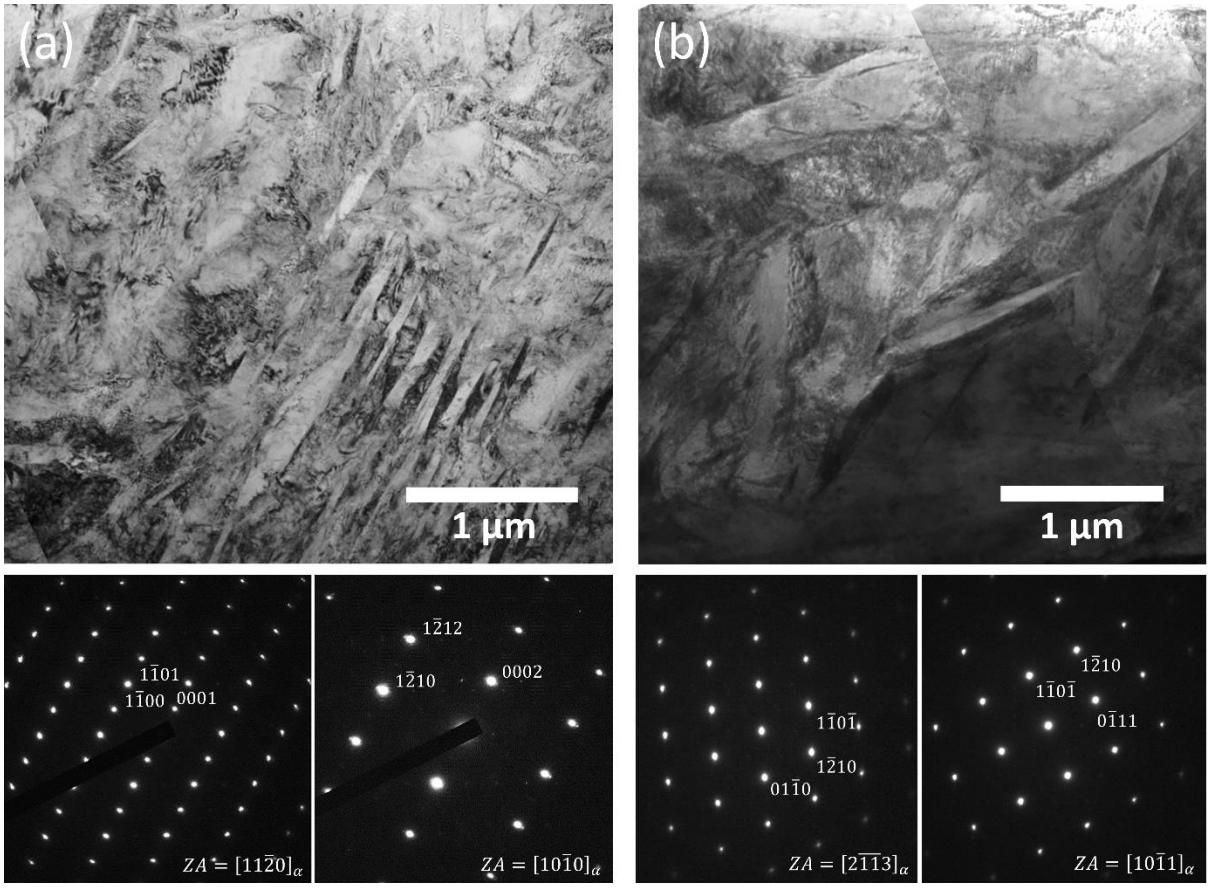

Figure 4-11: TEM brightfield images of the Ti25Ta (a) single melt and (b) remelt samples in regions with nominal composition (24 – 26 wt.% Ta). The SAD patterns indicate only α′ martensite. Reproduced from [346].

Table 4-6: Lattice parameters of phases observed in Ti25Ta single melt and remelt samples. Reproduced from [346].

Sample	Region	Phase	a, nm	b, nm	c, nm
Ti25Ta	nominal	α′ (P63/mmc)	0.2911	-	0.4605
Single Melt	Ta-rich	β (Im3m)	0.3283	-	-
		α′ (P63/mmc)	0.2906	-	0.4602
Ti25Ta Remelt	nominal	α′ (P63/mmc)	0.2938	-	0.4612
	Ta-rich	α′ (P63/mmc)	0.2951	-	0.4681
		α″ (Cmcm)	0.2992	0.4917	0.4640
Ti60Ta40 (00-052-0960)		α″ (Cmcm)	0.3038	0.4957	0.4686

The TEM brightfield image of a Ta rich region in the Ti25Ta single melt sample, Figure 4-12, spanned the transition from a BCC to a HCP crystal structure. The top right corner of the brightfield image returned a BCC crystal SAD pattern and corresponded with a concentration of approximately 80 wt.% Ta. This high Ta content region may correspond to a region of retained prior β phase, or more likely, a partially melted Ta particle. The Ta concentration, as shown by line scan 1, decreased away from the

centre of the region, and plateaus at the nominal composition of 25 wt.% Ta. Hence a range of compositions between 25 – 80 wt. % of Ta exist in this region. However, the analysis of several large lamellae on the boundary of the BCC region, B and C, both display α′ crystal structures, in addition to regions D and E, further from the boundary. The α′ structure is confirmed by the observation of $\{10\bar{1}1\}_{\alpha'}$ twins (region B), which has been observed in additively manufactured Ti-6Al-4V [351, 359, 360]. Despite the high Ta content, the α″ structure was not detected in these regions.

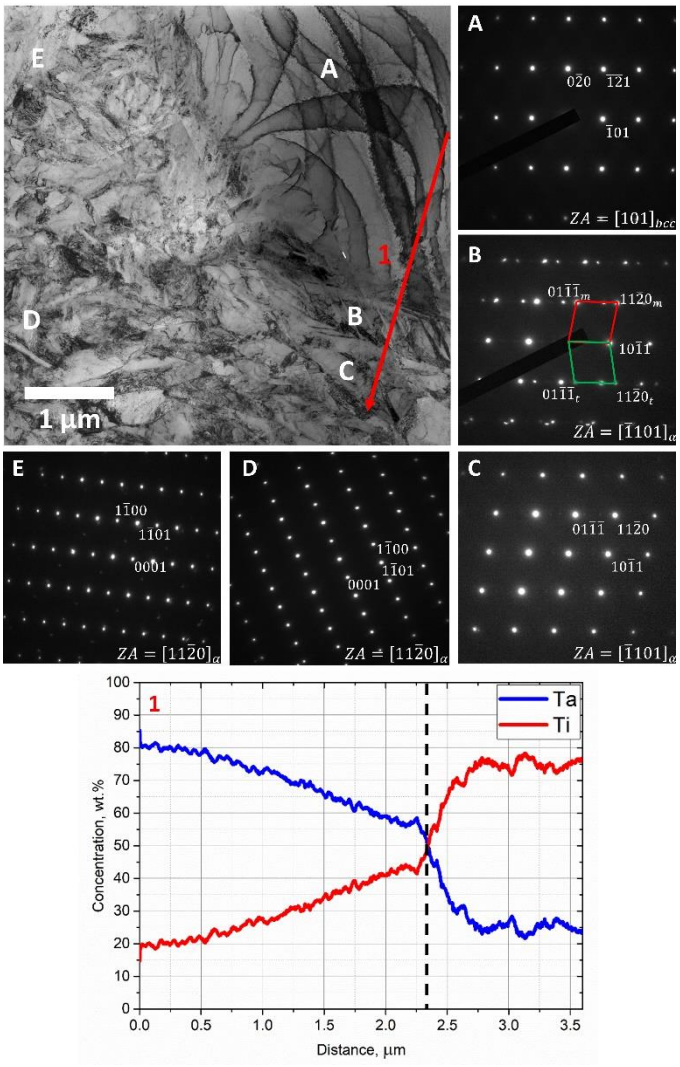

Figure 4-12: TEM brightfield image of a Ta rich region of the Ti25Ta single melt sample. A-E show several diffraction patterns from this region, including β and α' phase regions. The line scan shows the delineation between the β and α' phase regions and the accompanying elemental concentration. Reproduced from [346].

However, in a Ta rich region in the remelt material, the α″ was phase observed, Figure 4-13. The Ta concentration in this region was found to vary from 30 – 50 wt.%. A nano-scale discontinuity was also observed, represented by the white dashed line in the brightfield image. To the left of the discontinuity, regions A and B, where the composition was lowest at 30 wt.% Ta, the α′ crystal structure was observed whilst to the right of the discontinuity, regions C, D and E, where the composition was around 50 wt.%

Ta, the α″ crystal structure was observed. Regions A and B both displayed very fine martensite laths and hence only twinned regions could be analysed. The twin was determined to be $\{10\bar{1}1\}_{\alpha'}$ type, similar to that observed in the single melt sample. Coarser laths in the region to the right of the discontinuity allowed for analysis of three laths. Laths C and E were not twinned, showing the orthorhombic structure, with lattice parameters agreeing with the PDF card 00-052-0960, Table 4-6. Lath D showed $\{111\}_{\alpha''}$ twinning, agreeing with previous reports of orthorhombic twinning in TiNb [361] and Ti-Mo alloys [362].

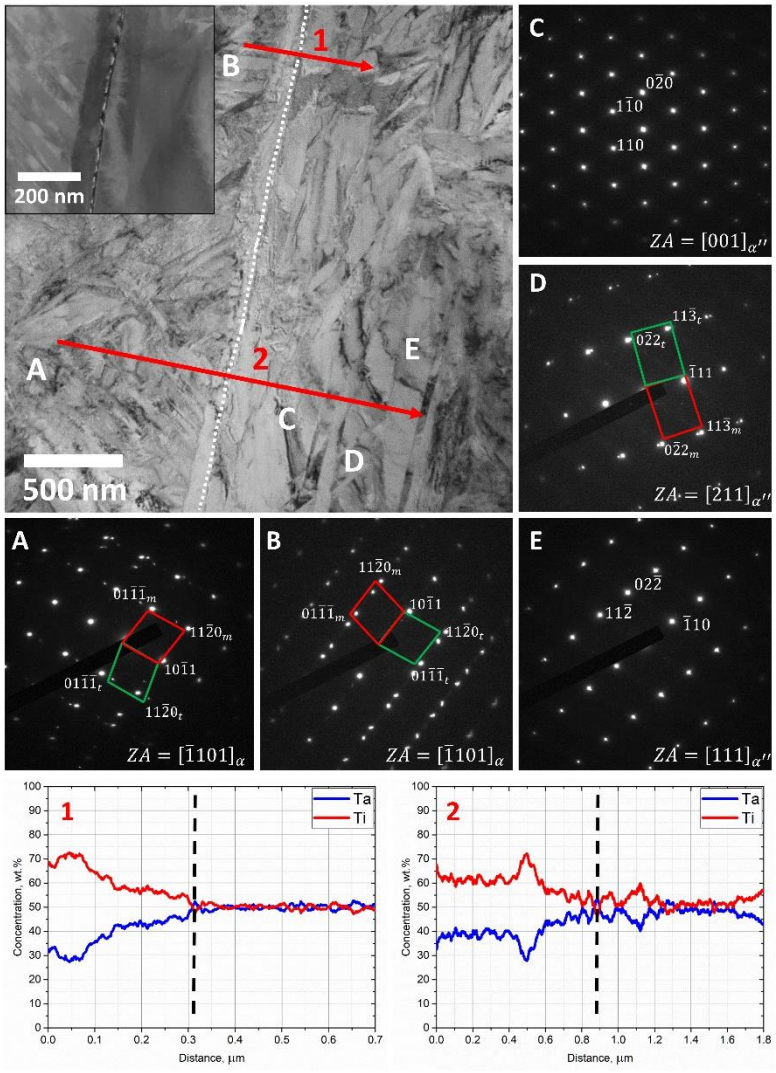

Figure 4-13: TEM brightfield image of Ti25Ta remelt showing a delineation between α′ and α″ phases. Reproduced from [346].

Therefore, for L-PBF produced Ti25Ta material the α′/α″ phase boundary appears to lie above 25 wt.% Ta as all analysis of areas of nominal composition displayed the α′ phase. The α″ phase was only seen to exist in regions with 50 wt.% Ta. While this disagrees with literature findings, it is likely that the rapid solidification of L-PBF alloys and the use of mixed powder heavily restricts Ta atomic diffusion

in comparison to the literature studies. The formation of α″ phase upon β phase decomposition, likely requires a larger compositional homogeneity. Hence the α″ phase was only seen in the remelt sample, which had a second opportunity for melting, atomic diffusion and greater homogeneity. The volume fraction of the α″ phase is also so small that is not possible to be discerned from the XRD analysis, and likely contributes very little to the mechanical performance of the alloy.

4.3 Mechanical Properties

The mechanical properties of the L-PBF TiTa alloys need to be characterised to determine which implant applications these alloys will be most suited for. The low elastic modulus must be confirmed in the L-PBF material and the material strength compared to the currently used biomedical alloys of CP Ti, pure Ta and Ti-6Al-4V ELI. Ultrasonic modulus and tensile testing were used to investigate these properties, supported with fractography analysis to assess how the remaining partially melted Ta particles affect mechanical behaviour.

4.3.1 Ultrasonic Modulus

As elastic modulus is one of the most important requirements for a new low modulus biomedical alloy, accurate measurement of elastic modulus is required. Elastic modulus derived from the linear region of stress-stain curves obtained from tensile testing tends to underestimate the modulus when compared with ultrasonic and free resonance methods [27]. Hence ultrasonic modulus testing was used in this study. Cuboid samples (15 mm × 15 mm × 10 mm) were printed using the single melt and remelt scanning strategies, cut from the build platform using EDM and ground to achieve parallel top and bottom surfaces. The sample thickness and density were recorded, and the sonic velocity of longitudinal and transverse waves measured using an Olympus 702 PR pulse processer and a Fluke 190 – 204 Scopemeter. The velocity measurements were used to calculate the elastic modulus as in Refs. [210, 363]. Both the single melt and remelt Ti25Ta material showed an elastic modulus of 65 ± 5 GPa, Table 4-7, which is in agreement with the literature value of conventionally produced Ti25Ta (64 GPa) [36]. The Ti65Ta single melt and remelt samples returned elastic modulus values of 71 ± 5 GPa and 67 ± 5 GPa respectively, slightly higher than the Ti25Ta material, but within the range of modulus experience by TiTa alloys from 60 – 70 wt.% Ta (84 – 66 GPa) [36]. The single melt Ti65Ta value is slightly higher than the remelt value, but still within the standard deviation of the measurement. As no differences in crystal structure or phase volume was noted between the single melt and remelt Ti65Ta material, this increase is likely negligible.

Table 4-7: Ultrasonic modulus measurements.

	Single Melt	**Remelt**
Ti25Ta	65 ± 5 GPa	65 ± 5 GPa
Ti65Ta	71 ± 5 GPa	67 ± 5 GPa

Both Ti25Ta and Ti65Ta alloys displayed an elastic modulus value almost half that of the most commonly used biomedical alloy, Ti-6Al-4V (114 GPa), and significantly lower than CP Ti (103 GPa) and pure Ta (186 GPa) [60]. Hence, the TiTa alloys are promising new biomedical alloys with a closer elastic modulus to bone, which may reduce stress-shielding effects and improve implant stability and lifetime. Hence, further study of their mechanical properties was undertaken via tensile testing.

4.3.2 Ti25Ta Standard Tensile Testing

To assess the strength and deformation behaviour of the L-PBF TiTa alloys, tensile testing was undertaken. Tensile sample dimensions were designed in accordance with ASTM standard E8 to fit within the Mlab Cusing R build volume, Figure 4-14(a). A vertical sample orientation was chosen, as this direction represents the minimum strength achievable from L-PBF tensile samples, attributed to elongated grains and inter-layer defects causing premature failure [192]. As this required a build height of 70 mm, and hence a large volume of powder, only the Ti25Ta alloy was investigated with this sample size. The Ti65Ta alloy was investigated with mini-tensile samples and will be discussed in Section 4.3.4. Net-shaped and bulk-type samples were produced. The bulk-type specimens were machined from printed blocks (20 mm × 15 mm × 70 mm), Figure 4-14(b). The samples were tested under uniaxial tensile loading in the build direction (z-axis), at a strain rate of 0.2 mm/min, on a 100 kN 4505 Instron tensile machine. An extensometer was used to accurately record the strain in the gauge region.

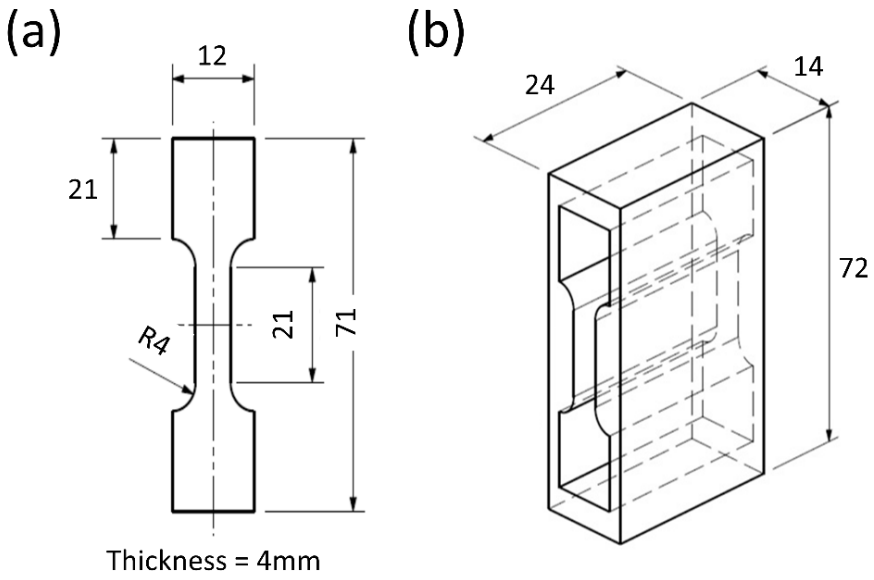

Figure 4-14: Tensile sample dimensions. (a) The net-shaped samples were printed to these dimensions, whilst the bulk-type samples were machined from (b) a printed block.

The net-shaped samples showed a higher strength (~ 150 MPa increase), but larger standard deviation (± 25 – 30 MPa), than the bulk-type samples (± 3 – 8 MPa), Figure 4-15(a). This agrees with literature findings which attribute the higher strength to net-shaped samples due to grain refinement and higher oxygen contents [192]. Grain refinement from an α′ lath width from 0.88 μm to 0.76 μm was noted for 3 mm thick samples of L-PBF Ti-6Al-4V when comparing bulk-type to net-shaped samples. Using the relationship of lath thickness to strength and the Hall-Petch slope derived by Cao et al. [351] for L-PBF Ti-6Al-4V, a minor refinement of lath width on this scale equates to an approximate 25 MPa increase in strength. Furthermore, Barba et al. [192] found net-shaped samples showed a minor increase in oxygen content (~ 0.05 wt.%) compared with bulk-type samples, attributed to the higher surface area to volume ratio. Oxygen has a strong solid solution strengthening effect on Ti and an increase in oxygen content of 0.05 wt.% oxygen could contribute a further 50 MPa of strength to the net-shaped samples.

Grain refinement and oxygen content likely only account for half of the increase in strength noted in the net-shaped samples. An additional strengthening mechanism contributing to the net-shaped sample strength is likely residual stress. Residual stresses are inherent in L-PBF processing due to the high cooling rates caused by the large thermal gradient between the melt pool and the cold build platform [189, 234, 237]. A study by Leuders et al. [232] measured residual stresses of 225 ± 25 MPa in the building direction of as-built Ti-6Al-4V tensile specimens and found this to equate to 50 MPa difference in strength between as-built and stress relieved samples. As residual stresses can be somewhat relieved by EDM, particularly as the highest residual stresses tend to occur at the surface of the L-PBF material [238-240], the bulk-type specimens are likely somewhat stress relieved, contributing to their lower strength. Measuring the residual stress after L-PBF processing was deemed beyond the scope of this

study. In addition, stress relieving heat treatments were not explored in this work as the focus was to explore as-built properties and how these could be altered *in situ* via the remelt scanning strategy. As the remelt scanning strategy was not yet fully understood in literature, it is unknown if the remelt material would respond similarly to the single melt material during stress relieving heat treatments. Stress relieving treatments will be explored in future work when the final implant geometry has been ascertained, as geometric factors can significantly alter regions of residual stress.

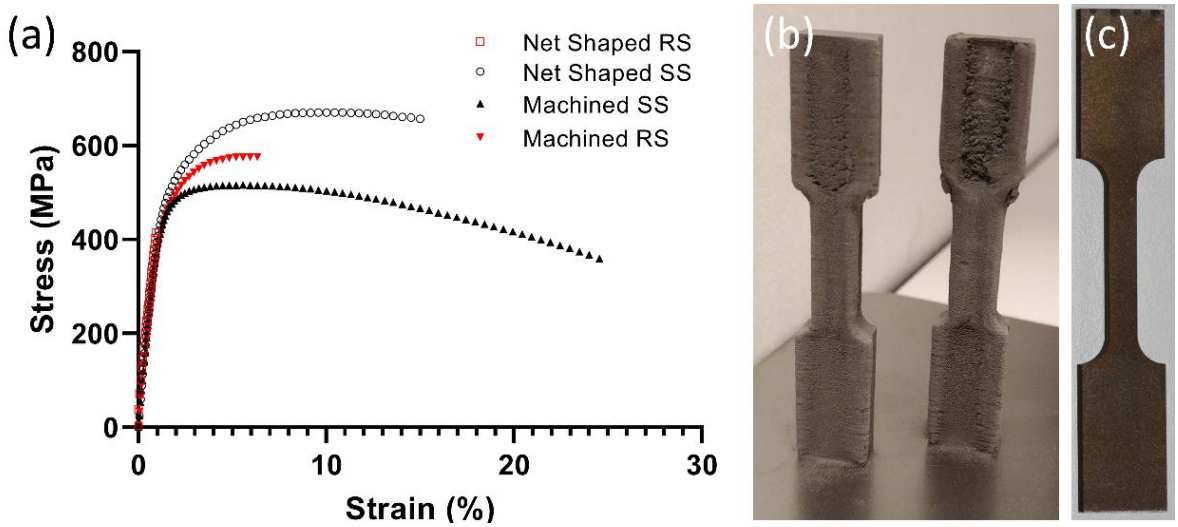

Figure 4-15: (a) Stress-strain curves for the Ti25Ta (b) net-shaped and (c) bulk-type samples. Adapted from [346].

The net-shaped samples also showed a much higher standard deviation in strength and elongation than the bulk-type samples, Table 4-8. The large standard deviation in net-shaped samples is commonly seen in literature and attributed mainly to the uneven surface produced during building [192, 248, 364]. Surface defects act as stress concentrators which can lead to premature failure and remain one of the largest issues for net-shaped AM parts. As can be seen in Figure 4-15(b), the net-shaped sample surfaces were coated in partially melted surface particles, which built-up significantly at the sample corners. The powder build-up was worse on the side of the sample which faced the powder coating blade and could be a result of powder spreading over the samples whilst they were still warm. Each net-shaped sample was ground to 1200 grit finish before testing, however two out of three of the net-shaped remelt samples failed in the elastic region and outside of the gauge length of the sample, revealing geometric defects on the fillet between the grip and gauge length. Whilst net-shaped parts must ultimately be considered before use in implant applications, the geometry, surface finish and residual stresses contribute to such large variations in sample testing, that it is difficult to assess the basic material properties of the new L-PBF TiTa alloys. Hence, it was concluded that bulk-type samples would be used for the following study to more accurately characterise the mechanical properties of the L-PBF TiTa alloys. Complications with

net-shaped parts will be discussed further in Chapter 5 when lattice structures, a much more relevant geometry for implant applications, are manufactured and their mechanical properties explored.

Table 4-8: Static mechanical properties of Ti25Ta net-shaped and bulk-type specimens in single melt and remelt conditions.

	Net-Shaped		**Bulk-Type**	
	Ti25Ta SS	**Ti25Ta RS**	**Ti25Ta SS**	**Ti25Ta RS**
Elastic Modulus (GPa)	69 ± 20	74 ± 35	35 ± 8	47 ± 3
Yield Strength (MPa)	588 ± 51	~ 880	425 ± 15	545 ± 9
UTS (MPa)	659 ± 36	> 915	509 ± 7	565 ± 6
Elongation (%)	10 ± 2	-	25 ± 1	11 ± 5

The bulk-type samples showed a lower standard deviation and a higher material elongation, as they were less affected by geometrical defects than the net-shaped samples. The enhanced elongation of the bulk-type single melt material revealed tensile softening, Figure 4-15. Tensile softening is observed in both conventionally and AM processed CP Ti [352, 365] and is attributed to the α Ti structure possessing a lower activation energy for self-diffusion than the activation energy for deformation [366-368]. Hence, a high rate of dislocation annihilation occurs during deformation and very little work hardening. The Ta content of the Ti25Ta alloy does not appear to inhibit self-diffusion of dislocations in the CP Ti at all.

The remelt material displayed a higher strength but significantly reduced elongation in both the net-shaped and bulk-type conditions. The increase in strength in the remelt material was approximately 50 – 200 MPa, similar to the 67, 100 and 180 MPa increases in strength of remelted L-PBF titanium alloys observed by Ali et al. [187], Wei et al. [190] and Xiao et al. [178] respectively. The strengthening mechanisms caused by the remelt scanning strategy are investigated in the following paragraphs considering the material homogeneity, grain morphology, oxygen content, residual stress and dislocation densities.

The remelt scan was shown to increase material homogeneity, Section 4.2.1. As Ta acts as a solid solution strengthening agent in the α′ phase, a more even Ta distribution may contribute to a higher strength. In addition, as the result of increased Ta diffusion, the remelt scan caused the formation of small volume fractions of the α″ phase, Section 4.2.3. The α″ phase was observed to cause higher strengths in alloys with greater than 25 wt.% Ta contents [36]. However, both these possible strengthening mechanisms occur in only minor volumes. The α″ phase was only noted in TEM analysis as the volume content was too low to notice in XRD analysis and the remelt scan only caused an

approximate 0.5 % reduction in the area of Ta particles. Therefore, the increased material homogenisation is unlikely a major contribution to the increase in strength of the remelt material.

The grain size and morphology was also altered by the remelt scan, as seen in Section 4.2.2. Even though there was no statistical difference in the α′ lath width and length between the single melt and remelt material, a statistically significant reduction in size of the β grains was noted in the Ti65Ta alloy. Hence, the prior β grains of the Ti25Ta alloy, which ultimately determine the martensite lath length, were likely slightly refined as well. This difference was possibly not observed in the analysis in Section 4.2.2 as, due to the difficulty of imaging highly dislocation dense α′ laths, a smaller region of prior β grains was analysed for the Ti25Ta alloy. Nevertheless, the average lath width was seen to decrease from 0.45 ± 0.28 µm to 0.30 ± 0.11 µm which equates to an increase in strength of up to 100 MPa, using the relationship of lath thickness to strength and the Hall-Petch slope derived by Cao et al. [351]. Hence, grain refinement caused by the remelt scan could be a significant contribution to the increased strength of the remelt material.

Furthermore, the remelt scan caused randomisation of lath orientation, Figure 4-7, which may also contribute to the lower ductility noted in the remelt scan sample. Slip can occur in α′ Ti through <a> slip, <a + c> slip and $\{10\bar{1}1\}_{\alpha'}$ twinning [369, 370]. However, twinning can be retarded by stacking faults and the presence of other phases, such as β, at the twin interface [371]. As the α′ laths are randomly oriented and no longer sharing grain boundaries with similarly oriented α′ laths, dislocation pile up [164], as well as the retardation of twinning mechanisms, may contribute to the brittle fracture observed in the remelt material.

Oxygen is known to be a strong interstitial strengthening element in Ti, with contents as low as 0.1 wt.% contributing to 100 MPa in strength [349]. The remelt material is exposed to the atmosphere in a molten state for twice the time experienced by the single melt material. The oxygen content analysis of printed material in Section 4.1.1 showed an increase of oxygen content in the remelt material of 0.02 % in the bulk and 0.07 % at the sample surface. Hence, oxygen enrichment could account for 20 – 70 MPa of increased strength in the remelt material and is likely to contribute a higher amount to the net-shaped samples than the bulk-type, due to their higher surface area to volume ratio. Furthermore, increases in strength in titanium alloys due to oxygen enrichment are also coupled with a strong decrease in ductility, as observed in the remelt material. Oxygen enrichment is likely not as strong a contributor to strength as grain refinement but cannot be discounted.

Different residual stress levels in the single melt and remelt material may also contribute to their different tensile behaviour. Several studies using identical parameters to the single scan to remelt material, as used in this study, reported an increase in residual stress from 22 – 68 % when the remelt scan was applied [178, 187, 190]. These studies hypothesised that the cooling rate is increased by the remelt scan, as the lower absorption of the laser by the reflective solidified metallic surface causes

smaller melt pools and the smaller melt pools cool faster than larger melt pools. A reduction in melt pool size was observed in Section 4.2.1 and hence, it is possible that residual stresses are higher in the remelt material. However, as residual stress is somewhat relieved during EDM [238-240], it is likely that any increased residual stresses are contributing significantly more to the strength of the net-shaped samples than the bulk-type samples.

Finally, increased dislocation concentration in the remelt samples, may also contribute to their higher strength. No literature studies have explored the effect of remelting on dislocation density, however high dislocation density is common in AM produced materials due to rapid solidification, thermal contractions and plastic strains generated from passing through the β transus [164, 226, 372]. If residual stresses are increased in the remelt material, it is likely that dislocation density is also increased. However, no visible increase in dislocation density could be noted in the TEM investigations in Section 4.3.2 or through peak broadening in the XRD analysis in Section 4.2 Manero et al. [370] observed that increased dislocation density in Ti-6Al-4V facilitated the formation of $\{10\bar{1}1\}_{\alpha'}$ twins by lowering the boundary energy for twin formation. This resulted in an accompanied increase in ductility, which was not observed in the remelt material.

Overall, the remelt material likely displayed a higher strength due to grain refinement, increased oxygen content, increased residual stress and dislocation levels. In addition, the ductility of the remelt material is likely affected by the oxygen content and the randomisation of the α′ lath orientation, hindering the deformation mechanisms of slip and twinning. Despite these changes in mechanical properties between the single melt and remelt material, the L-PBF Ti25Ta, in both conditions, performs well when compared with other currently used biomedical alloys.

When compared with L-PBF Grade II CP Ti, the Ti25Ta bulk-type samples displayed a similar strength but almost half the elastic modulus, Table 4-9. L-PBF CP Ti displays a yield strength of 353 – 587 MPa [201], whilst the Ti25Ta single melt material in this study displayed a yield strength of approximately 426 ± 14 MPa. A similar strength was also observed in the conventionally produced Ti25Ta (480 MPa) [36], suggesting that the grain refinement caused by the fast cooling rates in L-PBF is similar to that achieved during water quenching during conventional processing. The Ti25Ta alloy hence does not benefit significantly in strength from L-PBF processing, as in other alloy systems.

Table 4-9: Comparison of L-PBF Ti25Ta mechanical properties to other biomedical alloys.

	Total Elongation (%)	**Yield Strength (MPa)**	**Elastic Modulus (GPa)**	**Ref.**
L-PBF				
Ti25Ta Single Melt	25 ± 1	426 ± 14	65 ± 5	This work
Ti25Ta Remelt	11 ± 4	545 ± 9	65 ± 5	This work
CP Ti (Grade II)**	7 - 22	353 - 587	112 [221]	[201]
Pure Ta	2	450 - 654	-	[218]
Ti-24Nb-4Zr-8Sn (TNZS)	19	563	53	[173]
Ti50Ta	12	883	76	[221]
Ti-35Zr-28Nb (TNZ)	-	612	57	[213]
Ti-6Al-4V	1.6 - 11	910 - 1330	94 - 118	[196]
Conventional				
Ti25Ta	20	480	64	[84]
CP Ti (Grade I)	30	170 - 241	103	[60]
Pure Ta	20 - 50	165 - 220	186	[60]
Ti-24Nb-4Zr-8Sn (TNZS)	15	700	46	[99]
Ti50Ta	25	375	77	[36]
Ti-35Zr-28Nb (TNZ)	11	729	64	[373]
Ti-6Al-4V	10 - 15	795 - 875	105	[54]

In addition to a similar strength to conventionally produced Ti25Ta, the single melt L-PBF Ti25Ta also displays a similar elongation. Low ductility is often observed in L-PBF materials, with large reductions in ductility noted in CP Ti, pure Ta and Ti-6Al-4V, Table 4-9. The single melt Ti25Ta, on the other hand, appears to retain a high ductility, even higher than other recently developed β Ti alloys of TNZS and Ti50Ta. The high ductility is promising, suggesting the L-PBF Ti25Ta alloy will be particularly beneficial in fatigue, due to its high damage tolerance.

Furthermore, the L-PBF Ti25Ta displayed almost half the elastic modulus of L-PBF CP Ti. The elastic regions of the bulk-type tensile sample curves suggested an elastic modulus of 35 ± 8 GPa and 47 ± 3 GPa for the single melt and remelt samples, respectively. This supports the analysis of Niinomi et al. [27] that tensile testing often underestimates the value of elastic modulus. The ultrasonic modulus value was 65 ± 5 GPa for both the single melt and remelt conditions, similar to the resonance vibration value from literature of 64 GPa [36]. The tensile modulus does however suggest a higher elastic modulus in

**Note that the values quoted for the strength of CP Ti refer to Grade II with a higher oxygen content than the Grade I CP Ti used in this study.

the remelt material, which was not observed in the ultrasonic modulus testing. This will be discussed further with the addition of fatigue hysteresis data in Section 5.1.2.

Overall, the L-PBF Ti25Ta alloy is promising for low stress implant applications, such as mandible plates, due to its similar strength but much lower elastic modulus than CP Ti. However, to assess the effect of the remaining partially melted Ta particles on mechanical failure, fractography of the tensile samples was conducted.

4.3.3 Ti25Ta Standard Tensile Fractography

Fractography analysis of the bulk-type tensile samples was undertaken to clarify the mechanisms of failure in the L-PBF single melt and remelt Ti25Ta material. A JEOL 7001F FEG SEM was used in back-scatter imaging (BSI) mode to identify process-induced defects and remaining partially melted Ta particles in the matrix.

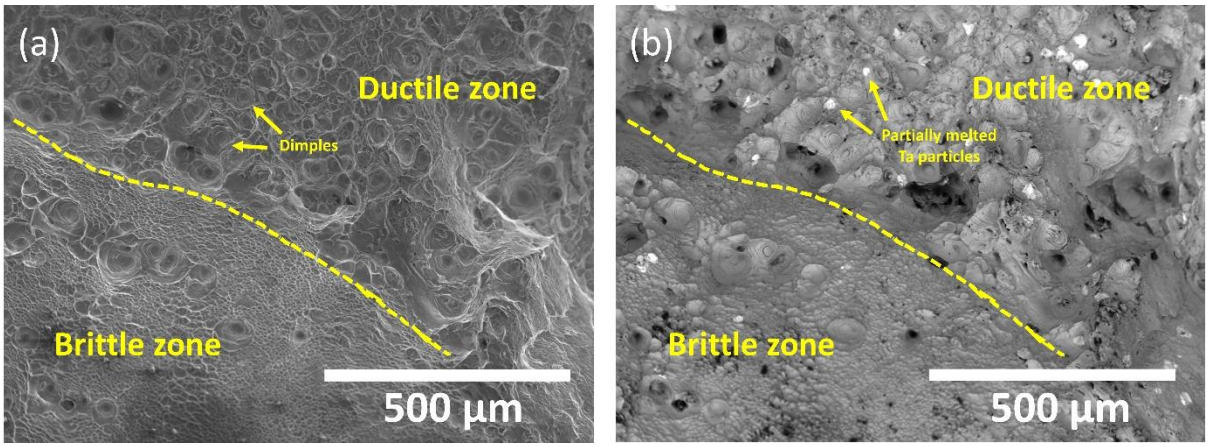

Figure 4-16: Fracture surface of Ti25Ta remelt sample showing transition from brittle to ductile fracture zones, as well as remaining Ta particles. SE image (a) and BSI (b). Reproduced from [346].

The fracture surfaces of the bulk-type tensile specimens showed very similar features between the single melt and remelt samples, and hence only the remelt sample is displayed in Figure 4-16 in (a) SE and (b) BSI modes. Each surface showed a ductile and brittle fracture region, characterised by ductile dimples and planar fracture surfaces respectively. The ductile zone encompassed a slightly larger area of the fracture surface on the single melt sample, corresponding to its superior elongation.

Both fracture surfaces showed process-induced porosity and remaining Ta particles. There was a larger number of remaining Ta particles observed in the single melt sample, corresponding with the increased homogenisation caused by the remelt scan. The BSI image, Figure 4-16(b), highlighted that the remaining Ta particles did not correspond with the major deformation sites, such as ductile dimples. In

addition, no remaining Ta particles were seen raised above the surface, as if pulled out of the matrix. Hence, there was no indication that the Ta particles were contributing to mechanical failure by acting as crack initiation sites. Instead, ductile dimples often corresponded with process-induced defects, suggesting that the pores acted as sites where cavitation began during plastic deformation.

4.3.4 Ti65Ta Mini-Tensile Testing

A mini-tensile sample was designed in accordance with ASTM standard E8, to require a maximum of 40 mm of powder in the Mlab Cusing R powder delivery system, Figure 4-17(a). This procedure reduced the volume of powder to be used in the Mlab chamber, while following the designated standard to obtain the mechanical properties of the Ti65Ta alloy. Sample blocks of 15 mm × 6 mm × 35 mm, Figure 4-17(b), were printed using the optimal parameters determined in Section 3.4, with both the single melt and remelt scanning conditions. Both the Ti25Ta and Ti65Ta alloys were printed to allow for consideration of the differences in mechanical behaviour caused by the change in part size. The samples were tested using a 100 N Zwick ZMART.PRO at a constant strain rate of 0.2 mm/min, with a 10 mm strain gauge.

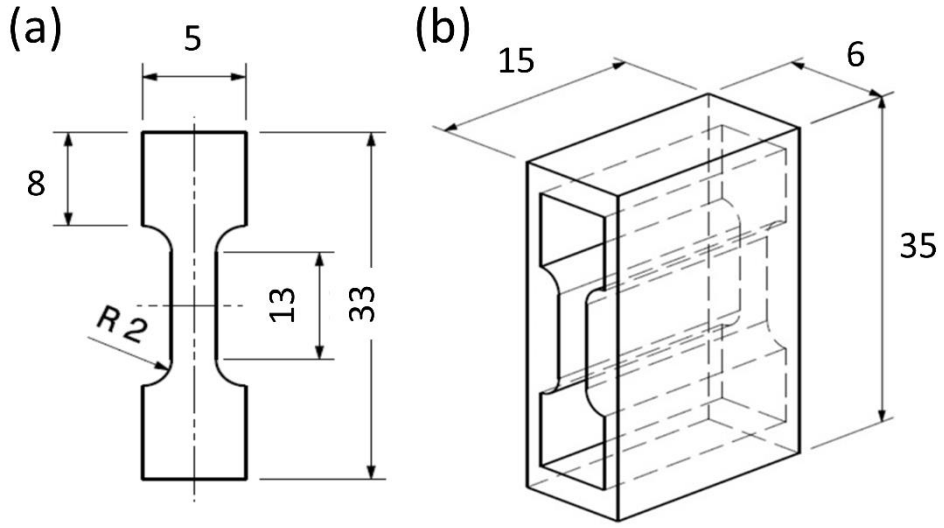

Figure 4-17: (a) Mini-tensile sample dimensions, EDM machined from the block in (b).

The Ti65Ta tensile curves displayed a UTS of 776 ± 21 MPa and 949 ± 83 MPa for the single melt and remelt conditions, respectively, Figure 4-18(a). Similar to the Ti25Ta material, the higher strength of the remelt scan material was coupled with a reduced ductility. Furthermore, the Ti65Ta material appeared to have two separate elastic regions and yield points, Figure 4-18(b). The initial yield point corresponds to the stress-induced transformation from the β to α″ phase, and hence the earlier linear region is more representative of the modulus of the β phase. The subsequent linear region represents

the elastic behaviour of the α″ and β phases together, as seen in other meta-stable β Ti alloys [374]. The stress-induced α″ formation results in the shape memory effects of β Ti alloys however exploring the shape memory properties was deemed beyond the scope of this thesis.

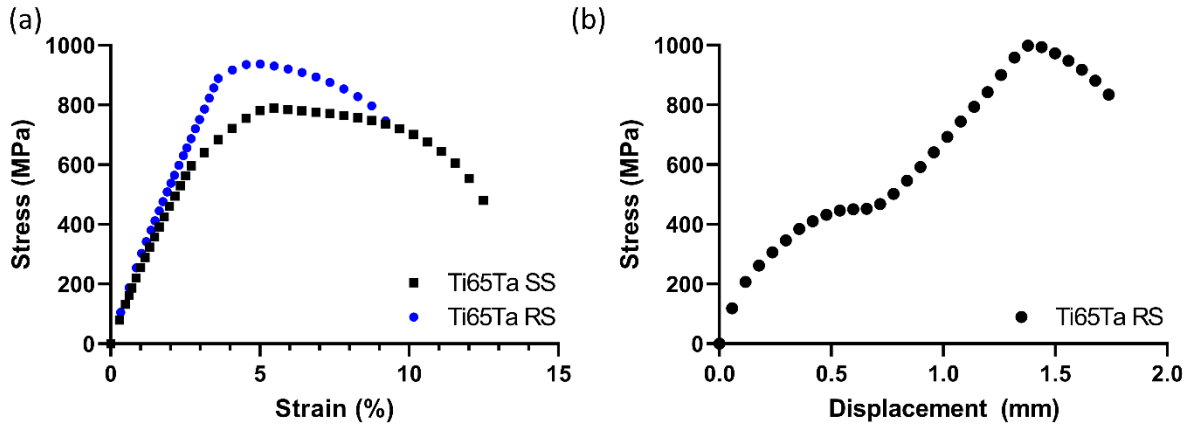

Figure 4-18: Mini-tensile data. (a) Stress-strain curves for Ti65Ta single melt (SS) and Ti65Ta remelt (RS) material. (b) Stress-displacement[††] curve for Ti65Ta remelt sample, showing double yield points.

The UTS of conventionally produced Ti65Ta is approximately 650 MPa [36]. The L-PBF single melt Ti65Ta shows an increase in UTS of approximately 100 – 150 MPa, likely attributed to the grain refinement, oxygen enrichment, and higher residual stresses and dislocation densities, caused by L-PBF processing, as discussed in Section 4.3.2 in regards to the Ti25Ta alloy. The Ti65Ta alloy, however, undergoes a higher increase in strength when L-PBF processed than the Ti25Ta alloy. The grain size of the Ti65Ta alloy is more significantly reduced when compared to conventionally produced material. Lath width is similar in conventional and L-PBF produced Ti25Ta due to the diffusion-less transformation between the β and α′ laths. However, the β grains in conventionally produced Ti65Ta were found to be up to 60 µm in diameter by Zhou et al. [36]. EBSD analysis in Section 4.2.2 revealed average β grain sizes of 4.8 ± 5.6 µm and 3.3 ± 2.9 µm for the single melt and remelt material, respectively. Hence, grain refinement caused by L-PBF processing has a much stronger effect on the strength of L-PBF Ti65Ta than L-PBF Ti25Ta.

The representative tensile curves of the Ti25Ta and Ti65Ta suggested that the two alloys have similar strengths, Figure 4-19. The Ti65Ta material also displayed a higher total elongation but similar uniform elongation to Ti25Ta. The mechanical properties of each alloy are summarised in Table 4-10. Elongation past the uniform elongation point is dependent more upon fracture mechanisms than work hardening. Work hardening is almost non-existent in both the Ti25Ta and Ti65Ta alloys due to a high dislocation annihilation rate discussed in Section 4.3.2. Sample fracture is caused by nucleation, growth

[††] Displacement is used in this graph to visually accentuate the dual yield points.

and coalescence of voids. In the both the L-PBF alloys, void nucleation likely corresponds to process induced defects, however, in the Ti25Ta alloy brittle failure occurs due to rapid crack propagation along the high-density martensite lath boundaries. The Ti65Ta alloy undergoes much more ductile failure due to the slower propagation of cracks along the β grain boundaries, which are at a much lower density than the martensite boundaries. Furthermore, twinning in the β phase was, observed by Ankem and Green to reduce with grain size [375], and hence the grain refinement of the Ti65Ta L-PBF material has likely contributed to the lower elongation (13 ± 1 %) than observed in conventionally produced Ti65Ta (~20 % [36]).

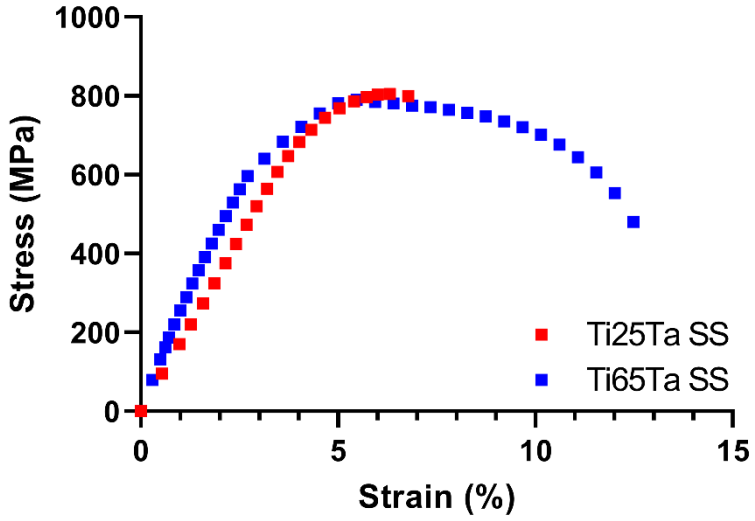

Figure 4-19: Comparative mini-tensile curves for single melt Ti25Ta and Ti65Ta

Table 4-10: Comparative mini-tensile data for L-PBF Ti25Ta and Ti65Ta.

	Ti25Ta SS	**Ti25Ta RS**	**Ti65Ta SS**		**Ti65Ta RS**	
	α′	**α′**	**β → α″**	**β + α″**	**β → α″**	**β + α″**
Elastic Modulus (GPa)	39 ± 3	35 ± 3	50 ± 6	86 ± 7	64 ± 12	99 ± 10
Yield Strength (MPa)	710 ± 10	-	212 ± 35	665 ± 45	245 ± 29	888 ± 52
UTS (MPa)	812 ± 9	> 962 ‡‡	776 ± 21		949 ± 83	
Elongation (%)	8 ± 1	-	13 ± 1		11 ± 3	

‡‡ The mini-tensile Ti25Ta remelt samples failed in the elastic region, and hence the yield strength, UTS and elongation were unable to be accurately determined for the mini-tensile geometry.

The elastic moduli values determined from the slope of the elastic region suggested a higher elastic modulus in the Ti65Ta alloy than the Ti25Ta alloy. Similarly, to the standard bulk-type specimens in Section 4.3.2, the elastic moduli values determined from tensile testing underestimate the elastic modulus compared to the ultrasonic modulus testing method. However, the ultrasonic modulus testing did not note a significant increase in the modulus between the Ti25Ta and Ti65Ta alloys, as observed in Table 4-10. It is possible that the ultrasonic modulus method was affected by the inhomogeneity of the material, as remaining Ta particles may have caused wave scattering. The moduli of each alloy will be further discussed in Section 5.1.2, with additional elastic moduli data derived from hysteresis loops during fatigue testing.

It should also be noted that the UTS of the mini-tensile Ti25Ta samples (812 ± 9 MPa) was considerably greater than that observed for the bulk-type standard sized tensile samples (509 ± 7 MPa). In addition, ductility was reduced significantly from 25 ± 1 % to 8 ± 1 %. The mini-samples were closer in strength and ductility to the net-shaped standard sized tensile samples (UTS = 659 ± 36 MPa and elongation = 10 ± 2%), suggesting similar part size effects contributed to the increase in strength. Recent studies show that part size and shape can alter the thermodynamic history of a part and hence affect microstructure and mechanical properties [192, 263, 376]. The mini-tensile material likely underwent grain refinement and obtained a higher oxygen content than the standard tensile samples, similar to the net-shaped standard size samples. Part size effects of the different sized samples was deemed beyond the scope of the study, particularly considering that very minor changes in oxygen content and α′ lath width contribute significantly to changes in strength in α′ Ti alloys. Measuring methods with sufficiently high accuracy to properly analyse these variables were not available for this study.

The Ti65Ta material shows a similar ultimate strength to the Ti25Ta material, with improved total elongation but similar uniform elongation, suggesting that the Ti65Ta material is similarly suitable to the Ti25Ta for bone implant applications. Furthermore, the shape memory effects resulting from the β to α″ stress-induced transformation could make the Ti65Ta applicable to other biological applications, such as heart stents.

4.4 Chapter 4 Summary

The microstructure and mechanical properties of the Ti25Ta and Ti65Ta alloys were investigated and the effects of the remelt scanning strategy elucidated. The following conclusions can be drawn from Chapter 4:

- Oxygen analysis of the printed material suggested that the remelt scanning strategy caused increases in oxygen content of up to 0.07 wt.% oxygen at the remelt sample surface. This oxygen content may be minor for some alloy systems however, oxygen is a strong interstitial

strengthening agent in Ti alloys and hence the oxygen increase caused by the remelt scan was not deemed negligible in this study.

- L-PBF Ti25Ta and Ti65Ta consisted of starkly different microstructures. The Ti25Ta alloy displayed an α′ microstructure, consisting of fine martensitic laths, whilst the Ti65Ta alloy displayed a full β microstructure, consisting of equiaxed grains. When the remelt scan was applied to the Ti25Ta alloy, the α″ phase was created in high Ta content regions of 40 – 50 wt.% Ta, due to enhanced Ta diffusion. Nevertheless, α′ was predominantly seen in L-PBF Ti25Ta, contrary to the α″ microstructure seen in conventionally produced Ti25Ta.

- The high Ta content, as well as the remaining partially melted Ta particles in the matrix, created an equiaxed grain structure in both the Ti25Ta and Ti65Ta alloys, avoiding columnar grain growth.

- The remelt scan caused grain refinement in both the Ti25Ta and Ti65Ta alloys and induced a randomised lath orientation in the Ti25Ta alloy, reducing the material texture. Grain refinement caused increased strength in both alloys, however the remelt scan also caused a reduction in ductility. Reduced ductility was attributed to a combination of increased oxygen content for both alloys, as well as randomisation of the lath orientation in the Ti25Ta alloy and grain refinement in the Ti65Ta alloy.

- Both the L-PBF Ti25Ta and Ti65T alloys possessed a superior strength to modulus ratio compared to L-PBF CP Ti, highlighting their suitability to replace CP Ti in bone implant applications. Both the TiTa alloys retained a high ductility when L-PBF processed, promising good fatigue performance.

Chapter 5 Cyclic Response of TiTa Implants

Understanding the fatigue response of an alloy is critical for their use as implant materials. Implants undergo millions of cycles of complex stresses when functioning in the body. It has been highlighted in the literature review that AM materials suffer from reduced fatigue life due to high surface roughness, internal residual stresses and process-induced defects. In addition, complex geometries such as lattices, intensify these effects due to their high surface areas, thin struts and complex stress distributions under load. To add further complexity to the design of bone implants, rough implant surfaces are beneficial for osseointegration and therefore, a balance between fatigue life and biological response must be met. It is important to investigate the new L-PBF TiTa alloys in both solid material and lattice structures with their corresponding machined and as-built surfaces, to fully understand the behaviour of AM implant materials.

5.1 Fatigue Response of Solid Ti25Ta and Ti65Ta

The fatigue behaviour of the solid Ti25Ta and Ti65Ta alloys, in both the single melt and remelt conditions, was first investigated. Sample blocks of 12 mm (x) × 22 mm (y) × 31 mm (z) were printed Figure 5-1(a), from the pre-mixed powder compositions and optimised parameters sets detailed in Section 3.4. Flat fatigue samples were electro-discharge machined (EDM) from these blocks to the dimensions shown in Figure 5-1(b). The flat fatigue sample geometry used is specifically designed for sub-sized dimension testing of costly materials and has been used numerously in published works (eg. in Aydinoz et al. [377]), despite not yet being captured in an official standard. The sample blocks were manufactured The samples were then ground using P1200 SiC paper to remove the surface layer which may have been altered by the EDM process. Residual material from the printed block was investigated by X-ray computed tomography (Micro-CT) analysis to provide a three-dimensional analysis of the material porosity and Ta particle distribution, Figure 5-1(a).

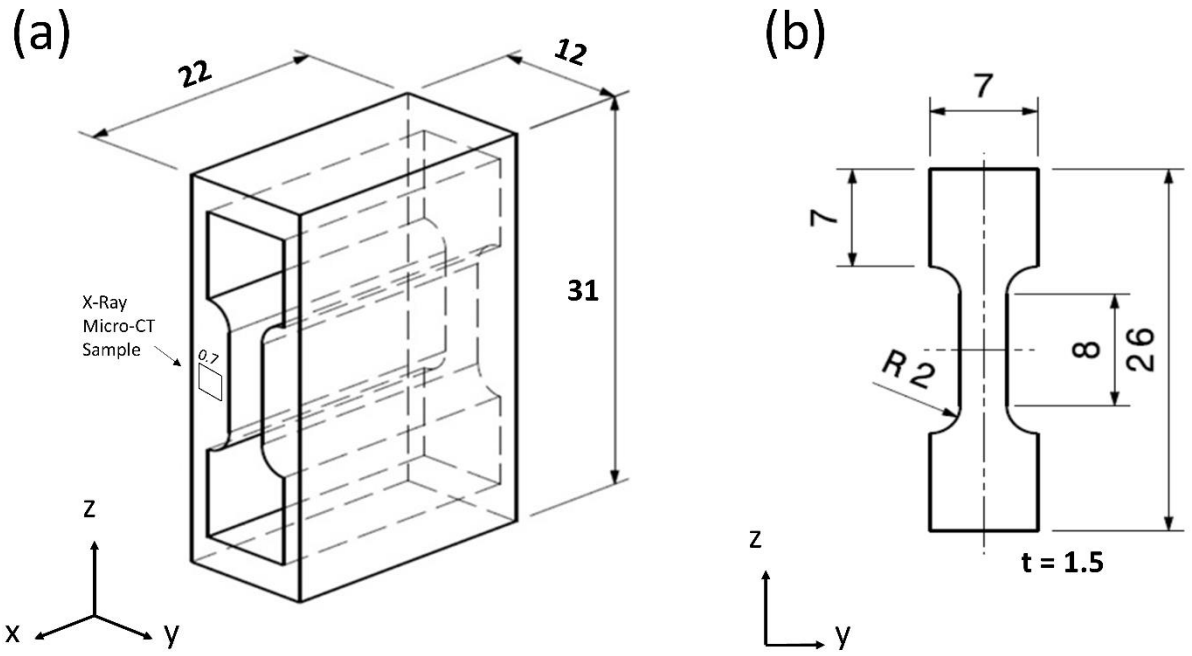

Figure 5-1: Geometry of (a) L-PBF produced blocks and (b) EDM machined flat fatigue samples. Measurements are in mm. The position of the X-ray Micro-CT samples cut from the residual block material is shown in (a) (not to scale). Reproduced from [378].

The machined fatigue samples were tested in the low-cycle fatigue (LCF) regime. The LCF regime was chosen to investigate the transition between plastic and elastic fatigue response. Any plastic deformation should be avoided in implant applications, however, as new AM implants aim to minimise strut thickness, plastic deformation becomes a greater risk. Therefore, it is important to understand the mechanical signals which denote the onset of cyclic softening. The number of cycles to failure of the LCF regime is dominated by crack propagation, as opposed to crack initiation life, which dominates

fatigue life in the (very) high-cycle fatigue (HCF) regime [379, 380]. As crack propagation is highly affected by material ductility, the low ductility noted in AM materials could lead to fast and sudden fatigue failure [232]. In addition, low ductility can also lead to high notch sensitivity, such as seen in AM Ti-6Al-4V, resulting in a low resistance to damage and low fatigue performance [233]. Therefore, the higher ductility of β Ti alloys noted in Section 2.3.1 suggest a promising improved fatigue performance in comparison to AM Ti-6Al-4V.

However, as the L-PBF Ti25Ta and Ti65Ta alloys still possess remaining Ta particles within their matrix, fractography and EDX analysis was also undertaken to support the Micro-CT analysis and to determine whether the Ta particles contribute to early fatigue failure and may be a risk for implants.

5.1.1 X-Ray Micro-CT Analysis of Solid Ti25Ta and Ti65Ta

To investigate the porosity and Ta particle distribution within the material, X-ray Micro-CT analysis was performed on 0.7 mm × 0.7 mm × 4 mm sections which were cut from the residual material following EDM machining. Analysis was undertaken using a Zeiss Xradia Versa 520 using an acceleration voltage of 140 kV, power of 10 W and voxel size of 2.20 µm. Data was reconstructed using Avizo 9.4 software and segmented using a grey-thresholding tool, to separate porosity and Ta particles from the matrix. Porosity and Ta particles less than 5 µm in diameter were deemed unreliable due to the voxel size and hence excluded from the data. The porosity and particle size distributions are presented in equivalent diameter (Figure 5-2); the diameter of a spherical particle of the same volume of the particle analysed. In addition, Avizo 9.4 software was used to assess the sphericity of the particles and pores. The total volume fractions of porosity and Ta particles are displayed in Table 5-1.

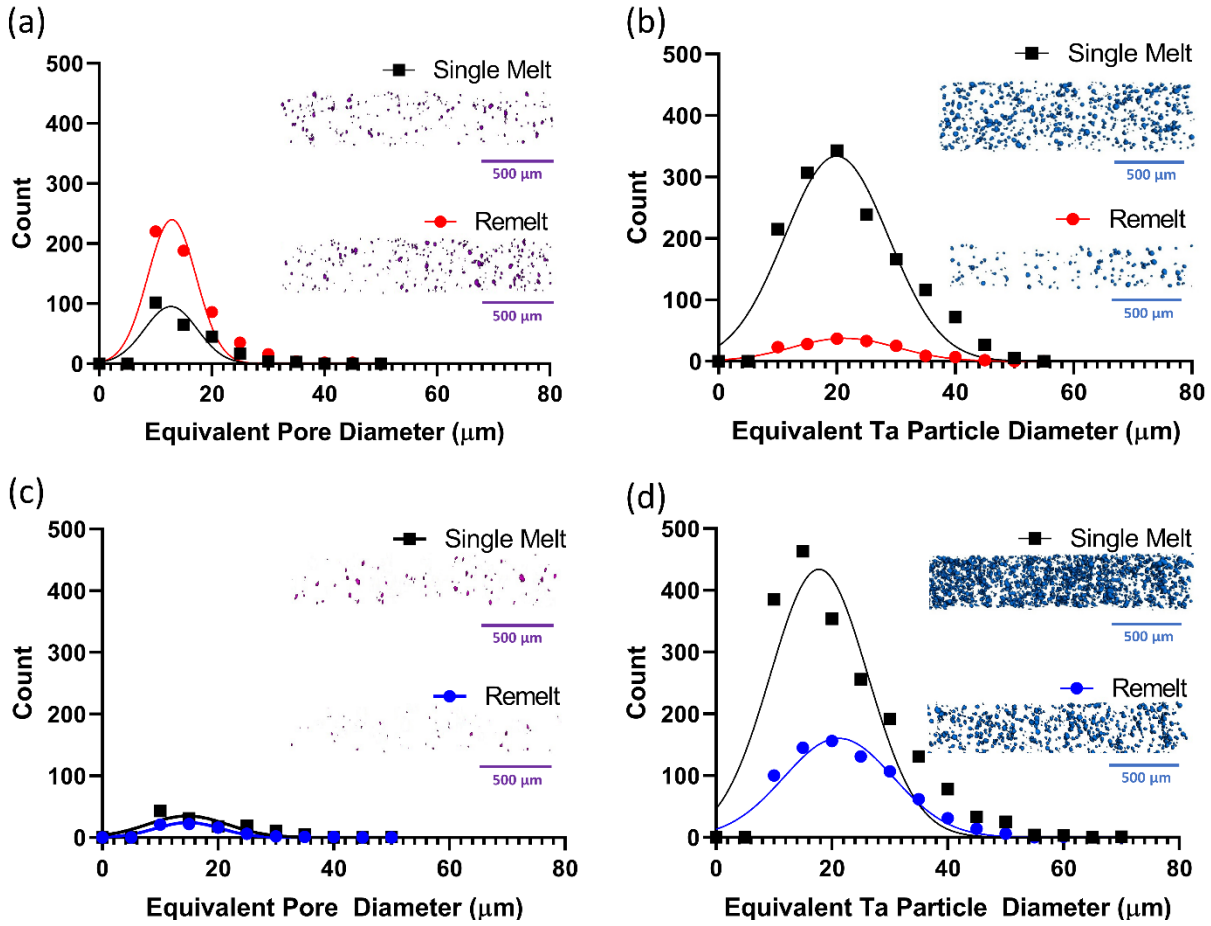

Figure 5-2: Micro-CT derived equivalent pore diameters of (a) Ti25Ta and (c) Ti65Ta and Ta particle diameters in (b) Ti25Ta and (d) Ti65Ta. Adapted from [378].

Table 5-1: Volume fraction of pores and partially melted Ta particles. Adapted from [378].

	Porosity Volume (%)	**Partially melted Ta Volume (%)**
Ti25Ta Single melt	0.15 ± 0.01	2.07 ± 0.01
Ti25Ta Remelt	0.37 ± 0.01	0.22 ± 0.01
Ti65Ta Single melt	0.12 ± 0.01	3.26 ± 0.01
Ti65Ta Remelt	0.03 ± 0.01	0.96 ± 0.01

Internal porosity and defects as a result of AM are known to have a detrimental effect on fatigue life. Hence, understanding the porosity size and distribution, as well as the remaining Ta particles is required to understand the fatigue performance. Micro-CT analysis showed that the single scan strategy produced a material porosity of 0.15 ± 0.01 vol. % in the Ti25Ta materials and 0.12 ± 0.01 vol. % in the Ti65Ta material, Figure 5-2(a) and (c). The porosity is evenly distributed throughout the material, with an average pore diameter of 15 µm. Few large pores between 30 – 40 µm were detected in either

composition. The average sphericity of pores in the Ti25Ta material was 0.96 ± 0.10, whilst the sphericity of the pores in the Ti65Ta material was 0.88 ± 0.10. The higher pore sphericity of the Ti25Ta material suggests that the pores are more likely due to entrapped gas, whilst the pores of the Ti65Ta are more likely due to lack of fusion between the higher content of Ta particles. This suggests that the process parameters used for the Ti25Ta material are approaching the keyhole vaporisation mode, supported by the remelt strategy porosity data. The remelt scan led to an increase in porosity level to 0.37 ± 0.01 vol. % in the Ti25Ta material, whilst a decrease of porosity level to 0.03 ± 0.01 vol. % was observed in the Ti65Ta. The pore size distribution in each case remained unchanged.

The initial parameter study in Section 3.4 showed no increase in porosity when the remelt scan was applied to the Ti25Ta material. It was however observed that the porosity could increase with the remelt scan at scanning speeds below 300 mm/s as the optimal parameter set chosen sits on the boundary between the keyhole mode and optimal Ta melting zones. Literature studies have shown the remelt scan is capable of increasing porosity [168, 178, 187] and Xiao et al. [178] hypothesised that an increase in porosity occurred upon remelting Ti-6Al-4V as heat was not transferred as quickly away from the melt pool as in other materials, due to the low thermal conductivity of Ti (22 W/m°C) [77]. The thermal conductivity of other commonly processed AM metals such as aluminium (237 W/m°C) [77] and iron (80 W/m°C) [77] are much higher than that of Ti, highlighting that Ti alloys may be more susceptible to keyhole formation upon remelt scanning.

The enhanced susceptibility of Ti alloys to keyhole formation upon remelt scanning does not explain why an increase in porosity was seen in the fatigue material, and not in the original parameter study. Slight variations to the feedstock powder, part size and machine functionality (such as laser condition) may have also contributed to the shift in the optimal printing zone for the Ti25Ta alloy.

The fatigue sample feedstock powder had been reused 15 times before sample manufacture. It has been shown that an increase in oxygen content of the powder can lead to porosity through the presence of particle oxides [179]. However, the reused powder chemical analysis, shown in Section 4.1.1, showed only a slight variation in some impurities, such as Fe, Al and V, however no increase in oxygen was observed. Interestingly, Leung et al. [179] also investigated the remelt scan strategy on high oxygen content powder and found that the remelt scan still increased material density by causing liquid flow to fill existing pores. Hence, the feedstock powder is unlikely the cause of increased porosity seen in the fatigue samples.

A change in sample shape and size may have also contributed to an increase in porosity. As discussed in Section 4.3.4, recent studies showed that part size and shape can alter microstructure, mechanical properties and material density, by altering the thermodynamic conditions [192, 263, 376]. A 34 decrease in scanning area, resulted in a decrease from 0.4 µm to 0.1 µm in Ti-6Al-4V, observed by Zhao et al. [376]. In addition, Barba et al. [192] showed that smaller volume parts were more susceptible

to defects due to their higher surface area to volume ratio. Sample volume was increased by 3.6-fold between the parameter optimisation samples and the fatigue blocks, however the surface area to volume ratio decreased from 3.6 to 3.1. Hence, a higher surface area to volume ratio of the fatigue blocks is not the cause of increase porosity. Furthermore, investigation of the martensite lath size from showed no significant difference in lath width between the parameter optimisation sample and fatigue blocks (0.5 ± 0.3 µm to 0.6 ± 0.3 µm). Hence, the change in sample size and shape between these studies has a negligible effect on the microstructure thermodynamic history.

In conclusion, the minor increase in porosity of the remelt samples was attributed to the original optimised parameters lying too close to the vaporisation zone and slight changes in machine functionality. A repeated parameter study was conducted to assess the degradation of the laser and is presented in Appendix Figure 8-3, which confirmed slight degradation of the laser during the three years of study. Despite the minor porosity increase, the density of the remelt Ti25Ta alloy produced for the fatigue samples (> 99.63 %) is still representative of well processed L-PBF Ti alloys [194, 381-383], and hence, the following discussion will focus on the effect of the remaining Ta particles on fatigue performance, as opposed to the porosity.

The Micro-CT analysis confirmed that the remelt scan was successful at reducing the remaining Ta particles in both the Ti25Ta and Ti65Ta compositions, Figure 5-2(b) and (d). The partially melted Ta particle concentration was reduced from 2.07 ± 0.01 vol. % to 0.22 ± 0.01 vol. % for the Ti25Ta composition, and from 3.26 ± 0.01 vol. % to 0.96 ± 0.01 vol. % in the Ti65Ta composition. These measurements agree well with the 0.3 and 1.1 area % calculated in the parameter optimisation study. The Ta particles are homogeneously distributed in each sample, supporting that the pre-mixed powder method is a viable method for testing different alloy compositions. The Ta particles are also spherical in shape, with an average equivalent particle diameter of 22 µm. The size distribution of the Ta particles corresponds well with the particle size distribution of the original powder.

In conclusion, Micro-CT analysis confirmed that the remelt strategy was successful at reducing the volume of remaining Ta particles in both the Ti25Ta and Ti65Ta compositions. The single melt material showed a similar level of porosity between the compositions; however, the defect sphericity indicates different pore formation mechanisms for each alloy. The Ti25Ta composition was more susceptible to material vaporisation and keyhole melting, characterised by spherical gas pores and these defects were compounded by the remelt scan. The Ti65Ta composition showed more irregular defects indicating insufficient melting, however porosity was reduced by the remelt scan, by allowing a second opportunity for metal flow. The porosity levels are slightly higher than those obtained in the initial parameter optimisation study, due to machine and laser instabilities. The porosity levels are still acceptable for well processed L-PBF Ti alloys and will be considered in relation to the fatigue life for each material.

5.1.2 Low-Cycle Fatigue Life

The fatigue behaviour of the Ti25Ta and Ti65Ta alloys was investigated using a digitally controlled servo-hydraulic load frame, under strain-controlled conditions, with a load ratio of R = -1. Fully reversed tension-compression fatigue conditions are representative of some of the complex and most demanding implant applications in the body. Strain amplitudes of $\Delta\varepsilon/2 = \pm 0.5$ %, ± 0.65 % and ± 0.8 % were tested to investigate the transition between plastic to elastic material response. A constant strain rate of 6×10^{-3} s^{-1} was applied and an MTS miniature extensometer, with a gauge length of 5 mm, was used to accurately record strain values. To avoid buckling of the thin 1.5 mm samples, the load was increased stepwise over the first 10 – 25 cycles. Due to the restrictions of costly feedstock materials, at least two, but in most cases three tests were conducted for each alloy and scanning condition (single melt and remelt). As the curves showed no pronounced scatter, one representative curve is displayed in Figure 5-3.

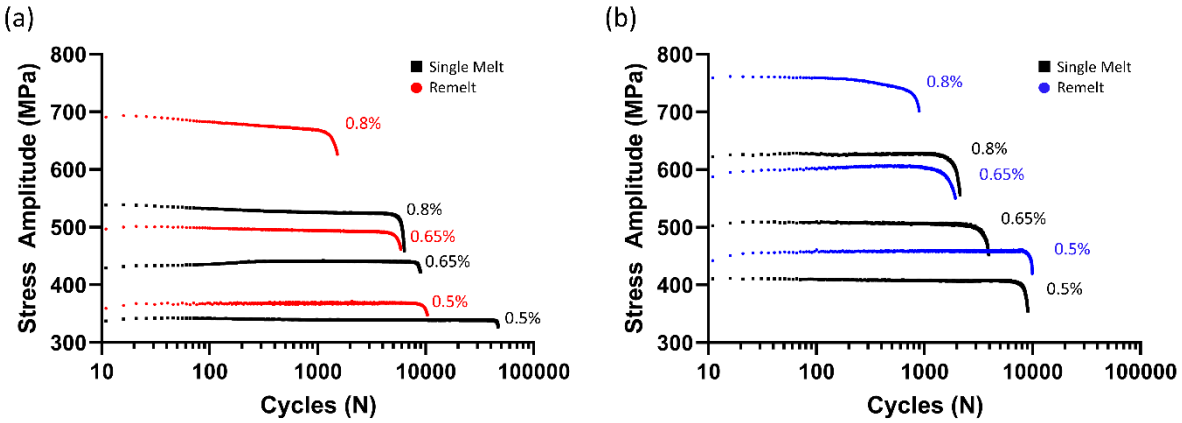

Figure 5-3: Low-cycle fatigue behaviour of (a) Ti25Ta and (b) Ti65Ta. Adapted from [378].

The fatigue life curves display an initial steady increase in stress amplitude, due to the stepwise increase in load. This initial increase is followed by either a stable stress plateau, indicative of full elastic behaviour or a slightly decreasing stress level, indicative of plastic behaviour and cyclic softening. For the Ti25Ta material, the $\Delta\varepsilon/2 = \pm 0.5$ % strain amplitude for both single melt and remelt conditions, as well as the single melt sample at $\Delta\varepsilon/2 = \pm 0.65$ % show a stable stress plateau. This elastic behaviour is also seen in all the Ti65Ta samples, except for the remelt sample at the highest strain amplitude of $\Delta\varepsilon/2 = \pm 0.8$ %. The remaining samples show cyclic softening, suggesting at least minor plasticity and indicating the cyclic yield strengths of the materials, Table 5-2. These values are generally in-line with the monotonic yield strengths determined through tensile testing, reinforcing the increased strength in the remelt material in both alloys. The Ti65Ta remelt material undergoes minor cyclic softening at a slightly lower stress than the monotonic determined yield strength likely due to the stress-induced phase transformation of β to α''.

Table 5-2: Estimated cyclic yield strengths compared to the monotonic yield strength range determined from standard and mini-sized tensile samples.

	Ti25Ta SS	Ti25Ta RS	Ti65Ta SS	Ti65Ta RS
Cyclic Yield Strength (MPa)	435 - 540	495 - 690	> 625	605 - 760
Monotonic Yield Strength (MPa)	426 - 710	545 - 962	665 ± 45	888 ± 52

For both alloys, the remelt material showed a higher stress amplitude response at all strain levels, accompanied by a reduced fatigue life. The higher stress amplitude response indicates a combination of higher strength and possible higher elastic modulus, whilst the lower fatigue life is likely due to a combination of decreased material ductility and the increased stress amplitude testing level. The remelt scan was designed to reduce the remaining volume of Ta particles, however the reduced volume of Ta particles in the remelt material has not led to an increase in fatigue life, as anticipated. Even at low strain levels where crack initiation life dominates fatigue response, the remelt material still shows a reduced fatigue life. The exception may be the 0.5 % strain amplitude test of the Ti65Ta material, which displayed the same number of cycles to failure for the single melt and remelt material, despite the higher testing stress experienced by the remelt material. To help separate the effects of increased strength and modulus, from reduced Ta particle concentration, the elastic modulus of each material was calculated from the data gradient of the half-life hysteresis loops, Figure 5-4 and Table 5-3.

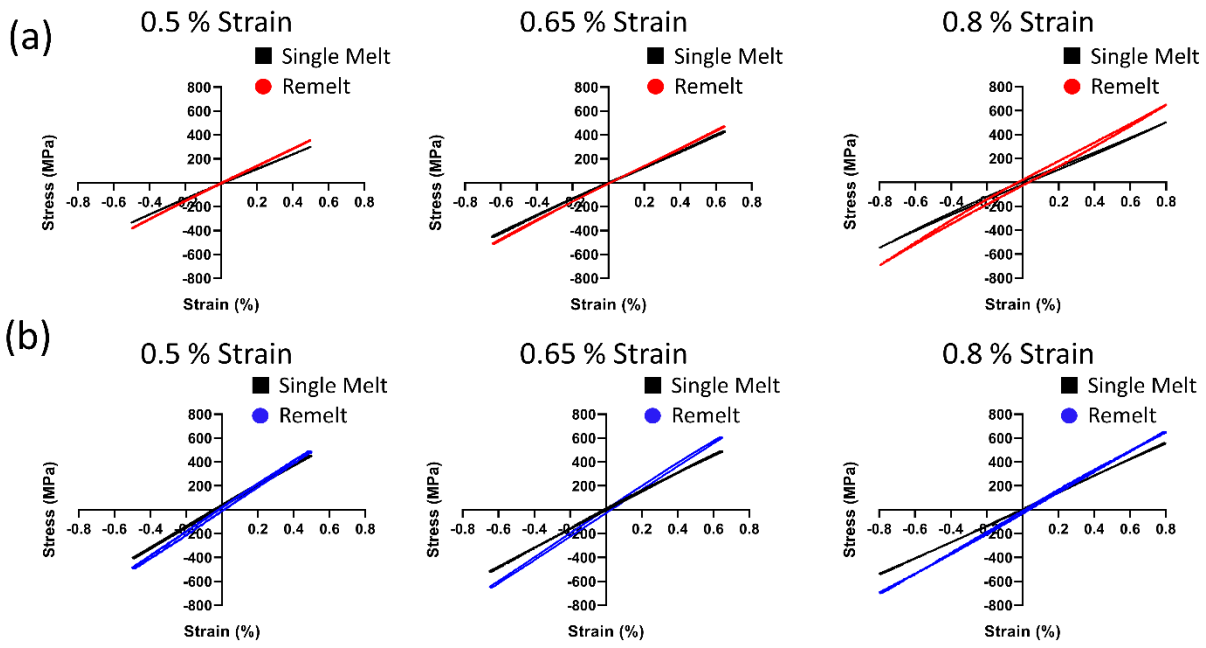

Figure 5-4: Half-life hysteresis loops of (a) Ti25Ta and (b) Ti65Ta. Adapted from [378].

Table 5-3: Elastic moduli values calculated using different methods.

	Ti25Ta SS	**Ti25Ta RS**	**Ti65Ta SS**	**Ti65Ta RS**
Cyclic Elastic Modulus (MPa)	65.4 ± 1.9	76.8 ± 3.3	81.1 ± 4.9	96.1 ± 6.5
Ultrasonic Elastic Modulus (GPa)	65 ± 5	65 ± 5	71 ± 5	67 ± 5
Monotonic Elastic Modulus (GPa)	35 ± 8	47 ± 3	68 ± 7 [§§]	82 ± 12

All testing conditions showed the remelt scan caused an increase in elastic modulus. This increase was not observed in the ultrasonic modulus testing, believed to be the more accurate method of modulus measurement [27]. It is possible that the ultrasonic modulus method was affected by the inhomogeneity of the material, as remaining Ta particles may have caused wave scattering. The larger difference between ultrasonic and cyclic modulus measurements was noted in the Ti65Ta composition, which had a higher concentration of Ta particles. The monotonic measurements were generally lower than the ultrasonic measurements, whilst the cyclic measurements were higher than the ultrasonic measurements. Niinomi et al. [27] reviewed studies investigating the modulus measurements of different β Ti alloys and found a similar characteristic effect of each testing method. It is concluded that the cyclic elastic modulus values likely give the most accurate representation of the elastic modulus of the alloys. Though the cyclic modulus values may be slightly overestimated, the cyclic modulus measurements more clearly differentiate the alloys and scanning conditions and will be considered as the most applicable for the rest of the work.

The remelt scan strategy caused an average increase of 18 % in the cyclic elastic modulus of both the Ti25Ta and Ti65Ta alloys and is likely attributed to enhanced Ta diffusion. Zhou et al. [36] showed that an increase in Ta in the α′ phases led to a decrease in elastic modulus, whilst conversely, increasing Ta in the α″ and β phases, led to an increase in elastic modulus. The change in elastic modulus was attributed to changes in the lattice volume, either increasing in the case of α′ or decreasing in the case of α″ and β. Decreasing lattice volume results in a higher density crystal structure, and hence higher elastic modulus. Therefore, increased diffusion of Ta in the Ti65Ta alloy, leading to a higher density β crystal lattice, logically increases the elastic modulus of the alloy. However, the opposite should be observed for the Ti25Ta material as it was shown in Section 4.2.3 that the L-PBF Ti25Ta material consisted of the α′ phase.

Here it is considered that the elastic modulus of the Ti25Ta alloy increases with the remelt scan as the remelt scan facilitates the formation of α″ phase on a local scale. Although the compositional boundary of α′ and α″ phases is still disputed, generally the α″ phase is only noted in compositions between 25 –

[§§] The monotonic elastic moduli of the Ti65Ta single melt and remelt material was calculated as an average of the two elastic zones noted in Section 4.3.4.

60 wt. % Ta [87, 161, 321]. However, the unique inhomogeneity seen in the L-PBF processed material leads to the creation of multiple Ta diffusion zones which would meet this compositional requirement. The remelt scan, which causes further diffusion of the Ta, may in fact not increase the lattice size of the α′ phase, but force formation of the α″ phase. The α″ phase has a smaller lattice volume, particularly at high Ta contents, and hence a higher elastic modulus [36]. TEM investigations in Section 4.2.3 revealed the presence of the α″ phase only in the remelt material, supporting this hypothesis.

The increased elastic modulus and strength of the remelt material resulted in a higher experienced stress at each strain level for the remelt material. As samples tested at higher forces are expected to fail at a lower number of cycles, the remelt material consistently showed inferior fatigue performance to the single melt material. Similarly, the Ti65Ta material showed a higher elastic modulus than the Ti25Ta material, and hence experienced higher stresses at the strain rates tested. To compare the fatigue behaviour of the Ti25Ta and Ti65Ta alloys, samples which experienced a similar stress level of approximately 400 MPa were considered.

The Ti25Ta single melt material had a lower remaining content of Ta particles when compared with the Ti65Ta single melt material, but a similar uniform elongation determined in tensile testing, Section 4.3.4. Both single melt alloys tested at 400 MPa revealed a fatigue life of approximately 10,000 cycles to failure. At the lowest stress level of 400 MPa, where crack initiation effect on fatigue life is strongest, the lower content of remaining Ta particles did not increase fatigue performance. This suggests that the remaining Ta particles are not acting as crack initiation sites. For further alloy comparison, cyclic testing of the lattice samples, Section 5.2.6, will be conducted at similar stress levels.

When comparing the single melt and remelt material, the remelt consistently fails at a lower number of cycles, despite its lower remaining Ta particle concentration. Under tensile loading it was observed for the Ti25Ta alloy that, the remelt scan increased the material ultimate tensile strength by 19 % but reduced the ductility by 56 %. Low ductility has already been highlighted as a major contributor to the low fatigue life of L-PBF Ti-6Al-4V, as low ductility causes high notch sensitivity [233] and fast crack propagation, due to the reduced plastic zone in front of the crack tip [232]. Hence, failure in both the elastic and plastic deformation regions are affected by the decreased ductility of the remelt material. For the elastically deformed samples, the remelt scan reduced the fatigue life by approximately 78%, whilst for the plastically deformed samples, fatigue life was reduced by a similar 76%, showing a similar decrease in fatigue life for both failure mechanisms.

The residual stress levels in the single melt and remelt samples must also be considered, as residual stress has been shown to be detrimental to fatigue life by promoting crack initiation [232, 233, 241, 242]. Studies show that remelt scanning can reduce residual stress if parameter optimisation is targeted at this result [187-189]. However, as previously discussed in Section 4.3.2, several studies reported an increase in residual stress of up 68 % when the remelt scan applied had identical parameters to the initial

scan [178, 187, 190]. Hence, it is possible that residual stresses are higher in the remelt material and are contributing to the reduced ductility and reduced fatigue life of the remelt material.

Secondly, a difference in dislocation density between the single melt and remelt conditions may also contribute to their different fatigue performance. XRD analysis in Section 4.1.2 showed no difference in peak broadening between the single melt and remelt conditions, suggesting no significant difference in dislocation density. However, the cyclic softening behaviour suggests otherwise. The Ti25Ta single melt 0.65 % strain amplitude sample showed a stress response of 423 MPa, close to its monotonic-derived yield strength of 426 ± 15 MPa. Despite the proximity of the testing stress to the yield stress, the Ti25Ta single melt 0.65 % strain amplitude sample showed no cyclic softening. The Ti25Ta remelt 0.65 % strain amplitude sample, on the other hand, showed a stress response of 498 MPa, much lower than its monotonic-derived yield strength of 545 ± 9 MPa, however, showed distinct cyclic softening. Enhanced dislocation annihilation during cyclic loading leads to distinct cyclic softening and a higher initial dislocation density enhances dislocation annihilation during cyclic loading. Further analysis of residual stresses and dislocation densities present in the L-PBF material, before and after EDM, is required to further elucidate the effects of the remelt scanning strategy on fatigue behaviour. Methods of testing residual stress and dislocation density were deemed beyond the scope of this thesis.

In conclusion, the Ti25Ta and Ti65Ta displayed similar fatigue behaviours, despite possessing different contents of remaining Ta particles. Furthermore, despite the intention of the remelt scan being to reduce remaining Ta particles and hence improve mechanical performance, the remelt scan was shown to decrease fatigue life due to decreased ductility and possible increased residual stresses. To further investigate the effect of the remaining Ta particles on fatigue crack initiation, fractography of the failed samples was conducted.

5.1.3 Effect of Partially Melted Ta Particles on Fatigue Life

The fractured fatigue specimens were analysed using a Zeiss ULTRA GEMINI high-resolution SEM with back scattered electron and electron dispersive X-ray detectors to assess the Ta particle distribution in relation to fracture features. The fracture surfaces of the Ti65Ta samples showed no notable differences to the Ti25Ta samples and hence, only the Ti25Ta samples are shown in Figure 5-5. The low strain amplitude single melt and remelt samples, Figure 5-5(a) and (b) respectively, were characterised by a stable fatigue crack growth zone (upper right of fracture surface). The striations within this zone indicate that the fatigue crack initiated at a process-induced defects at the sample surface. The killer defects appear as spherical, ribbed, indentations, about 20 µm in diameter, slightly larger than the average defect size (15 µm) detected by Micro-CT analysis (Section 5.1.1). At high

strain amplitudes, Figure 5-5(c) and (d), a smaller fatigue crack growth zone is observed in addition to multiple crack initiation sites (highlighted by rectangles).

The killer defects in Figure 5-5 insets (a) and (d) show what appears to be a particle within the defect. To assess whether these particles were remaining partially melted Ta, or whether their formation was related to the presence of partially melted Ta particles, higher magnification SEM and EDX analysis was undertaken.

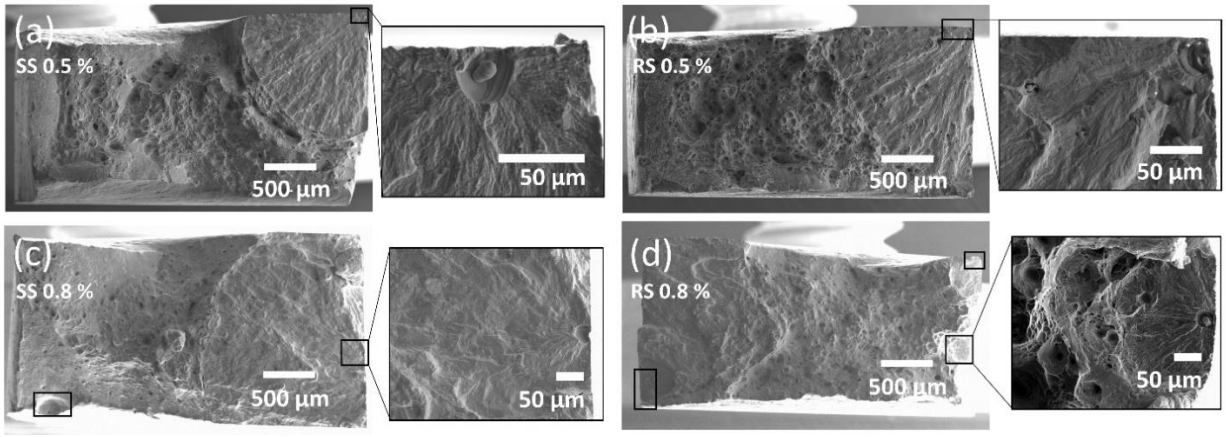

Figure 5-5: Fracture surfaces of low strain (a) (b) and high strain (c) (d) of Ti25Ta single melt (a) (c) and Ti25Ta remelt (b) (d). Adapted from [378].

The SEM and EDX analysis showed no correlation between remaining partially melted Ta particles and the process-induced defects, Figure 5-6. A larger surface area than that depicted in Figure 5-6 was investigated, included in Appendix Figure 8-4, and showed no correlation between the Ta particles and pores over a larger surface area, but due to shadowing caused by the uneven surface, Figure 5-6 was deemed more suitable. Overall, it could be seen that none of the internal pores or surface killer defects were related spatially to the remaining partially melted Ta particles. The particles observed in Figure 5-5 insets (a) and (d) also showed no increase in Ta concentration and reflected the matrix composition. Hence, it is suggested that the remaining partially melted Ta particles do not contribute to crack initiation.

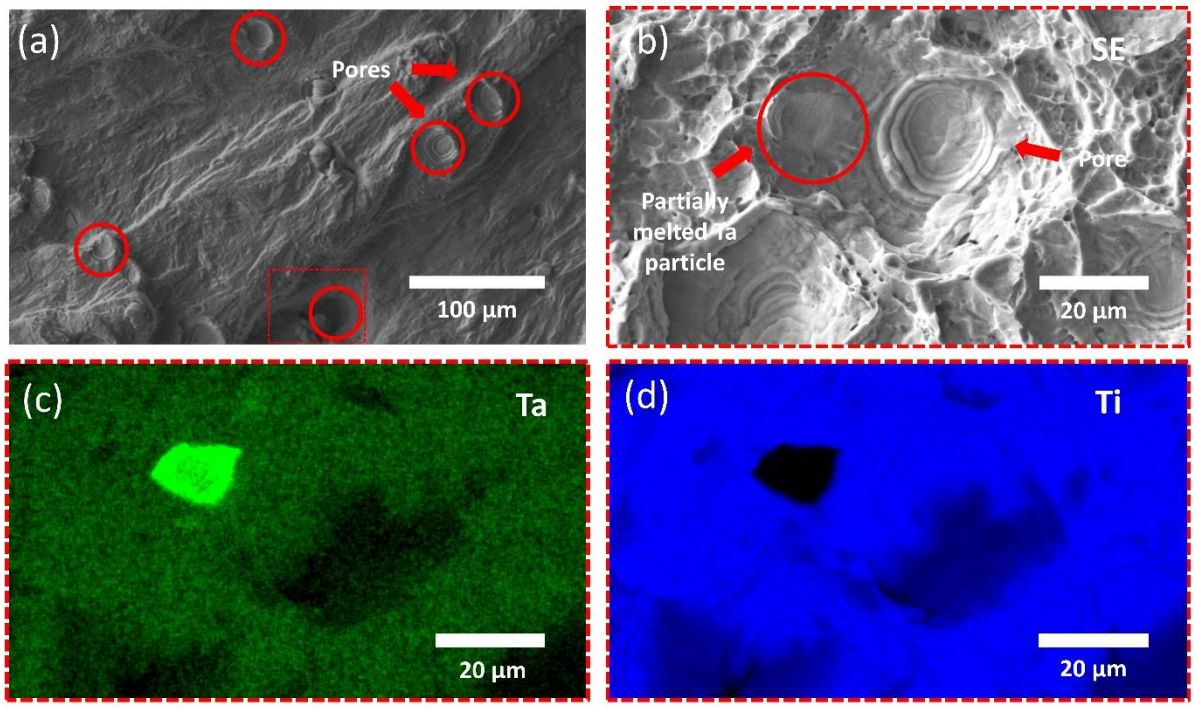

Figure 5-6: The fracture surface of the Ti25Ta single melt sample showing (a) SEM image of pores. (b) A higher magnification SEM image of a pore adjacent to a Ta particle, accompanied with EDX analysis showing (c) Ta and (d) Ti distributions. Reproduced from [378].

For the Ta particles to act as fatigue crack initiation sites, they need to cause high stress concentrations at the particle-matrix interface. If the particles are strongly bonded within the matrix, stress concentrations at the particle surfaces will be low. As the particles are seen to be partially melted, it is likely that a strong diffusion zone exists. To further investigate the cohesion of the partially melted Ta particles, hardness indentations were used on the polished fatigue sample grips in an attempt to cause decohesion of the particles from the matrix. As can be seen in Figure 5-7(a), no decohesion could be induced. Figure 5-7(a) inset shows deformation bands within the Ta particle, suggesting the Ta particles can deform equally to the surrounding matrix, likely due to their high ductility. EDX line scans 1 and 2 investigated lengths of approximately 3 µm stretching from the matrix to within the Ta particle and showed the Ta diffusion zone was approximately 1.2 µm in width, Figure 5-7(b). Line scan 3 investigated a slightly smaller distance of only 2.2 µm in total and returned a concentration of 60 wt.%

of Ti within the Ta particle. As EDX analysis investigates the first few µm of the material surface, this may indicate a Ti cavity in the particle below the immediate surface.

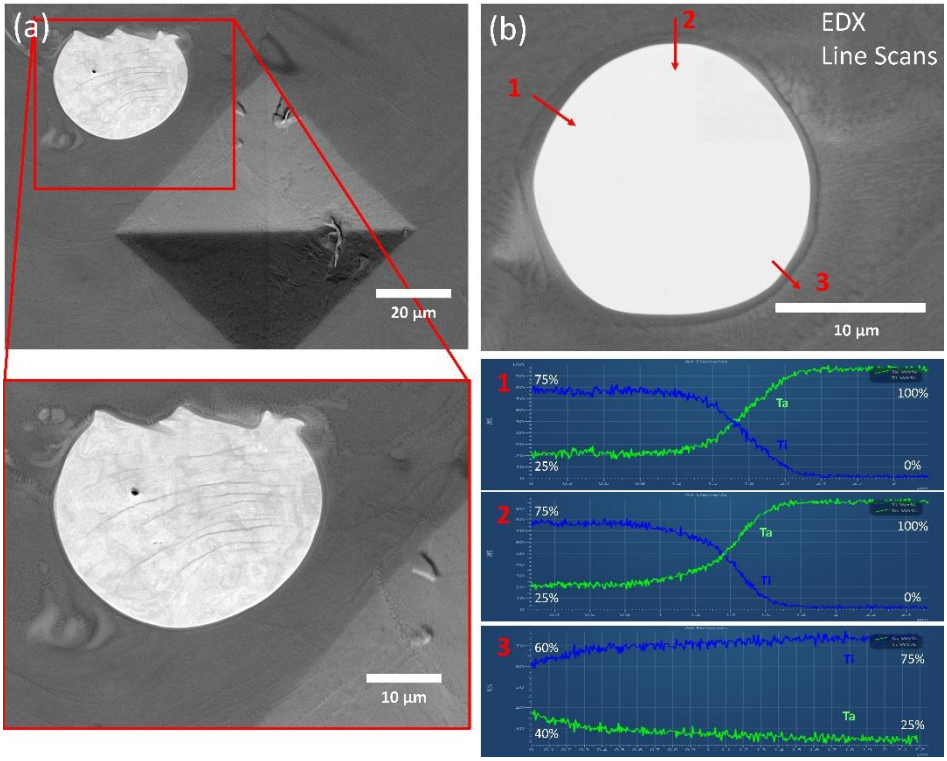

Figure 5-7: Cohesion analysis of Ta particles (a) Hardness indents did not induce decohesion between Ta particles and matrix. (b) EDX line scans analysis of approximately 2 µm sections, covering the diffusion zone around a Ta particle.

In conclusion, it is unlikely that the remaining Ta particles are acting as crack initiation sites. As the Ta particles retain a high ductility, no decohesion occurred between the particles and matrix upon deformation. In addition, the distribution of process-induced defects did not correlate to the distribution of remaining Ta particles, indicating that Ta particles were also not related to the pore formation mechanism. Process-induced defects acted as much higher stress concentrators and hence pores at the sample surfaces were the sole crack initiation sites. It is possible that the Ta particles could act as crack initiation sites in completely defect free material, however this is very unlikely in AM processing. This hypothesis could however be assessed through post-HIP treatment of the material, but this was deemed beyond the scope of the present work.

5.1.4 Fatigue Performance of TiTa Alloys Compared with other Biomedical Alloys

The fatigue life of the L-PBF TiTa alloys must be compared to currently used biomedical alloys to ascertain whether these new materials will be suitable for replacing the currently used alloys in implant applications. To compare the different alloys, the fatigue test stress is normalised by the yield strength of the material and plotted against the number of cycles to failure, Figure 5-8. This normalisation helps to assess the different alloys regardless of their ultimate strength, which has been shown in the case of Ti-6Al-4V, to be often extraneous for the suited application. In addition, normalisation by yield strength allows comparison of the solid L-PBF TiTa alloys with porous structures, as many L-PBF biomedical materials are tested in this form [60, 225, 252]. However, it must be noted that the samples investigated in this study were machined from a block, and hence had a fine machined surface. The porous structures are tested as-built, with a much higher surface roughness, and hence likely suffer from roughness induced minor performance [197, 229, 230, 248]. The equivalent machined surface data for L-PBF produced pure Ta, and CP Ti is lacking. Hence Ti-6Al-4V ELI data for both an as-built sample and sample with fine surface finish (R_a = 6.8 µm) [242] are included for comparison. However, the samples used in [242] were heat treated to relieve residual stress, whilst the material in the present work was not. As discussed in Section 5.1.2, residual stress can also contribute to a reduced fatigue performance. The values used to create Figure 5-8 are included in Appendix Table 8-3. Power curves were fitted to the data to extrapolate each data set for enhanced comparability.

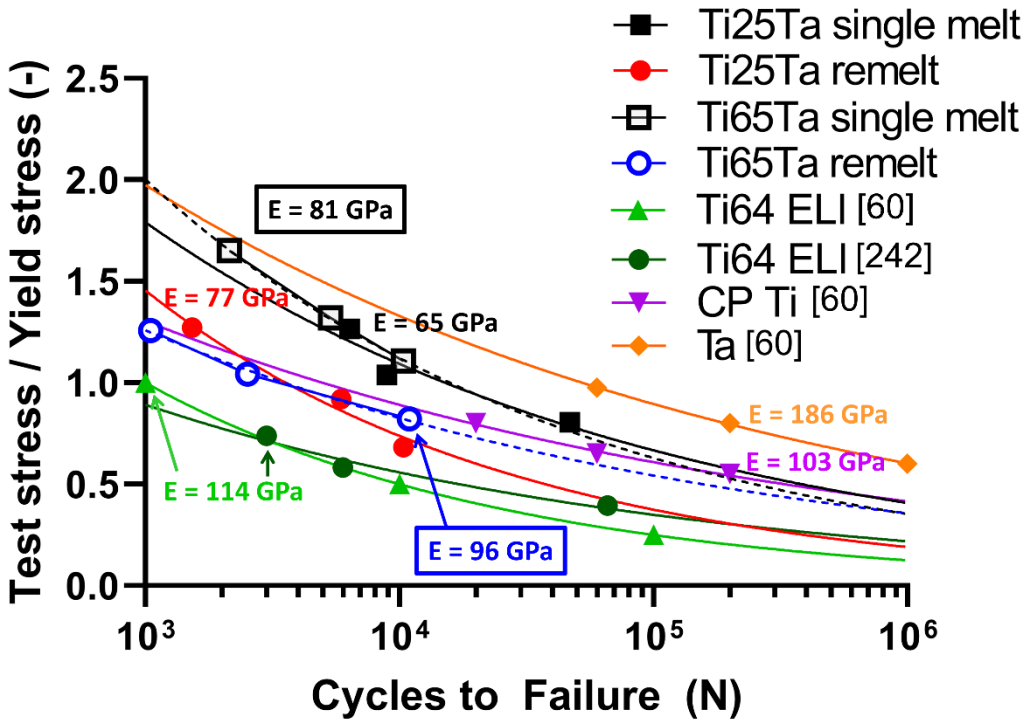

Figure 5-8: Comparison of the fatigue behaviour of L-PBF Ti25Ta and Ti65Ta with other commonly used biomaterials produced by L-PBF. Adapted from [378].

The Ti25Ta and Ti65Ta single melt material perform well in fatigue, inferior only to pure Ta, and possesses an elastic modulus approximately one third of that of pure Ta. The fatigue performance of the single melt TiTa alloys is also superior to CP Ti at high stresses, likely due to the solid solution strengthening caused by the Ta, in conjunction with retained ductility. Furthermore, the elastic modulus of the Ti25Ta single melt material is just over half of that of CP Ti, whilst the Ti65Ta single melt material displays approximately 80% of the elastic moduli of CP Ti. The remelt material also performs well but is outperformed by the single melt material due to its reduced ductility, as discussed in Section 5.1.2.

The comparison of the two L-PBF Ti-6Al-4V ELI samples with different surface finishes shows the heat-treated fine surface finish (dark green circle) to perform slightly better at lower stresses, whilst the as-built material performs better at higher stresses (light green triangle). The finer surface finish reduces the number and size of crack initiation sites at the surface of the material, and hence performs better in the HCF regime, where crack initiation life dominates fatigue performance. At higher stresses, the porous as-built material displays a superior fatigue performance, possibly due to the enhanced strength of the as-built material. Unfortunately the as-built yield strength of solid material was not included in [60] for comparison.

However, the surface finish comparison suggests that in as-built condition, the Ti25Ta and Ti65Ta compositions would perform slightly worse in the HCF regime. The power curves fitted to the data from this study display a much steeper gradient than the literature data, resulting in higher stresses at low cycle numbers and lower stresses at high cycle numbers. This is possibly an artefact of curve fitting as the Ti25Ta and Ti65Ta data points are more closely positioned than the literature data. The limited predictive capability of the power curve highlights the need to test the new TiTa L-PBF alloys in the HCF regime, particularly as implants, such as mandible implants, experience well above 10^6 cycles in their lifetime. As lattice structures are desired in the final implant, it was concluded that testing lattice structures in the HCF was more valuable than further testing machined solid material.

In conclusion, the L-PBF Ti25Ta and Ti65Ta material showed excellent fatigue performance for biomedical applications. Both alloys showed a reduced elastic modulus when compared with pure Ta and CP Ti, without a significant reduction in fatigue performance. Furthermore, the remaining partially melted Ta particles did not act as crack initiation sites. The remelt scan strategy was confirmed to successfully reduce the number of partially melted particles, but at a cost of material ductility, which was detrimental to fatigue performance. To further understand the behaviour of L-PBF Ti25Ta and Ti65Ta as biomedical materials, it was determined that analysis of lattice structures was required.

5.2 Fatigue Response of Ti25Ta and Ti65Ta Lattice Structures

Additive manufacturing facilitates the manufacture of fine, metallic, lattice structures, near impossible to create with conventional machining techniques and which provide great benefits for osseointegration of bone implants. Lattice structures not only reduce the elastic modulus of a bulk implant, but also provide space for bone ingrowth to encourage bone-implant integration. Exciting new geometries, such as triply periodic minimal surface (TPMS) structures, possess surface curvature and optimised interconnected pore networks which encourage osteogenic differentiation in stem cells and facilitate nutrient flow and tissue migration [290]. The literature investigating TiTa lattice structures is limited and focuses on biological compatibility as opposed to mechanical response [219, 384]. However, preliminary mechanical investigation by Ghouse et al. [385] found that a randomly distributed stochastic lattice manufactured from Ti30Ta had the greatest fatigue strength for a given stiffness when compared with pure Ta, CP Ti and Ti-6Al-4V identical structures. It was also highlighted that optimisation of laser parameters for lattice structures is critical as scanning parameters can affect the notch sensitivity, ductility, porosity and microstructure of the structures.

To investigate the new TiTa alloys in lattice form, parameter optimisation for new lattice geometries was conducted to reduce material porosity and to identify the geometric limits of L-PBF processing when creating fine lattice structures. Using the optimised parameters, mechanical testing samples were produced, and the microstructure investigated by EBSD analysis. The lattices were then tested in static and cyclic testing regimes and compared with identical Ti-6Al-4V lattices investigated by collaboration partners in [386].

5.2.1 L-PBF Parameter Modification for Lattice Structures

The surface finish of as-built parts is known to be critical to the fatigue performance of lattice structures. One scanning parameter that has shown strong effects on both the surface roughness and near-surface porosity of L-PBF parts is the contour scan [241, 364, 387]. When a contour scan is applied, the rough edges which are caused by the layer-wise process of AM are smoothed, increasing fatigue performance [387]. However, if the contour scan applies excessive incident energy, vaporisation can occur, causing keyhole defects near the part surface, severely impacting fatigue performance [241, 364].

Therefore, preliminary investigations into contour scan parameters were conducted, initially using the optimised process parameters for the Ti25Ta and Ti65Ta bulk material. A basic BCC lattice, Figure 5-9(a), was chosen for this investigation, as this lattice geometry has been extensively studied in literature [258, 261, 388-390]. Lattice samples were printed with a fast contour (600 mm/s), slow contour (200 mm/s) and no contour. Both contour scans had a laser power of 60 W, the optimal contour

laser power for Ti-6Al-4V provided by Concept Laser. In addition, the effect of the contour scan on the achievable dimensional tolerances was examined, by investigating a range of lattice strut sizes of 0.3 mm, 0.5 mm, and 0.8 mm. The effect of the remelt scan on dimensional tolerances was also examined by replicating the 0.8 mm lattice with the remelt scanning strategy.

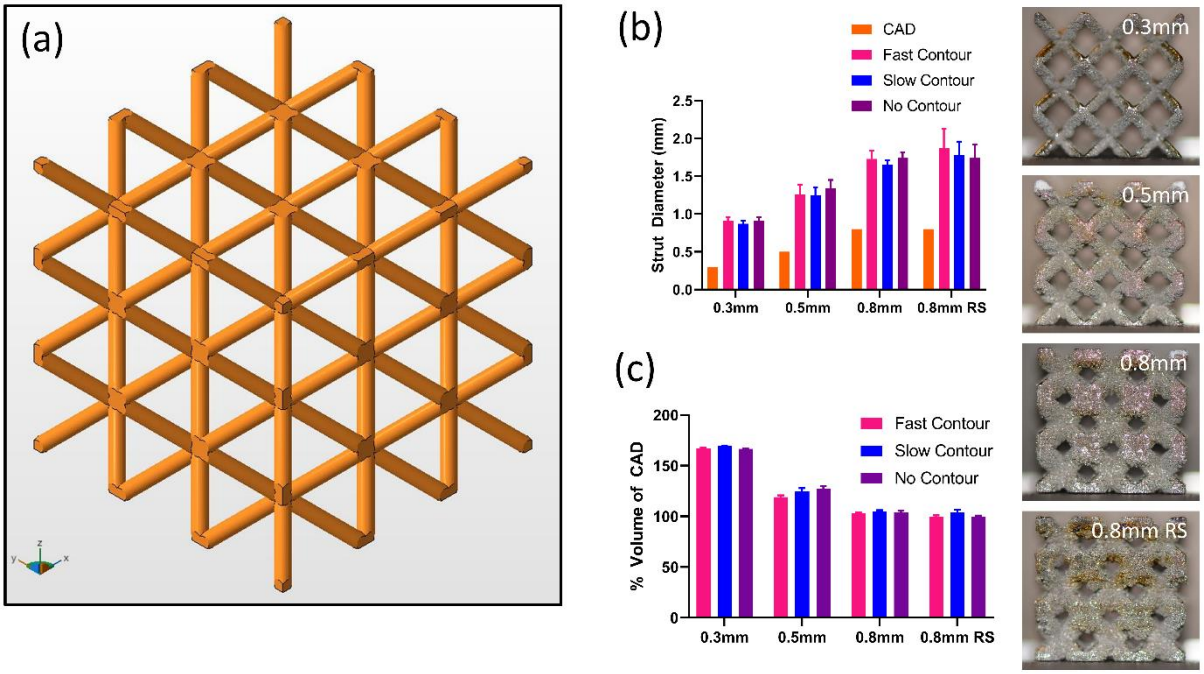

Figure 5-9: (a) CAD model of BCC lattice unit cell. The effect of contour parameters on dimensional tolerances investigated through (b) image analysis of strut diameter and (c) Archimedes measurements of lattice volume.

The strut diameter was assessed by image analysis and the volume of the printed lattice assessed by Archimedes volume measurements. Figure 5-9(b) and (c) show that the printed lattices are much larger than the computer aided design (CAD) model, in strut diameter and total lattice volume, respectively. However, the different contour scans caused no significant differences in lattice size. Due to the high surface area of lattices, it is commonly found that printed lattices show much larger dimensions than the CAD file [60, 213, 214, 222, 264]. Partially melted powder particles adhering to the strut surfaces, in conjunction with wide melt pools, result in larger strut dimensions than designed, Figure 5-10(a). The 'staircase effect' also contributes to this geometric mismatch, as layered structures cannot precisely replicate overhanging surfaces [391], Figure 5-10(b). The Archimedes measurements, Figure 5-9(c) confirmed the increase in lattice size compared to the CAD, however also showed no difference between the investigated contour parameters or the single melt and remelt scanning conditions. As the remelt scan has been shown to form smaller melt pools due to reduced laser adsorption, the part dimensions are not increased by the application of a second laser scan.

As the designed strut diameter increases from 0.3 mm to 0.8 mm, the increase in strut diameter compared to the CAD dimension decreases from 198 % to 114 %, corresponding to an absolute increase

of 0.59 mm and 0.91 mm in the 0.3 mm and 0.8 mm struts, respectively. Hence, the finer the struts, the larger the deviation from the designed CAD. As the powder particle size in this study ranged between 5 – 45 µm (see Section 3.4), the maximum strut increase due to adhered powder particles is likely only 0.05 mm, much smaller than the observed absolute increase. Hence, it is more likely that the wide and deep melt pool formed in the TiTa material, due to the high laser power and low scan speeds used, is contributing more strongly to the dimensional inaccuracy. Indeed, the single laser track analysis (see Section 3.3) showed melt pool widths of 147 ± 20 µm and depths of 65 ± 20 µm at scan speeds of 300 mm/s. For any individual layer, the large melt pool width could be expected to increase the surface area diameter by approximately 75 µm on each side, hence 0.15 mm in total. Hence, the major contribution to the increased strut diameter is likely due to the melt pool depth, in conjunction with the 'staircase effect'. The BCC structure only possesses angled struts and with a melt pool depth covering almost three powder layers, the 'staircase effect' increases the thickness of the struts by up to 3 times in the case of the 0.3 mm struts.

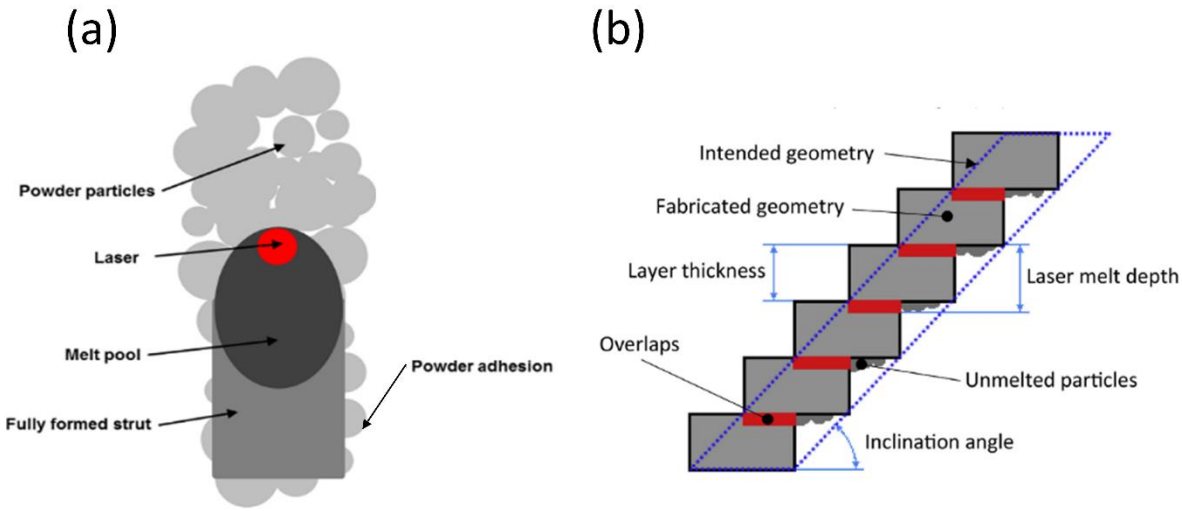

Figure 5-10: (a) Strut formation mechanism showing dimensional limitations due to melt pool size and powder adhesion. Reproduced with permission from [228] (b) The staircase effect resulting in discrepancy between CAD and fabricated strut size on diagonal struts. Reproduced with permission from [391].

To improve the dimensional accuracy of printing in TiTa alloys, it is likely that a higher laser power is required, than available on the current research equipment. The Mlab Cusing R has a maximum laser power of 100 W, restricting the parameter optimisation possible in this study. With a wider range of laser powers available, it is likely that improvements could be made to the dimensional accuracy of the optimal Ti25Ta and Ti65Ta process parameters by further adjusting the melt pool width and depth. A study by Sing et al. [227] investigating a statistical approach to parameter optimisation for lattice structures found the dimension lattice of struts produced in Ti50Ta were most affected by laser power,

as opposed to layer thickness and scanning speed. Hence, lattice dimensional accuracy of TiTa lattices could be improved by future investigations with a larger range of laser powers.

In addition to dimensional accuracy, the effect of the contour scan on the lattice porosity and partially melted Ta particle volume was assessed by cross-sectioning, polishing and imaging lattice nodes, Figure 5-11. There was little difference noted in the porosity level between the different contour scans in the single melt material. A density of ~ 99.0% was achieved with all contour conditions, however the sample with no contour showed a smaller standard deviation in porosity level, as the contour scan can cause irregular large pores at the edge of samples, Figure 5-11(c). The remelt scan caused an increase in porosity for all conditions, suggesting that the energy density of the bulk processing parameters is too high for the small volume of the lattice strut. A lower overall density was also seen in the lattices (~99.0%) when compared with the parameter optimisation cubes (~99.9%). As the lattices have a higher surface to volume ratio compared with the cubes, they suffer more from contour induced porosity. To reduce keyhole vaporisation in the lattice struts, the laser scan speed should be increased.

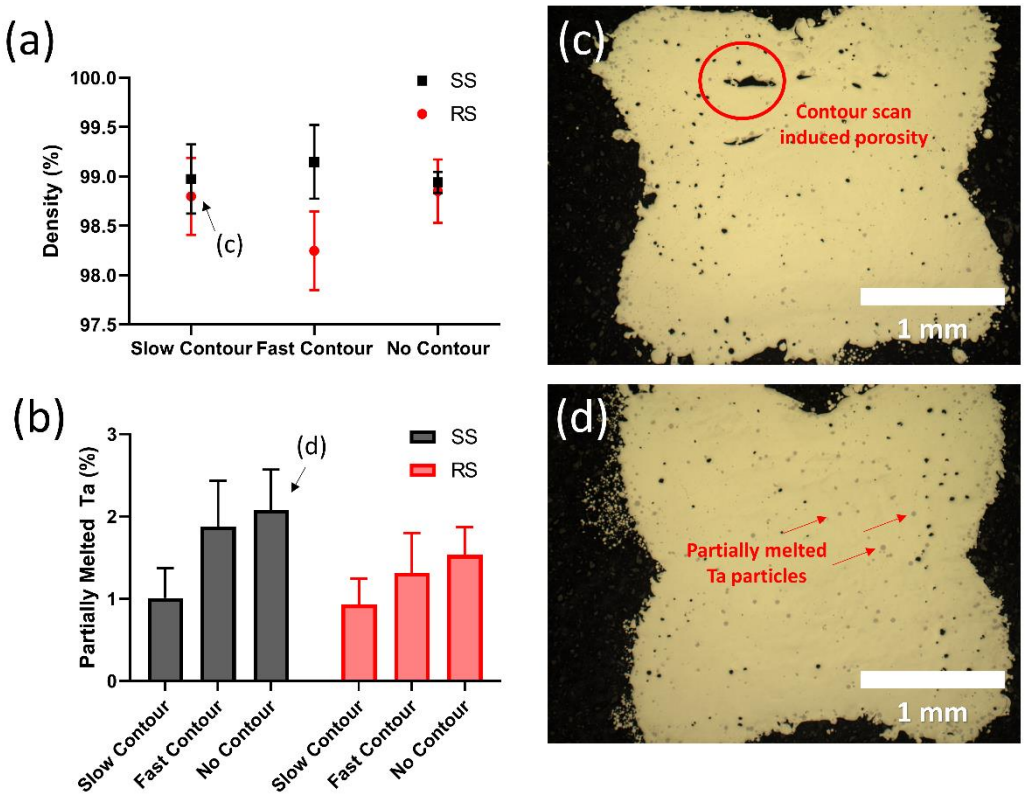

Figure 5-11: Effect of contour parameters on the area % of (a) porosity and (b) partially melted Ta particles. Optical micrographs of the lattice cross-sections displaying (c) contour scan induced porosity and (b) the higher area % of partially melted Ta particles in absence of a contour scan.

The level of remaining partially melted Ta particles was also affected by the type of contour scan, Figure 5-11(b). The slow contour scan, with the highest energy density, returned the lowest level of remaining partially melted Ta of 1.0 ± 0.4 %, whilst the fast contour and no contour conditions showed similar levels of Ta at 1.9 ± 0.6 and 2.1 ± 0.5 %, respectively. The remelt scan reduced the unmelted Ta in all contour conditions, due to the second opportunity for Ta melting, but could only reduce the level to 0.9 ± 0.3 %. A higher level of remaining Ta in the lattice samples, as opposed to the cubes (single melt = 0.7 ± 0.2 % and remelt = 0.3 ± 0.2 %), using identical scanning parameters, suggests that the lower volume and faster cooling rate of the lattice struts increases the difficulty of fully melting the Ta. However, as porosity was deemed more critical than the remaining partially melted Ta level in fatigue performance, the optimal parameters for printing lattice structures in TiTa should likely err on the side of insufficient Ta melting, as opposed to keyhole vaporisation. The fast contour scan parameters were chosen for further lattice analysis.

5.2.2 FCCZ Lattice Type Selection

Preliminary investigations into contour parameter selection using the BCC lattice structure showed that keyhole vaporisation was occurring in the centre of the struts, as well as being enhanced at the overlap between the contour scan and inner surface scan. Hence, the single melt parameters needed re-optimisation for the thin strut geometry of lattice structures.

The BCC lattice is a widely investigated structure [258, 261, 388-390], however, the lack of supporting material in the z-direction results in poor compressive performance [258]. Hence, the lattice geometry was changed to an FCCZ unit cell, Figure 5-13(a). The FCCZ structure shows promising stretch-dominated behaviour, with high specific compressive strength, due to the presence of vertical struts, and a superior stiffness-to-weight ratio [258, 392]. This lattice geometry also facilitates the use of data produced by collaborators, which investigated the FCCZ structure printed in L-PBF Ti-6Al-4V and 316L [386]. An identical lattice geometry to those produced by Brenne et al. [386], using a 2 × 2 × 2 mm unit cell, a nominal strut diameter of 0.35 mm and a 10 mm cube edge length, was used to directly compare the mechanical properties of the new TiTa alloys to Ti-6Al-4V, without requiring the reproduction and testing of the Ti-6Al-4V structures. The new FCCZ geometry required parameter optimisation specific to the structure and hence, the effect of laser speed on porosity and remaining Ta content was investigated.

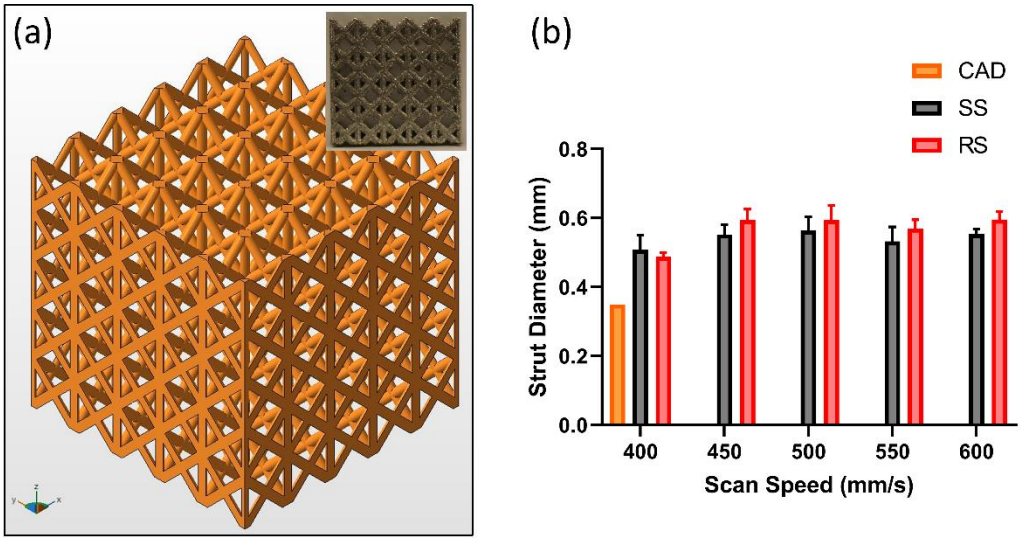

Figure 5-12: The FCCZ lattice structure (a) was manufactured at different scan speeds and (b) the strut diameter measured.

Adjusting the laser scan speed showed no significant change in the average strut diameter, Figure 5-12(b), agreeing with the statistical parameter optimisation study by Sing et al [227]. The single melt and remelt struts showed average strut diameters of 542 ± 33 µm and 569 ± 26 µm respectively, 80% and 85% larger than the CAD dimensions. Whilst no increase in strut diameter was observed when the remelt scan was applied to the 0.8 mm BCC lattices, a small increase in strut diameter was noted for the FCCZ structure. The increase is minor, approximately 5 % or 25 µm, and is hence was not likely detected on the larger 0.8 mm struts. As the melt pool formed by the remelt scan is smaller than that of the initial scan, the increase is likely caused by additional powder adhered to the strut surfaces. As noted in Section 4.3.2, as the remelt samples are hotter when the new powder layer is spread by the powder spreading blade, more powder particles tend to stick to the remelt part surface, particularly on the side the facing the powder spreading blade. The strut size increase or 25 µm falls within the particle diameter range of the powder.

When cross-sectioned and polished, the lattices showed densities ranging from 99.9 to 98.9 %, Figure 5-13(a). The highest density occurred in the single melt lattice at the highest scan speed of 600 mm/s, suggesting that the low scan speeds were applying too much laser energy and hence contributing to the porosity seen in the BCC lattices. In addition, the remelt scan increased porosity at all scanning speeds and showed a much larger standard deviation. The remelt scan enhances porosity in the lattices, often in the form of large pores near the strut surfaces, Figure 5-13(e).

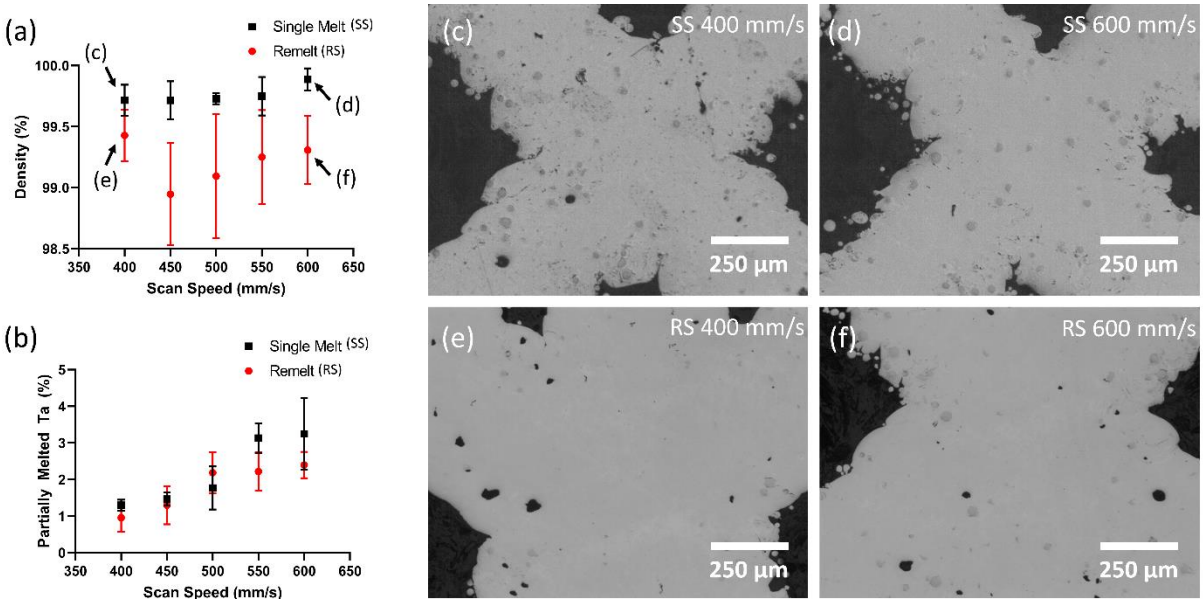

Figure 5-13: Effect of scan speed on (a) density and (b) partially melted Ta particles in FCCZ lattice structures. Optical micrographs (c) and (d) show the lattice node cross-section produced at low and high scan speeds respectively, for the single melt strategy. (e) and (f) show the low and high scan speeds respectively, for the remelt scan strategy.

The level of unmelted Ta decreased with decreasing scan speed and the remelt scan successfully reduced the amount of Ta particles, however to a lesser degree than seen in the optimisation cubes, Figure 5-13(b). As the lattices possess more diagonal surfaces, the deep melt pool does not penetrate as much material to enhance Ta melting. The highest scan speed of 600 mm/s was chosen for manufacture of the mechanical testing samples as this speed gave the lowest porosity in the single melt material. It is likely that an even higher scan speed would have reduced porosity further, however optimisation of lattice process parameters is a research field within itself, and other promising advancements, such as the use of a pulsed laser [214, 393], would likely be more effective at reducing the defect concentration seen in lattice struts. Hence, further optimisation of the lattice process parameters was deemed beyond the scope of this study. In addition, as the optimal process parameters determined for the Ti25Ta and Ti65Ta material where only different by 50 mm/s for the original cubic samples, it was decided that the parameters for the Ti25Ta lattices would also be suitable for the Ti65Ta lattices.

5.2.3 Geometric Characterisation of FCCZ Lattices

The FCCZ lattices were adapted with the addition of grips for mechanical testing, Figure 5-14(a). Samples were printed in Ti25Ta and Ti65Ta, using the 600 mm/s scan speed, fast contour and both the single and remelt scanning conditions, Figure 5-14(b). In Section 5.2.2 it was noted that the printed struts were larger than the CAD designed struts due to the wide melt pool, staircase effect and adhered powders. In addition, work by Brenne et al. [386] on identical Ti-6Al-4V mechanical samples showed

that geometric deviations occurred at the top lattice-grip interface, due to insufficient support from the lattice to create a horizontal solid layer. Therefore, to assess the geometric deviations, the mechanical testing lattices were examined by Archimedes density measurements and SEM observations.

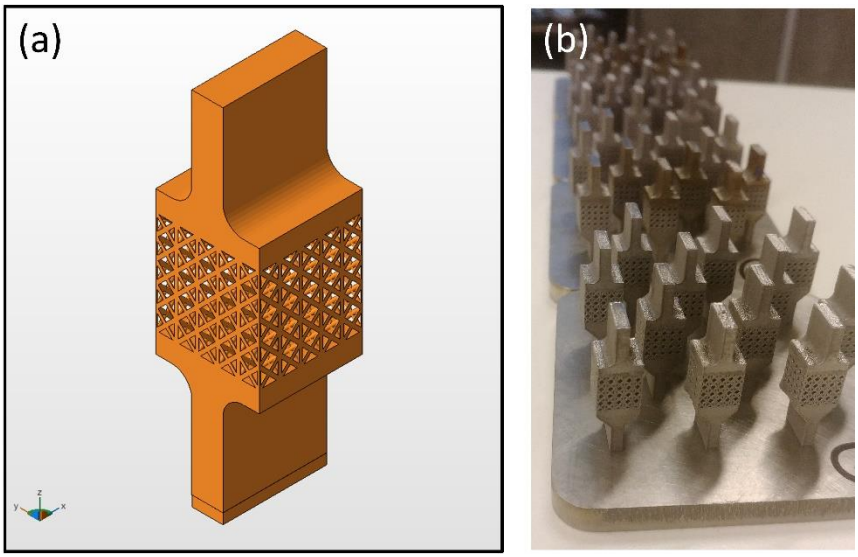

Figure 5-14: FCCZ lattice mechanical testing sample (a) CAD model and (b) L-PBF produced.

The volume of the mechanical testing lattices was measured by the Archimedes method. Each sample was weighed, then washed in a solution of water and ethanol in a 7:3 volume ratio, before weighing submersed in distilled water. The theoretical volume of the grips was then subtracted from the measured volume, to determine the volume of the printed lattice. The printed lattices were found to be almost three times the volume of the CAD file (Table 5-4). No significant difference in volume was noted between the Ti25Ta and Ti65Ta compositions, however the volume of the remelt scan samples (0.45 ± 0.04 cm^3) was slightly greater than the single melt samples (0.43 ± 0.03 cm^3). This agrees with earlier findings which showed a larger strut size caused by the remelt scan.

Table 5-4: Volume of mechanical testing lattices measured by Archimedes method.

	Single Melt	**Remelt**
CAD Volume 0.35 mm strut lattice (cm^3)	0.13	
Measured Volume 0.35 mm strut lattice (cm^3)	0.43 ± 0.03	0.45 ± 0.04
Measured Strut Diameter (µm)	581 ± 41	598 ± 42
Equivalent CAD Volume (cm^3)	0.31	0.32
Residual Volume (cm^3)	0.12 ± 0.03	0.13 ± 0.04

SEM imaging was used to investigate the position of the extra volume of material within the lattice. Strut diameter measurements were similar to those observed in Section 5.2.2, with the single melt and remelt samples showing 591 ± 41 µm and 598 ± 42 µm strut diameters, respectively. The diagonal struts were on average 8 % larger in diameter than the vertical struts as a result of the staircase effect. The downward facing side of the strut has increased irregularity and adhered powder, however, there is little difference in the surface quality between the single melt and remelt conditions, Figure 5-15(a) and (b). When the measured strut diameter is mimicked in CAD, the total lattice volume only reaches 0.31 - 0.32 cm^3, still under the measured lattice volume. Hence, the remaining volume is likely associated with the geometric instabilities at the top lattice-grip interface, Figure 5-15(c) and (d).

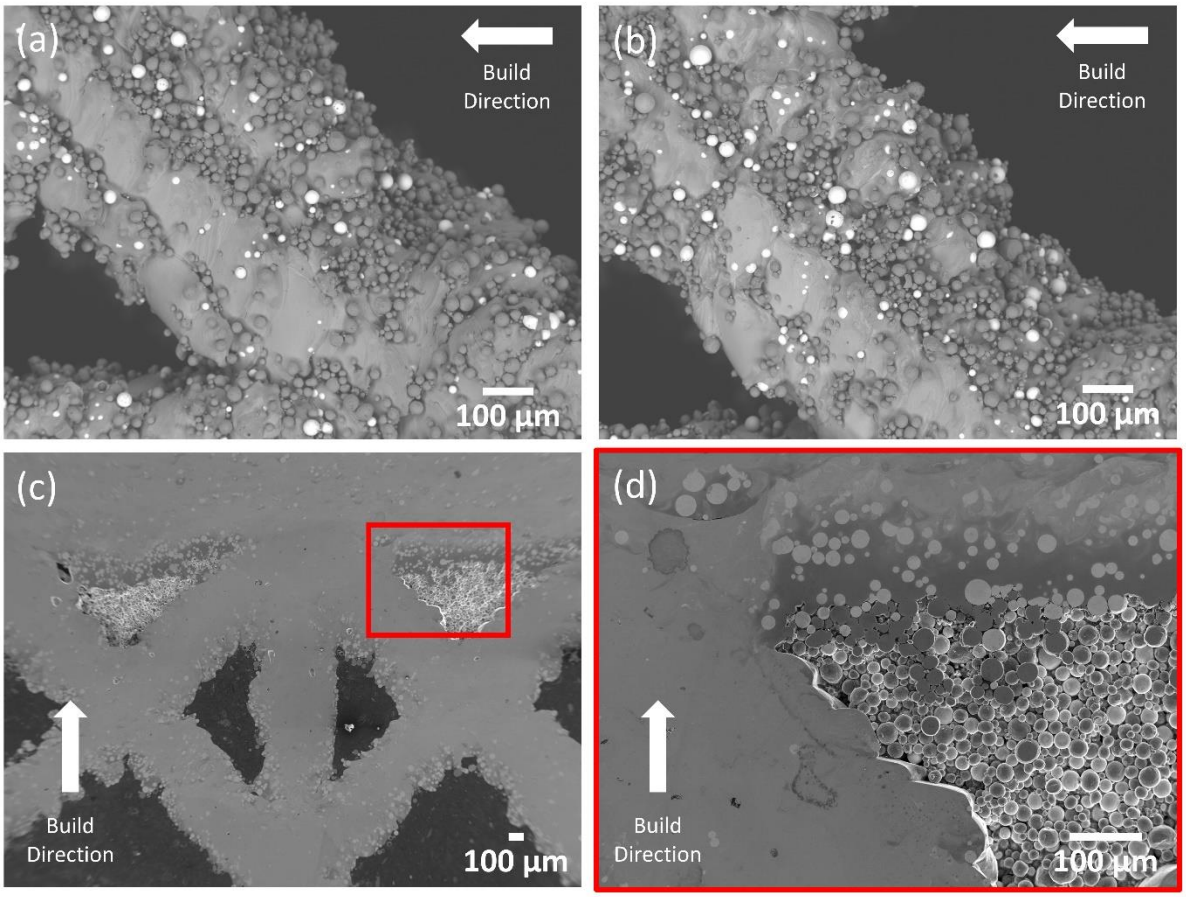

Figure 5-15: SEM surface analysis of (a) single melt and (b) remelt scan diagonal struts. (c) Top lattice interface showing geometric inconsistencies and (d) adhered powders.

The top lattice-grip interface is has not formed accurately due to the lack of supporting structures. The horizontal grip surface has almost entirely filled the adjacent lattice cavity with partially melted material and adhered powders, resulting in the residual volume detected by Archimedes testing. A similar geometric inconsistency was observed by Brenne et al. [386] which interestingly did not result in this region becoming the critical point of failure. In fact, the extra material caused unintentional but effective filleting of the sharp corners, and hence the top interface was shown to be less likely to cause failure

than the bottom interface. Methods to remove this type of geometric inconsistency involve the use of a gradient lattice structures which become smaller and hence more supportive when approaching horizontal surfaces. A software which automatically designs gradient lattice structures near potential geometric deformities could be valuable for implant manufacture and could be investigated as future work.

A small amount of extra material was also noted on the corner of the bottom lattice-grip interface, which faced the powder spreading blade during printing, Figure 5-16. The remelt scan increased the amount of adhered extra material, which also resulted in an outer ridge forming on the bottom lattice-grip surface, Figure 5-16(b). This outer ridge may act as a crack initiation site and should be kept in mind during mechanical testing.

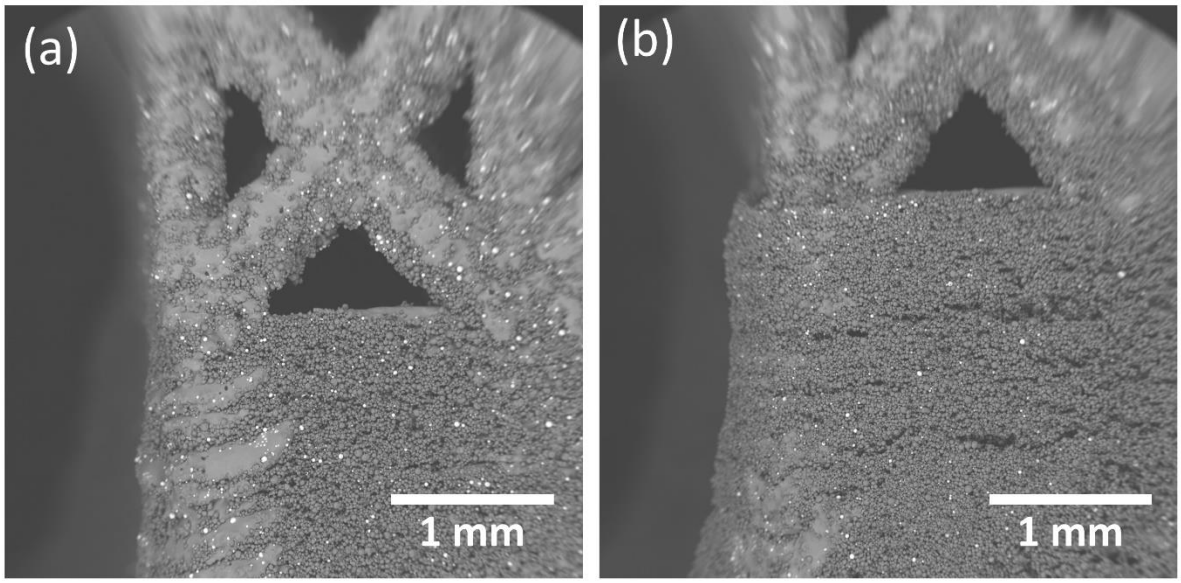

Figure 5-16: Geometric defects observed on the bottom corner facing the powder spreading blade for (a) single melt and (b) remelt scanning conditions.

In conclusion, both the Ti25Ta and Ti65Ta lattices show geometric deviations from the CAD file, with larger strut sizes and geometric defects at the top lattice-grip interface. The extra volume of material should be considered when investigating the mechanical properties of the lattices, instead of using the CAD relative density to calculate stress and strain. To further understand the mechanical behaviour of the TiTa lattices, the microstructure within the struts should be characterised.

5.2.4 Microstructure of FCCZ Lattices

A representative sample from each build plate of FCCZ mechanical testing lattices was cross-sectioned, ground using grades 180 - 4000 SiC paper and polished using OPS solution, in order to image the microstructure within the lattice struts. However, due to the complex nature of the structure, only the Ti65Ta samples could be sufficiently polished for EBSD analysis. The highly dislocation dense α′ laths in the Ti25Ta material returned poor indexing rates. However, the microstructure of the Ti65Ta lattice provides insight into the prior β grain size of the Ti25Ta material, and hence the α′ lath length can be estimated. EBSD analysis was conducted using a JEOL 7001F FEG SEM, with a 20kV accelerating voltage and step size of 0.4 μm for both the single melt and remelt material.

The heat flow along thin lattice struts from the melt pool to the cold build plate has been shown to induce long columnar and textured grains, which is enhanced the thinner the struts become [255]. Thinner struts are created by a much shorter laser scan length and result in a much stronger vertical thermal gradient than longer scan lengths, where the thermal gradient is tilted slightly in the direction of the laser scan. The elongated grains in thin struts cause anisotropic mechanical behaviour of the lattices and introduce weak points, where a single grain can span an entire diagonal strut. The 0.35 mm struts used in the current study showed no grain elongation in either the single melt (Figure 5-17) or remelt (Figure 5-18) Ti65Ta material.

The microstructure of the Ti65Ta material is similar to the microstructure seen in the parameter optimisation cubes (Section 4.2.2), with equiaxed grains and no texture. Even with the enhanced thermal gradient, the solidification rate of the Ti65Ta material is high enough to avoid epitaxial grain growth. This is attributed to constitutional supercooling and remaining Ta particles aiding grain nucleation. However, the grains of the single melt lattice appear less regular than those of the single melt parameter optimisation cubes, Figure 4-9. It is hypothesised that the faster cooling rates caused by the thin lattice struts results in grain formation being more heavily disrupted by the remnants of Marangoni flow in the melt pool, as well as remnants of the microstructure within the original powder particles. The grain structure of the remelted lattices shows more regular grain shapes and the melt pool shape is more easily discerned, Figure 5-18. Grain formation in the smaller pools, formed during remelt scanning, is less susceptible to Marangoni flow and no new powder particles are added to create new independent microstructure regions.

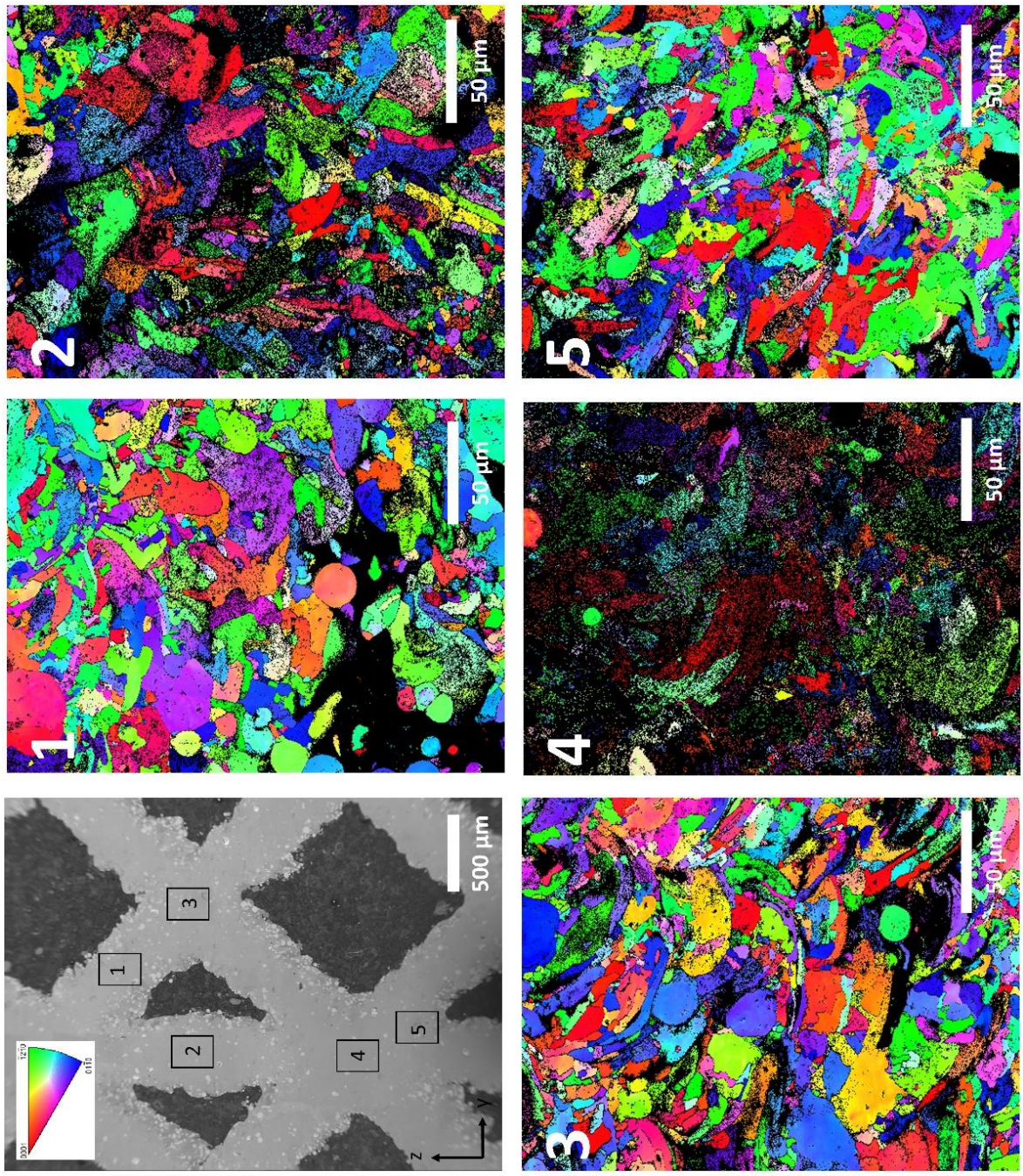

Figure 5-17: Microstructure of Ti65Ta single melt mechanical testing lattice.

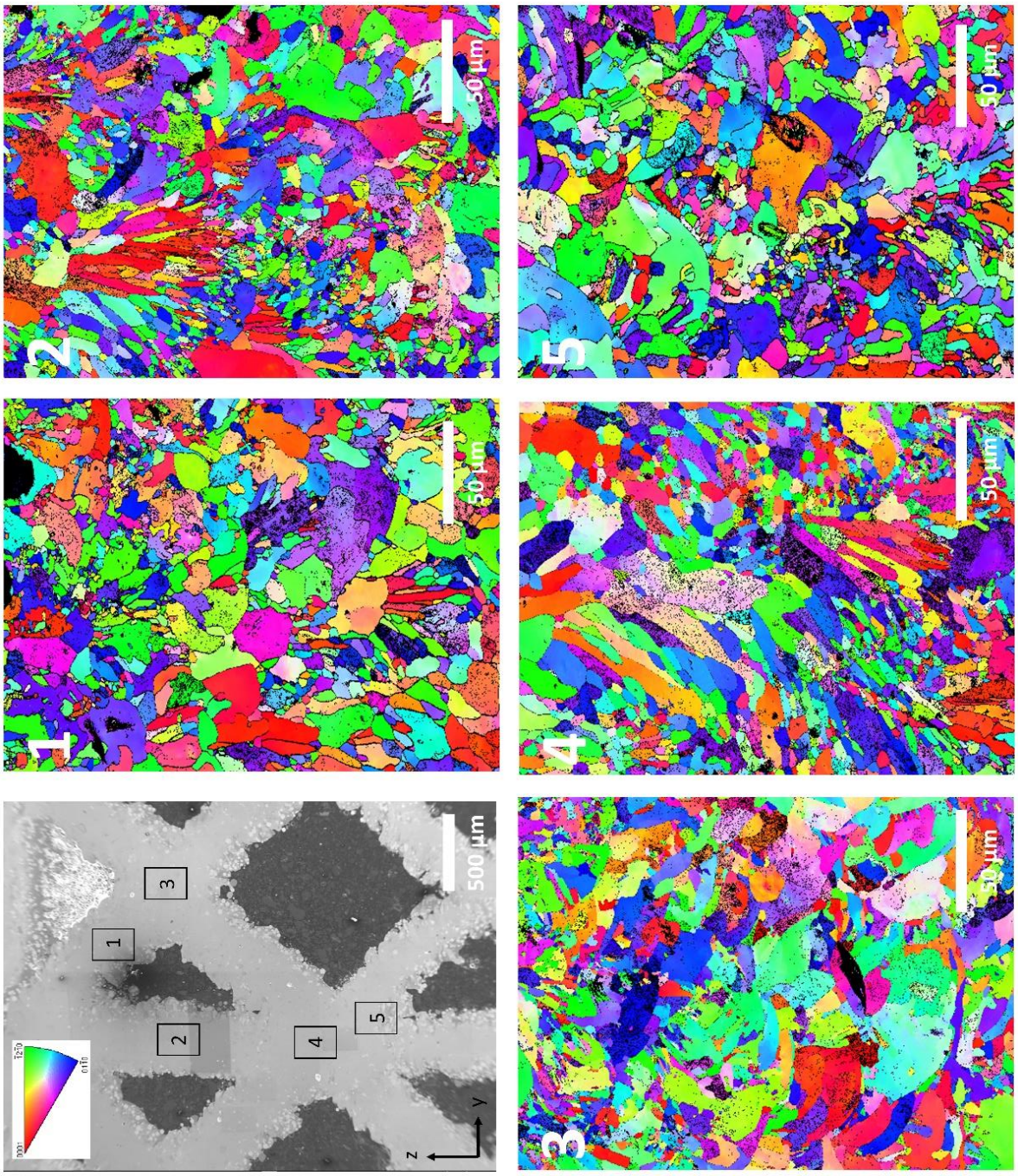

Figure 5-18: Microstructure of Ti65Ta remelt mechanical testing lattice.

Niendorf et al. [255] highlighted a difference in microstructure between the nodes with vertical members (Figure 5-18 (4)) and the diagonal struts (Figure 5-18 (1)) printed in FCCZ lattices of 316L stainless steel. The nodes with vertical members tended to show long elongated grains parallel to the building and heat flow directions. The diagonal struts, on the other hand, showed elongated grains tilted parallel to the strut direction, as the direction of heat flow is toward the diagonally placed pre-solidified layer of material, and not directly in the build direction. Both the strong vertical grain structure at nodes with vertical members, and the tilted elongated grain structure in diagonal struts, was not seen in the

Ti65Ta material. The lack of directional grain formation highlights that grain formation is driven by chemical as opposed to thermal solidification mechanisms in the TiTa alloys, promising isotropic mechanical properties.

For FCCZ lattices, it is known that failure occurs predominantly due to buckling of the vertical struts, which are directly parallel to the force direction. Hence, vertical elongation of grains in the vertical struts strongly reduces the compressive and tensile strength of FCCZ lattice structures [255]. The vertical struts of the Ti65Ta FCCZ lattices showed only minor elongation of grains in the building direction, Figure 5-18(2), suggesting the equiaxed microstructure of the Ti65Ta material could show superior compression and tension behaviour compared with other materials which undergo epitaxial growth, such as pure Ta [224].

The microstructure of the remelt scan mechanical testing lattice showed areas of refined grains, consistent with previous results, as well as some elongated grains in the vertical strut and vertical strut node, Figure 5-18(2) and (4). The smaller melt pool induced by the remelt scan strategy likely enhances the thermal gradient, as suggested in [178, 187, 190] increasing the likelihood of elongated grain formation. However, the area of these elongated grain regions is still very minor and unlikely to lead to anisotropic mechanical behaviour. The average grain size is also reduced compared with the single melt material, from 6.4 ± 6.0 μm to 5.3 ± 5.1 μm. However, this decrease is small, contributing to approximately 10 - 15 MPa in strength when modelled by the Hall-Petch relationship observed by Brice et al. [394] in L-DED Ti alloys and Cao et al. [351] in L-PBF Ti-6Al-4V, and hence unlikely to contribute significantly to an increase in strength of the remelt lattice samples.

The average β grain size of the Ti65Ta lattice struts was compared with the previously manufactured Ti65Ta bulk samples in Section 4.2.2. The average β grain size in the lattice struts was 6.41 ± 6.01 μm, slightly larger than that of the bulk samples (5.65 ± 5.33 μm). The thermodynamic conditions experienced by the lattice structures and bulk samples differ due to the difference in material volume, geometry and the change in processing parameters for each sample type. The smaller volume of lattice struts, coupled with their larger surface area and the higher scan speed parameters suggest higher cooling rates, which should lead to a decrease in grain size. As there is little to no difference in grain size between the two sample types, it is likely that chemical factors, such as constitutional supercooling, are much more dominant in solidification than thermodynamic factors. This is supported by the similarity of microstructure morphology noted in the different regions of the lattice.

In conclusion, the microstructure of the FCCZ TiTa struts was equiaxed, despite the thermal conditions of printing thin struts favouring the formation of long, elongated grains. The TiTa lattices will hence likely display isotropic behaviour and not suffer from mechanical weak points caused by single grains spanning an entire strut, or large concentrations of vertical grains oriented parallel to the building

direction. Slight grain refinement was still caused by the remelt scan, however the refinement was likely too small to contribute significantly to lattice strength.

5.2.5 Static Testing of FCCZ Lattices

Understanding the static strength of the FCCZ lattice structures is important to tailor them to the correct biological application. Hence, three FCCZ lattices were tested for each material and scanning condition (single melt and remelt) under both tension and compression and the data compared directly to identical lattices produced in Ti-6Al-4V from the work of Brenne et al. [386]. A displacement-controlled screw-driven load frame was used at a speed of 2 mm/min until fracture for tensile testing or until -30 % strain for compressing testing. The mechanical data was further supported with digital image correlation (DIC) analysis. Testing was stopped at 0.1 mm and 0.5 mm displacement increments for tension and compression respectively for images to be taken with a Nikon D60 digital camera, with a 10 megapixel resolution.

As the strain cannot be measured using an extensometer, the lattice strain was calculated as one tenth of the displacement, as the gauge length of the lattice was 10 mm. Brenne et al. [386] calculated the relative stress of each lattice structure using the designed density of the FCCZ unit cell structure, 10.37 %. The lattice stress was calculated as in Eq. 6, where F is measured force, A equal to 10×10 mm^2 and ρ^* is the designed density of the FCCZ unit cell.

$$\sigma^* = \frac{F \,/\, A}{\rho^*} \tag{6}$$

However, Section 5.2.2 showed that the printed struts and lattice volume were larger than designed in the CAD file. Hence using the designed FCCZ lattice density to calculate the lattice stress will likely overestimate the stress experienced during testing. On the other hand, using the measured lattice density from Section 5.2.2 will likely underestimate the stress, as a large portion of the increased lattice volume is due to areas filled with partially melted or adhered particles (Figure 5-15), unlikely contributing structurally to mechanical loading. As it is difficult to assess the exact volume of structural solidified material in the lattices without post-processing techniques, which would influence the surface quality of the parts, both the underestimated and overestimated stresses will be considered in the following analysis, to give a range of expected strength. The measured lattice density will be used initially to compare between the Ti25Ta and Ti65Ta material, whilst the designed lattice density will be used to compare to the Ti-6Al-4V data provided by Brenne et al. [386].

The tensile curves for the Ti25Ta single melt and Ti25Ta remelt lattices, calculated using their measured lattice density, showed very similar behaviour, reaching an ultimate tensile strength of approximately 150 MPa and elongation of 4 %, Figure 5-19(a). Only a slight difference was noted between the single

melt and remelt lattices, with the remelt sample showing a marginally higher tensile strength before failure, 148 MPa compared with 141 MPa. This increase is minimal and falls within the standard deviation of the repeated testing.

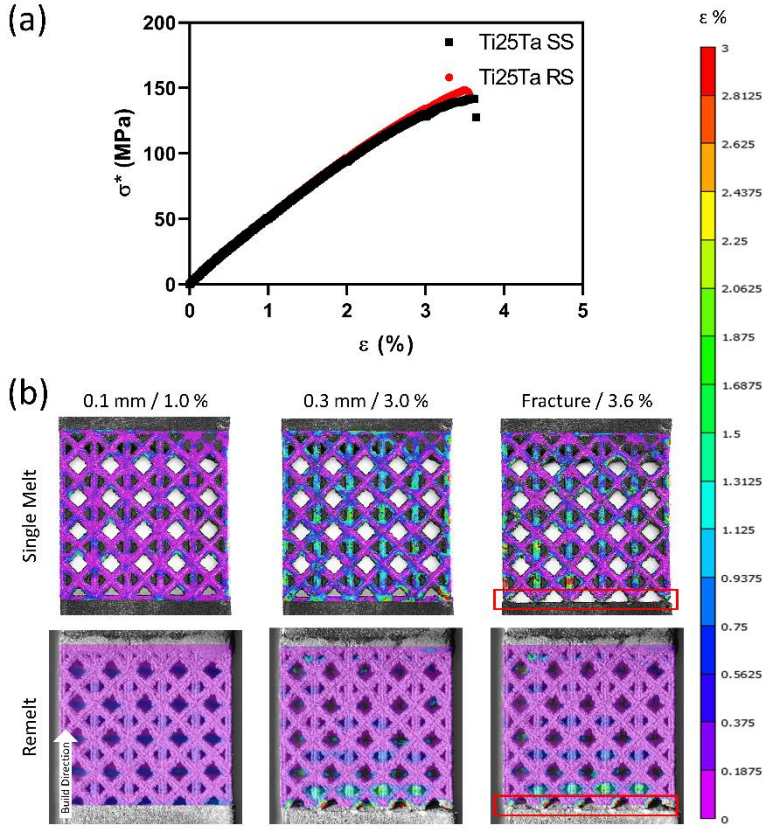

Figure 5-19: (a) Tensile curves of Ti25Ta single melt and remelt FCCZ lattices calculated using the Archimedes measured relative density, accompanied by (b) DIC analysis.

The DIC analysis showed the maximum strain occurred in the vertical struts, Figure 5-19(b), agreeing with results observed by Mazur et al. [258] and Brenne [386] who explored the tensile behaviour of the FCCZ structures through finite element modelling and experimentally with Ti-6Al-4V structures, respectively. The diagonal struts of the FCCZ lattice aligned at 45 ° to the force direction experience lower strain and hence the node acting as the intersection of four diagonal struts is not critical to failure. The six-strut nodes, which contain vertical elements, are much more likely to cause failure and are observed to be the points of fracture for both the single melt and remelt Ti25Ta material, highlighted with red rectangles in Figure 5-19(b). Only one of the Ti25Ta single melt lattices failed elsewhere; through the six-strut node plane, one unit cell below the top lattice-grip interface, Figure 5-21(d).

However, the increased strain in the vertical struts and nodes was not seen equally throughout the entire lattice. Each sample fails where the six-strut node intersects with the bottom grip. Failure at the bottom lattice-grip interface appears to be caused by a combination of the geometric defects of the printed

lattices, noted in Section 5.2.3. The bottom lattice-grip interface is formed more accurately than the top lattice-grip interface, and hence has less material to carry load. In addition, the more accurately formed bottom lattice-grip intersection possessed sharper node-grip intersections, with higher stress intensity factors. The decrease in geometric accuracy at the top lattice-grip interface has led to the accidental formation of an almost functionally graded structure. Functionally graded structures are promising for biological applications as they allow tailoring of mechanical properties within regions of implants and studies have shown failure consistently initiates at the thinnest struts of the structure [261, 395, 396]. In addition, the adhered material acts similar to a fillet, dispersing the stress concentration at the sharp node-grip intersection. Finite element simulations of FCCZ structures under tensile and compressive stress by Mazur et al. [392] showed high stress concentrations in this area and it was suggested that filleting could improve lattice mechanical properties.

The tensile curves for the Ti65Ta single melt and remelt material, showed similar strength to the Ti25Ta material with a UTS of 140 and 150 MPa, respectively, occurring at 4 % strain, Figure 5-20(a). Whilst the Ti25Ta material showed a sudden fracture, the Ti65Ta material showed gradual strut failure with increased elongation to 8.8 and 8.3 % for the single melt and remelt lattices, respectively. The gradual strut failure can be attributed to the higher total elongation of the Ti65Ta material, with crack propagation occurring much more slowly through each individual strut. The remelt scan had been previously shown to decrease ductility, both in tensile and fatigue testing of the solid material, and hence here slightly decreases the total elongation by 0.5 %. Similar to the Ti25Ta material, the remelt scan caused a very slight increase in the lattice UTS, and whilst this increase is again within the standard deviation of the testing samples, the remelt scan likely causes a minor but consistent higher lattice strength. As only approximately 1 μm difference in β grain size existed between the single melt and remelt lattice microstructures noted in 5.2.4, the slight increase in strength is likely due to a small increase in oxygen content, residual stresses and dislocation density in the remelt samples.

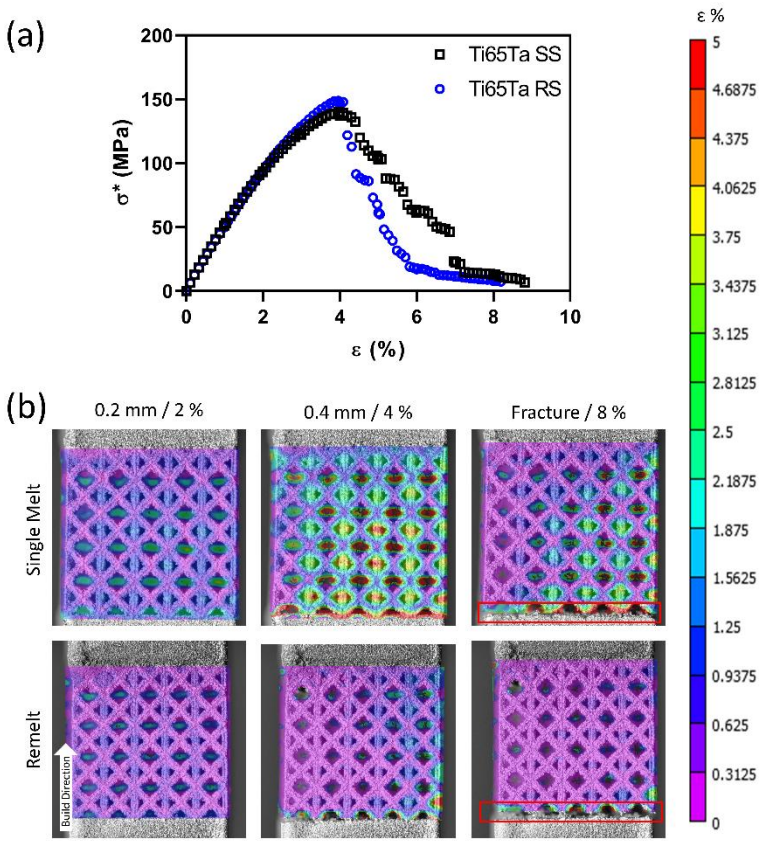

Figure 5-20: (a) Tensile curves of Ti65Ta single melt and remelt FCCZ lattices calculated using the Archimedes measured relative density, accompanied by (b) DIC analysis.

The DIC analysis again showed the highest strain occurring in the vertical struts, and failure initiating at the bottom lattice-grip interface, with high stress concentrations between the diagonal struts and horizontal grip, Figure 5-20(b). In addition, failure occurred consistently at the bottom lattice-grip intersection, mimicking the failure of the Ti25Ta lattices. Lattice failure often occurs as a combination of surface and geometric defects [397] and microstructure [255], however the starkly different α′ and β microstructures appear to have no effect on the lattice failure. It was hypothesised that the sharp microstructural interfaces, caused by the fine α′ laths in the Ti25Ta may act as stress concentrators, enhancing crack initiation. However, as the Ti25Ta and Ti65Ta material failure modes are identical, it is unlikely that the microstructure is contributing significantly to failure. The geometric defects noted in Section 5.2.3 are much more dominant causes of failure.

To compare to the Ti-6Al-4V lattices investigated by Brenne et al. [386], the tensile stress of the Ti25Ta and Ti65Ta lattices was recalculated using the designed FCCZ lattice density, altering the Ti25Ta and Ti65Ta material strengths to 580 – 630 MPa and 583 – 643 MPa, respectively, Figure 5-21(a) and (b). There is a larger deviation between the single melt and remelt material performance when the designed lattice density is used, as the increase in volume of the remelt material is no longer considered, giving the remelt material a slightly misleading higher strength. In addition, no Archimedes density data was

provided by Brenne et al. [386], however using images from the referenced work, the strut size of the Ti-6Al-4V lattices was found to be ~ 550 µm in size, suggesting a similar increase in lattice volume to the Ti25Ta and Ti65Ta materials, and supporting the designed lattice density comparison.

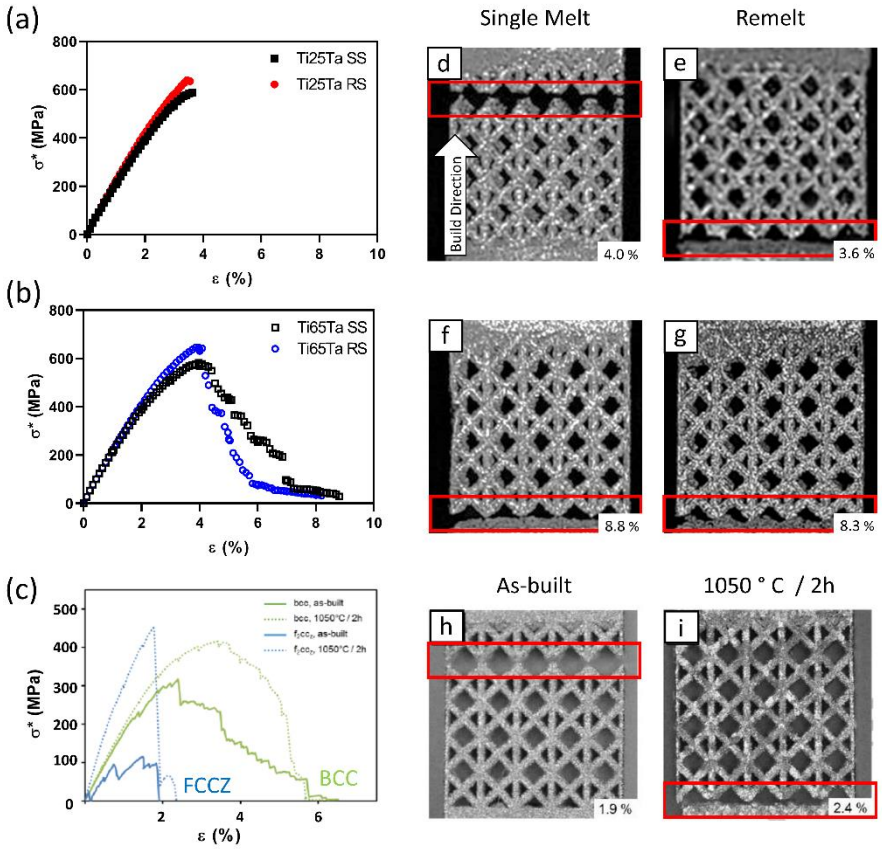

Figure 5-21: Tensile curves of FCCZ lattice structures for (a) Ti25Ta, (b) Ti65Ta and (c) Ti-6Al-4V data from [386]. (d – i) show the mode of fracture for each alloy, with the fracture strain indicated in the bottom right corner.

The comparative Ti-6Al-4V FCCZ structures were tested in both as-built (solid blue line) and heat-treated (dotted blue line) conditions. In addition, the behaviour of a BCC bending dominated structure is also presented (green lines). The as-built Ti-6Al-4V consisted of 4 µm α′ laths, whilst the heat-treated sample consisted of 100 µm sized α grains with a small and unquantified volume of β phase. The heat-treated samples however had much reduced internal stress [386]. The UTS of the Ti-6Al-4V as-built and heat-treated lattices was 100 MPa and 450 MPa respectively, with a total elongation of 2 %, Figure 5-21(c). The Ti-6Al-4V as-built samples failed at the six-node strut, one unit cell from the top lattice-grip interface, Figure 5-21(h), whilst the heat-treated samples failed at the bottom lattice-grip interface, Figure 5-21(i).

The higher ductility of the L-PBF TiTa alloys results in superior tensile behaviour compared to the Ti-6Al-4V lattices. The UTS of the Ti25Ta and Ti65Ta material was approximately 600 MPa, exceeding the as-built and heat-treated Ti-6Al-4V conditions, 100 MPa and 450 MPa, respectively. The extremely

low ductility of the as-built Ti-6Al-4V resulted in sample failure before reaching the UTS, as solid as-built Ti-6Al-4V has been shown to reach strengths of 1200 MPa, however with low elongations of 1.7 % [358]. When in lattice form, surface defects become more critical to failure and the low ductility of Ti-6Al-4V results in an extremely low notch resistance and hence premature tensile failure. When the Ti-6Al-4V is heat treated, the α′ microstructure is replaced with a more ductile α phase, but with a much larger grain size. The tensile strength of the Ti-6Al-4V lattice increases from 100 to 450 MPa with heat treatment, caused by a reduction in residual stress and increased in ductility, however not sufficiently to achieve as high strength as the TiTa lattices.

The Ti25Ta tensile curves are most closely matched in shape to the Ti-6Al-4V FCCZ heat-treated curve, whilst the Ti65Ta curves are more similar to the Ti-6Al-4V BCC curves. The BCC lattice is a bending dominated structure and increased ductility results in the diagonal struts orienting in the force direction and hence, increasing the load carrying capacity of the structure [390]. Hence, the heat-treated BCC Ti-6Al-4V lattice achieves a higher stress than the as-built BCC lattice. The BCC lattice generally shows a greater capacity to deal with strain than the FCCZ lattice, due to its lack of vertical struts. Here, the FCCZ Ti65Ta lattices, due to their increased total elongation, show a similar capacity to endure strain as the BCC lattices, but with a much higher tensile strength, due to the vertical struts. The BCC unit cell is favoured due to its lower achievable elastic modulus but is limited by its tensile strength. Here, the strain capacity of the Ti-6Al-4V BCC lattice, can be mimicked by the FCCZ unit cell in the Ti65Ta composition, however with an increased tensile strength and an intrinsically lower elastic modulus.

When tested under compression, the Ti25Ta single melt and remelt lattices showed a compressive strength ranging from 200 to 225 MPa and a gradual stepwise softening to the -30 % strain end point, Figure 5-22(a). Again, the single melt and remelt samples showed very similar behaviour with a slight increase in strength in the remelt material which is likely due to increased residual stress. The stepwise decrease in strength represents the sequential buckling of vertical struts, which can be seen in the DIC to occur along a 45 ° diagonal shear band in the single melt sample and horizontally through the top layer of vertical struts in the remelt material, Figure 5-22(b). Compression failure of FCCZ is commonly seen through 45 ° diagonal shear [392], but alters to layer-by-layer failure when functionally gradient structures are used [398].

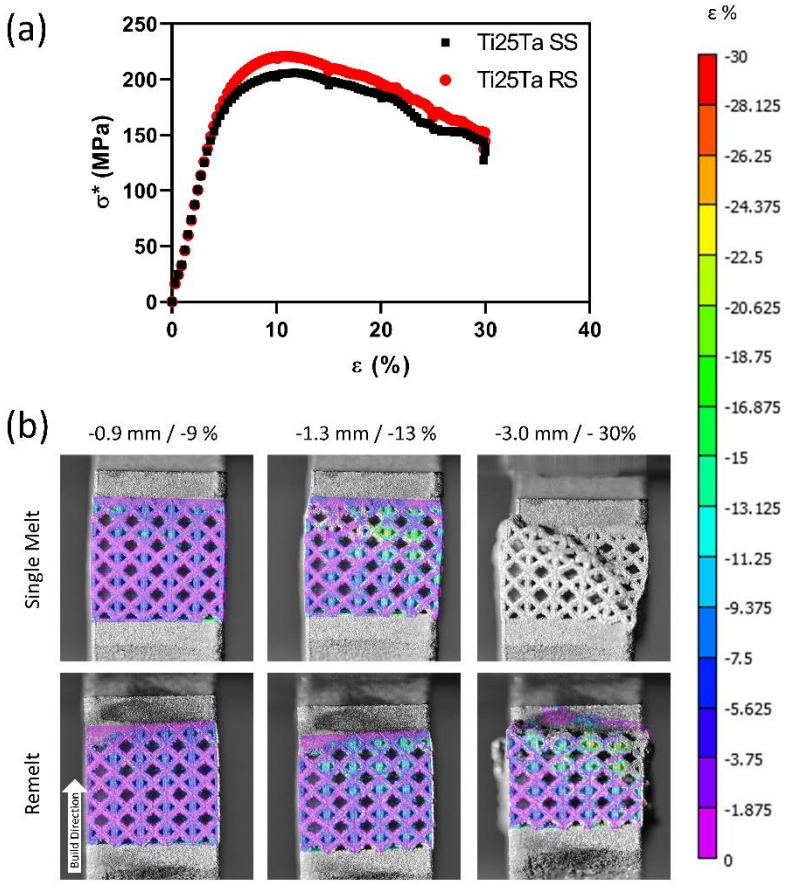

Figure 5-22: (a) Compression curves of Ti25Ta single melt and remelt FCCZ lattices calculated using the Archimedes measured relative density, accompanied by (b) DIC analysis.

Both the single melt and remelt material show higher strains and vertical buckling in struts adjoining the top lattice-grip interface. This is contrary to the tensile results, which showed failure occurring at the bottom lattice-grip interface. If the excess adhered material and geometric inconsistencies at the top lattice-grip interface were contributing to an increased capacity for loading, the top interface would also be strengthened under compression. The layer collapse of the remelt sample suggests the opposite. If the top lattice-grip interface struts were thickened, layer collapse should occur through any layer of thinner struts. Hence, the mechanism of failure in the tensile samples is likely more closely linked to the sharp angle caused by the accurately formed diagonal struts and grip at the bottom interface.

Under compression, failure is less likely to occur due to high stress concentrators, as crack propagation is not aided by compressive forces as it is by tensile forces. Hence, compressive failure initiating near the top of the mechanical lattices is likely caused by the residual stress state. Liu et al. [399] and Shiomi et al. [189] both confirmed an increase in internal stress with an increase in build height, as lower layers in an L-PBF part are heat treated and hence somewhat stress relieved as more layers are applied and melted. In addition, longer scan tracks were shown to cause higher residual stresses. Hence, the longer scan tracks required to create the grip horizontal surface increase the residual stress at the lattice grip

interfaces. As the remelt sample is hypothesised to have a higher residual stress, the enhanced residual stress at the top-lattice grip interface may have been sufficient to adjust the failure mode from 45 ° shear, to planar failure.

The compression curves of the Ti65Ta single melt and remelt material showed very similar compressive strengths of 187 – 189 MPa with slight material softening to the -30 % strain end point, Figure 5-23(a). The Ti65Ta lattices showed less softening (~ 15 MPa) compared with the Ti25Ta lattices (~ 50 MPa) which is likely linked to the higher dislocation density of the α′ laths in the Ti25Ta material. As hypothesised in the solid material fatigue analysis in Section 5.1.2, a higher initial concentration of dislocations leads to enhanced softening behaviour, due to enhanced dislocation annihilation. The DIC analysis showed 45 ° shear failure, originating at the top layer vertical struts, as seen in the Ti25Ta lattices and as expected for FCCZ compressive failure, Figure 5-23(b). The slower crack propagation in the Ti65Ta alloy results in ductile strut deformation and hence a lower total reduction in stress at 30 % strain than seen in the Ti25Ta alloy.

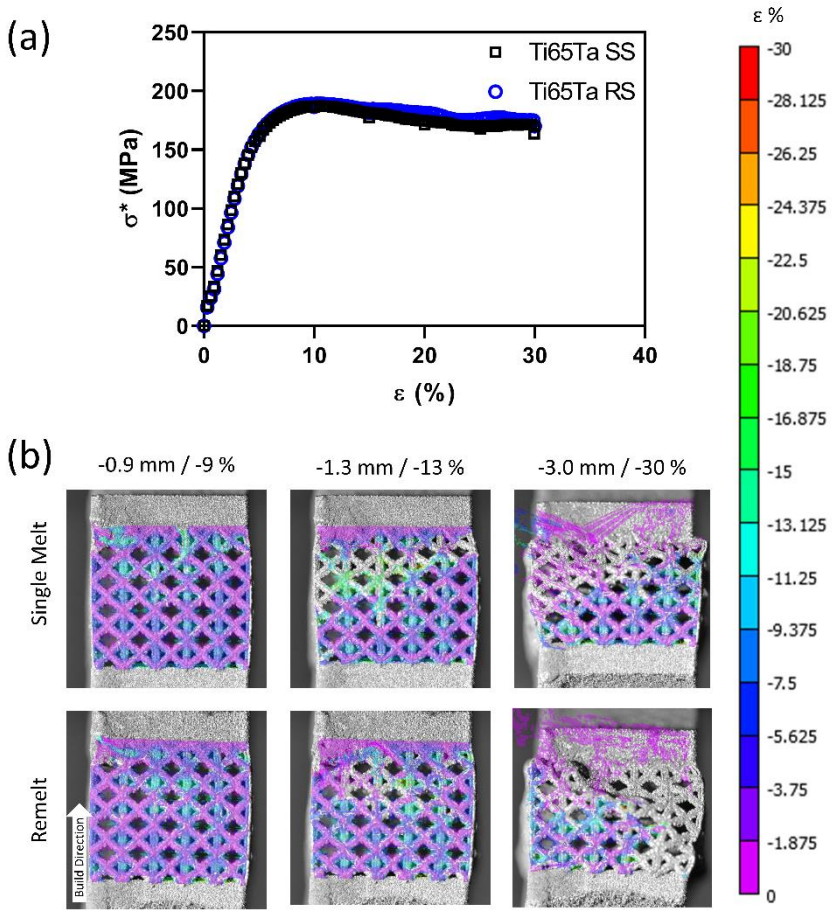

Figure 5-23: (a) Compression curves of Ti65Ta single melt and remelt FCCZ lattices calculated using the Archimedes measured relative density, accompanied by (b) DIC analysis.

When analysed using the designed lattice volume, the compressive strengths became 862 – 959 MPa and 777 – 821 MPa for the Ti25Ta and Ti65Ta material respectively, Figure 5-24(a) and (b). The Ti-6Al-4V lattices showed compressive strengths of 850 MPa and 750 MPa for the as-built and heat-treated material, respectively. It can also be observed that the FCCZ structure has a significantly increased compressive strength compared with the BCC structure, due to the presence of vertical struts.

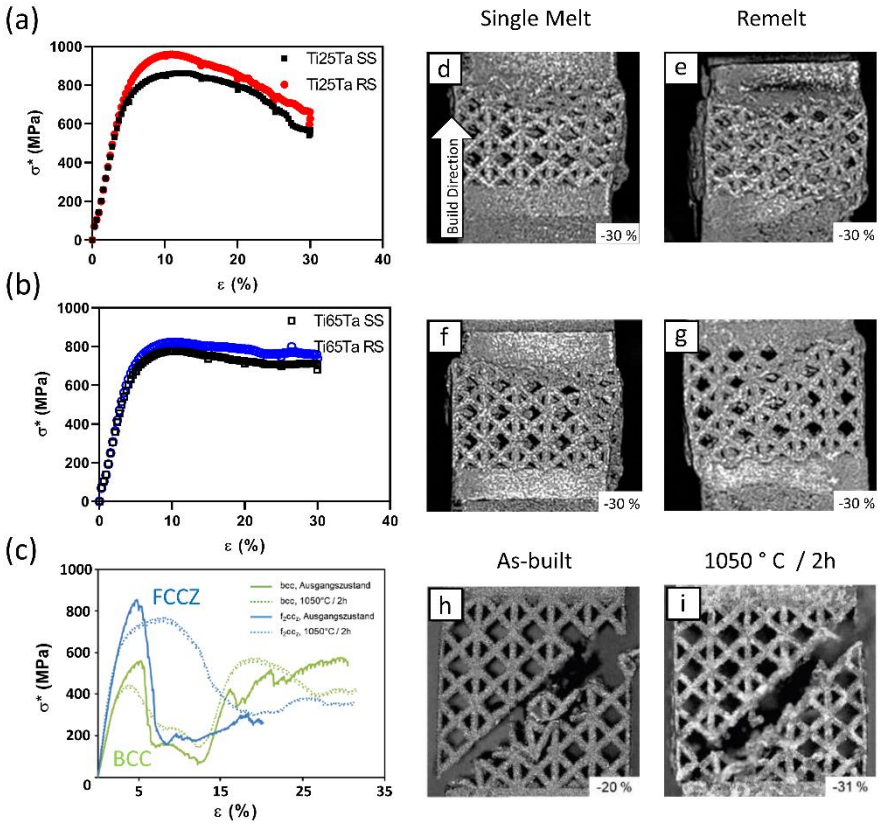

Figure 5-24: Compression curves of FCCZ lattice structures for (a) Ti25Ta, (b) Ti65Ta and (c) Ti-6Al-4V data from [386]. (d – i) show the mode of fracture for each alloy, with the fracture strain indicated in the bottom right corner.

The TiTa alloys showed similar ultimate compressive strengths to the Ti-6Al-4V material. The ultimate strength of the Ti-6Al-4V material is now able to reach that of the TiTa alloys as the high notch sensitivity of the low ductility Ti-6Al-4V lattices is less of an issue during compression testing, as it is less affected by crack initiation. However, the increased ductility of the TiTa alloys significantly alters the initial failure strain. The TiTa alloys both displayed stepwise failure over the entire -30 % applied strain, whilst the Ti-6Al-4V structures showed an abrupt failure, at approximately -5 % strain and -10 % strain for the as-built and heat-treated samples, respectively. Although yielding of any medical implant is to be avoided, a gradual failure such as seen in the TiTa material is much preferable to an abrupt failure as this would cause less damage to the surrounding tissues and maintain some level of functionality until a replacement could be inserted.

In conclusion, the increased ductility of the as-built TiTa lattices resulted in superior tensile and compressive behaviour when compared with identical Ti-6Al-4V lattices, in both as-built and heat-treated conditions. The TiTa lattices displayed an increase in tensile strength of almost 550 MPa when compared with the as-built Ti-6Al-4V lattices, as high notch sensitivity caused the Ti-6Al-4V lattices to fail before reaching their ultimate strength. In compression, the TiTa alloys showed a similar strength of 800 MPa to the Ti-6Al-4V lattices, however the TiTa material undergoes a ductile gradual failure over 30 % strain, preferable to the abrupt failure at 5 – 10 % strain of the Ti-6Al-4V lattices. Lattice failure in tension was caused by the accurate formation of sharp connecting angles between the lattice and bottom grip, whilst failure in compression was more susceptible to the higher residual stress formed at the top lattice-grip interface. Geometric improvements and parameter optimisation for stress relief could further enhance the tensile and compressive behaviour. Promising new curved surface geometries, such as triply minimal surfaces and gyroid structures [275, 395], remove sharp angles between struts and nodes and will reduce the geometric inaccuracy caused during printing as the structures are more self-supporting.

5.2.6 Cyclic Testing of FCCZ Lattices

Cyclic testing of the lattices is required to understand how the material will behave in functionally loaded implants. Mandible implants would experience fully reversed loading over millions of cycles per year. Ti-6Al-4V is conventionally used in fatigue applications, due to its high specific strength resulting in a good fatigue endurance. However, the low ductility of L-PBF Ti-6Al-4V significantly reduces its fatigue performance, and the static testing of the lattices in the previous section, highlighted the premature failure of Ti-6Al-4V lattices, due high notch sensitivity. The new TiTa alloys, with higher ductility and increased damage resistance, provide a promising alternative material.

To assess the fatigue behaviour of the TiTa lattices, force-controlled fatigue tests were conducted under fully reversed tension-compression loading (R = -1), with at least three specimens per condition, except at the lowest stress level where only two samples were tested due to the large time required for testing. A frequency of 5 Hz was used for three stress levels of 50 MPa, 120 MPa and 300 MPa, calculated using the designed lattice density. These stresses were chosen to bridge an elastic to plastic deformation response of the material, showing both low-cycle and high-cycle fatigue behaviour. As during tension testing, the first strut was seen to fail at approximately 200 MPa, this was considered as an estimate yield strength level, and the fatigue stress levels chosen around this value. The comparative Ti-6Al-4V lattices were only tested at 50 MPa in the work by Brenne et al. [386].

The low stress condition of 50 MPa resulted in approximately 10^6 cycles to failure for both the Ti25Ta and Ti65Ta single melt material, Figure 5-25(a) and (b). The 50 MPa and 120 MPa curves displayed a

relatively stable stress plateau, suggesting deformation within the elastic region. The 300 MPa curves displayed a slight upward trend to higher strain values over the lifetime of the specimens, suggesting plastic deformation during cycling, also noted in the solid fatigue material, Section 5.1.2. The Ti65Ta material also displayed a slightly higher number of cycles to failure at the 300 MPa testing level, reflecting the slower crack propagation in the Ti65Ta alloy.

The behaviour of the remelt material is similar to the single melt material, for both alloys. The remelt material only suffers a slight decrease in fatigue life, accentuated at the lower stress levels. This agrees well with the static lattice testing results which showed similar strengths and minor differences in elongation from each scanning strategy. At lower stresses, where crack initiation life dominates fatigue failure, the remelt material with its slightly lower ductility and enhanced notch sensitivity fails at a lower number of cycles.

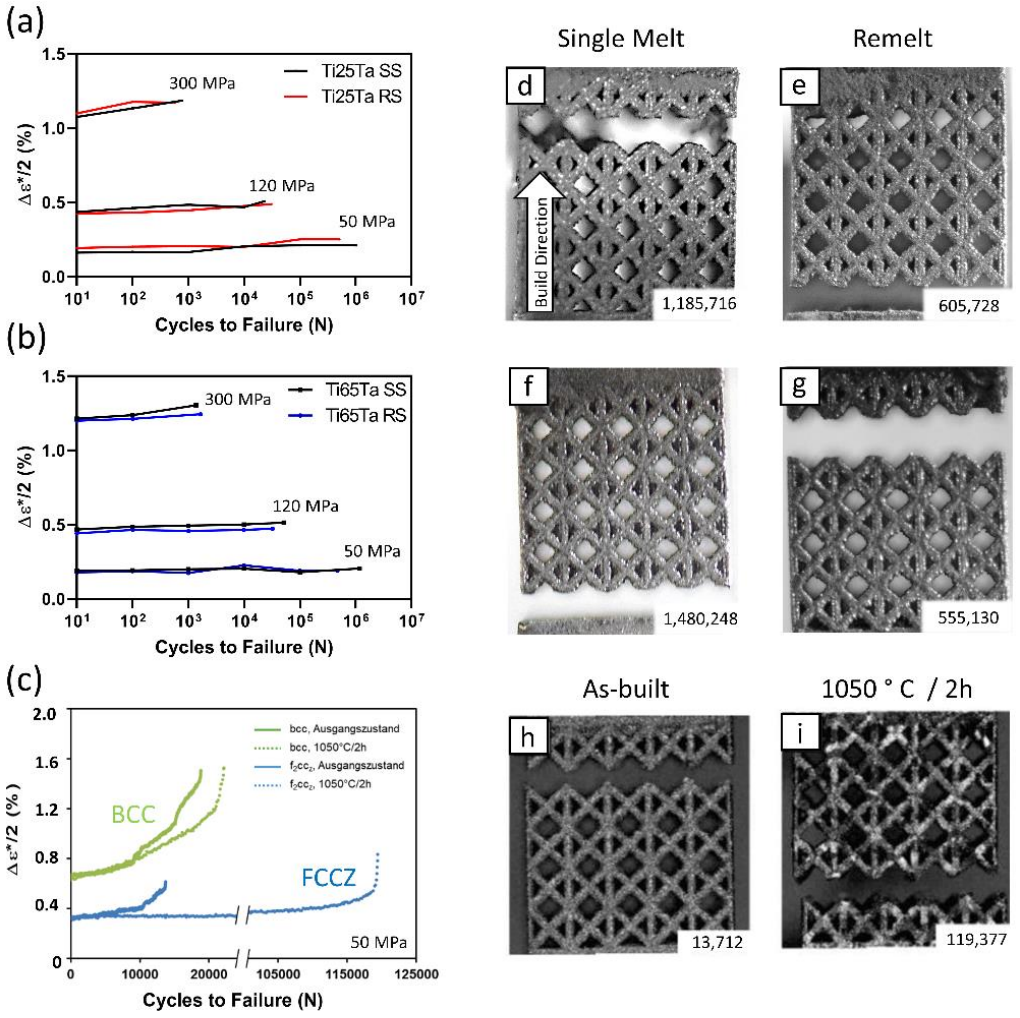

*Figure 5-25: Fatigue lifetime curves of (a) Ti25Ta, (b) Ti65Ta and (c) Ti-6Al-4V FCCZ lattice structures. Ti-6Al-4V*** *data from [386]. (d – i) show the mode of fracture for each alloy, with the number of cycles to failure indicated in the bottom right corner.*

*** Note that the Ti-6Al-4V x-axis scale is linear whilst that of the TiTa alloys is $\log_{10}$.

The Ti-6Al-4V as-built and heat-treated FCCZ lattices tested at 50 MPa failed at approximately 10^4 and 10^5 cycles, respectively, Figure 5-25(c). The heat treatment which increased the ductility of the Ti-6Al-4V lattices also reduces notch sensitivity. However, the TiTa alloys still showed superior fatigue life to both the as-built and heat-treated Ti-6Al-4V, by a factor of 10. Even with heat treatment, the high notch sensitivity of Ti-6Al-4V resulted in a significant decrease in fatigue life (10^6 cycles), when compared with the TiTa alloys (10^7 cycles).

In both static and cyclic testing, two failure modes occurred for the TiTa mechanical lattices; either fracture through the bottom lattice-grip interface, Figure 5-25(e) and (f), or fracture through the layer of six-strut nodes, one unit cell removed from the top lattice-grip interface, Figure 5-25(d) and (g). The number of occurrences of each failure mode is summarised in Table 5-5. The results showed that the least ductile TiTa material, Ti25Ta RS, failed consistently at the bottom lattice-grip interface, suggesting that the higher notch sensitivity of this material resulted in failure due to the sharp angle between the diagonal strut and grip. The single melt Ti25Ta material was also more susceptible to interface failure, despite having an increased ductility when compared with the remelt material. The Ti65Ta material, on the other hand, failed more commonly through the six-strut node layer in both the single melt and remelt conditions. The increased ductility of the Ti65Ta material, resulted in failure less likely caused by the sharp bottom lattice-grip interface, and more likely caused by the higher residual stress near the top of the lattice.

Table 5-5: Number of interface failures compared to number of lattice failures.

(Interface / Lattice)	**Tension**	**Fatigue**			**Total**
		50 MPa	**120 MPa**	**300 MPa**	
Ti25Ta SS	2 / 1	1 / 1	2 / 1	2 / 1	7 / 4
Ti25Ta RS	3 / 0	2 / 0	3 / 0	3 / 0	11 / 0
Ti65Ta SS	1 / 2	1 / 1	0 / 3	2 / 1	4 / 7
Ti65Ta RS	2 / 1	0 / 2	0 / 3	1 / 2	3 / 8
Ti-6Al-4V as-built	0 / 1	0 / 1	-	-	0 / 2
Ti-6Al-4V heat-treated	1 / 0	Defect failure	-	-	1 / 0
Total	9 / 5	4 / 5	5 / 7	8 / 4	**26 / 21**

However, contrary to this understanding, the overall least ductile material, the as-built Ti-6Al-4V failed through the six-strut node layer. Only one case of lattice-grip fracture was noted in [386] for the Ti-6Al-4V heat-treated sample when tested in tension, Figure 5-21(i), suggesting ductility is not the only contributing factor to the TiTa interface failure. The initial spikes of high strain in the tensile DIC imaging of the TiTa lattices occurred on the corner of the lattice, at the outer most junction between the

lattice and grip, Figure 5-26. This hot spot always occurs on the side of the lattice, which was facing the powder spreading blade during printing, which has resulted in a build-up of adhered material, as observed in Section 5.2.1. The excess material build-up appears to be concentrated at the corner of the horizontal grip surface, likely as this is the beginning or ending point of the laser per layer, and hence the hottest point on the part as a new layer of powder is applied. This material build-up increases the geometric deviation of the final printed lattice from the CAD file is likely contributing to the sample failure. This failure also occurs preferentially at the bottom interface as the material build up increases with the volume of grip printed. Hence, for the lower interface, the larger amount of adhered material forms at the lattice-grip interface, whilst for the top grip, the larger amount of adhered material forms away from the lattice-grip interface, at the top end of the grip.

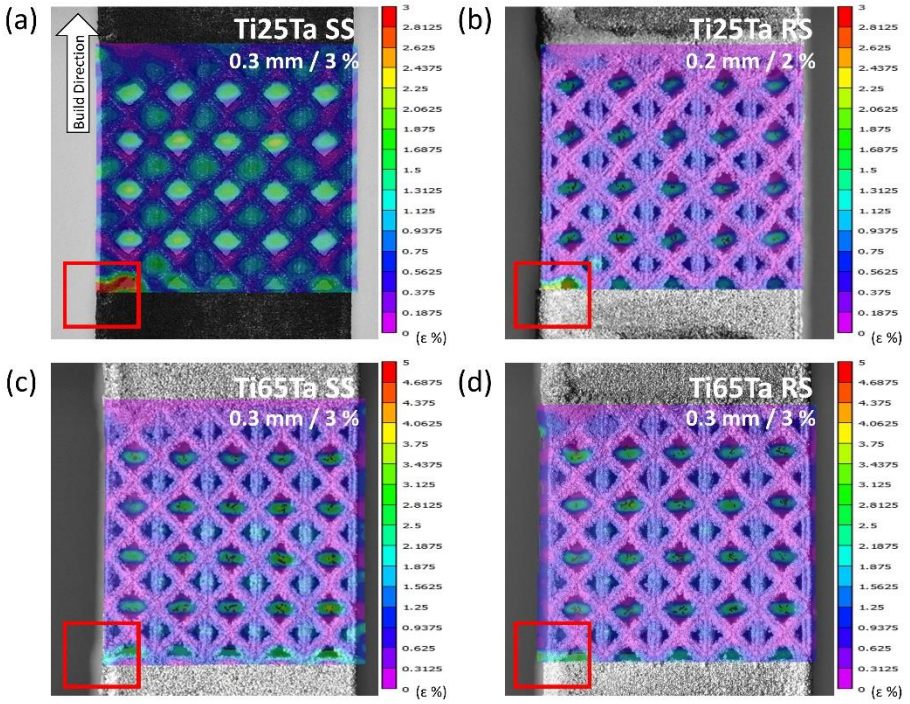

Figure 5-26: Initial point of failure in tension for (a) Ti25Ta single melt, (b) Ti25Ta remelt, (c) Ti65Ta single melt and (d) Ti65Ta remelt.

The second common mode of fracture, Figure 5-21(a) occurs through the six-strut nodes one unit cell removed from the top lattice-grip interface and is likely caused by residual internal stresses, as discussed in Section 5.2.5. This hypothesis is supported by the results of Brenne et al. [386] which displayed a change in the failure mode between the as-built and stress relieved heat-treated Ti-6Al-4V lattices. The as-built samples failed through the top layer of six-strut nodes whilst the heat-treated samples failed through the lattice region which showed the greatest printing defect. Hence, relieving residual stress of

the TiTa lattices will also likely alter the failure mode to become more dependent upon printing defects and random within the lattice structure.

Overall, the improved ductility of the FCCZ TiTa lattices results in a superior fatigue behaviour compared to the FCCZ Ti-6Al-4V as-built and heat-treated lattices, Figure 5-27. The ability of the TiTa alloys to absorb deformation reduces the probability for crack initiation, which is highly critical in lattice structures due to their large surface area. In addition, the inherent ductility of the TiTa alloys allows for gradual failure in lattice structures, much more appropriate to implant applications than the abrupt brittle failure of Ti-6Al-4V lattices. The Ti65Ta lattices also show a slight improvement in fatigue behaviour at high stresses when compared with the Ti25Ta lattices, likely due to slower crack propagation in the β phase.

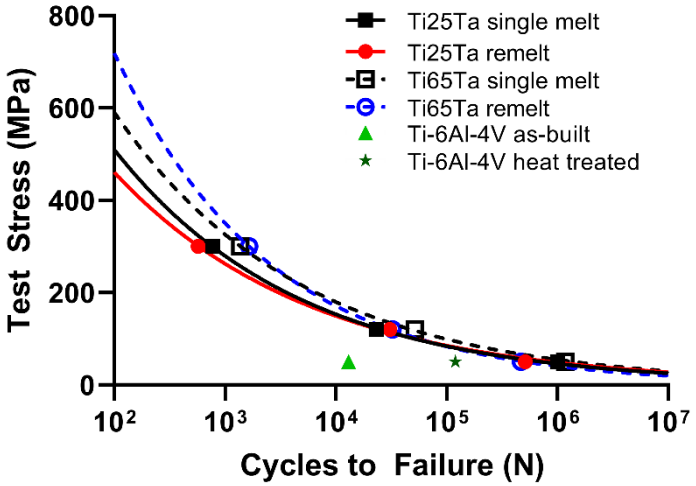

Figure 5-27: Comparison of fatigue performance of Ti25Ta and Ti65Ta FCCZ lattice structures with identical Ti-6Al-4V structures.Ti-6Al-4V data reproduced with permission from [386].

The TiTa lattices showed increased manufacturing geometric inconsistencies compared with the Ti-6Al-4V lattices, due to the wide and deep melt pools required to melt the Ta component. Despite the larger variation from the CAD design, the TiTa lattices showed superior mechanical behaviour, as their increased ductility negated the effect of the geometric inconsistencies, by increasing the material damage tolerance. Reducing manufacturing geometric inconsistencies can be achieved by altering the lattice type to more recent designs such as TPMS structures where have higher surface curvatures and hence improved forming capabilities for L-PBF techniques [277].

The remelt scan strategy made only a small difference to the mechanical behaviour of the lattices, as the microstructure undergoes a much smaller change in the thin struts when compared with larger parts. In addition, the reduced number of Ta particles appeared to have negligible effect on mechanical performance, as porosity and geometric defects always acted as higher stress concentrators and Ta particles never initiated failure. The remelt scan slightly decreases the material ductility, the effect of

which is more strongly seen at higher testing stresses, where crack propagation is enhanced leading to a lower number of cycles to failure.

The slower crack propagation in the Ti65Ta alloy compared with the Ti25Ta alloy does result in a minor increase in fatigue life, however, this minor increase is unlikely significant enough to benefit specific implant applications. Further biomechanical modelling and implant design is required to determine the actual minimum fatigue life required for particle implant applications, but both the Ti25Ta and Ti65Ta alloys are promising replacement implant materials to brittle L-PBF Ti-6Al-4V.

5.3 Chapter 5 Summary

In this chapter the fatigue behaviour of the L-PBF TiTa alloys was investigated for both solid and lattice structures. The following conclusions were drawn:

- X-ray Micro-CT confirmed that the remelt scan effectively reduced the number of remaining partially melted Ta particles, however fractography confirmed that the Ta particles do not act as fatigue crack initiation sites. The remelt scan did not improve fatigue life by reducing the remaining number of partially melted Ta particles as hypothesised. The remelt scan resulted in a reduction in fatigue performance of 5×10^3 cycles at high stress and 8×10^4 cycles at low stresses, attributed to decreased ductility.

- When normalised by yield strength, the solid TiTa alloys performed well in fatigue, only inferior to pure Ta. However, pure Ta is much less optimal for implant applications due to its high elastic modulus and density.

- Parameter optimisation was required when adjusting the printed geometry from cubes to fine lattice struts. A lower energy density, with a scanning speed of 600 mm/s was found to minimise the porosity formed within the struts and the remelt scanning strategy was still successful at reducing the number of remaining Ta particles.

- The microstructure of the FCCZ lattices was only slightly finer than previously built larger volume samples, with no columnar grains. The solidification of the TiTa alloys is hence heavily driven by constitutional supercooling and Ta particles acting as nucleation sites, as opposed to thermal gradients.

- The static and cyclic behaviour of the FCCZ TiTa lattices was superior to that of Ti-6Al-4V, without normalising by yield strength. The high notch sensitivity of the as-built and heat-treated

Ti-6Al-4V led to premature failure, whilst the TiTa lattices showed a high cycle fatigue life due to the alloys' higher ductility and increased damage tolerance.

- The Ti25Ta and Ti65Ta FCCZ lattices perform similarly in fatigue, with the slower crack propagation in the Ti65Ta material leading to a very slight increase in lattice fatigue life at high stresses. This minor increased fatigue performance is not significant enough to outweigh the higher elastic modulus, density and material cost of the Ti65Ta alloy and hence the Ti25Ta alloy will potentially prove more suitable in practice.

Chapter 6 *In Vitro* Biological Testing of TiTa Compositions

L-PBF TiTa alloys show promising mechanical properties for implant applications with low elastic modulus, improved ductility compared with Ti-6Al-4V and promising fatigue performance. However, the newly developed alloys should not only be mechanically suitable but also enhance bioactivity. Ta has been shown in multiple *in vitro* and *in vivo* studies to enhance the osteogenic response when compared with Ti, however the biological effect of the TiTa alloy system is yet to be investigated. It is yet unknown whether the TiTa alloy system displays any osteogenic benefit and whether such a benefit is proportional to the amount of Ta present in the alloy. In addition, whilst both Ti and Ta have been used extensively in biological applications, it is still important to confirm the biocompatibility of the new L-PBF TiTa alloys. Hence, preliminary investigations using the high-throughput L-DED produced TiTa alloys were undertaken to quickly assess the cytotoxicity of the alloy system and provide an initial insight into cell attachment and morphology to the polished alloy surface. Despite the different scale microstructures in the L-DED and L-PBF samples, the chemistry of the samples produced by each manufacturing technique was deemed similar enough for preliminary biocompatibility studies. The cell line used in the preliminary studies was MG63 human osteosarcoma cells; bone-like cells commonly used in *in vitro* bone scaffold studies. With promising preliminary results, the L-PBF Ti25Ta and Ti65Ta compositions were then assessed for both biocompatibility and osteogenic capability with hBMSCs. hBMSCs were used due to their differentiation capability which allowed the quantification of osteogenic potential of the different alloys, through measurement of ALP activity and mineral formation.

6.1 Preliminary Cytotoxicity and Morphology Studies of L-DED TiTa

It is important to confirm the biocompatibility of newly developed alloys early in the development process, to avoid wasting research time on possibly harmful materials. Hence, the preliminary L-DED TiTa material was assessed for cytotoxicity along with cell attachment, proliferation and morphology as an initial biocompatibility screening method for the AM TiTa system. According to the ISO 10993-5 standard, direct contact cytotoxicity, or cytotoxic leachables, can be detected using an MTS assay after 7 days of culture. MTS assays measure viable cell number through the production of a formazan product, the amount of which is affected by the number of cells initially attached to each substrate, the metabolic rate of the cells and the cell proliferation. Care should be taken to separate these factors, as opposed to simply assuming a high MTS reading confirms good biocompatibility. Cell morphology at early stages of proliferation can also provide deeper insight into the health and behaviour of the cells, as well as the ability of a material to support cell adhesion. Cell shape reflects the cell's mechanical and chemical environment. For example, cells attached to a stiffer substrate will tend to spread over larger areas, which has been linked to enhanced cell proliferation and osteogenesis, leading to improved implant integration [400, 401]. Different surface chemistries also attract different proteins from biological fluid and these proteins are responsible for cell attachment and behaviour [324].

MG63 human osteosarcoma cells were chosen for this preliminary study as they are bone-like cancer cells and show behaviour similar to human cells undergoing late stage osteoblastic differentiation. MG63 cells are heavily used to assess biocompatibility of new bone implant alloys [87, 117, 219, 289, 301]. Cells were cultured in basal media consisting of DMEM-high glucose (Gibco) with 10% foetal bovine serum (FBS) (Gibco) and 1% penicillin/streptomycin (Thermo Scientific) at 37 °C and 5% CO_2. The cells were used at passage 6.

The metallic substrates were prepared from the L-DED manufactured cubes of compositions CP Ti, Ti33Ta, Ti48Ta, Ti58Ta and pure Ta and cut into 5 mm × 5 mm × 2 mm square plates. It is well known that surface topography is a significant driver of cell morphology and fate [280] and this study aims to assess the effect of the chemical nature of the alloys. Therefore, the samples were polished using 0.04 µm OPS colloidal silica to negate any effects of surface topography, ultrasonically cleaned in an ethanol for 1 hr and then again soaked in 80 % ethanol for 30 mins and left to dry inside a biosafety cabinet, before being placed in a 48 well tissue culture plate.

Cells were seeded at 10^4 cells/cm^2 in a 40 µL basal media droplet placed directly onto the prepared metallic substrate surface. An empty well was used as a positive tissue culture plastic (TCP) control and surrounding wells were filled with PBS to reduce evaporation of the media droplet. After 4 hrs of incubation and cell attachment, the metallic substrates were covered with 300 µL of basal media. Cytotoxicity was assessed via an MTS assay (Cell Titre 96© Aqueous One Solution Cell Proliferation

Assay, Promega) at 4 hrs, 3 days and 7 days, following the ISO 10993-5 standard for biological evaluation of medical devices [291]. Culture media was replaced with MTS reagent diluted at a 1:5 ratio in basal media and incubated for three hours. 100 µL of this solution was then transferred to a 96 well tissue culture plate and the optical absorbance of the formazan product was measured at 490 nm with a plate reader (Thermo Scientific Multiskan Spectrophotometer). Cell viability was then calculated using Eq. 5 from the ISO 10993-5 standard (Section 2.4.2), using the tissue culture plastic as the positive control. To support viability analysis, the nuclei were counted after 4 hrs of seeding to indicate any differences in the ability of cells to attach to each composition. Proliferation curves were then normalised to the absorbance at the 4 hr timepoint.

Cell morphology was analysed by fixing cultures with 4 % paraformaldehyde (PFA) in PBS, incubating in 0.1 % Triton-X-100, blocking with 3 % bovine serum albumin (BSA) and staining with ActinRedTM 555 ReadyProbes© Reagent (Molecular ProbesTM) (red) to highlight the F-actin cytoskeleton and Hoechst 33342 (blue) to highlight the nuclei. Cells were then imaged using fluorescent microscopy (Nikon Eclipse Ti) and the images analysed using ImageJ. Morphological analysis investigated four cell shape parameters; spread area (μm^2), circularity (0 – 1, straight line to perfect circle), Feret's diameter (the longest distance between any two points on the cell perimeter) and aspect ratio (major axis / minor axis), Figure 6-1.

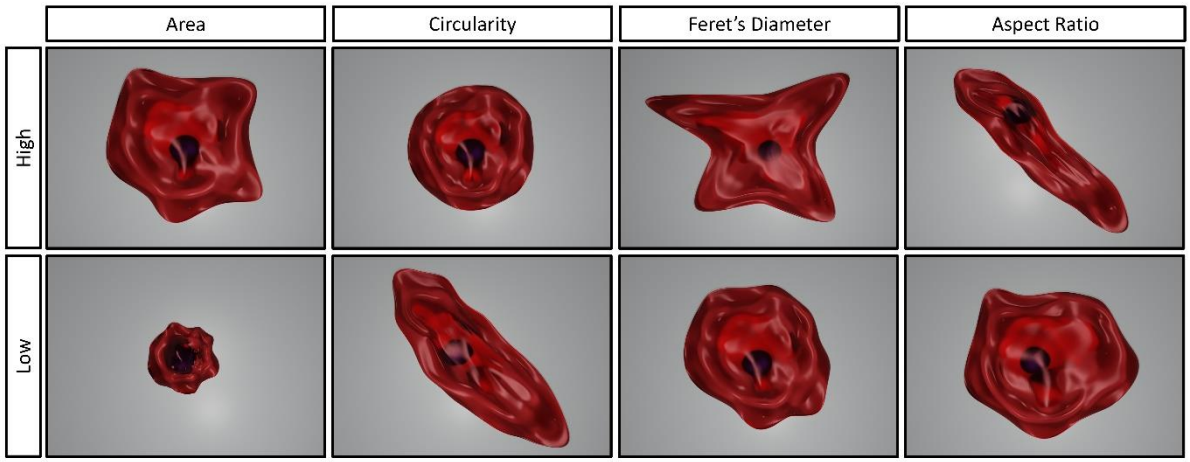

Figure 6-1: Schematic of the cell shape descriptors used for morphological analysis.

All biological tests were done in triplicate and statistical analysis conducted to determine significance between samples. GraphPad Prism 8.2.0 software was used to first analyse for normality, followed by a one-way analysis of variation (ANOVA), accompanied with a Tukey's multiple comparison test, at a significance level of $p < 0.05$. The Brown-Forsythe test was used to assess normality, with $p > 0.05$ indicating non-significant difference between data set standard deviations. * are used to signify

significant difference between alloys whilst # are used to signify significant difference between timepoints.

The viability of the cultured MG63 cells was greater than 70% for all the tested compositions relative to TCP, and hence each alloy was considered non-cytotoxic according to the ISO 10993-5 standard, Figure 6-2(a). The relative cell number for each alloy increases approximately four-fold to the 3 day time point, and then a further two-fold to the 7 day time point, suggesting normal cell proliferation. There was no significant difference in viability between each alloy and the TCP control at any time point. However, a slight downward trend is noted at the 3 day time point as the alloys increase in Ta content. The viability data on its own is very limited as to giving further explanation to this trend and hence cell attachment to and proliferation on each alloy should be considered separately. Figure 6-2(a) displays how easily a material can be classed as biocompatible without truly understanding the effects of contact with that material on cellular behaviour.

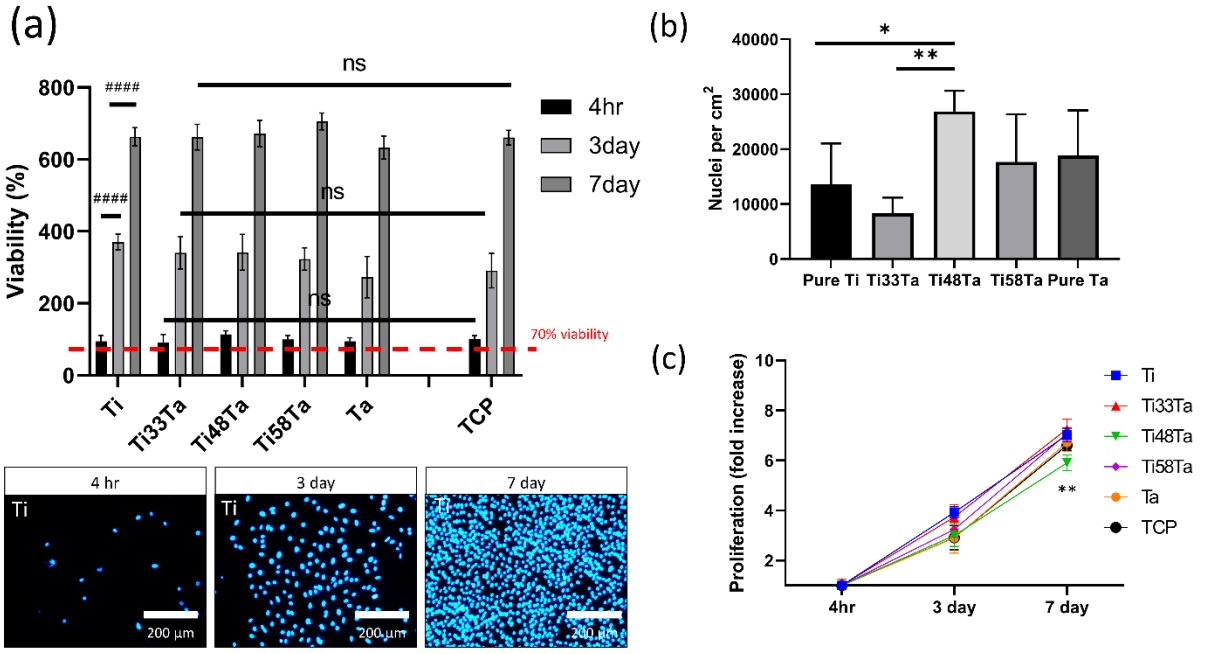

Figure 6-2: (a) Preliminary viability, at 4 hr, 3 day and 8 day timepoints, measured with an MTS assay. (b) Attachment at 4 hrs of nuclei counted per cm^2 across sample triplicates. (c) Proliferation by fold increase in cell number, displaying the mean MTS reading of each triplicate set relative to the 4 hr MTS reading.

Cell attachment to each alloy was assessed by nuclear staining and counting at the 4 hr timepoint, Figure 6-2(b). The highest cell attachment was seen on the Ti48Ta composition, with the Ti58Ta and pure Ta also showing slightly higher attachment than the pure Ti and Ti33Ta sample. A number of studies using osteoblast-like cells have shown preferential attachment to and proliferation on Ta compared with Ti [116, 117, 288, 314-317, 320], with one study attributing this to the higher surface energy of Ta compared to Ti (55 mN/m and 42 mN/m respectively) inducing improved wetting of the surface [315].

However, the results also suggest that inconsistencies exist in the seeding method. The Ti48Ta sample shows a much higher average value of almost 3×10^4 cells/cm^2, although the cells were seeded at 10^4 cells/cm^2, indicating inhomogeneous cell distribution in the seeding media or possibly pipetting errors. The large standard deviation also reflects the deviation between seeding within the triplicates for each alloy and may indicate that some of the seeding droplets may have evaporated more than others, resulting in significant cell death during seeding for some samples. Revisions to the seeding protocol were required and are discussed in the following section.

MTS absorbance, Figure 6-2(c), when normalised to the 4 hr time point measurement to negate effects of different attachment between samples, indicated similar proliferation on all compositions. Only the Ti48Ta composition showed a statistically lower proliferation at the 7 day time point, which is likely linked to the high number of cells seeded. Proliferation will gradually slow due to cell-cell contact inhibition as the cells reach confluence on the substrate surface. Ta has also been shown to result in higher proliferation in multiple studies [116, 310, 312, 314-317], however only two of these studies [312, 320] separate proliferation from the number of cells initially attached. Hence, higher initial attachment may be causing a misleading increase in proliferation in many studies. Cell type and topographical differences likely also contributed to the variations in literature proliferation results, as Li et al. [312] used goat mesenchymal stromal cells (MSCs), as opposed to osteoblast-like cells whilst Sagomonyants et al. [320] investigated porous Ta in comparison to a Ti fibre mesh.

Morphological analysis investigated four cell shape measurements; spread area (μm^2) (Figure 6-3(a)), circularity (Figure 6-3(b)), Feret's diameter (Figure 6-3(c)) and aspect ratio (Figure 6-3(d)). All these measures showed significant differences between samples, except for aspect ratio. Most notably cells attached to the Ta substrates show a lower circularity. This was coupled with a higher cell area and Feret's diameter, suggesting enhanced spreading. Figure 6-3(e) and (f) show this increased spreading on the Ti58Ta composition, in comparison to the Ti33Ta composition. A higher spread area suggests that the cells can interact more strongly with the substrate, which may reflect an increased ability to form focal adhesions [402]. This is likely to affect cell fate, particularly in the case of mesenchymal stromal cells (MSCs) and is important to monitor in future studies. Lu et al. [300] observed upregulated production of $\alpha_5\beta_1$ integrin on Ta surfaces and hypothesised that this upregulation caused the superior osteogenic behaviour of MSCs. However, increased integrin production is also triggered by increased integrin binding and osteogenic differentiation itself [403], making pinpointing the cause of increased osteogenic behaviour, difficult. It is possible that Ta surfaces are either enhancing the attachment of the $\alpha_5\beta_1$ integrin, possibly due to the attachment and conformation of the fibronectin protein on Ta surfaces, or structure of the Ta oxide provides a unique electrical configuration, which improves the signalling of the $\alpha_5\beta_1$ integrin, as suggested by Lu et al. [300]. As increased attachment and signalling of the $\alpha_5\beta_1$ integrin, leads to higher production of the $\alpha_5\beta_1$ integrin, future studies investigating the volume and confirmation of fibronectin attachment to Ta surfaces, as well as specific oxide energy configurations

may help to elucidate the mechanism through which Ta enhances osteogenic differentiation. In addition, assessing the morphology over a longer time period, such as at the 3 day time point, may also give a clearer indication of differences in morphology between the samples. This should help to lower the standard deviation in cell area for future experiments.

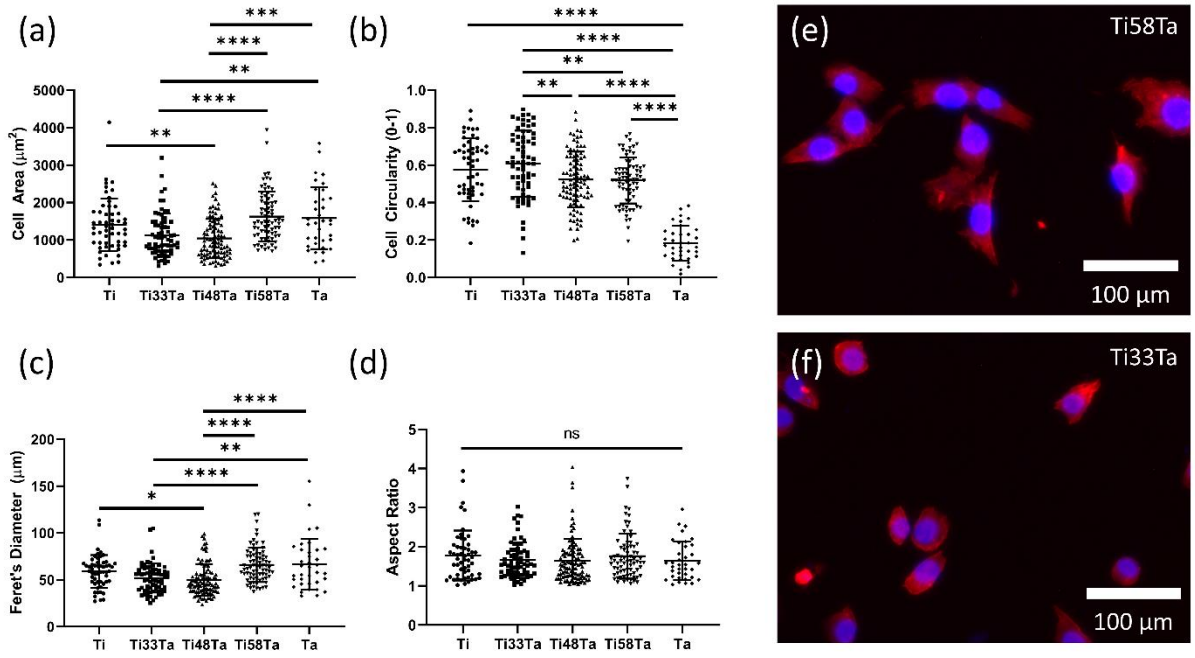

Figure 6-3: MG63 morphology at 4 hrs of seeding measured through (a) cell area, (b) cell circularity, (c) Feret's diameter and (d) aspect ratio. Each data point represents one cell, n > 50. Cell morphology analysed by cytoskeleton and nuclear staining for (e) Ti58Ta and (f) Ti33Ta compositions.

In conclusion, the preliminary analysis shows the L-DED TiTa alloys to be non-cytotoxic, however the measure of viability is limited for exploring the cell-material interactions. By counting nuclei, differing attachment between alloys was noted. This could indicate a slight increase in attachment to the higher content Ta compositions. However, it should be noted that there was a large variability within triplicates, suggesting improvements to the seeding method are required. Successful MG63 attachment to and proliferation was seen on all TiTa alloys, as well as the pure Ti and Ta controls, however no increase in cell proliferation on high content Ta alloys was noted, contrary to literature [116, 312, 320]. Quantitative measures of cell spread area, Feret's diameter and circularity displayed significant differences between samples and provide appropriate and insightful measures for further biological studies. Higher cell area and Feret's diameter, coupled with a lower circularity, was noted on higher Ta content alloys, suggesting a stronger cell-material interaction, which may lead to improved osteogenic differentiation in future stem cell studies.

6.2 Seeding Protocol Determination for hBMSCs on Metallic Substrates

A large standard deviation in attached cell number was noted in the preliminary investigations using MG63 cells, suggesting the preliminary seeding method required improvement. In addition, the culture of human bone marrow mesenchymal stromal cells (hBMSCs) can provide additional osteogenic insights over MG63 cell types, as hBMSCs are an osteogenic precursor cell. hBMSCs must commit to osteoblast lineage and mature, whilst MG63s are already mature osteoblast-like cells. hBMSCs differ from MG63 cells in size and behaviour, and hence the seeding density must be optimised to allow the hBMSCs to fully spread and hence undergo osteogenic changes.

hBMSCs (Lonza) were cultured in basal media consisting of DMEM-low glucose (Gibco), supplemented with 10% FBS (Gibco) and 1% penicillin/streptomycin antibiotic (Thermo Scientific), at 37 °C and 5% CO_2. The cells were used at passage 6.

Two different seeding methods were compared to reduce the standard deviation in cell attachment within triplicates seen in the preliminary work. Figure 6-4(a) shows the seeding protocol used in the preliminary work. 40 µL of cell suspension was placed on top of the metal plate within the well and incubated for 4 hrs before the well was then topped up with 300 µL of basal media. It was hypothesised that this seeding method resulted in evaporation of the seeding droplet during the 4 hr incubation period, likely changing the concentration of constituents in the media and leading to cell aggregation and death. Figure 6-4(b) shows a second method of seeding where 300 µL of the cell suspension is placed in the well with the metallic substrate, and incubated for 4 hrs. Whilst this second method has a greater chance that cells will fall from the top surface and seed on the surrounding well, the method is less susceptible to effects of evaporation and inconsistent seeding densities. To account for the cells which seed on the well-plate instead of the metallic substrate, the metallic substrates are moved after 4 hrs of seeding, to a fresh well-plate, and once again covered with 300 µL of basal media.

Figure 6-4(c) and (d) show fluorescent microscopy of the plate surfaces, with the cell nuclei stained with Hoechst. Method two achieved a better dispersity of a higher number of living cells on the plate surface, Figure 6-4(d). Method two may also result in cells attaching to the side of the plates however all plates were cut to the same height to ensure the side surface area would remain constant between samples. It was concluded that method two was the superior method for cell seeding, however cell seeding density required optimisation, to assess the percent of cells which attached to the plate surface, compared to those which attached to the well. In addition, the incubation time for attachment was investigated, to ensure the hBMSCs could attach within the 4 hr time point used previously.

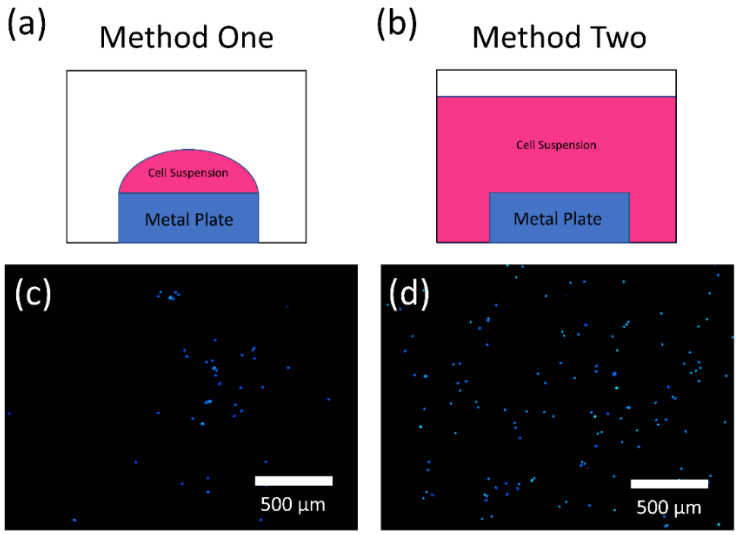

Figure 6-4: Cell seeding methods. (a) Method one resulted in clumped cell dispersion and fewer attached cells, shown in (c), than (b) method two, where the cells were more well dispersed (d).

The seeding time and density were assessed to ensure the best attachment and dispersion of cells. hBMSCs cells were seeded using seeding method two onto pure Ti substrates, at densities from 5 - 50 $\times 10^2$ cells/cm^2 and left to incubate for 2 hrs, 4 hrs and 24 hrs before an MTS assay was performed, Table 6-1. In addition, a control plate was prepared by seeding cell densities of 2.5 – 200 $\times 10^2$ cells/cm^2 directly into the well-plate and performing an MTS assay after 24 hrs, to gauge the relationship between absorbance and cell density.

Table 6-1: Seeding densities investigated.

Control Plate		**Metallic Substrate**	
Density (cells/cm^2)	**Comment**	**Density (cells/cm^2)**	**Comment**
2.5×10^2	Not detected by MTS assay	5×10^2	Not detected by MTS assay at 2 hr, 4 hr or 24 hr timepoints
5×10^2	Not detected by MTS assay	10×10^2	Not detected by MTS assay at 2 hr, 4 hr or 24 hr timepoints
10×10^2	Not detected by MTS assay	20×10^2	Detected by MTS at 4 hr and 24 hr timepoints
20×10^2	Good MTS assay reading range	50×10^2	Detected by MTS at 4 hr and 24 hr timepoints
50×10^2	Good MTS assay reading range		
100×10^2	Good MTS assay reading range		
150×10^2	Saturated MTS assay		
200×10^2	Saturated MTS assay		

The absorbance readings showed no statistical difference between all seeding densities at 2 hrs and no significant increase compared to the blank control, suggesting the 2 hr time point was not sufficient for cell attachment, Figure 6-5(a). At the 4 hr time point, no significant difference could be seen for the 5 and 10 × 10^2 cells/cm^2 densities, however an increase in absorbance was noted for the 20 and 50 × 10^2 cells/cm^2 densities. At the 24 hr time point, there were not any further significant changes in absorbance at any of the seeding densities, suggesting 4 hrs of attachment was sufficient for cell attachment and that cell densities of 5 and 10 × 10^2 cells/cm^2 are unlikely to be detected by the MTS assay. This was confirmed by the control curve, Figure 6-5(b), which showed only a minor increase in absorbance between the 2.5 – 10 × 10^2 cells/cm^2 seeding densities. The control curve also showed that, to achieve the most defined results from the MTS assay, densities between 2.5 – 100 × 10^2 cm^2 of cells remaining attached to the metallic substrates was optimal. The control curve suggests that 1/5 of the applied cell density remains attached to the metallic substrates.

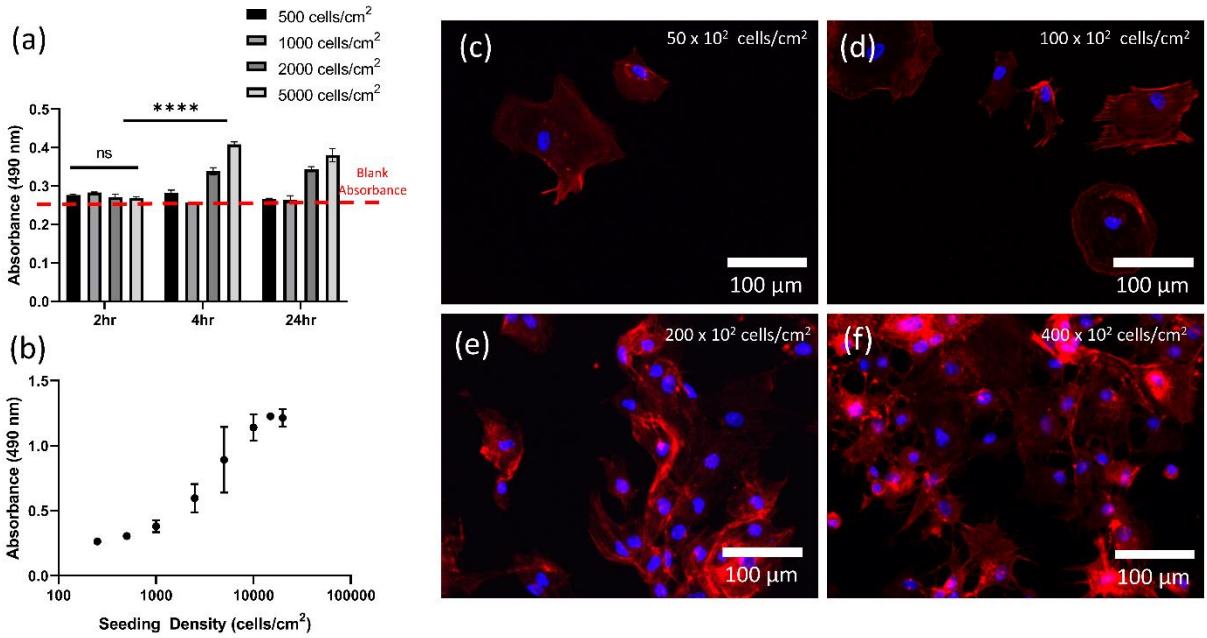

Figure 6-5: Optimisation of seeding time and density. (a) MTS absorbance (490 nm) of cells incubated for 2hrs, 4 hrs and 24 hrs. (b) Control curve of hBMSCs used in the seeding time experiment. (c-f) Cell morphology analysed by cytoskeleton and nuclear staining for (c) 50 × 10^2, (d) 100 × 10^2, (e) 200 × 10^2 and (f) 400 × 10^2 cells/cm^2 seeding densities.

hBMSCs were then seeded using 4 hrs of incubation for attachment, at densities of 50 × 10^2, 100 × 10^2, 200 × 10^2 and 400 × 10^2 cells/cm^2 and imaged to assess the cell spread area and cell interaction at these densities. Fluorescent imaging of the actin cytoskeleton and nuclei indicated that a density of 100 × 10^2 cells/cm^2 (Figure 6-5(d)) was optimal for morphology analysis as cells were not touching, which can artificially constrain the cell morphology, and makes cells hard to distinguish from one another for image analysis. In addition, a density of 400 × 10^2 cells/cm^2 (Figure 6-5(f)) was chosen for the future osteogenic assays as a high cell volume is required to detect changes in concentration of the low

abundance osteogenic markers. Despite the higher cell density, the cells still showed spreading behaviour and large cellular area, which is critical for osteogenic differentiation. Published osteogenic differentiation protocols generally use between 50 - 100 $\times 10^2$ [404-406] and hence the 1/5 attachment of the 400 $\times 10^2$ cells/cm^2 seeding density (80 $\times 10^2$ cells/cm^2) provides a promising attachment number for osteogenic studies.

In conclusion, a new seeding protocol was required to increase the homogeneity of cell seeding on the metallic substrates. Attachment time and density experimentation confirmed that a 4 hr attachment time was sufficient for hBMSC attachment and densities of 100 $\times 10^2$ cells/cm^2 and 400 $\times 10^2$ cells/cm^2 were suitable for morphology analysis and osteogenic assays, respectively.

6.3 hBMSC Determined Osteogenic Potential of L-PBF TiTa Alloys

TiTa alloys promise the benefit of improved osteogenic behaviour due to their Ta component, however, osteogenic testing of these alloys has not yet been conducted. It is yet unknown whether TiTa alloys show an improved osteogenic response compared to the commonly used Ti-6Al-4V alloy, or which compositions of TiTa alloy induce a beneficial osteogenic response. There is no existing standard for testing the effects of alloy composition on bone remodelling and osteogenesis *in vitro*, however, most studies make use of the differentiation capacity of mesenchymal stromal cells (MSCs) [309, 310, 318, 319, 407, 408]. This is because, *in vivo*¸ hBMSCs are largely responsible for bone repair and remodelling, contributing to implant success through surface colonisation and direct differentiation into osteogenic and chondrogenic lineages, as well as enhancing generalised wound healing. A positive MSC response *in vivo* is crucial to implant success. *In vitro*, MSCs maintain their ability to differentiate into bone, cartilage and fat and are highly mechanosensitive, responding to material stiffness, topography and chemical composition, by producing quantifiable markers. MSCs are also primary cells and in this study were of human origin, which strongly recapitulate an *in vivo* implant response, holding significant advantages over the use of non-human or immortalised cells (such as L929 and MG63) which lack comparable osteogenic differentiation trajectories and are significantly less predictive of an *in vivo* or clinical response.

Osteogenic differentiation of MSCs can be determined by the activity of osteogenic markers, such as alkaline phosphatase (ALP), and by cell morphology [280, 293, 296]. However, MSC behaviour is notoriously heterogeneous between donors and dependent upon the tissue type that the cells are isolated from [409]. To account for this heterogeneity, when undertaking experimental work it is important to use MSCs isolated from a single tissue type, such as human bone marrow (hBMSC), as well as to repeat experiments across a variety of MSC donors.

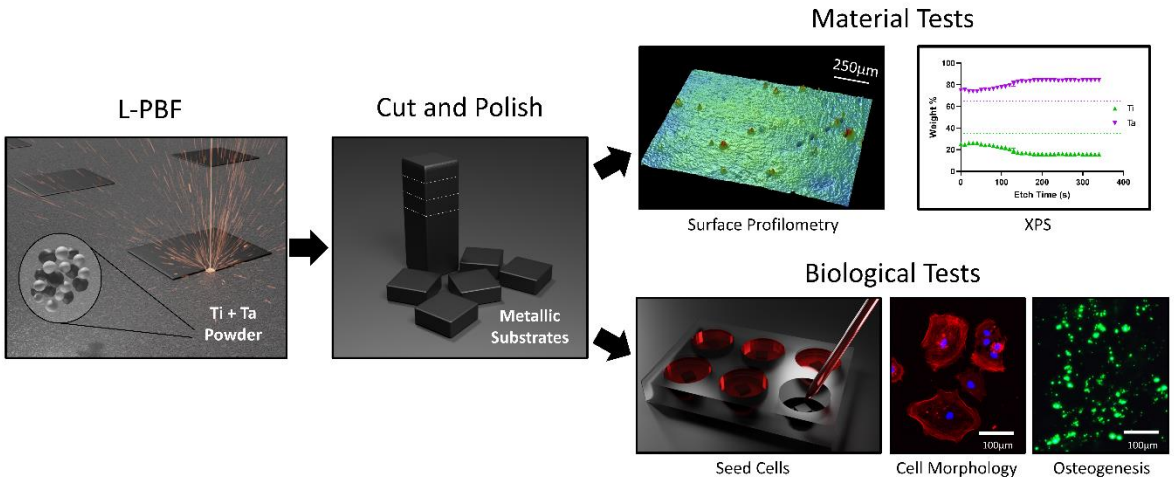

Figure 6-6: Experimental schematic. TiTa alloys were produced by L-PBF, cut into plates and polished. The plates were then assessed for topography, surface chemistry and wettability before being seeded with hBMSCs and attachment, proliferation and osteogenesis measured.

In the following study, the L-PBF compositions of Ti25Ta and Ti65Ta were compared with L-PBF Ti-6Al-4V plates using material characterisation and biological response testing (Figure 6-6). The Ti25Ta and Ti65Ta metallic substrates were produced by L-PBF, using the single scan process parameters determined in Section 3.4. The parameters for the Ti-6Al-4V control material were the optimal parameters for this material determined by ConceptLaser. Material was printed in the form of 5 mm (x) × 5 mm (y) × 15 mm (z) rectangular prisms, which were then cut into 3 mm thick plates (Figure 6-6). These plates were then prepared for biological testing by grinding and polishing with 0.4 µm OPS-silicon solution, in order to minimise confounding effects of surface topographies on cell fate and behaviour. The plate surfaces were analysed physically through contact angle testing and surface profilometry, as well as chemically with X-ray Photoelectron Spectroscopy (XPS) and electron dispersive X-ray (EDX) imaging to physically and chemically characterise the plate surfaces.

In vitro biological testing was conducted using the seeding protocol and morphology descriptors determined in Section 6.2. Each alloy was assessed for cell attachment and proliferation, using an MTS assay, supported by nuclear staining and counting. Cell morphology was assessed at 4 hr and 3 day timepoints, through cytoskeletal and nuclear staining and imaging. Finally, osteogenic potential of the alloys was determined through early and late osteogenic markers of alkaline phosphatase (ALP) and mineral formation, after 1 week and 4 weeks of culture, respectively. The experiments were conducted in triplicate and repeated with hBMSCs from five different donors to account for donor heterogeneity. The analysis from a representative donor is shown in the following figures, whilst the data for the other donors is included in the appendices.

6.3.1 Physical and Chemical Characterisation of Metallic Substrate Surface

Characterisation of the surface of the polished metallic substrates was conducted to investigate their topographical and chemical features. Increased wettability has been used to explain the enhanced spreading of cells on Ta surfaces compared with Ti [315, 319, 324] and hence, the contact angle of water droplets on each of the prepared plates was measured. Deionised water was dropped on the surface of each plate from 5 cm using an OCA21 optical contact angle measuring apparatus (DataPhysics Corporation, Germany). The contact angle was measured on five separate plates of each composition.

The contact angle on the Ti-6Al-4V plate was 73 ± 0.6 °, significantly higher than the contact angle on the Ti25Ta (67.0 ± 2.2 °) and Ti65Ta (63.9 ± 2.0 °) (Figure 6-7). As the Ta content increases, the contact angle decreases, indicating increased wettability. This finding agrees with previous studies [315, 319, 324] which highlight the improved hydrophilicity of Ta surfaces and link this to enhanced cell spreading. However, Lu et al. [300] found an equal contact angle between Ti and Ta surfaces, followed by equal cell attachment, spreading and proliferation, but still an increased osteogenic behaviour. Lu et al. [300] was also the only study to support their findings with surface topography analysis, showing no significant difference in surface topography between the prepared Ti and Ta surfaces. Surface topography has been shown to significantly alter contact angle by altering surface energy [410-412]. It is likely that the surface energy of Ti and Ta surfaces differs with their manufacturing and preparation techniques, which alters the thickness and crystal structure of the oxide layer. Hence, simply the presence of Ta on its own, or in an alloy, is not sufficient to enhance cell spreading on the surface. It does however seem to contribute in the current study.

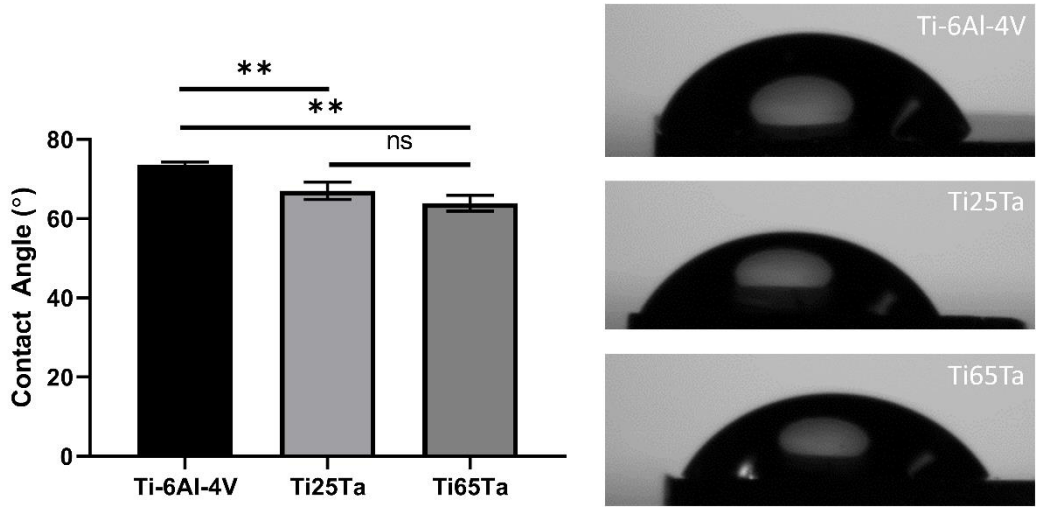

Figure 6-7: Contact angles measured on metallic substrates. The bar graph represents the average and standard deviation, n = 5.

In order to discount topographical effects of the post-polished surfaces of the L-PBF metallic substrates on contact angle or cell fate, surface profilometry was conducted using a Wyko NT1100 optical profilometer (Veeco). Vertical Scanning Interferometry (VSI) mode was used over an area of approximately 1 mm^2 to determine the average surface roughness (R_a) and average peak to trough height (R_z) of each alloy surface. Five separate regions were scanned on each sample and each region is represented by a single data point in Figure 6-8(a) and (b). A surface map of each surface is provided in Figure 6-8(c).

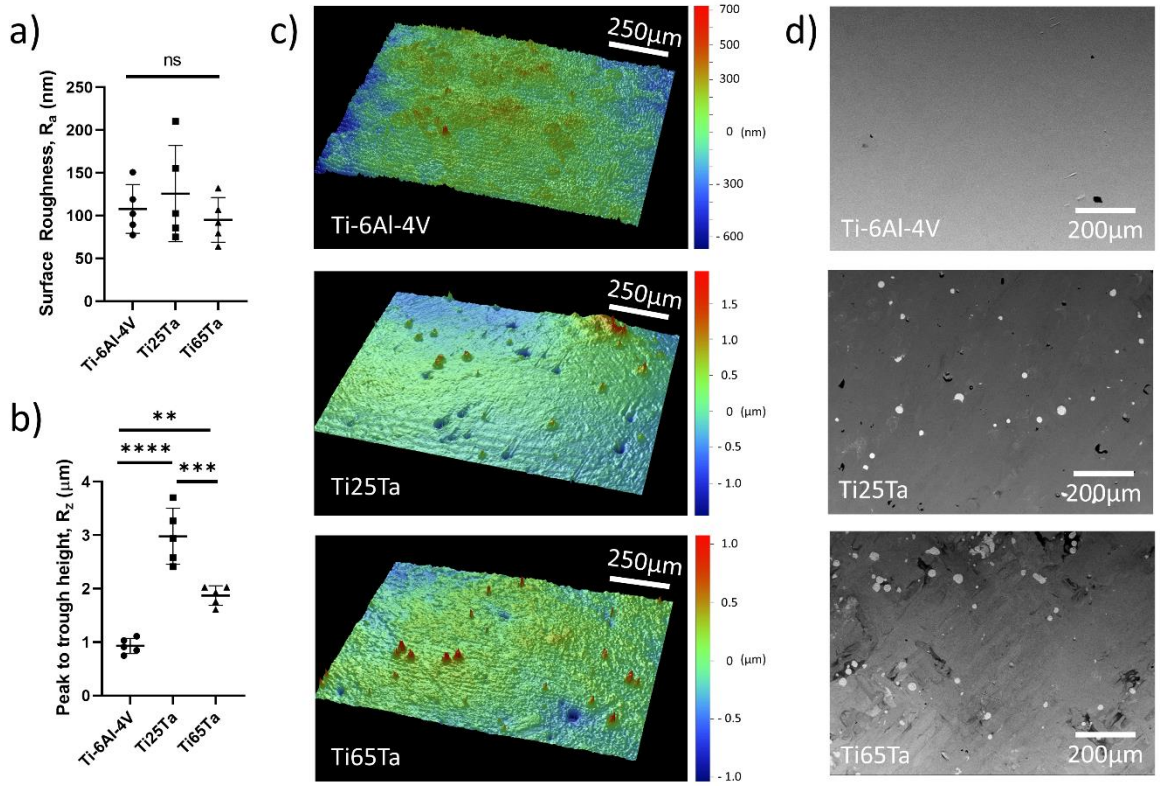

Figure 6-8: Surface topography of metallic substrates. (a) Surface roughness (R_a) and (b) peak to trough height (R_z). Graphs display individual measurements taken from different regions of each plate, with bars representing mean ± SD, n = 5. (c) Surface profilometry maps and (d) back scattered images of metallic substrate surfaces.

It was hypothesised that rigorous polishing to a mirror-finish would remove all topographical features from the metallic substrates and hence only alloy chemistry would affect cell fate. The average surface roughness of all the metallic substrates, Figure 6-8(a), was approximately 110 ± 37 nm with no significant difference between samples. However, the surface maps, Figure 6-8(c), show small protrusions of 3.0 ± 0.5 µm and 1.9 ± 0.2 µm on the Ti25Ta and Ti65Ta substrates, respectively. These protrusions are also accounted for in the peak to trough height measurement, which showed a significantly higher value in the Ti25Ta and Ti65Ta substrates, compared with the Ti-6Al-4V control, Figure 6-8(b). Back scattered imaging, Figure 6-8(d), and EDX analysis confirmed that these protrusions were remaining partially melted Ta particles. The particles are likely uncovered through

preferential polishing of the softer TiTa matrix, and protrude further on the Ti25Ta alloy, as compared with the Ti65Ta alloy, due to the lower Ta content and hence lower hardness of the Ti25Ta matrix.

Over the area investigated, the particles make no significant difference to the average roughness measure, however cells have been shown to detect and response to micron scale topographies [295, 413]. Roughness on the micron scale, can mimic natural bone features, such as bone resorption pits, and enhance cell proliferation and differentiation [414]. Bone resorption pits are generally up to 100 µm in diameter and 50 µm in depth, much larger than the features noted here. Surface roughness, in the form of 1 – 3 µm protrusions has been shown across multiple studies to enhance the production of osteogenic markers, such as ALP, osteocalcin (OC) and osteopontin (OP) [415-420]. In addition, it was shown that conversely, smoother samples enhanced cell attachment and proliferation. However, for these studies, the 1 – 3 µm surface roughness covered the entire sample, creating an entirely textured surface, as opposed to a surface with randomly dispersed protrusions. The protrusions are approximately 10 µm in diameter and hence cover less than 1% of the sample surface, agreeing with the area fraction of remaining Ta particles calculated through image analysis in Section 3.4. One in forty hBMSCs, with an average spread area of 2,500 μm^2, will likely encounter one of these particles when spread and hence the protrusions are unlikely contributing to cell fate.

The protrusions are also unlikely contributing significantly to the difference observed in material wetting, due to their rarity on the surface. The 10 µL water drop covered almost the entire surface of the plate, resulting in much more contact between the particles and droplet, however, the area of contact is still only 1%. The relationship between surface roughness and contact angle is not linear, as both surface roughness and chemistry contribute to wetting [421]. In an attempt to increase the wetting of Ta surfaces, oxide passivation in HNO_3 solution and activation through UV/ozone treatment were explored by Mas-Moruno et al. [282]. Results showed a nm scale increase in surface roughness for both treatments, but this resulted in no change in wetting for the HNO_3 sample, but a large increase in wetting on the UV/ozone treated sample, attributed to an increase of oxygen content in the metal oxide.

Hence, to ascertain the chemical composition of the surface of the metallic substrates, both EDX and XPS analysis were used. EDX has a depth of analysis of approximately 1 – 2 µm, much deeper than the penetration of the oxide layer, which is 4 – 6 nm for polished and room temperature oxidised TiTa surfaces [422]. Hence, EDX was used to investigate the chemistry of the top 1 – 2 µm surface layer, whilst XPS analysis was used to analyse the oxide layer.

EDX area scans of approximately 1 mm^2 showed that the concentration of Ta in the surface layer of the TiTa alloys is slightly higher than the intended nominal alloy compositions (Table 6-2). The Ti25Ta and Ti65Ta alloys showed surface Ta concentrations of 35 ± 0.2 wt.% and 68 ± 0.2 wt.%, respectively. To confirm that this difference was not due a powder mixing composition error, spectroscopic chemical analysis of each material showed a Ta content within 1% of the nominal compositions. Hence, it is

possible that Ta surface enrichment is occurring. Surface Ta enrichment of TiTa alloys is hypothesised as a result of lattice strain and preferential polishing [422, 423]. Due to the high cooling rates of L-PBF, residual strains are common, possibly enhancing surface enrichment caused by lattice strain. In addition, Ta surface enrichment may be a result of the polishing process. As noted in the surface profilometry, the remaining partially melted Ta particles showed a higher hardness than the surrounding TiTa matrix and hence were less likely to be ground away during polishing. This reduction in surface, at the expense of the Ti component, likely also contributes to surface Ta enrichment.

Table 6-2: EDX measurements showing surface composition of metallic substrates.

	Ti (wt.%)	**Ta (wt.%)**	**Al (wt.%)**	**V (wt.%)**
Ti-6Al-4V	90 ± 0.2 (87 at.%)	-	6 ± 0.2 (10 at.%)	4 ± 0.2 (3 at.%)
Ti25Ta	65 ± 0.2 (88 at.%)	35 ± 0.2 (12 at.%)	-	-
Ti65Ta	32 ± 0.2 (64 at.%)	68 ± 0.2 (36 at.%)	-	-

During cell colonisation of a material surface, the cells only ever contact the very upper layer of the metallic substrate, which is the oxide layer. Whilst the surface 1 - 2 µm surface composition likely affects the oxide composition, a finer analysis method is required to assess the oxide layer. Hence, XPS analysis was used to investigate the chemistry of the oxide layer of each metallic substrate, over a 400 × 400 µm area. A ThermoScientific Nexsa X-ray Photoelectron Spectrometer was used, with a monochromated Al Kα source (1486.68 eV, 6 mA, 12 kV). Survey and high-resolution scans were obtained with window widths of 1350 eV and 18 – 27 eV using pass energies of 150 eV and 50 eV, respectively. Depth profiles were also conducted using Ar^+ etching at 500 eV to investigate the oxide depth and oxide elemental consistency. High resolution scans were conducted after every 10 s of etching, for a total of 320 seconds. Data was analysed using CasaXPS Version 2.3.18. Further XPS conditions, such as calibration, and software fitting parameters are included in Appendix A4.

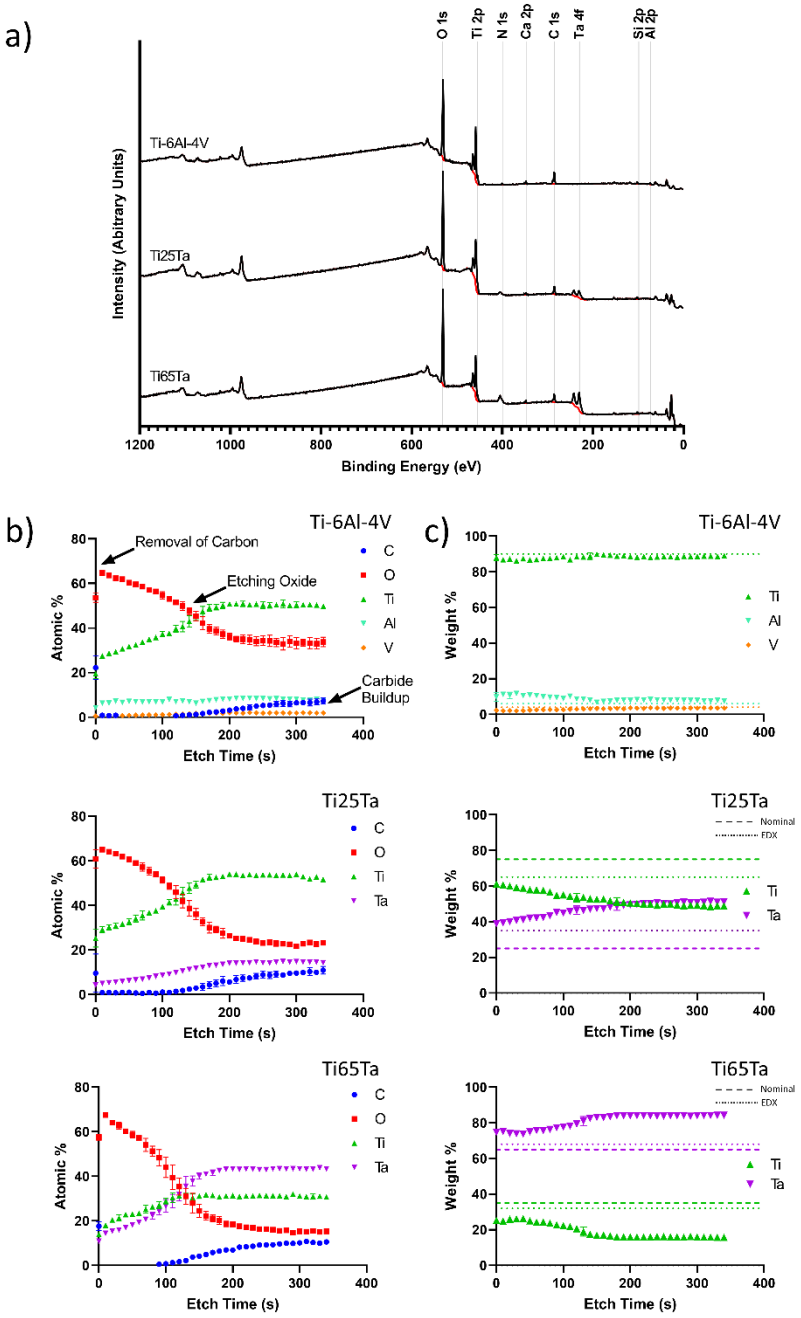

Figure 6-9: XPS surface analysis of metallic substrates. (a) Survey scan showing major metallic element peaks for each alloy, along with oxygen and surface contaminant peaks (e.g. Si and C). (b) Depth profiles showing the atomic % of the major elements for each alloy (n=2). (c) Corresponding depth profiles in weight % of only the metallic elements.

The survey scans showed peaks for the major alloy constituents of Ti, Ta in the TiTa alloys, as well as Al for the Ti-6Al-4V, Figure 6-9(a). Strong oxide peaks were noted on each sample, as well as peaks showing adventitious carbon and very small amounts of nitrogen, calcium and silicon, in the form of silica (due to indicative shift to higher binding energy (103.8 eV)). During depth profiling, an initial removal of the adventitious C layer was noted, followed by a slow etch through the oxide layer until an oxygen content plateau was achieved, Figure 6-9(b). The etch time required for the oxygen level to

plateau was 133s, 125s and 107s for Ti64, Ti25Ta and Ti65Ta, respectively. This indicated that either the oxide layer was thinnest for the Ti65Ta alloy, or that the Ti65Ta was most susceptible to etching. The former hypothesis is more likely, as the increasing hardness of the TiTa alloys with increasing Ta content was confirmed through preferential polishing of the Ti25Ta matrix, leaving larger Ta particle protrusions. Mendis et al. [422] observed a decrease in oxide layer thickness from 6.0 – 5.3 nm with increasing Ta content from 10 – 75 wt.%, and hence it is likely the Ti65Ta oxide layer is thinner than that of the Ti25Ta alloy. CP Ti showed an oxide thickness of 6.6 nm, likely closest to the thickness of the Ti-6Al-4V oxide, which shows the lowest atomic % of additives. Whilst the oxide thickness likely has no effect on cell behaviour, it is important in understanding the possible oxide formation and structure.

The depth profiles, including only the metallic elements, Figure 6-9(c), showed a higher level of Ta in the oxide than in the surface composition measured by EDX (dotted line). The Ti25Ta and Ti65Ta substrates showed oxide concentrations of 39 wt.% and 75 wt.% Ta, respectively, which converted to a 10 – 11 % Ta increase in the oxide, compared with the surface. Figure 6-9(c) also shows the Ta concentration increasing with etching time, supporting the previous hypothesis of preferential Ti etching. Single spot analyses were used to confirm the depth profile determined oxide compositions (Table 6-3). Each oxide showed a similar atomic percentage of oxygen and the Ti25Ta and Ti65Ta compositions showed atomic Ta contents of 8.0 ± 1.2 at.% and 16.5 ± 2.4 at.%, respectively. Hence, an increased oxygen content of the oxide is not responsible for the increased wetting, as seen in [282]. The increased Ta content is much more likely the cause.

Table 6-3: Elemental composition of the oxide layer determined by spot analyses (n=5).

	Relative Concentration (at. %)				
	Al 2p	**O 1s**	**Ta 4d**	**Ti 2p**	**V 2p**
Ti-6Al-4V	10 ± 2.4	56.4 ± 2.6	-	32.8 ± 2.8	0.8 ± 0.4
Ti25Ta	-	57.0 ± 4.2	8.0 ± 1.2	35.0 ± 3.8	-
Ti65Ta	-	54.7 ± 3.3	16.5 ± 2.4	28.7 ± 3.0	-

A 2.1-fold increase in Ta content, from 8.0 - 16.5 at.% is seen in the oxides of Ti25Ta compared with Ti65Ta. However, a 3-fold increase in Ta content was observed in the surface layer through EDX analysis (12 at.% - 36 at.%). This highlights that the relationship between Ta content in the surface is not linear with the Ta content in the oxide. The summary table (Table 6-4) highlights that the fold increase in the Ta content in the nominal compositions from to Ti25Ta and Ti65Ta, is reduced at the surface of the alloy and further reduced in the oxide layer. Hence, changing the nominal composition from Ti25Ta to Ti65Ta unlikely has a linear effect on the biological response to the alloy surface and

the extra Ta in the Ti65Ta alloy, may not provide as large an improvement in osteogenic capabilities as first thought.

Table 6-4: Summary of at.% Ta content from different measuring techniques, with corresponding different penetration depths.

	Ti25Ta (Ta at.%)	**Ti65Ta (Ta at.%)**	**Fold Increase**
Nominal composition	8.1	33.0	4.1
EDX surface composition (< 2 µm)	12.0	36.0	3
XPS oxide composition (< 10 nm)	8.0 (18.6[†††])	16.5 (36.5[††])	2.1 (2[††])

In conclusion, the prepared metallic substrates showed a similar average roughness, with the TiTa compositions showing small 1 – 3 µm protrusions, indicative of the remaining partially melted Ta particles in the matrix. However, as these particles only cover 1 % of the plate surface, their contribution to altering cell fate is negligible. The chemical analysis of each composition showed a higher Ta concentration in the surface of each of the TiTa alloys, than the nominal composition intended. The increase of Ta in the oxide, however, showed a non-linear relationship to the Ta nominal composition, suggesting the Ti65Ta may not show as high osteogenic response as expected, when compared with the Ti25Ta composition.

6.3.2 hBMSC Attachment and Proliferation

Cell attachment to and proliferation on implant surfaces is critical for implant integration. To assess hBMSC attachment to and proliferation on the metallic substrates, cells were seeded at 10,000 cells/cm^2 using seeding method 2, Section 6.2. Attachment and proliferation of cells was measured at 4 hr, 3 day and 7 day timepoints using an MTS assay (Cell Titre 96 Aqueous One Solution Cell Proliferation Assay, Promega) and fluorescent imagine. At each timepoint, the metallic substrates supporting hBMSC cultures were moved from culture conditions to a clean well plate and incubated in MTS working solution (1:5 dilution of MTS reagent in culture media) for 3 hrs at 37 °C. 100 µL of the incubated solution was then transferred to a 96 well tissue culture plate and the optical absorbance measured, at 490 nm (Thermo Scientific Multiskan Spectrophotometer). To verify the MTS readings, each sample was fixed by incubating cultures in 4% paraformaldehyde (PFA) (15 mins, room temperature), permeabilised using 0.1% Triton-X-100 (10 mins, room temperature), blocking with 3% bovine serum albumin (BSA) (1 hr, room temperature) and staining with ActinRedTM 555 ReadyProbes© Reagent

[†††] Atomic % Ta, excluding oxygen from analysis

(Molecular ProbesTM) (red) to highlight the F-actin cytoskeleton and Hoechst 33342 (blue) to highlight the nuclei (1 hr, room temperature). Fluorescent images were taken using an inverted microscope (Nikon Eclipse Ti) and ImageJ software was used to count nuclei. Five images were taken at low magnification, covering the entire surface area of the sample. The counted nuclei data is supplied in Appendix Figure 8-7.

hBMSCs attached equally to each alloy, Figure 6-10(a), with no statistical difference noted between the alloys using both the MTS assay and nuclear counting. The proliferation, normalised to the MTS reading at 4 hrs, Figure 6-10(b), showed an increase in cell number over 3 and 7 days for all alloys. Across the donors, no recurring significant difference in proliferation rate or final cell number was noted for any alloy. Nuclear imaging, Figure 6-10(c), confirmed successful cell attachment to and proliferation on all alloys. The equal hBMSCs attachment to and proliferation on all alloys suggest that the TiTa compositions will act similarly to the currently used Ti-6Al-4V for encouraging surface colonisation of cells after implantation.

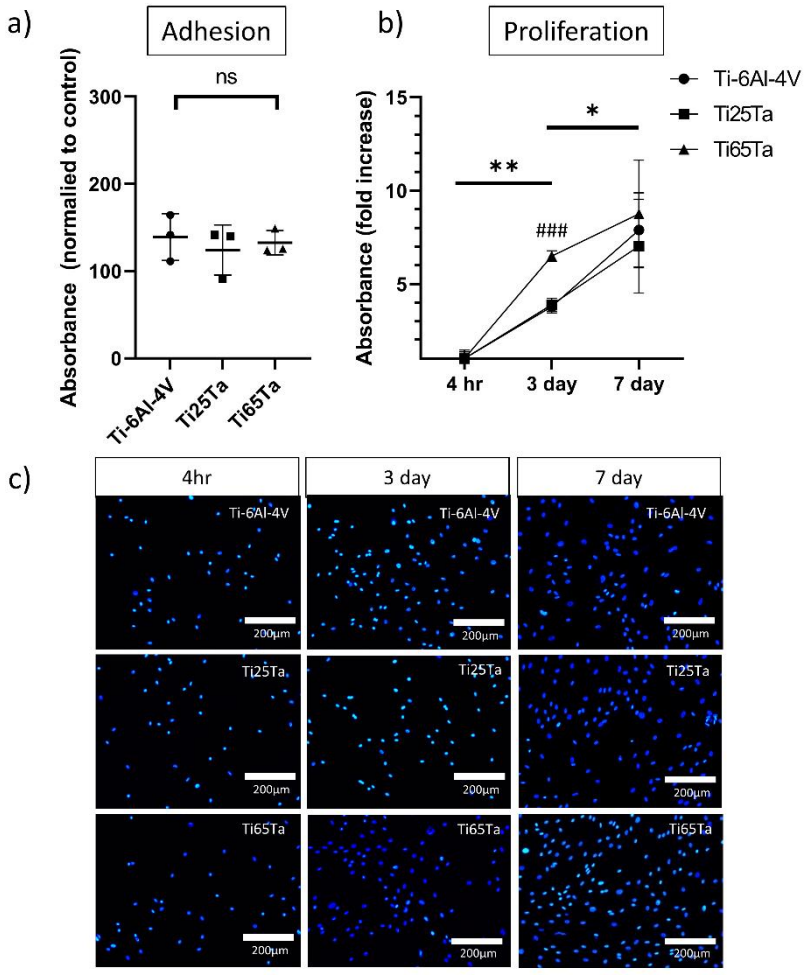

Figure 6-10: Adhesion to and proliferation of hBMSCs on metallic substrates. MTS assay used to assess; (a) number of cells attached after 4 hrs, each data point representing the MTS reading relative to the glass control for each individual sample within the triplicate and (b) proliferation of cells at 4 hr, 3 day and 7 day timepoints, each data point representing the average of MTS readings of each triplicate set. Bars represent mean ± SD. (c) Fluorescent microscopy of nuclei attached at 4 hr, 3 day and 7 day timepoints.

Literature studies which investigated attachment differences between Ti and Ta surfaces, using MSCs, are contradictory, with many claiming an increased attachment to Ta surfaces [310, 311, 319], while others claim equal attachment [309, 312, 318]. Similarly, studies investigating proliferation using MSCs are split between those that show Ta increases proliferation [310, 312] and those that show Ta shows equal proliferation to Ti [300, 309]. However, all the studies which show improved attachment and/or proliferation of MSCs to Ta surfaces investigated 3D structures, such as lattices or micropatterned surfaces. Hence, enhanced attachment to Ta surfaces may occur when the overall surface area of the structure is greater, emphasising the increased interaction between Ta and cells.

Furthermore, studies have shown that an increase in surface roughness on the micron scale decreases cell attachment and proliferation [415]. Despite the 1 – 3µm Ta protrusions noted on the TiTa alloys, no increase in cell attachment or proliferation was observed. This supports the hypothesis that the protrusions seen in Section 6.3.1 are not covering a large enough surface area to affect cell behaviour and hence, topographical cues cause negligible difference in cell behaviour on the TiTa and Ti-6Al-4V substrates.

In conclusion, hBMSCs attach to and proliferate equally well on all alloys, indicating no direct cytotoxic effects of the TiTa composition and an equal *in vivo* potential when compared to the standard material Ti-6Al-4V. As there was no increase seen in cell attachment to or proliferation on the Ta containing alloys, any observed changes in osteogenic potential between the TiTa and Ti-6Al-4V are likely caused by an increased osteogenic differentiation of cells, as opposed to enhanced surface colonisation.

6.3.3 hBMSC Morphology

Cell morphology of hBMSCs cultured on the metallic substrates was analysed after 4 hrs and 3 days using the fluorescently stained cultures prepared in Section 6.3.2.The 4 hr time point was used to capture the cells at a very early stage of attachment, whilst the 3 day timepoint captured cell morphology once the cells were established on the surface and had reached a steady state conformation.

At 4 hrs the cells were trapezoidal in shape, with actin filaments concentrated at the boundary of the cell, Figure 6-11(e). Lamellipodia were observed, indicating that the cells were actively moving and spreading. No significant increase in cell spread area on any one composition was noted consistently across all five donors (Appendix Figure 8-9), though the cells in Figure 6-11(a) showed a higher cell area on the Ti65Ta alloy. A higher circularity index was observed across the five donors on the TiTa alloys across at the 4 hr timepoint, Figure 6-11(b). This is in contrast to earlier experiments using the MG63 cells, which exhibited a lower circularity index on the high content Ta alloys (Section 6.1). According to literature, larger area but less regular cell shapes are more likely to undergo osteogenesis [295, 296, 424]. Hence the high circularity index suggests the TiTa alloys may show reduced osteogenic

potential compared with the Ti-6Al-4V alloy. However, higher cell circularity at the early 4 hr time point may also indicate slower adhesion and be a reflection that the cell has not reached its final spread state.

At 3 days, the cells on all alloys had reached a steady state conformation, with established actin fibres crossing the entire length of the cell. Additionally, cells on the TiTa alloys were spread over a significantly larger area than those on the Ti-6Al-4V alloy, Figure 6-11(c). The increased area of cell-substrate interface presumably leads to an increase in focal adhesions and integrin binding sites, which are known to be important drivers for osteogenic differentiation [295, 300, 411]. At day 3, fully spread hBMSCs showed no significant differences in circularity, Figure 6-11(d). The larger cell area of hBMSCs cultured on TiTa alloys may help to enhance osteogenic differentiation through modulation of a range of cellular mechanisms including cellular tension and integrin binding sites. Furthermore, the increase in cell area was conserved between the Ti25Ta and Ti65Ta compositions with significant differences noted across all fiver donors.

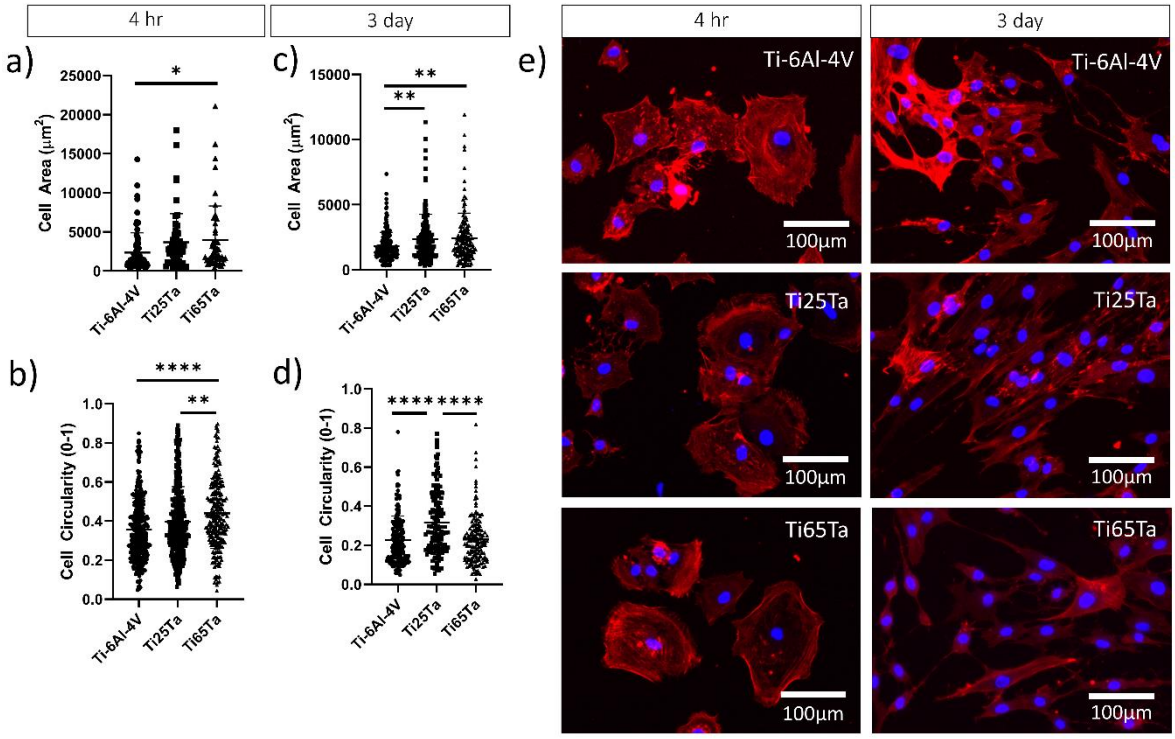

Figure 6-11: hBMSC morphology. (a) (c) Cell area and (b) (d) circularity measured at 4 hrs and 3 day timepoints. Each data point represents one cell, n > 100. (e) Cell morphology analysed by cytoskeletal and nuclear staining.

hBMSC morphology suggests that the cells have a stronger initial interaction with the TiTa alloys, resulting in a greater number of anchor points and higher spread area. Lu et al. [300] observed an increased ability to activate the α5β1/ERK1/2 signalling pathway on polished Ta surfaces compared with polished Ti surfaces, by measuring α5β1 integrin expression. This increased integrin expression

was coupled with increased osteogenic capability, however, no increase in cellular area was observed with the increased α5β1 integrin expression. In the study by Lu et al. [300], cells were cultured for 24 hrs before morphological analysis was conducted. Whilst this is longer than the 4 hr early stage timepoint used in the current study, it is possible that no difference in cell area is noted as the cells had not yet reached their fully spread and steady conformation. Early increased α5β1 expression however does suggest that osteogenic enhancement is occurring before tension can be developed in the cell due to spread morphology. Higher integrin expression causes more integrins to form into focal adhesions and more strongly activates osteogenic signalling cascades in the nucleus and cytoskeleton [425]. Increased integrin binding could be caused by differences in the amount and conformation of fibrinogen protein absorbed on the metal surface or by electronic interactions between the metal oxides and the binding functionality of the integrins. Further characterisation of the absorbed protein layer could be used to further elucidate the reason behind enhanced integrin binding, however is beyond the scope of this study.

In conclusion, the cellular morphology suggested that the cells observed at the 4 hr timepoint are not fully spread. A greater cellular area was observed on the TiTa alloys at day 3, a strong indicator for enhanced osteogenic potential. The TiTa surfaces may trigger higher integrin production and binding at early stages (~ 1 day) of attachment, however further investigation into signalling pathways is required to confirm this hypothesis.

6.3.4 hBMSC Osteogenic Assays

Osteogenic analysis of the substrates was undertaken using an ALP activity assay as a marker of early osteogenesis, and mineral formation as a late bone marker. Both basal and osteogenic media conditions were used for each assay. The osteogenic media consisted of basal media supplemented with 1% β-glycerophosphate, 0.1% ascorbic acid 2-phosphate and 0.01% dexamethasone. The ALP activity was measured after 1 week of cell culture with a colorimetric p-nitrophenol (pNP) assay (Sigma-Aldrich) and normalised to DNA content in each well, measured with a Picogreen dsDNA assay (Invitrogen). At 1 week, samples were washed with PBS and lysed with 0.1%-Trion X. The lysate was mechanically scraped from substrates and were subjected to three freeze-thaw cycles before the pNP agent was added. The ALP activity was measured by spectrophotometry, at 410 nm and calculated from a standard curve. Results are displayed as pNP (n mol), normalised to incubation time (min) and DNA (µg). Mineralisation was measured after 4 weeks of culture using OsteoImage (Lonza) fluorescent green stain. The plates were fixed with 4% PFA and stained before constant exposure images were taken, covering the plate surface. ImageJ was used to quantify the intensity of fluorescence in each image.

All alloys showed the ability to support hBMSC osteogenesis, however there was strong variation between efficiency of osteogenesis of separate donors. Similar trends were noted in the ALP activity and mineralisation measurements for three donors, with the magnitude of differences being greater for donors with a stronger osteogenic response.

The ALP activity was increased on the TiTa alloys compared with the Ti-6Al-4V substrate, Figure 6-12(a). ALP activity has been widely shown to increase on Ta surfaces compared with Ti surfaces [288, 300, 309, 310, 314, 316, 317], however never on the TiTa alloy system. High ALP activity is a promising sign for early commitment to the osteogenic pathway and hence may lead to improved implant integration. There was no statistical difference in ALP activity noted between the Ti25Ta and Ti65Ta alloys. Successful mineral formation was also observed on all alloys, Figure 6-12(c). However, when quantified through image analysis, a higher mineral fluorescence intensity was noted on the TiTa alloys, when compared with Ti-6Al-4V substrate, Figure 6-12(b). Again, there was no statistical difference in mineral fluorescence intensity between the Ti25Ta and Ti65Ta alloys.

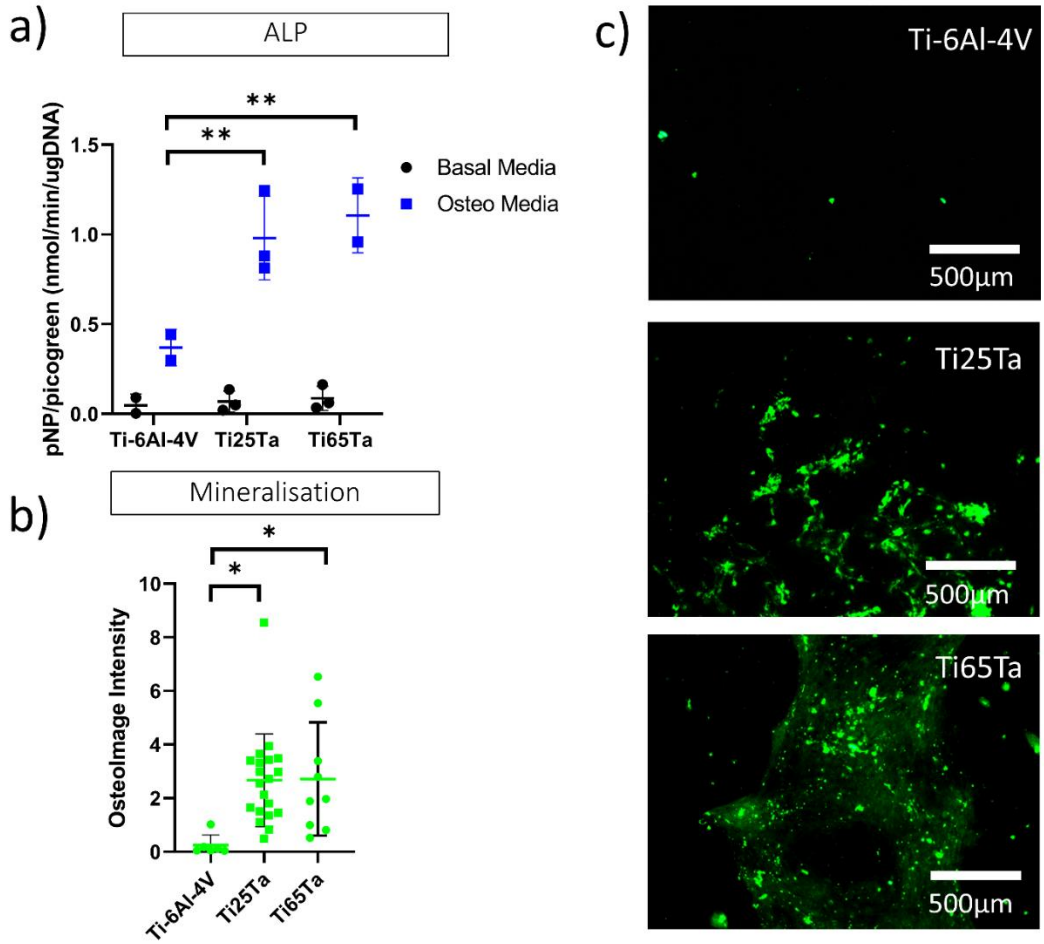

Figure 6-12: (a) ALP activity measured by pNP assay with each data point representing individual samples within triplicate. (b) Mineralisation measured using OsteoImage stain intensity using multiple readings (n > 5) for the viable plates within the triplicate. (c) Fluorescent images showing mineral formation.

The results suggest that increased ALP activity on the TiTa alloys in the first week has led to enhanced mineral formation at 4 weeks. In light of morphological results, this is likely due to enhanced adhesion and spreading on the TiTa alloys. The osteogenic behaviour of the Ti25Ta and Ti65Ta alloys are quite similar, likely due to the non-linear relationship between Ta oxide content and the nominal Ta composition. As the higher Ta content of the Ti65Ta alloy is not respectively expressed in the oxide composition, the cells in contact with the Ti65Ta material benefit less than initially expected from the increased Ta content, when compared with the Ti25Ta alloy.

6.4 Chapter 6 Summary

The L-PBF TiTa alloys were investigated in direct comparison with L-PBF Ti-6Al-4V to assess their cytotoxicity and osteogenic capability. The following conclusions can be drawn from Chapter 6:

- The TiTa alloys showed a measurable improvement of *in vitro* osteogenic response when compared with Ti-6Al-4V. Both early ALP production and late mineral formation are increased, likely linked to early strong interactions between cells and the TiTa substrates, characterised by increased binding. This likely lead to the higher cellular area measured at the 3 day timepoint.

- Both cell attachment and proliferation on the new TiTa alloys were shown to be equal to the standard Ti-6Al-4V material, suggesting cell colonisation of implant scaffolds will perform equally well to current Ti-6Al-4V implants.

- When the Ti25Ta and Ti65Ta alloys are directly compared, no significant difference in osteogenic behaviour is noted, likely linked to the non-linear relationship between nominal Ta content and oxide Ta content. Therefore, as the Ti25Ta alloy shows similar mechanical and osteogenic properties to the Ti65Ta alloy, the Ti25Ta alloy, with lower cost and density, is deemed most suitable for implant applications.

Chapter 7 Conclusions and Future Work

7.1 Conclusions

In this thesis, the additive manufacturing processing of the TiTa alloy system was explored, in order to improve the range of materials available for next generation bone implants. Additive manufacturing in both L-DED and L-PBF systems of mixed elemental titanium and tantalum powders was conducted and the material characterised for its microstructure, mechanical properties and biological response is reported.

Overall, this thesis provides a greater understanding of TiTa alloys and their manufacture for biomedical applications. It explored how different processing parameters and scanning strategies can be used to manufacture solid and homogeneous material from mixed powders containing components with starkly different melting characteristics. The designed remelt strategy was shown to be effective at improving the homogeneity of L-PBF material and provided a promising strategy for improving the quality of refractory materials produced by L-PBF. It is suggested that this strategy can also be adopted for processing of other refractory based alloys, such as refractory high-entropy alloys.

The link between the unique microstructures formed and the thermodynamic conditions produced by L-PBF has been explored. Epitaxial grain growth was avoided through compositional supercooling and partially melted particles contributing to heterogeneous nucleation. The Ti25Ta and Ti65Ta alloys demonstrated a similar strength to CP Ti while reducing the elastic modulus by half, promising a reduction to stress-shielding effects caused by elastic modulus mismatch between implant alloys and bone. Furthermore, the fatigue performance of the Ti25Ta and Ti65Ta alloys surpassed that of L-PBF Ti-6Al-4V, due to their enhanced ductility, which reduced notch sensitivity in the manufactured lattice structures. The small volume % of remaining refractory particles did not contribute to crack initiation. Process-induced defects consistently initiated failure. The encouraging mechanical properties of the alloys was coupled with positive *in vitro* biological results, which showed improved osteogenic behaviour of the TiTa alloys when compared with Ti-6Al-4V. Whilst this finding still must be confirmed *in vivo*, it is a promising sign for improved implant integration. Finally, the β phase of the Ti65Ta alloy led to a slightly slower crack propagation but no significant improvement in fatigue performance or osteogenic capability. Hence, the lower density and lower cost Ti25Ta alloy was concluded to be the most beneficial alloy for low stress bone implant applications.

Broadly, this thesis has provided a new alloy for additive manufacturing of bone implants and contributed to a greater understanding of the mechanisms behind its processing, mechanical performance and biological response. The Ti25Ta alloy has the potential to increase implant stability

and significantly reduce implant failures caused by stress-shielding and loss of bone mass around the implant.

The detailed contributions of this research are as follows.

7.1.1 Additive Manufacturing of Mixed Powder Ti25Ta and Ti65Ta

Additive manufacturing was shown to be an effective tool for both preliminary alloy screening and implant manufacture. Although the exact composition could not be precisely controlled in L-DED processing, a large range of alloys were successfully and rapidly manufactured, providing the opportunity to examine microstructure and biological response and quickly highlight or preclude particular alloy compositions from further study.

L-PBF processing of the Ti25Ta and Ti65Ta parameters confirmed that single scan tracks were a useful tool for determining the optimal processing window by analysing track stability and melt pool morphology. Furthermore, multi-layer single scan tracks provided an indication of material homogeneity, by analysing the remaining refractory particles within the layer overlap zones. Dense material (> 99.9%) was successfully formed in both the Ti25Ta and Ti65Ta compositions, however partially melted Ta particles remained in the matrix. A remelt scanning strategy was shown to be successful at reducing the area fraction of remaining Ta particles by allowing a second opportunity for melting and mixing. Modelling of the TiTa process parameters was improved by considering the normalised melting enthalpy of each composition. Variables of material absorptivity, melting temperature and thermal conductivity improved the model predictive capability, however it was still limited by the mixed powder nature of the compositions. A similar laser spot size and powder particle diameter led to a combination of vaporisation of the Ti and insufficient melting of the Ta, regardless of the calculated normalised enthalpy.

Overall, insight into the optimal laser scan speed for producing TiTa alloys through L-PBF was gained and a remelt scan strategy was developed as an effective homogenisation tool. The remelt strategy is recommended for increased homogenisation of other alloy systems with refractory components.

7.1.2 Microstructure and Mechanical Properties

Phase analysis of the alloy systems was conducted to give insight into their mechanical performance and highlighted the effect of the rapid cooling in L-PBF processing on microstructure formation. Initial XRD phase analysis of the L-PBF produced cubes showed a fully α structure in the Ti25Ta alloy and a fully β structure in the Ti65Ta alloy, despite equilibrium calculations suggesting each alloy should be

dual phase. The discrepancies in phases were attributed to the fast cooling rates of L-PBF and oxygen content. A minor increase of oxygen content was noted in the printed material, which was enhanced by the remelt scanning strategy. No oxygen increase was noted in the reused powder. Oxygen is a strong interstitial strengthening agent in titanium and hence the minor increases in oxygen were still considered relevant to mechanical analysis.

BSI analysis revealed inhomogeneity within the melt pools of the single melt material, in the form of swirling pattern, which disappeared with the application of the remelt scan. This hinted to the remelt scanning causing a change in microstructure. EBSD analysis of the Ti25Ta and Ti65Ta alloys revealed microstructures consisting of fine martensitic α′ laths and equiaxed β grains, respectively. The remelt scan caused slight grain refinement and randomisation of the α′ laths. Grain refinement was attributed to a shallower melt pool caused by the remelt scan. TEM analysis confirmed that the L-PBF Ti25Ta consisted of predominantly α′ hexagonal laths, as opposed to the α″ orthorhombic laths seen in literature. Remelt scanning facilitated the formation of the α″ phase in areas with high Ta content (over 50 wt.%), confirming that enhanced Ta diffusion in L-PBF Ti25Ta is required for the formation of the α″ phase.

The mechanical properties of the L-PBF material showed a promising low elastic modulus of 65 ± 5 GPa and 71 ± 5 GPa in the Ti25Ta and Ti65Ta single melt material, respectively. Both the Ti25Ta and Ti65Ta alloys displayed a similar tensile strength and ductility to CP Ti. The remelt strategy caused an increase in material strength coupled with a significant decrease in ductility, likely due to grain refinement and increased oxygen levels. The mechanical properties of the Ti65Ta alloy were more strongly affected by L-PBF processing due to enhanced β grain refinement. The Ti25Ta alloy showed a similar sized microstructure in conventional and L-PBF processing. Fractography of the tensile samples showed no spatial correlation between process-induced defects and remaining Ta particles. Hence, it was concluded that the Ta particles were not significantly contributing to specimen failure.

Overall, both the Ti25Ta and Ti65Ta alloys showed promising mechanical properties for bone implant applications, achieving low elastic moduli and similar strength to CP Ti. The L-PBF TiTa alloys are well suited for strength specific implant applications, such as mandible implants. Furthermore, the TiTa alloys did not suffer from a significant reduction in ductility, as often seen in L-PBF materials, and hence are more favourable than other biomedical alloys for additively manufactured bone implants.

7.1.3 Fatigue Performance

The L-PBF TiTa alloys were characterised under cyclic loading in both solid and lattice forms. The low-cycle fatigue results for solid material showed a higher stress response for equal strain in the Ti65Ta compared with the Ti25Ta alloy, caused by a higher elastic modulus. The elastic moduli, calculated

from the half-life hysteresis curves, were found to be higher than the values observed during ultrasonic modulus testing. It was hypothesised that this was due to wave scattering by remaining partially melted Ta particles.

Both the Ti25Ta and Ti65Ta alloys also performed well when compared to CP Ti, Ta and Ti-6Al-4V. When normalised by yield strength, the TiTa alloys performed second to only pure Ta, with the Ti25Ta composition displaying a third of the elastic modulus of pure Ta. For both alloys, the remelt scan caused a decrease in fatigue life, despite decreasing the number of remaining Ta particles and fractography analysis confirmed that the remaining Ta particles did not act as crack initiation sites. X-ray Micro-CT analysis confirmed a minor increase in porosity was coupled with the decrease in Ta particles for the Ti25Ta remelted material. However, as there was no observed increase in the number of large pores (> 60 μm in diameter), the effect of the increased porosity on fatigue life was likely negligible. The reduced fatigue life of the remelt material was instead attributed to reduced material ductility and increased residual stresses.

Tension and compression testing of FCCZ lattices showed a gradual strut-by-strut failure in tension in the Ti65Ta lattices compared with abrupt fracture of the Ti25Ta lattices, due to the different rates of crack propagation between the β and α′ microstructures. Both the Ti25Ta and Ti65Ta lattices showed superior tensile strength to identical FCCZ Ti-6Al-4V structures, which failed in their elastic region due to low ductility and high notch sensitivity. Fatigue testing of the lattices confirmed the superiority of the more ductile TiTa alloys, as both the Ti25Ta and Ti65Ta showed superior fatigue life to both as-built and even heat-treated Ti-6Al-4V.

DIC analysis indicated that failure initiated consistently at a corner of the lattice which faced the powder spreading blade and had acquired excessive adhered partially melted material. Strut size and lattice volume increases were observed when compared to the CAD file, particularly around the upper lattice-grip interface where the horizontal grip was not fully supported by the lattice struts during building. The geometric deviations from the CAD were concluded as the main contributors to the TiTa lattice failure, highlighted the need for further L-PBF lattice parameter optimisation. Analysis of the microstructure of the Ti65Ta lattice struts showed no decrease in grain size in the thin lattice struts or columnar grains, emphasizing that grain formation in the TiTa alloys is driven strongly by constitutional supercooling and nucleation on Ta particles, as opposed to thermal gradients.

Overall, the high ductility of the L-PBF TiTa alloys resulted in a superior fatigue performance to other common biomedical alloys produced by L-PBF. This effect is enhanced when the material is used in lattice form, as the high damage tolerance of the TiTa alloys avoids failure caused by the large rough surface area.

7.1.4 Biological Response

The biological response of the AM TiTa alloys was assessed for biocompatibility and osteogenic behaviour, in comparison to AM Ti-6Al-4V. Preliminary material from the L-DED processing confirmed a basic biocompatibility of the AM TiTa alloys. However, the viability assay recommended in ISO 10993 to confirm biocompatibility was found to lack an understanding of how cell attachment and proliferation separately effect material biocompatibility. Preliminary morphology experiments showed enhanced spreading and reduced circularity of cells on Ta containing surfaces, highlighted as indicative markers for enhanced osteogenic behaviour. A seeding protocol was developed for analysis of the osteogenic capability of metallic substrate plates which could be standardised for future alloy testing.

Metallic substrates were produced by L-PBF in Ti25Ta, Ti65Ta and Ti-6AL-4V and polished to remove topographical features, which could influence hBMSC cell fate. After polishing, the substrate surfaces revealed 1 – 3 µm protrusions on the TiTa alloys, corresponding to the remaining partially melted Ta particles. These protrusions were deemed too disperse to have a topographical effect on cell behaviour. Preferential polishing and lattice strain did, however, cause an enrichment in Ta at the surface and in the oxide of the TiTa alloys. The four-fold increase in at. % of Ta in the nominal compositions from Ti25Ta to Ti65Ta was only reflected as a two-fold increase in the oxide. Hence, the higher content of Ta in the Ti65Ta alloy contributed less than expected to biological performance.

Both the Ti25Ta and Ti65Ta alloys displayed an improved osteogenic capability compared with Ti-6Al-4V, however no significant difference in behaviour was noted between the Ti25Ta and Ti65Ta alloys. Increased cell spreading on the TiTa compositions and a higher number of attachment points indicated a stronger material-cell interaction. The osteogenic assays supported the morphological analysis, showing enhanced ALP activity on the TiTa compositions, followed by enhanced mineralisation. Furthermore, the TiTa alloys showed equal cell attachment and proliferation to the Ti-6Al-4V control, confirming that the new alloys would perform equally well for implant surface cell colonisation.

Overall, the TiTa compositions showed equal cell attachment and proliferation to Ti-6Al-4V but with enhanced osteogenic potential. The similar biocompatibility but increased osteogenic potential of the TiTa alloys strongly favours the new TiTa compositions for clinical use, particularly considering their lower elastic moduli and strong fatigue performance, even when L-PBF processed. Despite the higher Ta content of the Ti65Ta alloy, it did not display a significantly improved biological response when compared with the Ti25Ta alloy. Hence, as the Ti25Ta alloy is lighter and cheaper, whilst displaying similar mechanical and biological properties to the Ti65Ta alloy, the Ti25Ta alloy was deemed most optimal for implant applications.

7.2 Future Work

This thesis has highlighted potential areas for new research in the area of additive manufacturing, biomedical alloy development and implant structures, which could be valuable to the bone implant industry.

7.2.1 Improvements to L-PBF Processing

The current work has shown the limitations of the current L-PBF processing systems and outline the implications on the mechanical and biological performance of TiTa alloys. Implant manufacture requires high quality assurances and certification from specific agencies, such as the FDA. Hence developments of more robust and versatile hardware and processes for optimisation of process parameters could significantly further this field. Particular areas of beneficial study include:

- Artificial networks to reduce time and material wasted during parameter optimisation analysis. In most current studies, parameter optimisation is conducted by printing material with a limited range of processing parameters, which then undergoes metallographic analysis, consuming sometimes very valuable powders and many hours of cutting, polishing and imaging. The range of processing parameters explored in this thesis only touch on the number of processing parameters which can be altered during the process, which has been estimated to be close to a hundred. Artificial networks can be used to highlight the most significant combinations of parameters which contribute to part density to significantly reduce the experimental processing window. Furthermore, for refractory component mixed powder alloys, material homogeneity could be considered alongside density as an optimisation condition.

- *In situ* process monitoring. Monitoring variables such as temperature, gas flow, surface roughness and laser energy, in real time, could not only identify positioning of possible critical defects, but allow for the implementation of process improving alterations. As this study has shown, remelting of a layer can reduce surface roughness and defects by allowing a second opportunity for molten flow to smooth out previously formed inconsistencies and defects. A remelt strategy could be implemented mid-process if a monitoring system were to alert the presence of a particularly inconsistent melted layer. This would significantly reduce the time and money required for quality assurance of AM parts and be able to provide reassurance over the fatigue behaviour. Furthermore, monitoring of temperature would provide much needed *in situ* data to assist in microstructure formation modelling, as well as prevention of detrimental internal stress.

- New scanning strategies for lattice structures. Due to the high porosity of lattice structures and thin members and walls incorporated in the geometry, L-PBF processing of lattice structures is thermodynamically different from processing of solid material. There are many exciting new lattice geometries being designed specifically for biological applications, however optimising the process parameters for these structures is more difficult than that of uniform solid material. New scanning approaches, such as pulsed lasers, provide exciting possibilities for the formation of much more accurate lattice structures, however significant research into the thermodynamic effects of this new laser strategy on microstructure and mechanical properties is required.

7.2.2 Further Advances for L-PBF Ti25Ta

The L-PBF alloy produced in this study has shown very promising mechanical and biological properties for use in bone implant applications. To further understand the processing and resulting of this alloy and to make it widely applicable to the implant industry, the following areas of research are suggested:

- Optimisation of the remelt scan for reducing residual stress. An optimised remelt scan could be used to reduce residual stress in the final part and help to minimise the reduced ductility seen in the remelted material. Residual stress measurements should be taken over a variety of remelt scan parameter combinations, as a tool to understand the minimisation of residual stress through new scanning techniques and to further elucidate how much residual stress or dislocation density was contributing to the strength of the L-PBF Ti25Ta. This study would improve the applicability of the remelt scanning strategy to a range of other materials with refractory components and help to show elucidate methods of *in situ* thermodynamic and microstructure control.

- Mixed powder vs pre-alloyed powder. This study has shown that the use of mixed titanium and tantalum powders provides extra difficulties to produce homogeneous material. Whilst the processing of the mixed powder alloys could be improved by modelling of individual particle and laser interactions, pre-alloyed powders would reduce the disparity between single Ta or Ti particle laser interactions and create a more homogeneous material. Now that the Ti25Ta alloy has been highlighted as a promising candidate from within the TiTa alloy system, there is sufficient backing to support the production of pre-alloyed Ti25Ta powder. Furthermore, as partially melted Ta particles were often seen as grain nucleation sites in the Ti25Ta mixed powder alloy, it is possible that a different microstructure would be achieved with the pre-alloyed powder. Further experiments using synchrotron beam lines could be used to investigate the differences between the real time solidification of the mixed powder and pre-alloyed powder systems.

- Oxygen solution strengthening. Promising studies have highlighted how oxygen additions can improve the static and cyclic strength of the TNTZ β Ti alloy system, with only minor increases in elastic modulus. Oxygen additions, in the form of Grade I – IV Ti powders, could be investigated to explore the full range of strength obtainable from the Ti25Ta alloy.

- Post printing heat treatments. For mixed powder Ti25Ta, post printing heat treatments such as HIP are often required before clinical use of implants and have the potential to increase alloy homogeneity. However, this thesis has shown that the L-PBF process does not result in an equilibrium phase structure and, hence, a range of heat treatments should be explored for further optimisation of mechanical properties. In addition, the effects of any other required heat treatments on the alloy, such as heating for implant sterilisation, should be considered, as heating for long periods at low temperatures has shown to nucleate the ω phase, significantly altering mechanical properties.

- Further *in vitro* and *in vivo* Ti25Ta testing. Whilst *in vitro* studies are still important in understanding cellular-material interactions, the lack of agreement in *in vitro* and *in vivo* osteogenic studies is worrying. The L-PBF Ti25Ta alloy must be tested *in vivo* in direct comparison to Ti-6Al-4V to determine whether the Ti25Ta does enhance the bone formation. Lattice structures could be used in a rat femur model and CT analysis used to determine the volume of bone formed around each implant, such as the model used by van der Stok et al. [426]. In addition, to identify the mechanism of increased osteogenic behaviour on Ta containing surfaces seen *in vitro* in this thesis, studies into characterisation of the protein layer formed on Ta surfaces could provide valuable insights into material osteogenic potential.

7.2.3 A Range of Alloys and Geometries for a Range of Implant Applications

Additive manufacturing has widened the palette of new materials and geometries which can be explored for bone implants. Whilst mandible implants were used as the motivation for this thesis, many other types of applications exist which could benefit from new materials and implant design. Areas of research which could begin to explore this exciting new field are:

- A review and biomechanical modelling of current bone implants. The ability to explore new biomedical alloys through AM creates the possibility of not only designing an implant geometry specific to a patient's bone shape, but designing the alloy specifically for the application. Natural bone covers a wide range of mechanical properties as it develops responding to its

mechanical environment. Therefore, it is unlikely that one alloy, such as Ti-6Al-4V or even Ti25Ta will possess the optimum mechanical properties in every bone implant application. To be able to create materials and implant combinations with specific properties for each application, the range of bone implants must be assessed and thoroughly mechanically understood through biomechanical modelling. By creating FEA simulations of different implant applications, a range of material properties could be cycled through the simulations to determine the optimum material for the implant. This would be coupled with research exploring topographical optimisation of the implant shape.

- High throughput manufacture coupled with high throughput biological testing of new biomedical alloys. L-DED was shown to be a successful method of manufacturing a range of alloy compositions quickly from mixed powders. This method should be further employed across the wider range of β Ti alloys to improve the speed of development for new biomedical alloys. This high throughput manufacture must be coupled with high throughput biocompatibility testing. Developments into new testing techniques which do not require cutting, polishing and individual small substrate seeding are required.

- Optimisation of surface roughness for balance between osseointegration and fatigue performance. The optimal surface roughness which allows bone integration but does not significantly deteriorate fatigue properties, must be found. Very high cycle fatigue testing must be more heavily used to ensure the lifetime of implants, which undergo millions of cycles per year. There is also much to learn from the range of new geometries available for lattice structured implants. Promising preliminary studies highlight both the mechanical and biological benefits of triply periodic surfaces, however the mechanical response, and particularly the fatigue behaviour of these structures, is little understood.

- Further developments of biocompatibility standards. The definition of biocompatibility is developing as new biologically ‘smart’ materials have entered the market. Simple cytotoxic testing converted to a viability reading is insufficient to characterise the cell-material interactions and separate the performance of compositions within alloy systems. The biocompatibility standards need to be extended to include standard experimental measures for different ‘bioactive’ material qualities, such as enhancing osteogenesis or antibacterial activity.

References

1. Sigston, E., *Emergence and Margins in Head and Neck Cancer: A new understanding*. 2019.

2. Braakhuis, B.J.M., Leemans, C.R., and Visser, O., *Incidence and survival trends of head and neck squamous cell carcinoma in the Netherlands between 1989 and 2011.* Oral Oncology, 2014. **50**(7): p. 670-675.

3. Vigneswaran, N. and Williams, M.D., *Epidemiologic trends in head and neck cancer and aids in diagnosis.* Oral and maxillofacial surgery clinics of North America, 2014. **26**(2): p. 123-141.

4. Chin, D., Boyle, G.M., Theile, D.R., Parsons, P.G., and Coman, W.B., *Molecular introduction to head and neck cancer (HNSCC) carcinogenesis.* British Journal of Plastic Surgery, 2004. **57**(7): p. 595-602.

5. Gibo, T., Yamada, S.-i., Kawamoto, M., Uehara, T., and Kurita, H., *Immunohistochemical Investigation of Predictive Biomarkers for Mandibular Bone Invasion in Oral Squamous Cell Carcinoma.* Pathology & Oncology Research, 2020.

6. Maurer, P., Eckert, A.W., Kriwalsky, M.S., and Schubert, J., *Scope and limitations of methods of mandibular reconstruction: a long-term follow-up.* British Journal of Oral and Maxillofacial Surgery, 2010. **48**(2): p. 100-104.

7. Anthony, J.P. and Foster, R.D., *Mandibular reconstruction with the fibula osteocutaneous free flap.* Operative Techniques in Plastic and Reconstructive Surgery, 1996. **3**(4): p. 233-240.

8. Mascha, F., Winter, K., Pietzka, S., Heufelder, M., Schramm, A., and Wilde, F., *Accuracy of computer-assisted mandibular reconstructions using patient-specific implants in combination with CAD/CAM fabricated transfer keys.* Journal of Cranio-Maxillofacial Surgery, 2017. **45**(11): p. 1884-1897.

9. Katakura, A., Shibahara, T., Noma, H., and Yoshinari, M., *Material analysis of AO plate fracture cases.* Journal of Oral and Maxillofacial Surgery, 2004. **62**(3): p. 348-352.

10. Goh, B.T., Lee, S., Tideman, H., and Stoelinga, P.J.W., *Mandibular reconstruction in adults: a review.* International Journal of Oral and Maxillofacial Surgery, 2008. **37**(7): p. 597-605.

11. Shibahara, T., Noma, H., Furuya, Y., and Takaki, R., *Fracture of mandibular reconstruction plates used after tumor resection.* Journal of Oral and Maxillofacial Surgery, 2002. **60**(2): p. 182-185.

12. Martola, M., Lindqvist, C., Hänninen, H., and Al-Sukhun, J., *Fracture of titanium plates used for mandibular reconstruction following ablative tumor surgery.* Journal of Biomedical Materials Research Part B: Applied Biomaterials, 2007. **80B**(2): p. 345-352.

13. Lindqvist, C., Söderholm, A.-L., Salo, A., Subasinghe, J., Ylijoki, S., Skutnabb, K., and Hallikainen, D., *A comparative study on four screw-plate locking systems in sheep: a clinical and radiological study.* International Journal of Oral and Maxillofacial Surgery, 2001. **30**(2): p. 160-166.

14. Ang, E., Black, C., Irish, J., Brown, D.H., Gullane, P., O'Sullivan, B., and Neligan, P.C., *Reconstructive options in the treatment of osteoradionecrosis of the craniomaxillofacial skeleton.* British Journal of Plastic Surgery, 2003. **56**(2): p. 92-99.

15. Yi, Z., Jian-Guo, Z., Guang-Yan, Y., Ling, L., Fu-Yun, Z., and Guo-Cheng, Z., *Reconstruction plates to bridge mandibular defects: a clinical and experimental investigation in biomechanical aspects.* International Journal of Oral and Maxillofacial Surgery, 1999. **28**(6): p. 445-450.

16. Schöning, H. and Emshoff, R., *Primary temporary AO plate reconstruction of the mandible.* Oral Surgery, Oral Medicine, Oral Pathology, Oral Radiology, and Endodontology, 1998. **86**(6): p. 667-672.

17. Lopez, R., Dekeister, C., Sleiman, Z., and Paoli, J.-R., *Mandibular reconstruction using the titanium functionally dynamic bridging plate system: a retrospective study of 34 cases.* Journal of Oral and Maxillofacial Surgery, 2004. **62**(4): p. 421-426.

18. Gellrich, N.-C., Suarez-Cunqueiro, M.M., Otero-Cepeda, X.L., Schön, R., Schmelzeisen, R., and Gutwald, R., *Comparative study of locking plates in mandibular reconstruction after ablative tumor surgery: THORP versus UniLOCK system.* Journal of Oral and Maxillofacial Surgery, 2004. **62**(2): p. 186-193.

19. Merema, B.J., Kraeima, J., de Visscher, S.A.H.J., van Minnen, B., Spijkervet, F.K.L., Schepman, K.P., and Witjes, M.J.H., *Novel finite element based plate design for bridging mandibular defects; reducing mechanical failure.* Oral Diseases, 2020. **n/a**(n/a).

20. Huiskes, R., Weinans, H., and van Rietbergen, B., *The relationship between stress shielding and bone resorption around total hip stems and the effects of flexible materials.* Clinical orthopaedics and related research, 1992(274): p. 124-134.

21. Zadpoor, A.A. and Weinans, H., *Patient-specific bone modeling and analysis: The role of integration and automation in clinical adoption.* Journal of Biomechanics, 2015. **48**(5): p. 750-760.

22. Di Prima, M., Coburn, J., Hwang, D., Kelly, J., Khairuzzaman, A., and Ricles, L., *Additively manufactured medical products – the FDA perspective.* 3D Printing in Medicine, 2016. **2**(1): p. 1.

23. Zopf, D.A.M.D., Hollister, S.J.P., Nelson, M.E.M.D., Ohye, R.G.M.D., and Green, G.E.M.D., *Bioresorbable Airway Splint Created with a Three-Dimensional Printer.* The New England Journal of Medicine, 2013. **368**(21): p. 2043-5.

24. Tunchel, S., Blay, A., Kolerman, R., Mijiritsky, E., and Jamil Awad, S., *3D Printing/Additive Manufacturing Single Titanium Dental Implants: A Prospective Multicenter Study with 3 Years of Follow-Up.* International Journal of Dentistry, 2016.

25. Koeck, F.X., Beckmann, J., Luring, C., Rath, B., Grifka, J., and Basad, E., *Evaluation of implant position and knee alignment after patient-specific unicompartmental knee arthroplasty.* The Knee, 2011. **18**(5): p. 294-299.

26. Goble, V., *MATERIALISE's 3D-Printed Maxillofacial Implants in Titanium are First to Get Green Light for U.S. Market*. 2017, Materialise: Leuven, Belgium.

27. Niinomi, M., Nakai, M., and Hieda, J., *Development of new metallic alloys for biomedical applications.* Acta Biomaterialia, 2012. **8**(11): p. 3888-3903.

28. Matsuno, H., Yokoyama, A., Watari, F., Uo, M., and Kawasaki, T., *Biocompatibility and osteogenesis of refractory metal implants, titanium, hafnium, niobium, tantalum and rhenium.* Biomaterials, 2001. **22**(11): p. 1253-1262.

29. Findlay, D.M., Welldon, K., Atkins, G.J., Howie, D.W., Zannettino, A.C.W., and Bobyn, D., *The proliferation and phenotypic expression of human osteoblasts on tantalum metal.* Biomaterials, 2004. **25**(12): p. 2215-2227.

30. Helsen, J.A. and Missirlis, Y., *Zirconium and Other Newcomers*, in *Biomaterials: A Tantalus Experience*. 2010, Springer Berlin Heidelberg: Berlin, Heidelberg. p. 99-120.

31. Edelmann, A.R., Patel, D., Allen, R.K., Gibson, C.J., Best, A.M., and Bencharit, S., *Retrospective analysis of porous tantalum trabecular metal–enhanced titanium dental implants.* The Journal of Prosthetic Dentistry, 2019. **121**(3): p. 404-410.

32. Sandiford, N.A., Misur, P., Garbuz, D.S., Greidanus, N.V., and Masri, B.A., *No Difference Between Trabecular Metal Cones and Femoral Head Allografts in Revision TKA: Minimum 5-year Followup.* Clinical Orthopaedics and Related Research®, 2017. **475**(1): p. 118-124.

33. Macheras, G.A., Lepetsos, P., Leonidou, A.O., Anastasopoulos, P.P., Galanakos, S.P., and Poultsides, L.A., *Survivorship of a Porous Tantalum Monoblock Acetabular Component in Primary Hip Arthroplasty With a Mean Follow-Up of 18 Years.* The Journal of Arthroplasty, 2017. **32**(12): p. 3680-3684.

34. Papacci, F., Rigante, L., Fernandez, E., Meglio, M., and Montano, N., *Anterior cervical discectomy and interbody fusion with porous tantalum implant. Results in a series with long-term follow-up.* Journal of Clinical Neuroscience, 2016. **33**: p. 159-162.

35. Sagherian, B.H. and Claridge, R.J., *Salvage of Failed Total Ankle Replacement Using Tantalum Trabecular Metal: Case Series.* Foot & Ankle International, 2014. **36**(3): p. 318-324.

36. Zhou, Y.L., Niinomi, M., and Akahori, T., *Effects of Ta content on Young's modulus and tensile properties of binary Ti–Ta alloys for biomedical applications.* Materials Science and Engineering: A, 2004. **371**(1–2): p. 283-290.

37. Kunčická, L., Kocich, R., and Lowe, T.C., *Advances in metals and alloys for joint replacement.* Progress in Materials Science, 2017. **88**: p. 232-280.

38. Zhang, L., Yang, G., Johnson, B.N., and Jia, X., *Three-dimensional (3D) printed scaffold and material selection for bone repair.* Acta Biomaterialia, 2019. **84**: p. 16-33.

39. Weng, W., Biesiekierski, A., Li, Y., and Wen, C., *Effects of selected metallic and interstitial elements on the microstructure and mechanical properties of beta titanium alloys for orthopedic applications.* Materialia, 2019. **6**: p. 100323.

40. Feng, X., Lin, G., Fang, C.X., Lu, W.W., Chen, B., and Leung, F.K.L., *Bone resorption triggered by high radial stress: The mechanism of screw loosening in plate fixation of long bone fractures.* Journal of Orthopaedic Research, 2019. **37**(7): p. 1498-1507.

41. Uhthoff, H. and Dubuc, F., *Bone Structure Changes in the Dog Under Rigid Internal Fixation.* Clin Orthop, 1971. **81**: p. 165-170.

42. Balogh, Z.J., *The Surgical Burden of Musculoskeletal Conditions and Injuries.* World Journal of Surgery, 2020. **44**(4): p. 1007-1008.

43. Festas, A.J., Ramos, A., and Davim, J.P., *Medical devices biomaterials – A review.* Proceedings of the Institution of Mechanical Engineers, Part L: Journal of Materials: Design and Applications, 2019. **234**(1): p. 218-228.

44. *Medical Device Standards and Implant Standards*. 2020 03/04/2020]; Available from: https://www.astm.org/Standards/medical-device-and-implant-standards.html.

45. *Preformed Reconstrution Plates*, in *MatrixMANDIBLE*, DePuySynthes, Editor. 2015: Oberdorf, Switzerland. p. 40.

46. *Mandible Plating System*, in *MatrixMANDIBLE*, DePuySynthes, Editor. 2015: Oberdorf, Switzerland.

47. *Orthognathic surgery and traumatology*, in *GlobalD Therapeutic arsenal*, GlobalD, Editor. 2019: Brignais, France.

48. *Orthognathics 1.5 / 2.0*, in *Surgical Technique - Step by step*, medartis, Editor. 2016: Basel, Switzerland. p. 42.

49. *Lorenz Plating System*, in *TraumaOne*, Biomet, Editor. 2013: Dordrecht, The Netherlands. p. 18.

50. Brunette, D.M., Tengvall, P., Textos, M., and Thomsen, P., *Titanium in Medicine*. 2001, Berlin Heidelberg: Springer.

51. Silva, M., Shepherd, E.F., Jackson, W.O., Dorey, F.J., and Schmalzried, T.P., *Average patient walking activity approaches 2 million cycles per year: Pedometers under-record walking activity.* The Journal of Arthroplasty, 2002. **17**(6): p. 693-697.

52. Bergmann, G., Bender, A., Dymke, J., Duda, G., and Damm, P., *Standardized Loads Acting in Hip Implants.* PLoS ONE, 2016. **11**(5).

53. Semlitsch, M.F., Weber, H., Streicher, R.M., and Schön, R., *Joint replacement components made of hot-forged and surface-treated Ti-6Al-7Nb alloy.* Biomaterials, 1992. **13**(11): p. 781-788.

54. Zhang, L.-C. and Chen, L.-Y., *A Review on Biomedical Titanium Alloys: Recent Progress and Prospect.* Advanced Engineering Materials, 2019. **21**(4): p. 1801215.

55. Dehghan-Manshadi, A., Yu, P., Dargusch, M., StJohn, D., and Qian, M., *Metal injection moulding of surgical tools, biomaterials and medical devices: A review.* Powder Technology, 2020. **364**: p. 189-204.

56. Mirzaali, M.J., Schwiedrzik, J.J., Thaiwichai, S., Best, J.P., Michler, J., Zysset, P.K., and Wolfram, U., *Mechanical properties of cortical bone and their relationships with age, gender, composition and microindentation properties in the elderly.* Bone, 2016. **93**: p. 196-211.

57. Li, Y.-H. and Shang, X.-Y., *Recent progress in porous TiNb-based alloys for biomedical implant applications.* Materials Science and Technology, 2020. **36**(4): p. 385-392.

58. Goldstein, S.A., *The mechanical properties of trabecular bone: Dependence on anatomic location and function.* Journal of Biomechanics, 1987. **20**(11): p. 1055-1061.

59. Kaur, M. and Singh, K., *Review on titanium and titanium based alloys as biomaterials for orthopaedic applications.* Materials Science and Engineering: C, 2019. **102**: p. 844-862.

60. Wauthle, R., Ahmadi, S.M., Amin Yavari, S., Mulier, M., Zadpoor, A.A., Weinans, H., Van Humbeeck, J., Kruth, J.-P., and Schrooten, J., *Revival of pure titanium for dynamically loaded*

porous implants using additive manufacturing. Materials Science and Engineering C, 2015. **54**(C): p. 94-100.

61. Zhang, X.Z., Leary, M., Tang, H.P., Song, T., and Qian, M., *Selective electron beam manufactured Ti-6Al-4V lattice structures for orthopedic implant applications: Current status and outstanding challenges.* Current Opinion in Solid State and Materials Science, 2018. **22**(3): p. 75-99.

62. Lanyon, L.E., Magee, P.T., and Baggott, D.G., *The relationship of functional stress and strain to the processes of bone remodelling. An experimental study on the sheep radius.* Journal of Biomechanics, 1979. **12**(8): p. 593-600.

63. Polmear, I.J., StJohn, D., Nie, J., and Qian, M., *Titanium Alloys*, in *Light Alloys: Metallurgy of the Light Metals*. 2017, Butterworth-Heinemann: Oxford. p. 369-459.

64. Im, Y.-D. and Lee, Y.-K., *Effects of Mo concentration on recrystallization texture, deformation mechanism and mechanical properties of Ti–Mo binary alloys.* Journal of Alloys and Compounds, 2020. **821**: p. 153508.

65. Hacisalihoglu, I., Samancioglu, A., Yildiz, F., Purcek, G., and Alsaran, A., *Tribocorrosion properties of different type titanium alloys in simulated body fluid.* Wear, 2015. **332-333**: p. 679-686.

66. Martins Júnior, J.R.S., Matos, A.A., Oliveira, R.C., Buzalaf, M.A.R., Costa, I., Rocha, L.A., and Grandini, C.R., *Preparation and characterization of alloys of the Ti–15Mo–Nb system for biomedical applications.* Journal of Biomedical Materials Research Part B: Applied Biomaterials, 2018. **106**(2): p. 639-648.

67. Lee, S.H., Todai, M., Tane, M., Hagihara, K., Nakajima, H., and Nakano, T., *Biocompatible low Young's modulus achieved by strong crystallographic elastic anisotropy in Ti–15Mo–5Zr–3Al alloy single crystal.* Journal of the Mechanical Behavior of Biomedical Materials, 2012. **14**: p. 48-54.

68. Nag, S., Banerjee, R., and Fraser, H.L., *Microstructural evolution and strengthening mechanisms in Ti–Nb–Zr–Ta, Ti–Mo–Zr–Fe and Ti–15Mo biocompatible alloys.* Materials Science and Engineering: C, 2005. **25**(3): p. 357-362.

69. Haghighi, S.E., Lu, H.B., Jian, G.Y., Cao, G.H., Habibi, D., and Zhang, L.C., *Effect of α″ martensite on the microstructure and mechanical properties of beta-type Ti–Fe–Ta alloys.* Materials & Design, 2015. **76**: p. 47-54.

70. Cho, K., Niinomi, M., Nakai, M., Hieda, J., and Kawasaki, Y., *Development of High Modulus Ti–Fe–Cu Alloys for Biomedical Applications.* MATERIALS TRANSACTIONS, 2013. **54**(4): p. 574-581.

71. Zhang, L.-C., Lu, H.-B., Mickel, C., and Eckert, J., *Ductile ultrafine-grained Ti-based alloys with high yield strength.* Applied Physics Letters, 2007. **91**(5): p. 051906.

72. Ehtemam-Haghighi, S., Liu, Y., Cao, G., and Zhang, L.-C., *Influence of Nb on the β→α″ martensitic phase transformation and properties of the newly designed Ti–Fe–Nb alloys.* Materials Science and Engineering: C, 2016. **60**: p. 503-510.

73. Zadorozhnyy, V.Y., Shi, X., Kozak, D.S., Wada, T., Wang, J.Q., Kato, H., and Louzguine-Luzgin, D.V., *Electrochemical behavior and biocompatibility of Ti-Fe-Cu alloy with high strength and ductility.* Journal of Alloys and Compounds, 2017. **707**: p. 291-297.

74. Zadorozhnyy, V.Y., Inoue, A., and Louzguine-Luzgin, D.V., *Ti-based nanostructured low-alloy with high strength and ductility.* Materials Science and Engineering: A, 2012. **551**: p. 82-86.

75. Zadorozhnyy, V., Ketov, V.S., Wada, T., Wurster, S., Nayak, V., Louzguine-Luzgin, V.D., Eckert, J., and Kato, H., *Novel α + β Type Ti-Fe-Cu Alloys Containing Sn with Pertinent Mechanical Properties.* Metals, 2019. **10**(1).

76. Rydzynski, K. and Pakulska, D., *Vanadium, Niobium, and Tantalum.* Patty's Toxicology, 2012: p. 511-564.

77. *CES EduPack*. 2019, Granta Design Limited.

78. Lee, C.M., Ju, C.P., and Chern Lin, J.H., *Structure–property relationship of cast Ti–Nb alloys.* Journal of Oral Rehabilitation, 2002. **29**(4): p. 314-322.

79. Hon, Y.-H., Wang, J.-Y., and Pan, Y.-N., *Composition/Phase Structure and Properties of Titanium-Niobium Alloys.* MATERIALS TRANSACTIONS, 2003. **44**(11): p. 2384-2390.

80. Mantani, Y. and Tajima, M., *Effect of ageing on internal friction and elastic modulus of Ti–Nb alloys.* Materials Science and Engineering: A, 2006. **442**(1): p. 409-413.

81. Wang, Y.B. and Zheng, Y.F., *The microstructure and shape memory effect of Ti–16 at.%Nb alloy.* Materials Letters, 2008. **62**(2): p. 269-272.

82. Bönisch, M., Calin, M., van Humbeeck, J., Skrotzki, W., and Eckert, J., *Factors influencing the elastic moduli, reversible strains and hysteresis loops in martensitic Ti–Nb alloys.* Materials Science and Engineering: C, 2015. **48**: p. 511-520.

83. Ramarolahy, A., Castany, P., Prima, F., Laheurte, P., Péron, I., and Gloriant, T., *Microstructure and mechanical behavior of superelastic Ti–24Nb–0.5O and Ti–24Nb–0.5N biomedical alloys.* Journal of the Mechanical Behavior of Biomedical Materials, 2012. **9**: p. 83-90.

84. Zhou, Y.-L. and Niinomi, M., *Ti–25Ta alloy with the best mechanical compatibility in Ti–Ta alloys for biomedical applications.* Materials Science and Engineering: C, 2009. **29**(3): p. 1061-1065.

85. Bywater, K.A. and Christian, J.W., *Martensitic transformations in titanium-tantalum alloys.* The Philosophical Magazine: A Journal of Theoretical Experimental and Applied Physics, 1972. **25**(6): p. 1249-1273.

86. Fedotov, S.G., Chelidze, T.V., Kovneristyy, Y.K., and Sanadze, V.V., *Phase structure, critical points Ms and As of martensitic transformations and elastic properties of metastable alloys of the Ti-Ta system.* Phys. Met. Metall., 1985. **60**(3): p. 139-143.

87. Wu, C.-M., Peng, P.-W., Chou, H.-H., Ou, K.-L., Sugiatno, E., Liu, C.-M., and Huang, C.-F., *Microstructural, mechanical and biological characterizations of the promising titanium-tantalum alloy for biomedical applications.* Journal of Alloys and Compounds, 2018. **735**: p. 2604-2610.

88. Buenconsejo, P.J.S., Kim, H.Y., Hosoda, H., and Miyazaki, S., *Shape memory behavior of Ti–Ta and its potential as a high-temperature shape memory alloy.* Acta Materialia, 2009. **57**(4): p. 1068-1077.

89. Niendorf, T., Krooß, P., Batyrsina, E., Paulsen, A., Motemani, Y., Ludwig, A., Buenconsejo, P., Frenzel, J., Eggeler, G., and Maier, H.J., *Functional and structural fatigue of titanium tantalum high temperature shape memory alloys (HT SMAs).* Materials Science and Engineering: A, 2015. **620**: p. 359-366.

90. Zhou, Y.-L. and Niinomi, M., *Microstructures and mechanical properties of Ti–50 mass% Ta alloy for biomedical applications.* Journal of Alloys and Compounds, 2008. **466**(1–2): p. 535-542.

91. Maier, H.J., Karsten, E., Paulsen, A., Langenkämper, D., Decker, P., Frenzel, J., Somsen, C., Ludwig, A., Eggeler, G., and Niendorf, T., *Microstructural evolution and functional fatigue of a Ti–25Ta high-temperature shape memory alloy.* Journal of Materials Research, 2017. **32**(23): p. 4287-4295.

92. Geetha, M., Kamachi Mudali, U., Gogia, A.K., Asokamani, R., and Raj, B., *Influence of microstructure and alloying elements on corrosion behavior of Ti–13Nb–13Zr alloy.* Corrosion Science, 2004. **46**(4): p. 877-892.

93. Geetha, M., Singh, A.K., Gogia, A.K., and Asokamani, R., *Effect of thermomechanical processing on evolution of various phases in Ti-Nb-Zr alloys.* Journal of Alloys and Compounds, 2004. **384**(1-2): p. 131-144.

94. Chicardi, E., Gutiérrez-González, C.F., Sayagués, M.J., and García-Garrido, C., *Development of a novel TiNbTa material potentially suitable for bone replacement implants.* Materials & Design, 2018. **145**: p. 88-96.

95. Akahori, T., Niinomi, M., Fukui, H., Ogawa, M., and Toda, H., *Improvement in fatigue characteristics of newly developed beta type titanium alloy for biomedical applications by thermo-mechanical treatments.* Materials Science and Engineering: C, 2005. **25**(3): p. 248-254.

96. Tane, M., Akita, S., Nakano, T., Hagihara, K., Umakoshi, Y., Niinomi, M., and Nakajima, H., *Peculiar elastic behavior of Ti–Nb–Ta–Zr single crystals.* Acta Materialia, 2008. **56**(12): p. 2856-2863.

97. Liu, H., Niinomi, M., Nakai, M., Obara, S., and Fujii, H., *Improved fatigue properties with maintaining low Young's modulus achieved in biomedical beta-type titanium alloy by oxygen addition.* Materials Science and Engineering: A, 2017. **704**: p. 10-17.

98. Hao, Y.L., Li, S.J., Sun, S.Y., Zheng, C.Y., Hu, Q.M., and Yang, R., *Super-elastic titanium alloy with unstable plastic deformation.* Applied Physics Letters, 2005. **87**(9): p. 091906.

99. Li, S.J., Zhang, Y.W., Sun, B.B., Hao, Y.L., and Yang, R., *Thermal stability and mechanical properties of nanostructured Ti–24Nb–4Zr–7.9Sn alloy.* Materials Science and Engineering: A, 2008. **480**(1): p. 101-108.

100. Li, X., Ye, S., Yuan, X., and Yu, P., *Fabrication of biomedical Ti-24Nb-4Zr-8Sn alloy with high strength and low elastic modulus by powder metallurgy.* Journal of Alloys and Compounds, 2019. **772**: p. 968-977.

101. Hao, Y.L., Li, S.J., Sun, S.Y., Zheng, C.Y., and Yang, R., *Elastic deformation behaviour of Ti-24Nb-4Zr-7.9Sn for biomedical applications.* Acta Biomaterialia, 2007. **3**(2): p. 277-286.

102. Exley, C. and Mold, M.J., *Aluminium in human brain tissue: how much is too much?* Journal of Biological Inorganic Chemistry, 2019.

103. Niu, Q.e. and SpringerLink, *Neurotoxicity of aluminum*. 2018: Singapore : Springer.

104. Lu, X., Liang, R., Jia, Z., Wang, H., Pan, B., Zhang, Q., and Niu, Q., *Cognitive Disorders and Tau-Protein Expression Among Retired Aluminum Smelting Workers.* Journal of Occupational and Environmental Medicine, 2014. **56**(2): p. 155-160.

105. Challa, V.S.A., Mali, S., and Misra, R.D.K., *Reduced toxicity and superior cellular response of preosteoblasts to Ti-6Al-7Nb alloy and comparison with Ti-6Al-4V.* Journal of Biomedical Materials Research Part A, 2013. **101A**(7): p. 2083-2089.

106. Fretwurst, T., Buzanich, G., Nahles, S., Woelber, J.P., Riesemeier, H., and Nelson, K., *Metal elements in tissue with dental peri-implantitis: a pilot study.* Clinical Oral Implants Research, 2016. **27**(9): p. 1178-1186.

107. Fretwurst, T., Nelson, K., Tarnow, D.P., Wang, H.L., and Giannobile, W.V., *Is Metal Particle Release Associated with Peri-implant Bone Destruction? An Emerging Concept.* Journal of Dental Research, 2017. **97**(3): p. 259-265.

108. He, X., Reichl, F.-X., Wang, Y., Michalke, B., Milz, S., Yang, Y., Stolper, P., Lindemaier, G., Graw, M., Hickel, R., and Högg, C., *Analysis of titanium and other metals in human jawbones with dental implants – A case series study.* Dental Materials, 2016. **32**(8): p. 1042-1051.

109. Okazaki, Y., Gotoh, E., Manabe, T., and Kobayashi, K., *Comparison of metal concentrations in rat tibia tissues with various metallic implants.* Biomaterials, 2004. **25**(28): p. 5913-5920.

110. Malhotra, R., Han, Y.M., Morin, J.L.P., Luong-Van, E.K., Chew, R.J.J., Castro Neto, A.H., Nijhuis, C.A., and Rosa, V., *Inhibiting Corrosion of Biomedical-Grade Ti-6Al-4V Alloys with Graphene Nanocoating.* Journal of Dental Research, 2020. **99**(3): p. 285-292.

111. Hallab, N.J., Mikecz, K., Vermes, C., Skipor, A., and Jacobs, J.J., *Orthopaedic implant related metal toxicity in terms of human lymphocyte reactivity to metal-protein complexes produced from cobalt-base and titanium-base implant alloy degradation*, in *Molecular Mechanisms of Metal Toxicity and Carcinogenesis*, X. Shi, et al., Editors. 2001, Springer US: Boston, MA. p. 127-136.

112. Urban, R.M., Jacobs, J.J., Tomlinson, M.J., Gavrilovic, J., Black, J., and Peoc'h, M., *Dissemination of Wear Particles to the Liver, Spleen, and Abdominal Lymph Nodes of Patients with Hip or Knee Replacement**. JBJS, 2000. **82**(4).

113. Franchi, M., Bacchelli, B., Martini, D., Pasquale, V.D., Orsini, E., Ottani, V., Fini, M., Giavaresi, G., Giardino, R., and Ruggeri, A., *Early detachment of titanium particles from various different surfaces of endosseous dental implants.* Biomaterials, 2004. **25**(12): p. 2239-2246.

114. Martini, D., Fini, M., Franchi, M., Pasquale, V.D., Bacchelli, B., Gamberini, M., Tinti, A., Taddei, P., Giavaresi, G., Ottani, V., Raspanti, M., Guizzardi, S., and Ruggeri, A., *Detachment of titanium and fluorohydroxyapatite particles in unloaded endosseous implants.* Biomaterials, 2003. **24**(7): p. 1309-1316.

115. Morais, L.S., Serra, G.G., Muller, C.A., Andrade, L.R., Palermo, E.F.A., Elias, C.N., and Meyers, M., *Titanium alloy mini-implants for orthodontic anchorage: Immediate loading and metal ion release.* Acta Biomaterialia, 2007. **3**(3): p. 331-339.

116. Eisenbarth, E., Velten, D., Müller, M., Thull, R., and Breme, J., *Biocompatibility of β-stabilizing elements of titanium alloys.* Biomaterials, 2004. **25**(26): p. 5705-5713.

117. Zhang, D., Wong, C.S., Wen, C., and Li, Y., *Cellular responses of osteoblast-like cells to 17 elemental metals.* Journal of Biomedical Materials Research Part A, 2017. **105**(1): p. 148-158.

118. Song, Y.-H., Kim, M.-K., Park, E.-J., Song, H.-J., Anusavice, K.J., and Park, Y.-J., *Cytotoxicity of alloying elements and experimental titanium alloys by WST-1 and agar overlay tests.* Dental Materials, 2014. **30**(9): p. 977-983.

119. Rae, T., *The haemolytic action of particulate metals (Cd, Cr, Co, Fe, Mo, Ni, Ta, Ti, Zn, Co-Cr alloy).* The Journal of Pathology, 1978. **125**(2): p. 81-89.

120. Sakai, T., Takeda, S., and Nakamura, M., *The Effects of Particulate Metals on Cell Viability of Osteoblast-like Cells in vitro*. Dental Materials Journal, 2002. **21**(2): p. 133-146.

121. Kuroda, S., Takeda, S., and Nakamura, M., *Effects of Six Particulate Metals on Osteoblast-like MG-63 and HOS Cells in vitro*. Dental Materials Journal, 2003. **22**(4): p. 507-520.

122. Wataha, J.C., Hanks, C.T., and Sun, Z., *Effect of cell line on in vitro metal ion cytotoxicity.* Dental Materials, 1994. **10**(3): p. 156-161.

123. Dias Corpa Tardelli, J., Lima da Costa Valente, M., Theodoro de Oliveira, T., and Cândido dos Reis, A., *Influence of chemical composition on cell viability on titanium surfaces: A systematic review.* The Journal of Prosthetic Dentistry, 2020.

124. Guo, S., Lu, Y., Wu, S., Liu, L., He, M., Zhao, C., Gan, Y., Lin, J., Luo, J., Xu, X., and Lin, J., *Preliminary study on the corrosion resistance, antibacterial activity and cytotoxicity of selective-laser-melted Ti6Al4V-xCu alloys.* Materials Science and Engineering: C, 2017. **72**: p. 631-640.

125. Macpherson, A., Li, X., McCormick, P., Ren, L., Yang, K., and Sercombe, T.B., *Antibacterial Titanium Produced Using Selective Laser Melting.* JOM, 2017. **69**(12): p. 2719-2724.

126. Krakhmalev, P., Yadroitsev, I., Yadroitsava, I., and de Smidt, O., *Functionalization of Biomedical Ti6Al4V via In Situ Alloying by Cu during Laser Powder Bed Fusion Manufacturing.* Materials, 2017. **10**(10).

127. Wang, Q., Ren, L., Li, X., Zhang, S., Sercombe, T.B., and Yang, K., *Antimicrobial Cu-bearing stainless steel scaffolds.* Materials Science and Engineering: C, 2016. **68**: p. 519-522.

128. Shi, A., Zhu, C., Fu, S., Wang, R., Qin, G., Chen, D., and Zhang, E., *What controls the antibacterial activity of Ti-Ag alloy, Ag ion or Ti2Ag particles?* Materials Science and Engineering: C, 2020. **109**: p. 110548.

129. Ouyang, S., Zheng, K., Zhang, W., Chen, W., and Liu, Y., *Microscale electric fields induced by galvanically coupled Ti-Mg metal-metal composites promote antibacterial activity.* Materialia, 2020. **9**: p. 100621.

130. King, D.E., Mainous, A.G., Geesey, M.E., and Woolson, R.F., *Dietary Magnesium and C-reactive Protein Levels.* Journal of the American College of Nutrition, 2005. **24**(3): p. 166-171.

131. Ouyang, S., Liu, Y., Huang, Q., Gan, Z., and Tang, H., *Effect of composition on in vitro degradability of Ti–Mg metal-metal composites.* Materials Science and Engineering: C, 2020. **107**: p. 110327.

132. Meenashisundaram, G.K., Wang, N., Maskomani, S., Lu, S., Anantharajan, S.K., Dheen, S.T., Nai, S.M.L., Fuh, J.Y.H., and Wei, J., *Fabrication of Ti + Mg composites by three-dimensional printing of porous Ti and subsequent pressureless infiltration of biodegradable Mg.* Materials Science and Engineering: C, 2020. **108**: p. 110478.

133. Balog, M., Ibrahim, A.M.H., Krizik, P., Bajana, O., Klimova, A., Catic, A., and Schauperl, Z., *Bioactive Ti + Mg composites fabricated by powder metallurgy: The relation between the microstructure and mechanical properties.* Journal of the Mechanical Behavior of Biomedical Materials, 2019. **90**: p. 45-53.

134. Liu, Y., Li, K., Luo, T., Song, M., Wu, H., Xiao, J., Tan, Y., Cheng, M., Chen, B., Niu, X., Hu, R., Li, X., and Tang, H., *Powder metallurgical low-modulus Ti–Mg alloys for biomedical applications.* Materials Science and Engineering: C, 2015. **56**: p. 241-250.

135. Li, Y., Zhou, J., Pavanram, P., Leeflang, M.A., Fockaert, L.I., Pouran, B., Tümer, N., Schröder, K.U., Mol, J.M.C., Weinans, H., Jahr, H., and Zadpoor, A.A., *Additively manufactured biodegradable porous magnesium.* Acta Biomaterialia, 2018. **67**: p. 378-392.

136. Balla, V.K., Bose, S., Davies, N.M., and Bandyopadhyay, A., *Tantalum—A bioactive metal for implants.* JOM, 2010. **62**(7): p. 61-64.

137. Albrektsson, T., Brånemark, P.I., Hansson, H.A., and Lindström, J., *Osseointegrated Titanium Implants: Requirements for Ensuring a Long-Lasting, Direct Bone-to-Implant Anchorage in Man.* Acta Orthopaedica Scandinavica, 1981. **52**(2): p. 155-170.

138. Johansson, C.B., Hansson, H.A., and Albrektsson, T., *Qualitative interfacial study between bone and tantalum, niobium or commercially pure titanium.* Biomaterials, 1990. **11**(4): p. 277-280.

139. Prigent, H., Pellen-Mussi, P., Cathelineau, G., and Bonnaure-Mallet, M., *Evaluation of the biocompatibility of titanium-tantalum alloy versus titanium.* Journal of Biomedical Materials Research, 1998. **39**(2): p. 200-206.

140. Bobyn, J.D., Stackpool, G.J., Hacking, S.A., Tanzer, M., and Krygier, J.J., *Characteristics of bone ingrowth and interface mechanics of a new porous tantalum biomaterial.* Journal of Bone & Joint Surgery, British Volume, 1999. **81-B**(5): p. 907-914.

141. Zardiackas, L.D., Parsell, D.E., Dillon, L.D., Mitchell, D.W., Nunnery, L.A., and Poggie, R., *Structure, metallurgy, and mechanical properties of a porous tantalum foam.* Journal of Biomedical Materials Research, 2001. **58**(2): p. 180-187.

142. Shimko, D.A., Shimko, V.F., Sander, E.A., Dickson, K.F., and Nauman, E.A., *Effect of porosity on the fluid flow characteristics and mechanical properties of tantalum scaffolds.* Journal of Biomedical Materials Research Part B: Applied Biomaterials, 2005. **73B**(2): p. 315-324.

143. *Zimmer Holdings, Inc. Annual Report 2012*. 2012, Zimmer: Warsaw, USA. p. 84.

144. Borland, W.S., Bhattacharya, R., Holland, J.P., and Brewster, N.T., *Use of porous trabecular metal augments with impaction bone grafting in management of acetabular bone loss: Early to medium-term results.* Acta Orthopaedica, 2012. **83**(4): p. 347-352.

145. Baad-Hansen, T., Kold, S., Nielsen, P.T., Laursen, M.B., Christensen, P.H., and Soballe, K., *Comparison of trabecular metal cups and titanium fiber-mesh cups in primary hip arthroplasty: A randomized RSA and bone mineral densitometry study of 50 hips.* Acta Orthopaedica, 2011. **82**(2): p. 155-160.

146. Lakstein, D., Backstein, D., Safir, O., Kosashvili, Y., and Gross, A.E., *Trabecular Metal™ Cups for Acetabular Defects With 50% or Less Host Bone Contact.* Clinical Orthopaedics and Related Research®, 2009. **467**(9): p. 2318-2324.

147. Stiehl, J.B.M.D., *Trabecular Metal in Hip Reconstructive Surgery.* Orthopedics, 2005. **28**(7): p. 662-670.

148. Bobyn, J.D., Poggie, R.A., Krygier, J.J., Lewallen, D.G., and et al., *CLINICAL VALIDATION OF A STRUCTURAL POROUS TANTALUM BIOMATERIAL FOR ADULT RECONSTRUCTION.* Journal of Bone and Joint Surgery, 2004. **86**: p. 123-9.

149. Henricson, A. and Nilsson, K.G., *Trabecular metal tibial knee component still stable at 10 years.* Acta Orthopaedica, 2016. **87**(5): p. 504-510.

150. Levine, B.R., Sporer, S., Poggie, R.A., Della Valle, C.J., and Jacobs, J.J., *Experimental and clinical performance of porous tantalum in orthopedic surgery.* Biomaterials, 2006. **27**(27): p. 4671-4681.

151. Hayakawa, K., Date, H., Tsujimura, S., Nojiri, S., Yamada, H., and Nakagawa, K., *Mid-term results of total knee arthroplasty with a porous tantalum monoblock tibial component.* The Knee, 2014. **21**(1): p. 199-203.

152. Stilling, M., Madsen, F., Odgaard, A., Rømer, L., Andersen, N.T., Rahbek, O., and Søballe, K., *Superior fixation of pegged trabecular metal over screw-fixed pegged porous titanium fiber mesh: A randomized clinical RSA study on cementless tibial components.* Acta Orthopaedica, 2011. **82**(2): p. 177-186.

153. Löfgren, H., Engquist, M., Hoffmann, P., Sigstedt, B., and Vavruch, L., *Clinical and radiological evaluation of Trabecular Metal and the Smith–Robinson technique in anterior cervical fusion for degenerative disease: a prospective, randomized, controlled study with 2-year follow-up.* European Spine Journal, 2010. **19**(3): p. 464-473.

154. Patil, N. and Goodman, S.B., *The Use of Porous Tantalum for Reconstructing Bone Loss in Orthopedic Surgery*, in *Advances in Metallic Biomaterials: Tissues, Materials and Biological Reactions*, M. Niinomi, T. Narushima, and M. Nakai, Editors. 2015, Springer Berlin Heidelberg: Berlin, Heidelberg. p. 223-243.

155. Bencharit, S., Byrd, W.C., Altarawneh, S., Hosseini, B., Leong, A., Reside, G., Morelli, T., and Offenbacher, S., *Development and Applications of Porous Tantalum Trabecular Metal-Enhanced Titanium Dental Implants.* Clinical Implant Dentistry and Related Research, 2014. **16**(6): p. 817-826.

156. Bencharit, S., Byrd, W.C., and Hosseini, B., *Immediate placement of a porous-tantalum, trabecular metal-enhanced titanium dental implant with demineralized bone matrix into a socket with deficient buccal bone: A clinical report.* The Journal of Prosthetic Dentistry, 2015. **113**(4): p. 262-269.

157. Schlee, M., van der Schoor, W.P., and van der Schoor, A.R.M., *Immediate Loading of Trabecular Metal-Enhanced Titanium Dental Implants: Interim Results from an International*

Proof-of-Principle Study. Clinical Implant Dentistry and Related Research, 2015. **17**: p. e308-e320.

158. Romanos, G.E., Delgado-Ruiz, R.A., Sacks, D., and Calvo-Guirado, J.L., *Influence of the implant diameter and bone quality on the primary stability of porous tantalum trabecular metal dental implants: an in vitro biomechanical study.* Clinical Oral Implants Research, 2016: p. n/a-n/a.

159. Sikri, N., Kaur, M., and Lahori, M., *TANTALUM DENTAL IMPLANTS: AN INSIGHT*, in *Guident*. 2016, Guident: Bljnor. p. 16-19.

160. Li, H., Yao, Z., Zhang, J., Cai, X., Li, L., Liu, G., Liu, J., Cui, L., and Huang, J., *The progress on physicochemical properties and biocompatibility of tantalum-based metal bone implants.* SN Applied Sciences, 2020. **2**(4): p. 671.

161. Chen, G., Yin, J., Zhao, S., Tang, H., and Qu, X., *Microstructure and tensile properties of a Ti-28Ta alloy studied by transmission electron microscopy and digital image correlation.* International Journal of Refractory Metals and Hard Materials, 2019. **81**: p. 71-77.

162. Singh, S., Ramakrishna, S., and Singh, R., *Material issues in additive manufacturing: A review.* Journal of Manufacturing Processes, 2017. **25**: p. 185-200.

163. *Standard Terminology for Additive Manufacturing*, in *General Principles - Terminology*. 2015, ASTM International: West Conshohocken, PA.

164. DebRoy, T., Wei, H.L., Zuback, J.S., Mukherjee, T., Elmer, J.W., Milewski, J.O., Beese, A.M., Wilson-Heid, A., De, A., and Zhang, W., *Additive manufacturing of metallic components – Process, structure and properties.* Progress in Materials Science, 2018. **92**: p. 112-224.

165. Biffi, C.A., Demir, A.G., Coduri, M., Previtali, B., and Tuissi, A., *Laves phases in selective laser melted TiCr1.78 alloys for hydrogen storage.* Materials Letters, 2018. **226**: p. 71-74.

166. Wang, J.C., Liu, Y.J., Qin, P., Liang, S.X., Sercombe, T.B., and Zhang, L.C., *Selective laser melting of Ti–35Nb composite from elemental powder mixture: Microstructure, mechanical behavior and corrosion behavior.* Materials Science and Engineering: A, 2019. **760**: p. 214-224.

167. Huang, S., Sing, S.L., and Yeong, W.Y., *Selective Laser Melting of Ti42Nb Composite Powder and the Effect of Laser Re-Melting.* Key Engineering Materials, 2019. **801**: p. 270-275.

168. Xiong, Z., Zhang, P., Tan, C., Dong, D., Ma, W., and Yu, K., *Selective Laser Melting and Remelting of Pure Tungsten.* Advanced Engineering Materials, 2020. **22**(3): p. 1901352.

169. Yusuf, S.M. and Gao, N., *Influence of energy density on metallurgy and properties in metal additive manufacturing.* Materials Science and Technology, 2017: p. 1-21.

170. Prashanth, K.G., Scudino, S., Maity, T., Das, J., and Eckert, J., *Is the energy density a reliable parameter for materials synthesis by selective laser melting?* Materials Research Letters, 2017. **5**(6): p. 386-390.

171. Liu, Y.J., Li, S.J., Wang, H.L., Hou, W.T., Hao, Y.L., Yang, R., Sercombe, T.B., and Zhang, L.C., *Microstructure, defects and mechanical behavior of beta-type titanium porous*

structures manufactured by electron beam melting and selective laser melting. Acta Materialia, 2016. **113**: p. 56-67.

172. Cunningham, R., Zhao, C., Parab, N., Kantzos, C., Pauza, J., Fezzaa, K., Sun, T., and Rollett, A.D., *Keyhole threshold and morphology in laser melting revealed by ultrahigh-speed x-ray imaging.* Science, 2019. **363**(6429): p. 849.

173. Zhang, L.C., Klemm, D., Eckert, J., Hao, Y.L., and Sercombe, T.B., *Manufacture by selective laser melting and mechanical behavior of a biomedical Ti–24Nb–4Zr–8Sn alloy.* Scripta Materialia, 2011. **65**(1): p. 21-24.

174. Wang, Z., Xiao, Z., Tse, Y., Huang, C., and Zhang, W., *Optimization of processing parameters and establishment of a relationship between microstructure and mechanical properties of SLM titanium alloy.* Optics & Laser Technology, 2019. **112**: p. 159-167.

175. King, W.E., Barth, H.D., Castillo, V.M., Gallegos, G.F., Gibbs, J.W., Hahn, D.E., Kamath, C., and Rubenchik, A.M., *Observation of keyhole-mode laser melting in laser powder-bed fusion additive manufacturing.* Journal of Materials Processing Technology, 2014. **214**(12): p. 2915-2925.

176. Xu, W., Brandt, M., Sun, S., Elambasseril, J., Liu, Q., Latham, K., Xia, K., and Qian, M., *Additive manufacturing of strong and ductile Ti–6Al–4V by selective laser melting via in situ martensite decomposition.* Acta Materialia, 2015. **85**: p. 74-84.

177. Yu, W., Sing, S.L., Chua, C.K., and Tian, X., *Influence of re-melting on surface roughness and porosity of AlSi10Mg parts fabricated by selective laser melting.* Journal of Alloys and Compounds, 2019. **792**: p. 574-581.

178. Xiao, Z., Chen, C., Hu, Z., Zhu, H., and Zeng, X., *Effect of rescanning cycles on the characteristics of selective laser melting of Ti6Al4V.* Optics & Laser Technology, 2020. **122**: p. 105890.

179. Leung, C.L.A., Marussi, S., Towrie, M., Atwood, R.C., Withers, P.J., and Lee, P.D., *The effect of powder oxidation on defect formation in laser additive manufacturing.* Acta Materialia, 2019. **166**: p. 294-305.

180. Liu, B., Li, B.-Q., and Li, Z., *Selective laser remelting of an additive layer manufacturing process on AlSi10Mg.* Results in Physics, 2019. **12**: p. 982-988.

181. AlMangour, B., Grzesiak, D., and Yang, J.-M., *Scanning strategies for texture and anisotropy tailoring during selective laser melting of TiC/316L stainless steel nanocomposites.* Journal of Alloys and Compounds, 2017. **728**: p. 424-435.

182. Yasa, E. and Kruth, J.P., *Microstructural investigation of Selective Laser Melting 316L stainless steel parts exposed to laser re-melting.* Procedia Engineering, 2011. **19**: p. 389-395.

183. Yao, Y., Li, X., Wang, Y.Y., Zhao, W., Li, G., and Liu, R.P., *Microstructural evolution and mechanical properties of Ti–Zr beta titanium alloy after laser surface remelting.* Journal of Alloys and Compounds, 2014. **583**: p. 43-47.

184. Vaithilingam, J., Goodridge, R.D., Hague, R.J.M., Christie, S.D.R., and Edmondson, S., *The effect of laser remelting on the surface chemistry of Ti6al4V components fabricated by selective laser melting.* Journal of Materials Processing Technology, 2016. **232**: p. 1-8.

185. Gustmann, T., Schwab, H., Kühn, U., and Pauly, S., *Selective laser remelting of an additively manufactured Cu-Al-Ni-Mn shape-memory alloy.* Materials & Design, 2018. **153**: p. 129-138.

186. Griffiths, S., Rossell, M.D., Croteau, J., Vo, N.Q., Dunand, D.C., and Leinenbach, C., *Effect of laser rescanning on the grain microstructure of a selective laser melted Al-Mg-Zr alloy.* Materials Characterization, 2018. **143**: p. 34-42.

187. Ali, H., Ghadbeigi, H., and Mumtaz, K., *Effect of scanning strategies on residual stress and mechanical properties of Selective Laser Melted Ti6Al4V.* Materials Science and Engineering: A, 2018. **712**: p. 175-187.

188. Mercelis, P. and Kruth, J.-P., *Residual stresses in selective laser sintering and selective laser melting.* Rapid Prototyping Journal, 2006. **12**(5): p. 254-265.

189. Shiomi, M., Osakada, K., Nakamura, K., Yamashita, T., and Abe, F., *Residual Stress within Metallic Model Made by Selective Laser Melting Process.* CIRP Annals, 2004. **53**(1): p. 195-198.

190. Wei, K., Lv, M., Zeng, X., Xiao, Z., Huang, G., Liu, M., and Deng, J., *Effect of laser remelting on deposition quality, residual stress, microstructure, and mechanical property of selective laser melting processed Ti-5Al-2.5Sn alloy.* Materials Characterization, 2019. **150**: p. 67-77.

191. Yang, X., Liu, J., Cui, X., Jin, G., Liu, Z., Chen, Y., and Feng, X., *Effect of remelting on microstructure and magnetic properties of Fe-Co-based alloys produced by laser additive manufacturing.* Journal of Physics and Chemistry of Solids, 2019. **130**: p. 210-216.

192. Barba, D., Alabort, C., Tang, Y.T., Viscasillas, M.J., Reed, R.C., and Alabort, E., *On the size and orientation effect in additive manufactured Ti-6Al-4V.* Materials & Design, 2020. **186**: p. 108235.

193. Attar, H., Calin, M., Zhang, L.C., Scudino, S., and Eckert, J., *Manufacture by selective laser melting and mechanical behavior of commercially pure titanium.* Materials Science and Engineering: A, 2014. **593**(Supplement C): p. 170-177.

194. Wysocki, B., Maj, P., Krawczyńska, A., Rożniatowski, K., Zdunek, J., Kurzydłowski, K.J., and Święszkowski, W., *Microstructure and mechanical properties investigation of CP titanium processed by selective laser melting (SLM).* Journal of Materials Processing Technology, 2017. **241**: p. 13-23.

195. Gu, D., Hagedorn, Y.-C., Meiners, W., Meng, G., Batista, R.J.S., Wissenbach, K., and Poprawe, R., *Densification behavior, microstructure evolution, and wear performance of selective laser melting processed commercially pure titanium.* Acta Materialia, 2012. **60**(9): p. 3849-3860.

196. Beese, A.M. and Carroll, B.E., *Review of Mechanical Properties of Ti-6Al-4V Made by Laser-Based Additive Manufacturing Using Powder Feedstock.* JOM, 2016. **68**(3): p. 724-734.

197. Kelly, C.N., Evans, N.T., Irvin, C.W., Chapman, S.C., Gall, K., and Safranski, D.L., *The effect of surface topography and porosity on the tensile fatigue of 3D printed Ti-6Al-4V fabricated by selective laser melting.* Materials Science and Engineering: C, 2019. **98**: p. 726-736.

198. Barbas, A., Bonnet, A.S., Lipinski, P., Pesci, R., and Dubois, G., *Development and mechanical characterization of porous titanium bone substitutes.* Journal of the Mechanical Behavior of Biomedical Materials, 2012. **9**(Supplement C): p. 34-44.

199. Attar, H., Bermingham, M.J., Ehtemam-Haghighi, S., Dehghan-Manshadi, A., Kent, D., and Dargusch, M.S., *Evaluation of the mechanical and wear properties of titanium produced by three different additive manufacturing methods for biomedical application.* Materials Science and Engineering: A, 2019. **760**: p. 339-345.

200. Kang, N., Yuan, H., Coddet, P., Ren, Z., Bernage, C., Liao, H., and Coddet, C., *On the texture, phase and tensile properties of commercially pure Ti produced via selective laser melting assisted by static magnetic field.* Materials Science and Engineering: C, 2017. **70**: p. 405-407.

201. Pehlivan, E., Roudnicka, M., Dzugan, J., Koukolikova, M., Králík, V., Seifi, M., Lewandowski, J.J., Dalibor, D., and Daniel, M., *Effects of build orientation and sample geometry on the mechanical response of miniature CP-Ti Grade 2 strut samples manufactured by laser powder bed fusion.* Additive Manufacturing, 2020. **35**: p. 101403.

202. Bhardwaj, T., Shukla, M., Paul, C.P., and Bindra, K.S., *Direct Energy Deposition - Laser Additive Manufacturing of Titanium-Molybdenum alloy: Parametric studies, microstructure and mechanical properties.* Journal of Alloys and Compounds, 2019. **787**: p. 1238-1248.

203. Ishimoto, T., Hagihara, K., Hisamoto, K., Sun, S.-H., and Nakano, T., *Crystallographic texture control of beta-type Ti–15Mo–5Zr–3Al alloy by selective laser melting for the development of novel implants with a biocompatible low Young's modulus.* Scripta Materialia, 2017. **132**(Supplement C): p. 34-38.

204. Yan, L., Yu, J., Zhong, Y., Gu, Y., Ma, Y., Li, W., Yan, J., Ge, Y., Yin, J., Luo, Y., Mirzasadeghi, A., and Yuan, Y., *Influence of Scanning on Nano Crystalline β-Ti Alloys Fabricated by Selective Laser Melting and Their Applications in Biomedical Science.* Journal of Nanoscience and Nanotechnology, 2020. **20**(3): p. 1605-1612.

205. Schwab, H., Prashanth, G.K., Löber, L., Kühn, U., and Eckert, J., *Selective Laser Melting of Ti-45Nb Alloy.* Metals, 2015. **5**(2): p. 686-694.

206. Schulze, C., Weinmann, M., Schweigel, C., Keßler, O., and Bader, R., *Mechanical Properties of a Newly Additive Manufactured Implant Material Based on Ti-42Nb.* Materials, 2018. **11**(1): p. 124.

207. Weinmann, M., Schnitter, C., Stenzel, M., Markhoff, J., Schulze, C., and Bader, R., *Development of bio-compatible refractory Ti/Nb(/Ta) alloys for application in patient-specific orthopaedic implants.* International Journal of Refractory Metals and Hard Materials, 2018. **75**: p. 126-136.

208. Zhuravleva, K., Bönisch, M., Prashanth, K.G., Hempel, U., Helth, A., Gemming, T., Calin, M., Scudino, S., Schultz, L., Eckert, J., and Gebert, A., *Production of Porous β-Type Ti–40Nb Alloy for Biomedical Applications: Comparison of Selective Laser Melting and Hot Pressing.* Materials, 2013. **6**(12): p. 5700-5712.

209. Wei, J., Sun, H., Zhang, D., Gong, L., Lin, J., and Wen, C., *Influence of Heat Treatments on Microstructure and Mechanical Properties of Ti–26Nb Alloy Elaborated In Situ by Laser Additive Manufacturing with Ti and Nb Mixed Powder.* Materials (Basel, Switzerland), 2018. **12**(1): p. 61.

210. Fischer, M., Joguet, D., Robin, G., Peltier, L., and Laheurte, P., *In situ elaboration of a binary Ti–26Nb alloy by selective laser melting of elemental titanium and niobium mixed powders.* Materials Science and Engineering: C, 2016. **62**: p. 852-859.

211. Zhou, L., Yuan, T., Li, R., Tang, J., Wang, M., Li, L., and Chen, C., *Microstructure and mechanical performance tailoring of Ti-13Nb-13Zr alloy fabricated by selective laser melting after post heat treatment.* Journal of Alloys and Compounds, 2019. **775**: p. 1164-1176.

212. Speirs, M., Humbeeck, J.V., Schrooten, J., Luyten, J., and Kruth, J.P., *The Effect of Pore Geometry on the Mechanical Properties of Selective Laser Melted Ti-13Nb-13Zr Scaffolds.* Procedia CIRP, 2013. **5**: p. 79-82.

213. Li, Y., Ding, Y., Munir, K., Lin, J., Brandt, M., Atrens, A., Xiao, Y., Kanwar, J.R., and Wen, C., *Novel β-Ti35Zr28Nb alloy scaffolds manufactured using selective laser melting for bone implant applications.* Acta Biomaterialia, 2019(87): p. 273-284.

214. Luo, J.P., Sun, J.F., Huang, Y.J., Zhang, J.H., Zhang, Y.D., Zhao, D.P., and Yan, M., *Low-modulus biomedical Ti–30Nb–5Ta–3Zr additively manufactured by Selective Laser Melting and its biocompatibility.* Materials Science and Engineering: C, 2019. **97**: p. 275-284.

215. Hafeez, N., Liu, S., Lu, E., Wang, L., Liu, R., lu, W., and Zhang, L.-C., *Mechanical behavior and phase transformation of β-type Ti-35Nb-2Ta-3Zr alloy fabricated by 3D-Printing.* Journal of Alloys and Compounds, 2019. **790**: p. 117-126.

216. Hernandez, J., Li, S.J., Martinez, E., Murr, L.E., Pan, X.M., Amato, K.N., Cheng, X.Y., Yang, F., Terrazas, C.A., Gaytan, S.M., Hao, Y.L., Yang, R., Medina, F., and Wicker, R.B., *Microstructures and Hardness Properties for β-Phase Ti–24Nb–4Zr–7.9Sn Alloy Fabricated by Electron Beam Melting.* Journal of Materials Science & Technology, 2013. **29**(11): p. 1011-1017.

217. Liu, Y.J., Wang, H.L., Li, S.J., Wang, S.G., Wang, W.J., Hou, W.T., Hao, Y.L., Yang, R., and Zhang, L.C., *Compressive and fatigue behavior of beta-type titanium porous structures fabricated by electron beam melting.* Acta Materialia, 2017. **126**: p. 58-66.

218. Zhou, L., Yuan, T., Li, R., Tang, J., Wang, G., and Guo, K., *Selective laser melting of pure tantalum: Densification, microstructure and mechanical behaviors.* Materials Science and Engineering: A, 2017. **707**(Supplement C): p. 443-451.

219. Huang, S., Sing, S.L., Delooze, G., Wilson, R., and Yeong, W.Y., *Laser powder bed fusion of titanium-tantalum alloys: Compositions and designs for biomedical applications.* Journal of the Mechanical Behavior of Biomedical Materials, 2020: p. 103775.

220. Zhao, D., Han, C., Li, Y., Li, J., Zhou, K., Wei, Q., Liu, J., and Shi, Y., *Improvement on mechanical properties and corrosion resistance of titanium-tantalum alloys in-situ fabricated via selective laser melting.* Journal of Alloys and Compounds, 2019. **804**: p. 288-298.

221. Sing, S.L., Yeong, W.Y., and Wiria, F.E., *Selective laser melting of titanium alloy with 50 wt% tantalum: Microstructure and mechanical properties.* Journal of Alloys and Compounds, 2016. **660**: p. 461-470.

222. Soro, N., Attar, H., Brodie, E., Veidt, M., Molotnikov, A., and Dargusch, M.S., *Evaluation of the mechanical compatibility of additively manufactured porous Ti–25Ta alloy for load-bearing implant applications.* Journal of the Mechanical Behavior of Biomedical Materials, 2019. **97**: p. 149-158.

223. Liu, Y., Li, S., Hou, W., Wang, S., Hao, Y., Yang, R., Sercombe, T.B., and Zhang, L.-C., *Electron Beam Melted Beta-type Ti–24Nb–4Zr–8Sn Porous Structures With High Strength-to-Modulus Ratio.* Journal of Materials Science & Technology, 2016. **32**(6): p. 505-508.

224. Thijs, L., Montero Sistiaga, M.L., Wauthle, R., Xie, Q., Kruth, J.-P., and Van Humbeeck, J., *Strong morphological and crystallographic texture and resulting yield strength anisotropy in selective laser melted tantalum.* Acta Materialia, 2013. **61**(12): p. 4657-4668.

225. Wauthle, R., van der Stok, J., Amin Yavari, S., Van Humbeeck, J., Kruth, J.-P., Zadpoor, A.A., Weinans, H., Mulier, M., and Schrooten, J., *Additively manufactured porous tantalum implants.* Acta Biomaterialia, 2015. **14**: p. 217-225.

226. Livescu, V., Knapp, C.M., Gray, G.T., Martinez, R.M., Morrow, B.M., and Ndefru, B.G., *Additively manufactured tantalum microstructures.* Materialia, 2018. **1**: p. 15-24.

227. Sing, S.L., Edith Wiria, F., and Yeong, W.Y., *Selective laser melting of lattice structures: A statistical approach to manufacturability and mechanical behavior*. Vol. 49. 2018. 170-180.

228. Sing, S.L., Wiria, F.E., and Yeong, W.Y., *Selective laser melting of titanium alloy with 50 wt% tantalum: Effect of laser process parameters on part quality.* International Journal of Refractory Metals and Hard Materials, 2018. **77**: p. 120-127.

229. Zhang, J. and Fatemi, A., *Surface roughness effect on multiaxial fatigue behavior of additive manufactured metals and its modeling.* Theoretical and Applied Fracture Mechanics, 2019. **103**: p. 102260.

230. Yu, H., Li, F., Wang, Z., and Zeng, X., *Fatigue performances of selective laser melted Ti-6Al-4V alloy: Influence of surface finishing, hot isostatic pressing and heat treatments.* International Journal of Fatigue, 2019. **120**: p. 175-183.

231. Ahmadi, S.M., Hedayati, R., Li, Y., Lietaert, K., Tümer, N., Fatemi, A., Rans, C.D., Pouran, B., Weinans, H., and Zadpoor, A.A., *Fatigue performance of additively manufactured meta-biomaterials: The effects of topology and material type.* Acta Biomaterialia, 2018. **65**: p. 292-304.

232. Leuders, S., Thöne, M., Riemer, A., Niendorf, T., Tröster, T., Richard, H.A., and Maier, H.J., *On the mechanical behaviour of titanium alloy TiAl6V4 manufactured by selective laser melting: Fatigue resistance and crack growth performance.* International Journal of Fatigue, 2013. **48**(Supplement C): p. 300-307.

233. Edwards, P. and Ramulu, M., *Fatigue performance evaluation of selective laser melted Ti–6Al–4V.* Materials Science and Engineering: A, 2014. **598**(Supplement C): p. 327-337.

234. Parry, L., Ashcroft, I.A., and Wildman, R.D., *Understanding the effect of laser scan strategy on residual stress in selective laser melting through thermo-mechanical simulation.* Additive Manufacturing, 2016. **12**: p. 1-15.

235. Chastand, V., Quaegebeur, P., Maia, W., and Charkaluk, E., *Comparative study of fatigue properties of Ti-6Al-4V specimens built by electron beam melting (EBM) and selective laser melting (SLM).* Materials Characterization, 2018. **143**: p. 76-81.

236. Lu, Y., Wu, S., Gan, Y., Huang, T., Yang, C., Junjie, L., and Lin, J., *Study on the microstructure, mechanical property and residual stress of SLM Inconel-718 alloy manufactured by differing island scanning strategy.* Optics & Laser Technology, 2015. **75**: p. 197-206.

237. Mugwagwa, L., Dimitrov, D., Matope, S., and Yadroitsev, I., *Evaluation of the impact of scanning strategies on residual stresses in selective laser melting.* The International Journal of Advanced Manufacturing Technology, 2019. **102**(5): p. 2441-2450.

238. Bleys, P., Kruth, J.P., Lauwers, B., Schacht, B., Balasubramanian, V., Froyen, L., and Van Humbeeck, J., *Surface and Sub-Surface Quality of Steel after EDM.* Advanced Engineering Materials, 2006. **8**(1-2): p. 15-25.

239. Shoba, C., Ramanaiah, N., and Rao, D.N., *Influence of dislocation density on the residual stresses induced while machining Al/SiC/RHA hybrid composites.* Journal of Materials Research and Technology, 2015. **4**(3): p. 273-277.

240. Baczmański, A., Wierzbanowski, K., Lipinski, P., Bacroix, B., and Lodini, A., *Residual stresses, dislocation density and recrystallization process.* Journal of Neutron Research, 2007. **15**: p. 281-287.

241. Beretta, S. and Romano, S., *A comparison of fatigue strength sensitivity to defects for materials manufactured by AM or traditional processes.* International Journal of Fatigue, 2017. **94**: p. 178-191.

242. Benedetti, M., Fontanari, V., Bandini, M., Zanini, F., and Carmignato, S., *Low- and high-cycle fatigue resistance of Ti-6Al-4V ELI additively manufactured via selective laser melting: Mean stress and defect sensitivity.* International Journal of Fatigue, 2018. **107**: p. 96-109.

243. Greitemeier, D., Palm, F., Syassen, F., and Melz, T., *Fatigue performance of additive manufactured TiAl6V4 using electron and laser beam melting.* International Journal of Fatigue, 2017. **94**: p. 211-217.

244. Leung, C.L.A., Marussi, S., Atwood, R.C., Towrie, M., Withers, P.J., and Lee, P.D., *In situ X-ray imaging of defect and molten pool dynamics in laser additive manufacturing.* Nature Communications, 2018. **9**(1): p. 1355.

245. Romano, S., Abel, A., Gumpinger, J., Brandão, A.D., and Beretta, S., *Quality control of AlSi10Mg produced by SLM: Metallography versus CT scans for critical defect size assessment.* Additive Manufacturing, 2019. **28**: p. 394-405.

246. Romano, S., Brückner-Foit, A., Brandão, A., Gumpinger, J., Ghidini, T., and Beretta, S., *Fatigue properties of AlSi10Mg obtained by additive manufacturing: Defect-based modelling and prediction of fatigue strength.* Engineering Fracture Mechanics, 2018. **187**: p. 165-189.

247. Romano, S., Miccoli, S., and Beretta, S., *A new FE post-processor for probabilistic fatigue assessment in the presence of defects and its application to AM parts.* International Journal of Fatigue, 2019. **125**: p. 324-341.

248. Chen, Z., Cao, S., Wu, X., and Davies, C.H.J., *13 - Surface roughness and fatigue properties of selective laser melted Ti–6Al–4V alloy,* in *Additive Manufacturing for the Aerospace Industry,* F. Froes and R. Boyer, Editors. 2019, Elsevier. p. 283-299.

249. Boyan, B.D., Batzer, R., Kieswetter, K., Liu, Y., Cochran, D.L., Szmuckler-Moncler, S., Dean, D.D., and Schwartz, Z., *Titanium surface roughness alters responsiveness of MG63 osteoblast-like cells to 1α,25-(OH)2D3.* Journal of Biomedical Materials Research, 1998. **39**(1): p. 77-85.

250. Cohen, D.J., Cheng, A., Sahingur, K., Clohessy, R.M., Hopkins, L.B., Boyan, B.D., and Schwartz, Z., *Performance of laser sintered Ti–6Al–4V implants with bone-inspired porosity*

and micro/nanoscale surface roughness in the rabbit femur. Biomedical Materials, 2017. **12**(2): p. 025021.

251. Shan, L., Abdul Amir, H.K., Al-Furjan, M.S.H., Weng, W., Gong, Y., Cheng, K., Zhou, M., Dong, L., Chen, G., Takriff, M.S., and Abu Bakar, S., *In Situ Controlled Surface Microstructure of 3D Printed Ti Alloy to Promote Its Osteointegration.* Materials, 2019. **12**(5).

252. Amin Yavari, S., Wauthle, R., van der Stok, J., Riemslag, A.C., Janssen, M., Mulier, M., Kruth, J.P., Schrooten, J., Weinans, H., and Zadpoor, A.A., *Fatigue behavior of porous biomaterials manufactured using selective laser melting.* Materials Science and Engineering: C, 2013. **33**(8): p. 4849-4858.

253. Hrabe, N.W., Heinl, P., Flinn, B., Körner, C., and Bordia, R.K., *Compression-compression fatigue of selective electron beam melted cellular titanium (Ti-6Al-4V).* Journal of Biomedical Materials Research Part B: Applied Biomaterials, 2011. **99B**(2): p. 313-320.

254. Zadpoor, A.A., *Mechanical performance of additively manufactured meta-biomaterials.* Acta Biomaterialia, 2019. **85**: p. 41-59.

255. Niendorf, T., Brenne, F., and Schaper, M., *Lattice Structures Manufactured by SLM: On the Effect of Geometrical Dimensions on Microstructure Evolution During Processing.* Metallurgical and Materials Transactions B, 2014. **45**(4): p. 1181-1185.

256. Amin Yavari, S., Ahmadi, S.M., Wauthle, R., Pouran, B., Schrooten, J., Weinans, H., and Zadpoor, A.A., *Relationship between unit cell type and porosity and the fatigue behavior of selective laser melted meta-biomaterials.* Journal of the Mechanical Behavior of Biomedical Materials, 2015. **43**: p. 91-100.

257. Köhnen, P., Haase, C., Bültmann, J., Ziegler, S., Schleifenbaum, J.H., and Bleck, W., *Mechanical properties and deformation behavior of additively manufactured lattice structures of stainless steel.* Materials & Design, 2018. **145**: p. 205-217.

258. Mazur, M., Leary, M., McMillan, M., Sun, S., Shidid, D., and Brandt, M., *5 - Mechanical properties of Ti6Al4V and AlSi12Mg lattice structures manufactured by Selective Laser Melting (SLM),* in *Laser Additive Manufacturing*. 2017, Woodhead Publishing. p. 119-161.

259. Ashby, M.F., *The properties of foams and lattices.* Philosophical Transactions of the Royal Society A: Mathematical, Physical and Engineering Sciences, 2006. **364**(1838): p. 15-30.

260. Gibson, L.J., *Cellular materials in nature and medicine*, ed. M.F. Ashby and B.A. Harley. 2010, New York: New York : Cambridge University Press.

261. Onal, E., Frith, E.J., Jurg, M., Wu, X., and Molotnikov, A., *Mechanical Properties and In Vitro Behavior of Additively Manufactured and Functionally Graded Ti6Al4V Porous Scaffolds.* Metals, 2018. **8**(4).

262. Soro, N., Attar, H., Wu, X., and Dargusch, M.S., *Investigation of the structure and mechanical properties of additively manufactured Ti-6Al-4V biomedical scaffolds designed with a Schwartz primitive unit-cell.* Materials Science and Engineering: A, 2019. **745**: p. 195-202.

263. Liang, H., Xie, D., Mao, Y., Shi, J., Wang, C., Shen, L., and Tian, Z., *The Size Effect on Forming Quality of Ti–6Al–4V Solid Struts Fabricated via Laser Powder Bed Fusion.* Metals, 2019. **9**(4).

264. Burton, H.E., Eisenstein, N.M., Lawless, B.M., Jamshidi, P., Segarra, M.A., Addison, O., Shepherd, D.E.T., Attallah, M.M., Grover, L.M., and Cox, S.C., *The design of additively manufactured lattices to increase the functionality of medical implants.* Materials Science and Engineering: C, 2019. **94**: p. 901-908.

265. Sun, Y.Y., Gulizia, S., Fraser, D., Oh, C.H., Lu, S.L., and Qian, M., *Layer Additive Production or Manufacturing of Thick Sections of Ti-6Al-4V by Selective Electron Beam Melting (SEBM).* JOM, 2017. **69**(10): p. 1836-1843.

266. Cameron, A.R., Frith, J.E., and Cooper-White, J.J., *The influence of substrate creep on mesenchymal stem cell behaviour and phenotype.* Biomaterials, 2011. **32**(26): p. 5979.

267. Attar, H., Ehtemam-Haghighi, S., Soro, N., Kent, D., and Dargusch, M.S., *Additive manufacturing of low-cost porous titanium-based composites for biomedical applications: Advantages, challenges and opinion for future development.* Journal of Alloys and Compounds, 2020. **827**: p. 154263.

268. Alabort, E., Barba, D., and Reed, R.C., *Design of metallic bone by additive manufacturing.* Scripta Materialia, 2019. **164**: p. 110-114.

269. Bobbert, F.S.L., Lietaert, K., Eftekhari, A.A., Pouran, B., Ahmadi, S.M., Weinans, H., and Zadpoor, A.A., *Additively manufactured metallic porous biomaterials based on minimal surfaces: A unique combination of topological, mechanical, and mass transport properties.* Acta Biomaterialia, 2017. **53**: p. 572-584.

270. Ataee, A., Li, Y., Brandt, M., and Wen, C., *Ultrahigh-strength titanium gyroid scaffolds manufactured by selective laser melting (SLM) for bone implant applications.* Acta Materialia, 2018. **158**: p. 354-368.

271. Rumpler, M., Woesz, A., Dunlop, J.W.C., van Dongen, J.T., and Fratzl, P., *The effect of geometry on three-dimensional tissue growth.* Journal of The Royal Society Interface, 2008. **5**(27): p. 1173-1180.

272. Knychala, J., Bouropoulos, N., Catt, C.J., Katsamenis, O.L., Please, C.P., and Sengers, B.G., *Pore Geometry Regulates Early Stage Human Bone Marrow Cell Tissue Formation and Organisation.* Annals of Biomedical Engineering, 2013. **41**(5): p. 917-930.

273. Bidan, C.M., Kommareddy, K.P., Rumpler, M., Kollmannsberger, P., Fratzl, P., and Dunlop, J.W.C., *Geometry as a Factor for Tissue Growth: Towards Shape Optimization of Tissue Engineering Scaffolds.* Advanced Healthcare Materials, 2013. **2**(1): p. 186-194.

274. Montazerian, H., Davoodi, E., Asadi-Eydivand, M., Kadkhodapour, J., and Solati-Hashjin, M., *Porous scaffold internal architecture design based on minimal surfaces: A compromise between permeability and elastic properties.* Materials & Design, 2017. **126**: p. 98-114.

275. Bobbert, F.S.L. and Zadpoor, A.A., *Effects of bone substitute architecture and surface properties on cell response, angiogenesis, and structure of new bone.* Journal of Materials Chemistry B, 2017. **5**(31): p. 6175-6192.

276. Li, F., Li, J., Huang, T., Kou, H., and Zhou, L., *Compression fatigue behavior and failure mechanism of porous titanium for biomedical applications.* Journal of the Mechanical Behavior of Biomedical Materials, 2017. **65**: p. 814-823.

277. Hedayati, R., Janbaz, S., Sadighi, M., Mohammadi-Aghdam, M., and Zadpoor, A.A., *How does tissue regeneration influence the mechanical behavior of additively manufactured*

porous biomaterials? Journal of the Mechanical Behavior of Biomedical Materials, 2017. **65**: p. 831-841.

278. Ratner, B.D., Hoffman, A.S., Schoen, F.J., and Lemons, J.E., *Introduction - Biomaterials Science: An Evolving, Multidisciplinary Endeavor*, in *Biomaterials Science (Third Edition)*. 2013, Academic Press. p. xxv-xxxix.

279. Kang, S., Kim, J., Kim, S., Wufuer, M., Park, S., Kim, Y., Choi, D., Jin, X., Kim, Y., Huang, Y., Jeon, B., Choi, T.H., Park, J.-U., and Lee, Y., *Efficient reduction of fibrous capsule formation around silicone breast implants densely grafted with 2-methacryloyloxyethyl phosphorylcholine (MPC) polymers by heat-induced polymerization.* Biomaterials Science, 2020. **8**(6): p. 1580-1591.

280. Schwartz, Z. and Boyan, B.D., *Underlying mechanisms at the bone–biomaterial interface.* Journal of Cellular Biochemistry, 1994. **56**(3): p. 340-347.

281. Wang, H., Li, Q., Wang, Q., Zhang, H., Shi, W., Gan, H., Song, H., and Wang, Z., *Enhanced repair of segmental bone defects in rabbit radius by porous tantalum scaffolds modified with the RGD peptide.* Journal of Materials Science: Materials in Medicine, 2017. **28**(3): p. 50.

282. Mas-Moruno, C., Garrido, B., Rodriguez, D., Ruperez, E., and Gil, F.J., *Biofunctionalization strategies on tantalum-based materials for osseointegrative applications.* Journal of Materials Science: Materials in Medicine, 2015. **26**(2): p. 109.

283. Holzapfel, B.M., Reichert, J., Schantz, J., Gbureck, U., Rackwitz, L., Noth, U., Jakob, F., Rudert, M., Groll, J., and Hutmacher, D., *How smart do biomaterials need to be? A translational science and clinical point of view*, in *Adv. Drug Deliv. Rev.* 2013. p. 581-603.

284. Milazzo, M., Contessi Negrini, N., Scialla, S., Marelli, B., Farè, S., Danti, S., and Buehler, M.J., *Additive Manufacturing Approaches for Hydroxyapatite-Reinforced Composites.* Advanced Functional Materials, 2019. **0**(0): p. 1903055.

285. Ho-Shui-Ling, A., Bolander, J., Rustom, L.E., Johnson, A.W., Luyten, F.P., and Picart, C., *Bone regeneration strategies: Engineered scaffolds, bioactive molecules and stem cells current stage and future perspectives.* Biomaterials, 2018. **180**: p. 143-162.

286. Bose, S., Ke, D., Sahasrabudhe, H., and Bandyopadhyay, A., *Additive manufacturing of biomaterials.* Progress in Materials Science, 2018. **93**: p. 45-111.

287. Wegst, U.G.K., Bai, H., Saiz, E., Tomsia, A.P., and Ritchie, R.O., *Bioinspired structural materials.* Nature Materials, 2015. **14**(1): p. 23-36.

288. Wang, F., Li, C., Zhang, S., and Liu, H., *Tantalum coated on titanium dioxide nanotubes by plasma spraying enhances cytocompatibility for dental implants.* Surface and Coatings Technology, 2020. **382**: p. 125161.

289. Shuai, C., Zhou, Y., Yang, Y., Gao, C., Peng, S., and Wang, G., *Ag-Introduced Antibacterial Ability and Corrosion Resistance for Bio-Mg Alloys.* BioMed Research International, 2018. **2018**: p. 6023460.

290. Zadpoor, A.A., *Bone tissue regeneration: the role of scaffold geometry.* Biomaterials Science, 2015. **3**(2): p. 231-245.

291. Standardization, I.O.f., *Biological Evaluation of Medical Devices*, in *Part 5: Tests for in vitro cytotoxicity*. 2009: Switzerland.

292. Orr, A.W., Helmke, B.P., Blackman, B.R., and Schwartz, M.A., *Mechanisms of Mechanotransduction.* Developmental Cell, 2006. **10**(1): p. 11-20.

293. Boyan, B.D., Cheng, A., Olivares-Navarrete, R., and Schwartz, Z., *Implant Surface Design Regulates Mesenchymal Stem Cell Differentiation and Maturation.* Advances in Dental Research, 2016. **28**(1): p. 10-17.

294. Wrobel, E., Leszczynska, J., and Brzoska, E., *The Characteristics Of Human Bone-Derived Cells (HBDCS) during osteogenesis in vitro.* Cellular & molecular biology letters, 2016. **21**: p. 26-26.

295. Yang, L., Ge, L., and van Rijn, P., *Synergistic Effect of Cell-Derived Extracellular Matrices and Topography on Osteogenesis of Mesenchymal Stem Cells.* ACS Applied Materials & Interfaces, 2020.

296. Lee, J., Abdeen, A.A., Huang, T.H., and Kilian, K.A., *Controlling cell geometry on substrates of variable stiffness can tune the degree of osteogenesis in human mesenchymal stem cells.* Journal of the Mechanical Behavior of Biomedical Materials, 2014. **38**: p. 209-218.

297. Frith, J. and Genever, P., *Transcriptional Control of Mesenchymal Stem Cell Differentiation.* Transfusion Medicine and Hemotherapy, 2008. **35**(3): p. 216-227.

298. Jia, B., Yang, H., Han, Y., Zhang, Z., Qu, X., Zhuang, Y., Wu, Q., Zheng, Y., and Dai, K., *In vitro and in vivo studies of Zn-Mn biodegradable metals designed for orthopedic applications.* Acta Biomaterialia, 2020. **108**: p. 358-372.

299. Conserva, E., Pisciotta, A., Borghi, F., Nasi, M., Pecorini, S., Bertoni, L., de Pol, A., Consolo, U., and Carnevale, G., *Titanium Surface Properties Influence the Biological Activity and FasL Expression of Craniofacial Stromal Cells.* Stem cells international, 2019. **2019**: p. 4670560-4670560.

300. Lu, M., Zhuang, X., Tang, K., Wu, P., Guo, X., Yin, L., Cao, H., and Zou, D., *Intrinsic Surface Effects of Tantalum and Titanium on Integrin α5β1/ ERK1/2 Pathway-Mediated Osteogenic Differentiation in Rat Bone Mesenchymal Stromal Cells.* Cellular Physiology and Biochemistry, 2018. **51**(2): p. 589-609.

301. Blanquer, A., Musilkova, J., Barrios, L., Ibáñez, E., Vandrovcova, M., Pellicer, E., Sort, J., Bacakova, L., and Nogués, C., *Cytocompatibility assessment of Ti-Zr-Pd-Si-(Nb) alloys with low Young's modulus, increased hardness, and enhanced osteoblast differentiation for biomedical applications.* Journal of Biomedical Materials Research Part B: Applied Biomaterials, 2018. **106**(2): p. 834-842.

302. Wilkinson, A., Hewitt, R.N., McNamara, L.E., McCloy, D., Dominic Meek, R.M., and Dalby, M.J., *Biomimetic microtopography to enhance osteogenesis in vitro.* Acta Biomaterialia, 2011. **7**(7): p. 2919-2925.

303. Li, J., Mutreja, I., Tredinnick, S., Jermy, M., Hooper, G.J., and Woodfield, T.B.F., *Hydrodynamic control of titania nanotube formation on Ti-6Al-4V alloys enhances osteogenic differentiation of human mesenchymal stromal cells.* Materials Science and Engineering: C, 2020. **109**: p. 110562.

304. Hulsart-Billström, G., Dawson, J.I., Hofmann, S., Müller, R., Stoddart, M.J., Alini, M., Redl, H., El Haj, A., Brown, R., Salih, V., Hilborn, J., Larsson, S., and Oreffo, R.O., *A surprisingly poor correlation between in vitro and in vivo testing of biomaterials for bone regeneration: results of a multicentre analysis.* European cells & materials, 2016. **31**: p. 312.

305. Guo, Y., Wu, J., Xie, K., Tan, J., Yang, Y., Zhao, S., Wang, L., Jiang, W., and Hao, Y., *Study of bone regeneration and osseointegration effect of a novel selective laser melted titanium-tantalum-niobium-zirconium alloy scaffold.* ACS Biomaterials Science & Engineering, 2019.

306. Li, G., Wang, L., Pan, W., Yang, F., Jiang, W., Wu, X., Kong, X., Dai, K., and Hao, Y., *In vitro and in vivo study of additive manufactured porous Ti6Al4V scaffolds for repairing bone defects.* Scientific Reports, 2016. **6**(1): p. 34072.

307. Amin Yavari, S., van der Stok, J., Chai, Y.C., Wauthle, R., Tahmasebi Birgani, Z., Habibovic, P., Mulier, M., Schrooten, J., Weinans, H., and Zadpoor, A.A., *Bone regeneration performance of surface-treated porous titanium.* Biomaterials, 2014. **35**(24): p. 6172-6181.

308. Taniguchi, N., Fujibayashi, S., Takemoto, M., Sasaki, K., Otsuki, B., Nakamura, T., Matsushita, T., Kokubo, T., and Matsuda, S., *Effect of pore size on bone ingrowth into porous titanium implants fabricated by additive manufacturing: An in vivo experiment.* Materials Science and Engineering: C, 2016. **59**: p. 690-701.

309. Stiehler, M., Lind, M., Mygind, T., Baatrup, A., Dolatshahi-Pirouz, A., Li, H., Foss, M., Besenbacher, F., Kassem, M., and Bünger, C., *Morphology, proliferation, and osteogenic differentiation of mesenchymal stem cells cultured on titanium, tantalum, and chromium surfaces.* Journal of Biomedical Materials Research Part A, 2008. **86A**(2): p. 448-458.

310. Tang, Z., Xie, Y., Yang, F., Huang, Y., Wang, C., Dai, K., Zheng, X., and Zhang, X., *Porous Tantalum Coatings Prepared by Vacuum Plasma Spraying Enhance BMSCs Osteogenic Differentiation and Bone Regeneration In Vitro and In Vivo.* PLOS ONE, 2013. **8**(6): p. e66263.

311. Zhu, Y., Gu, Y., Qiao, S., Zhou, L., Shi, J., and Lai, H., *Bacterial and mammalian cells adhesion to tantalum-decorated micro-/nano-structured titanium.* Journal of Biomedical Materials Research Part A, 2017. **105**(3): p. 871-878.

312. Li, X., Wang, L., Yu, X., Feng, Y., Wang, C., Yang, K., and Su, D., *Tantalum coating on porous Ti6Al4V scaffold using chemical vapor deposition and preliminary biological evaluation.* Materials Science and Engineering: C, 2013. **33**(5): p. 2987-2994.

313. Sagomonyants, K.B., Hakim-Zargar, M., Jhaveri, A., Aronow, M.S., and Gronowicz, G., *Porous tantalum stimulates the proliferation and osteogenesis of osteoblasts from elderly female patients.* Journal of Orthopaedic Research, 2011. **29**(4): p. 609-616.

314. Balla, V.K., Bodhak, S., Bose, S., and Bandyopadhyay, A., *Porous tantalum structures for bone implants: Fabrication, mechanical and in vitro biological properties.* Acta Biomaterialia, 2010. **6**(8): p. 3349-3359.

315. Balla, V.K., Banerjee, S., Bose, S., and Bandyopadhyay, A., *Direct laser processing of a tantalum coating on titanium for bone replacement structures.* Acta Biomaterialia, 2010. **6**(6): p. 2329-2334.

316. Tae-Sik, J., Hyun-Do, J., Sungwon, K., Byeong-Seok, M., Jaeuk, B., Cheonil, P., Juha, S., and Hyoun-Ee, K., *Multiscale porous titanium surfaces via a two-step etching process for improved mechanical and biological performance.* Biomedical Materials, 2017. **12**(2): p. 025008.

317. Wang, L., Hu, X., Ma, X., Ma, Z., Zhang, Y., Lu, Y., Li, X., Lei, W., and Feng, Y., *Promotion of osteointegration under diabetic conditions by tantalum coating-based surface*

modification on 3-dimensional printed porous titanium implants. Colloids and Surfaces B: Biointerfaces, 2016. **148**: p. 440-452.

318. Blanco, J.F., Sánchez-Guijo, F.M., Carrancio, S., Muntion, S., García-Briñon, J., and del Cañizo, M.-C., *Titanium and tantalum as mesenchymal stem cell scaffolds for spinal fusion: an in vitro comparative study.* European Spine Journal, 2011. **20**(3): p. 353.

319. Myllymaa, S., Kaivosoja, E., Myllymaa, K., Sillat, T., Korhonen, H., Lappalainen, R., and Konttinen, Y.T., *Adhesion, spreading and osteogenic differentiation of mesenchymal stem cells cultured on micropatterned amorphous diamond, titanium, tantalum and chromium coatings on silicon.* Journal of Materials Science Materials in Medicine, 2010. **21**(1): p. 329-341.

320. Sagomonyants Karen, B., Hakim-Zargar, M., Jhaveri, A., Aronow Michael, S., and Gronowicz, G., *Porous tantalum stimulates the proliferation and osteogenesis of osteoblasts from elderly female patients.* Journal of Orthopaedic Research, 2010. **29**(4): p. 609-616.

321. Zhou, Y.-L., Niinomi, M., Akahori, T., Nakai, M., and Fukui, H., *Comparison of Various Properties between Titanium-Tantalum Alloy and Pure Titanium for Biomedical Applications.* MATERIALS TRANSACTIONS, 2007. **48**(3): p. 380-384.

322. Zeng, G., Zahiri, S.H., Gulizia, S., Chen, Y., Xu, C., Chen, X.-B., and Cole, I., *A comparative study of cell growth on a cold sprayed Ti–Ta composite.* Journal of Alloys and Compounds, 2020. **826**: p. 154014.

323. Khang, D., Lu, J., Yao, C., Haberstroh, K.M., and Webster, T.J., *The role of nanometer and sub-micron surface features on vascular and bone cell adhesion on titanium.* Biomaterials, 2008. **29**(8): p. 970-983.

324. Hemmersam, A.G., Foss, M., Chevallier, J., and Besenbacher, F., *Adsorption of fibrinogen on tantalum oxide, titanium oxide and gold studied by the QCM-D technique.* Colloids and Surfaces B: Biointerfaces, 2005. **43**(3): p. 208-215.

325. Capellato, P., Riedel, N.A., Williams, J.D., Machado, J.P.B., Popat, K.C., and Claro, A.P.R.A., *Surface Modification on Ti-30Ta Alloy for Biomedical Application.* Engineering, 2013. **Vol.05No.09**: p. 7.

326. Williams, D.F., *On the mechanisms of biocompatibility.* Biomaterials, 2008. **29**(20): p. 2941-2953.

327. Dittrick, S., Balla, V.K., Bose, S., and Bandyopadhyay, A., *Wear performance of laser processed tantalum coatings.* Materials Science and Engineering: C, 2011. **31**(8): p. 1832-1835.

328. Niinomi, M. and Boehlert, C.J., *Titanium Alloys for Biomedical Applications*, in *Advances in Metallic Biomaterials: Tissues, Materials and Biological Reactions*. 2015, Springer Heidelberg: Heidelberg. p. 179-213.

329. Nag, S., Banerjee, R., and Fraser, H.L., *A novel combinatorial approach for understanding microstructural evolution and its relationship to mechanical properties in metallic biomaterials.* Acta Biomaterialia, 2007. **3**(3): p. 369-376.

330. Lin, C.-W., Ju, C.-P., and Lin, J.-H.C., *Comparison among Mechanical Properties of Investment-Cast c.p. Ti, Ti-6Al-7Nb and Ti-15Mo-1Bi Alloys.* MATERIALS TRANSACTIONS, 2004. **45**(10): p. 3028-3032.

331. Trillo, E.A., Ortiz, C., Dickerson, P., Villa, R., Stafford, S.W., and Murr, L.E., *Evaluation of mechanical and corrosion biocompatibility of TiTa alloys.* Journal of Materials Science: Materials in Medicine, 2001. **12**(4): p. 283-292.

332. Feenstra, D.R., Cruz, V., Gao, X., Molotnikov, A., and Birbilis, N., *Effect of build height on the properties of large format stainless steel 316L fabricated via directed energy deposition.* Additive Manufacturing, 2020. **34**: p. 101205.

333. Xiao, W., Li, S., Wang, C., Shi, Y., Mazumder, J., Xing, H., and Song, L., *Multi-scale simulation of dendrite growth for direct energy deposition of nickel-based superalloys.* Materials & Design, 2019. **164**: p. 107553.

334. Tedman-Jones, S.N., McDonald, S.D., Bermingham, M.J., StJohn, D.H., and Dargusch, M.S., *A new approach to nuclei identification and grain refinement in titanium alloys.* Journal of Alloys and Compounds, 2019. **794**: p. 268-284.

335. Bania, P.J., *Beta titanium alloys and their role in the titanium industry.* JOM, 1994. **46**(7): p. 16-19.

336. Kempen, K., Thijs, L., Van Humbeeck, J., and Kruth, J.P., *Processing AlSi10Mg by selective laser melting: parameter optimisation and material characterisation.* Materials Science and Technology, 2015. **31**(8): p. 917-923.

337. Kruth, J.-P., Dadbakhsh, S., Vrancken, B., Kempen, K., Vleugels, J., and Van Humbeeck, J., *Additive Manufacturing of Metals via Selective Laser Melting: Process Aspects and Material Developments*, in *Additive Manufacturing*. 2015, CRC Press. p. 69-99.

338. Yadroitsev, I., Gusarov, A., Yadroitsava, I., and Smurov, I., *Single track formation in selective laser melting of metal powders.* Journal of Materials Processing Technology, 2010. **210**(12): p. 1624-1631.

339. Seede, R., Shoukr, D., Zhang, B., Whitt, A., Gibbons, S., Flater, P., Elwany, A., Arroyave, R., and Karaman, I., *An ultra-high strength martensitic steel fabricated using selective laser melting additive manufacturing: Densification, microstructure, and mechanical properties.* Acta Materialia, 2020. **186**: p. 199-214.

340. Brandt, M., *The role of lasers in additive manufacturing*, in *Laser Additive Manufacturing*. 2017, Woodhead Publishing: Kent. p. 1-18.

341. Cunningham, R., Narra, S.P., Montgomery, C., Beuth, J., and Rollett, A.D., *Synchrotron-Based X-ray Microtomography Characterization of the Effect of Processing Variables on Porosity Formation in Laser Power-Bed Additive Manufacturing of Ti-6Al-4V.* JOM, 2017. **69**(3): p. 479-484.

342. Roehling, J.D., Perron, A., Fattebert, J.-L., Haxhimali, T., Guss, G., Li, T.T., Bober, D., Stokes, A.W., Clarke, A.J., Turchi, P.E.A., Matthews, M.J., and McKeown, J.T., *Rapid Solidification in Bulk Ti-Nb Alloys by Single-Track Laser Melting.* JOM, 2018. **70**(8): p. 1589-1597.

343. Yadroitsev, I., Yadroitsava, I., Bertrand, P., and Smurov, I., *Factor analysis of selective laser melting process parameters and geometrical characteristics of synthesized single tracks.* Rapid Prototyping Journal, 2012. **18**(3): p. 201-208.

344. Letenneur, M., Kreitcberg, A., and Brailovski, V., *Optimization of Laser Powder Bed Fusion Processing Using a Combination of Melt Pool Modeling and Design of Experiment Approaches: Density Control.* Journal of Manufacturing and Materials Processing, 2019. **3**(1).

345. King, W.E., Anderson, A.T., Ferencz, R.M., Hodge, N.E., Kamath, C., Khairallah, S.A., and Rubenchik, A.M., *Laser powder bed fusion additive manufacturing of metals; physics, computational, and materials challenges.* Applied Physics Reviews, 2015. **2**(4): p. 041304.

346. Brodie, E.G., Medvedev, A.E., Frith, J.E., Dargusch, M.S., Fraser, H.L., and Molotnikov, A., *Remelt processing and microstructure of selective laser melted Ti25Ta.* Journal of Alloys and Compounds, 2020. **820**: p. 153082.

347. Geiger, M., Leitz, K.H., Koch, H., and Otto, A., *A 3D transient model of keyhole and melt pool dynamics in laser beam welding applied to the joining of zinc coated sheets.* Production Engineering, 2009. **3**(2): p. 127-136.

348. Guo, Q., Zhao, C., Escano, L.I., Young, Z., Xiong, L., Fezzaa, K., Everhart, W., Brown, B., Sun, T., and Chen, L., *Transient dynamics of powder spattering in laser powder bed fusion additive manufacturing process revealed by in-situ high-speed high-energy x-ray imaging.* Acta Materialia, 2018. **151**: p. 169-180.

349. Niinomi, M.e., Narushima, T.e., Nakai, M.e., and SpringerLink, *Advances in Metallic Biomaterials : Tissues, Materials and Biological Reactions*. 2015: Heidelberg Germany : Springer.

350. Wang, X., Xu, S., Zhou, S., Xu, W., Leary, M., Choong, P., Qian, M., Brandt, M., and Xie, Y.M., *Topological design and additive manufacturing of porous metals for bone scaffolds and orthopaedic implants: A review.* Biomaterials, 2016. **83**: p. 127-141.

351. Cao, S., Chu, R., Zhou, X., Yang, K., Jia, Q., Lim, C.V.S., Huang, A., and Wu, X., *Role of martensite decomposition in tensile properties of selective laser melted Ti-6Al-4V.* Journal of Alloys and Compounds, 2018. **744**: p. 357-363.

352. Tao, Q., Wang, Z., Chen, G., Cai, W., Cao, P., Zhang, C., Ding, W., Lu, X., Luo, T., Qu, X., and Qin, M., *Selective laser melting of CP-Ti to overcome the low cost and high performance trade-off.* Additive Manufacturing, 2020. **34**: p. 101198.

353. Carrion, P.E., Soltani-Tehrani, A., Phan, N., and Shamsaei, N., *Powder Recycling Effects on the Tensile and Fatigue Behavior of Additively Manufactured Ti-6Al-4V Parts.* JOM, 2019. **71**(3): p. 963-973.

354. Collins, P.C., Brice, D.A., Samimi, P., Ghamarian, I., and Fraser, H.L., *Microstructural Control of Additively Manufactured Metallic Materials.* Annual Review of Materials Research, 2016. **46**(1): p. 63-91.

355. Simonelli, M., Tse, Y.Y., and Tuck, C., *The formation of [alpha] + [beta] microstructure in as-fabricated selective laser melting of Ti-6Al-4V.* Journal of Materials Research, 2014. **29**(17): p. 2028-2035.

356. Barriobero-Vila, P., Gussone, J., Stark, A., Schell, N., Haubrich, J., and Requena, G., *Peritectic titanium alloys for 3D printing.* Nature Communications, 2018. **9**(1): p. 3426.

357. Dobromyslov, A.V., Dolgikh, G.V., Dutkevich, Y., and Trenogina, T.L., *Phase and structural transformations in Ti-Ta alloys.* The Physics of Metals and Metallography, 2009. **107**(5): p. 502-510.

358. Stef, J., Poulon-Quintin, A., Redjaimia, A., Ghanbaja, J., Ferry, O., De Sousa, M., and Gouné, M., *Mechanism of porosity formation and influence on mechanical properties in selective laser melting of Ti-6Al-4V parts.* Materials & Design, 2018. **156**: p. 480-493.

359. Zhong, H.Z., Zhang, X.Y., Wang, S.X., and Gu, J.F., *Examination of the twinning activity in additively manufactured Ti-6Al-4V.* Materials & Design, 2018. **144**: p. 14-24.

360. Tan, X., Kok, Y., Tan, Y.J., Descoins, M., Mangelinck, D., Tor, S.B., Leong, K.F., and Chua, C.K., *Graded microstructure and mechanical properties of additive manufactured Ti–6Al–4V via electron beam melting.* Acta Materialia, 2015. **97**: p. 1-16.

361. Chai, Y.W., Kim, H.Y., Hosoda, H., and Miyazaki, S., *Interfacial defects in Ti–Nb shape memory alloys.* Acta Materialia, 2008. **56**(13): p. 3088-3097.

362. Ji, X., Gutierrez-Urrutia, I., Emura, S., Liu, T., Hara, T., Min, X., Ping, D., and Tsuchiya, K., *Twinning behavior of orthorhombic-α" martensite in a Ti-7.5Mo alloy.* Science and Technology of Advanced Materials, 2019. **20**(1): p. 401-411.

363. Majumdar, P., Singh, S.B., and Chakraborty, M., *Elastic modulus of biomedical titanium alloys by nano-indentation and ultrasonic techniques—A comparative study.* Materials Science and Engineering: A, 2008. **489**(1): p. 419-425.

364. Yang, K.V., Rometsch, P., Jarvis, T., Rao, J., Cao, S., Davies, C., and Wu, X., *Porosity formation mechanisms and fatigue response in Al-Si-Mg alloys made by selective laser melting.* Materials Science and Engineering: A, 2018. **712**: p. 166-174.

365. Yamanaka, K., Saito, W., Mori, M., Matsumoto, H., and Chiba, A., *Preparation of weak-textured commercially pure titanium by electron beam melting.* Additive Manufacturing, 2015. **8**: p. 105-109.

366. Senkov, O.N. and Jonas, J.J., *Dynamic strain aging and hydrogen-induced softening in alpha titanium.* Metallurgical and Materials Transactions A, 1996. **27**(7): p. 1877-1887.

367. Weiss, I. and Semiatin, S.L., *Thermomechanical processing of alpha titanium alloys—an overview.* Materials Science and Engineering: A, 1999. **263**(2): p. 243-256.

368. Zeng, Z., Zhang, Y., and Jonsson, S., *Deformation behaviour of commercially pure titanium during simple hot compression.* Materials & Design, 2009. **30**(8): p. 3105-3111.

369. Beyerlein, I.J. and Tóth, L.S., *Texture evolution in equal-channel angular extrusion.* Progress in Materials Science, 2009. **54**(4): p. 427-510.

370. Manero, J.M., Gil, F.J., and Planell, J.A., *Deformation mechanisms of Ti–6Al–4V alloy with a martensitic microstructure subjected to oligocyclic fatigue.* Acta Materialia, 2000. **48**(13): p. 3353-3359.

371. Matsumoto, H., Yoneda, H., Sato, K., Kurosu, S., Maire, E., Fabregue, D., Konno, T.J., and Chiba, A., *Room-temperature ductility of Ti–6Al–4V alloy with α′ martensite microstructure.* Materials Science and Engineering: A, 2011. **528**(3): p. 1512-1520.

372. Al-Bermani, S.S., Blackmore, M.L., Zhang, W., and Todd, I., *The Origin of Microstructural Diversity, Texture, and Mechanical Properties in Electron Beam Melted Ti-6Al-4V.* Metallurgical and Materials Transactions A, 2010. **41**(13): p. 3422-3434.

373. Ozan, S., Lin, J., Li, Y., Ipek, R., and Wen, C., *Development of Ti–Nb–Zr alloys with high elastic admissible strain for temporary orthopedic devices.* Acta Biomaterialia, 2015. **20**: p. 176-187.

374. Paradkar, A.G., Kamat, S.V., Gogia, A.K., and Kashyap, B.P., *On the validity of Hall–Petch equation for single-phase β Ti–Al–Nb alloys undergoing stress-induced martensitic transformation.* Materials Science and Engineering: A, 2009. **520**(1): p. 168-173.

375. Ankem, S. and Greene, C.A., *Recent developments in microstructure/property relationships of beta titanium alloys.* Materials Science & Engineering A, 1999. **263**(2): p. 127-131.

376. Zhao, X., Li, S., Zhang, M., Liu, Y., Sercombe, T.B., Wang, S., Hao, Y., Yang, R., and Murr, L.E., *Comparison of the microstructures and mechanical properties of Ti–6Al–4V fabricated by selective laser melting and electron beam melting.* Materials & Design, 2016. **95**: p. 21-31.

377. Aydinöz, M.E., Brenne, F., Schaper, M., Schaak, C., Tillmann, W., Nellesen, J., and Niendorf, T., *On the microstructural and mechanical properties of post-treated additively manufactured Inconel 718 superalloy under quasi-static and cyclic loading.* Materials Science and Engineering: A, 2016. **669**: p. 246-258.

378. Brodie, E.G., Richter, J., Wegener, T., Niendorf, T., and Molotnikov, A., *Low-cycle fatigue performance of remelted laser powder bed fusion (L-PBF) biomedical Ti25Ta.* Materials Science and Engineering: A, 2020. **798**: p. 140228.

379. Günther, J., Krewerth, D., Lippmann, T., Leuders, S., Tröster, T., Weidner, A., Biermann, H., and Niendorf, T., *Fatigue life of additively manufactured Ti–6Al–4V in the very high cycle fatigue regime.* International Journal of Fatigue, 2017. **94**(Part 2): p. 236-245.

380. Mughrabi, H., *Microstructural mechanisms of cyclic deformation, fatigue crack initiation and early crack growth.* Philosophical Transactions of the Royal Society A: Mathematical, Physical and Engineering Sciences, 2015. **373**(2038): p. 20140132.

381. Haubrich, J., Gussone, J., Barriobero-Vila, P., Kürnsteiner, P., Jägle, E.A., Raabe, D., Schell, N., and Requena, G., *The role of lattice defects, element partitioning and intrinsic heat effects on the microstructure in selective laser melted Ti-6Al-4V.* Acta Materialia, 2019. **167**: p. 136-148.

382. Wysocki, B., Idaszek, J., Zdunek, J., Rożniatowski, K., Pisarek, M., Yamamoto, A., and Święszkowski, W., *The Influence of Selective Laser Melting (SLM) Process Parameters on In-Vitro Cell Response.* International Journal of Molecular Sciences, 2018. **19**(6): p. 1619.

383. Thijs, L., Verhaeghe, F., Craeghs, T., Humbeeck, J.V., and Kruth, J.-P., *A study of the microstructural evolution during selective laser melting of Ti–6Al–4V.* Acta Materialia, 2010. **58**(9): p. 3303-3312.

384. Sing, S.L., Wang, S.G., and Agarwala, S., *Fabrication of titanium based biphasic scaffold using selective laser melting and collagen immersion.* International Journal of Bioprinting, 2017. **3**(1): p. 1-7.

385. Ghouse, S., Babu, S., Nai, K., Hooper, P.A., and Jeffers, J.R.T., *The influence of laser parameters, scanning strategies and material on the fatigue strength of a stochastic porous structure.* Additive Manufacturing, 2018. **22**: p. 290-301.

386. Brenne, F., *Selektives Laserschmelzen metallischer Materialien: Einfluss von Prozessparametern und Miniaturisierung auf Mikrostruktur und mechanisches Verhalten*

geometrisch komplexer Strukturen, in *Institut für Werkstofftechnik Metallische Werkstoffe*. 2018, Universität Kassel: Kassel. p. 217.

387. Tian, Y., Tomus, D., Rometsch, P., and Wu, X., *Influences of processing parameters on surface roughness of Hastelloy X produced by selective laser melting.* Additive Manufacturing, 2017. **13**: p. 103-112.

388. Pham, M.-S., Liu, C., Todd, I., and Lertthanasarn, J., *Damage-tolerant architected materials inspired by crystal microstructure.* Nature, 2019. **565**(7739): p. 305-311.

389. Murr, L.E., *Open-cellular metal implant design and fabrication for biomechanical compatibility with bone using electron beam melting.* Journal of the Mechanical Behavior of Biomedical Materials, 2017.

390. Brenne, F., Niendorf, T., and Maier, H.J., *Additively manufactured cellular structures: Impact of microstructure and local strains on the monotonic and cyclic behavior under uniaxial and bending load.* Journal of Materials Processing Technology, 2013. **213**(9): p. 1558-1564.

391. Maconachie, T., Leary, M., Lozanovski, B., Zhang, X., Qian, M., Faruque, O., and Brandt, M., *SLM lattice structures: Properties, performance, applications and challenges.* Materials & Design, 2019. **183**: p. 108137.

392. Mazur, M., Leary, M., Sun, S., Vcelka, M., Shidid, D., and Brandt, M., *Deformation and failure behaviour of Ti-6Al-4V lattice structures manufactured by selective laser melting (SLM).* The International Journal of Advanced Manufacturing Technology, 2016. **84**(5): p. 1391-1411.

393. Abele, E., Stoffregen, H.A., Klimkeit, K., Hoche, H., and Oechsner, M., *Optimisation of process parameters for lattice structures.* Rapid Prototyping Journal, 2015. **21**(1): p. 117-127.

394. Brice, C.A., *Dispersion strengthened titanium alloys produced via direct laser deposition*. 2000, The Ohio State University.

395. Yang, L., Mertens, R., Ferrucci, M., Yan, C., Shi, Y., and Yang, S., *Continuous graded Gyroid cellular structures fabricated by selective laser melting: Design, manufacturing and mechanical properties.* Materials & Design, 2019. **162**: p. 394-404.

396. Wang, S., Liu, L., Li, K., Zhu, L., Chen, J., and Hao, Y., *Pore functionally graded Ti6Al4V scaffolds for bone tissue engineering application.* Materials & Design, 2019: p. 107643.

397. Reinhart, G., Teufelhart, S., and Riss, F., *Investigation of the Geometry-Dependent Anisotropic Material Behavior of Filigree Struts in ALM-Produced Lattice Structures.* Physics Procedia, 2012. **39**: p. 471-479.

398. Al-Saedi, D.S.J., Masood, S.H., Faizan-Ur-Rab, M., Alomarah, A., and Ponnusamy, P., *Mechanical properties and energy absorption capability of functionally graded F2BCC lattice fabricated by SLM.* Materials & Design, 2018. **144**: p. 32-44.

399. Liu, Y., Yang, Y., and Wang, D., *A study on the residual stress during selective laser melting (SLM) of metallic powder.* The International Journal of Advanced Manufacturing Technology, 2016. **87**(1): p. 647-656.

400. Yeung, T., Georges, P.C., Flanagan, L.A., Marg, B., Ortiz, M., Funaki, M., Zahir, N., Ming, W., Weaver, V., and Janmey, P.A., *Effects of substrate stiffness on cell morphology,*

cytoskeletal structure, and adhesion. Cell Motility and the Cytoskeleton, 2005. **60**(1): p. 24-34.

401. Anselme, K., *Osteoblast adhesion on biomaterials.* Biomaterials, 2000. **21**(7): p. 667-681.

402. Ventre, M., Causa, F., and Netti, P.A., *Determinants of cell-material crosstalk at the interface: towards engineering of cell instructive materials.* Journal of the Royal Society, Interface, 2012. **9**(74): p. 2017-2032.

403. Marie, P.J., *Targeting integrins to promote bone formation and repair.* Nature Reviews Endocrinology, 2013. **9**(5): p. 288-295.

404. Frith, J.E., Kusuma, G.D., Carthew, J., Li, F., Cloonan, N., Gomez, G.A., and Cooper-White, J.J., *Mechanically-sensitive miRNAs bias human mesenchymal stem cell fate via mTOR signalling.* Nature Communications, 2018. **9**(1): p. 257.

405. Quarto, R. and Giannoni, P., *Bone Tissue Engineering: Past–Present–Future*, in *Mesenchymal Stem Cells: Methods and Protocols*, M. Gnecchi, Editor. 2016, Springer New York: New York, NY. p. 21-33.

406. Abo-Aziza, F.A.M. and A A, Z., *The Impact of Confluence on Bone Marrow Mesenchymal Stem (BMMSC) Proliferation and Osteogenic Differentiation.* International journal of hematology-oncology and stem cell research, 2017. **11**(2): p. 121.

407. Carthew, J., Donderwinkel, I., Shrestha, S., Truong, V.X., Forsythe, J.S., and Frith, J.E., *In situ miRNA delivery from a hydrogel promotes osteogenesis of encapsulated mesenchymal stromal cells.* Acta Biomaterialia, 2020. **101**: p. 249-261.

408. Vogel, S., Ullm, F., Damaris Müller, C., Pompe, T., and Hempel, U., *Remodeling of Three-Dimensional Collagen I Matrices by Human Bone Marrow Stromal Cells during Osteogenic Differentiation In Vitro.* ACS Applied Bio Materials, 2020. **3**(10): p. 6967-6978.

409. Wilson, A., Hodgson-Garms, M., Frith, J.E., and Genever, P., *Multiplicity of Mesenchymal Stromal Cells: Finding the Right Route to Therapy.* Frontiers in Immunology, 2019. **10**: p. 1112.

410. Mei, S., Yang, L., Pan, Y., Wang, D., Wang, X., Tang, T., and Wei, J., *Influences of tantalum pentoxide and surface coarsening on surface roughness, hydrophilicity, surface energy, protein adsorption and cell responses to PEEK based biocomposite.* Colloids and Surfaces B: Biointerfaces, 2019. **174**: p. 207-215.

411. An, R., Fan, P.P., Zhou, M.J., Wang, Y., Goel, S., Zhou, X.F., Li, W., and Wang, J.T., *Nanolamellar Tantalum Interfaces in the Osteoblast Adhesion.* Langmuir, 2019. **35**(7): p. 2480-2489.

412. Ding, D., Xie, Y., Li, K., Huang, L., and Zheng, X., *Micro/Nano Structural Tantalum Coating for Enhanced Osteogenic Differentiation of Human Bone Marrow Stem Cells.* Materials, 2018. **11**(4).

413. Vallés, G., Bensiamar, F., Crespo, L., Arruebo, M., Vilaboa, N., and Saldaña, L., *Topographical cues regulate the crosstalk between MSCs and macrophages.* Biomaterials, 2015. **37**: p. 124-133.

414. Gittens, R.A., McLachlan, T., Olivares-Navarrete, R., Cai, Y., Berner, S., Tannenbaum, R., Schwartz, Z., Sandhage, K.H., and Boyan, B.D., *The effects of combined micron-/submicron-*

scale surface roughness and nanoscale features on cell proliferation and differentiation. Biomaterials, 2011. **32**(13): p. 3395-3403.

415. Kim, H.J., Kim, S.H., Kim, M.S., Lee, E.J., Oh, H.G., Oh, W.M., Park, S.W., Kim, W.J., Lee, G.J., Choi, N.G., Koh, J.T., Dinh, D.B., Hardin, R.R., Johnson, K., Sylvia, V.L., Schmitz, J.P., and Dean, D.D., *Varying Ti-6Al-4V surface roughness induces different early morphologic and molecular responses in MG63 osteoblast-like cells.* Journal of Biomedical Materials Research Part A, 2005. **74A**(3): p. 366-373.

416. Olivares-Navarrete, R., Hyzy, S.L., Hutton, D.L., Erdman, C.P., Wieland, M., Boyan, B.D., and Schwartz, Z., *Direct and indirect effects of microstructured titanium substrates on the induction of mesenchymal stem cell differentiation towards the osteoblast lineage.* Biomaterials, 2010. **31**(10): p. 2728-2735.

417. Schwartz, Z., Raz, P., Zhao, G., Barak, Y., Tauber, M., Yao, H., and Boyan, B.D., *Effect of micrometer-scale roughness of the surface of Ti6Al4V pedicle screws in vitro and in vivo*. The Journal of bone and joint surgery. American Volume, 2008. **90**(11): p. 2485-2498.

418. Wennerberg, A. and Albrektsson, T., *Effects of titanium surface topography on bone integration: a systematic review*. Clinical Oral Implants Research, 2009. **20**(s4): p. 172-184.

419. Boyan, B.D., Schwartz, Z., Lohmann, C.H., and Sylvia, V.L., *Pretreatment of bone with osteoclasts affects phenotypic expression of osteoblast-like cells.* Journal of Orthopaedic Research, 2003. **21**(4): p. 638.

420. Raines, A.L., Olivares-Navarrete, R., Wieland, M., Cochran, D.L., Schwartz, Z., and Boyan, B.D., *Regulation of angiogenesis during osseointegration by titanium surface microstructure and energy.* Biomaterials, 2010. **31**(18): p. 4909-4917.

421. Gittens, R.A., Olivares-Navarrete, R., Cheng, A., Anderson, D.M., McLachlan, T., Stephan, I., Geis-Gerstorfer, J., Sandhage, K.H., Fedorov, A.G., Rupp, F., Boyan, B.D., Tannenbaum, R., and Schwartz, Z., *The roles of titanium surface micro/nanotopography and wettability on the differential response of human osteoblast lineage cells.* Acta Biomaterialia, 2013. **9**(4): p. 6268-6277.

422. Mendis, S., Xu, W., Tang, H.P., Jones, L.A., Liang, D., Thompson, R., Choong, P., Brandt, M., and Qian, M., *Characteristics of oxide films on Ti-(10–75)Ta alloys and their corrosion performance in an aerated Hank's balanced salt solution.* Applied Surface Science, 2020. **506**: p. 145013.

423. Bouwman, R., *Surface enrichment in alloys.* Gold Bulletin, 1978. **11**(3): p. 81-85.

424. Virjula, S., Zhao, F., Leivo, J., Vanhatupa, S., Kreutzer, J., Vaughan, T.J., Honkala, A.-M., Viehrig, M., Mullen, C.A., Kallio, P., McNamara, L.M., and Miettinen, S., *The effect of equiaxial stretching on the osteogenic differentiation and mechanical properties of human adipose stem cells.* Journal of the Mechanical Behavior of Biomedical Materials, 2017. **72**: p. 38-48.

425. Park, J., Bauer, S., Schlegel, K.A., Neukam, F.W., von der Mark, K., and Schmuki, P., *TiO2 Nanotube Surfaces: 15 nm—An Optimal Length Scale of Surface Topography for Cell Adhesion and Differentiation.* Small, 2009. **5**(6): p. 666-671.

426. van der Stok, J., Wang, H., Amin Yavari, S., Siebelt, M., Sandker, M., Waarsing, J.H., Verhaar, J.A.N., Jahr, H., Zadpoor, A.A., Leeuwenburgh, S.C.G., and Weinans, H., *Enhanced Bone Regeneration of Cortical Segmental Bone Defects Using Porous Titanium Scaffolds*

Incorporated with Colloidal Gelatin Gels for Time- and Dose-Controlled Delivery of Dual Growth Factors. Tissue Engineering Part A, 2013. **19**(23-24): p. 2605-14.

427. Zhou, K., Wang, H.P., Chang, J., and Wei, B., *Experimental study of surface tension, specific heat and thermal diffusivity of liquid and solid titanium.* Chemical Physics Letters, 2015. **639**: p. 105-108.

428. Pottlacher, G. and Seifter, A., *Microsecond Laser Polarimetry for Emissivity Measurements on Liquid Metals at High Temperatures—Application to Tantalum.* International Journal of Thermophysics, 2002. **23**(5): p. 1281-1291.

429. Tolochko, N.K., Khlopkov, Y.V., Mozzharov, S.E., Ignatiev, M.B., Laoui, T., and Titov, V.I., *Absorptance of powder materials suitable for laser sintering.* Rapid Prototyping Journal, 2000. **6**(3): p. 155-160.

430. Ordal, M.A., Bell, R.J., Alexander, R.W., Newquist, L.A., and Querry, M.R., *Optical properties of Al, Fe, Ti, Ta, W, and Mo at submillimeter wavelengths.* Applied Optics, 1988. **27**(6): p. 1203-1209.

431. Rai, R., Elmer, J.W., Palmer, T.A., and DebRoy, T., *Heat transfer and fluid flow during keyhole mode laser welding of tantalum, Ti–6Al–4V, 304L stainless steel and vanadium.* Journal of Physics D: Applied Physics, 2007. **40**(18): p. 5753-5766.

432. du Plessis, A. and Beretta, S., *Killer notches: The effect of as-built surface roughness on fatigue failure in AlSi10Mg produced by laser powder bed fusion.* Additive Manufacturing, 2020. **35**: p. 101424.

433. du Plessis, A., Tshibalanganda, M., and le Roux, S.G., *Not all scans are equal: X-ray tomography image quality evaluation.* Materials Today Communications, 2020. **22**: p. 100792.

434. Biesinger, M.C., Lau, L.W.M., Gerson, A.R., and Smart, R.S.C., *Resolving surface chemical states in XPS analysis of first row transition metals, oxides and hydroxides: Sc, Ti, V, Cu and Zn.* Applied Surface Science, 2010. **257**(3): p. 887-898.

Chapter 8 Appendices

A1. Point EDX analysis of TiTa matrix

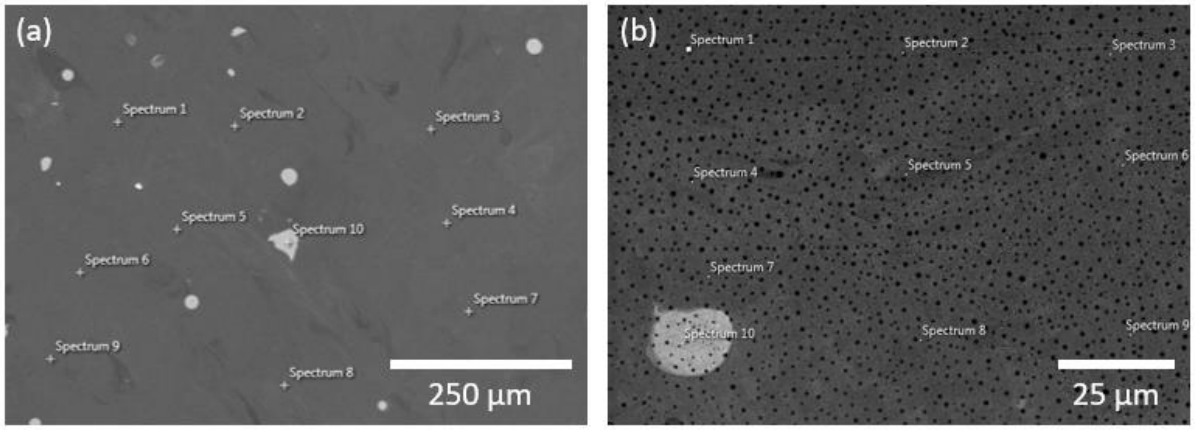

Figure 8-1: Matrix elemental analysis of (a) Ti25Ta and (b) Ti65Ta L-PBF material.

Table 8-1: Wt.% statistics of spectra 1 – 9.

	Ti25Ta		Ti65Ta	
	Ta (wt.%)	**Ti (wt.%)**	**Ta (wt.%)**	**Ti (wt.%)**
Max	28.08	76.84	65.69	39.28
Min	23.16	71.92	60.72	34.31
Average	25.52	74.48	63.81	36.19
Standard Deviation	1.59	1.59	1.46	1.46

A2. Literature values used for normalised enthalpy calculations

Table 8-2: Physical properties of Ti and Ta powders used in normalised enthalpy calculations.

	Ti	**Ta**	**Ti25Ta**	**Ti65Ta**
Thermal Conductivity (W/m °C)	21.9 [77]	57.5 [77]	24.7 *	33.6 *
Melting Temperature (°C)	1660 [77]	3000 [77]	1733 **	1913 **
Thermal Diffusivity (cm^2/s)	0.120 [427]	0.200 [428]	0.126 *	0.146 *
Absorptivity	0.71 [345, 429]	0.75 ***	0.71 *	0.72 *

Due to lack of experimental data in literature, starred values are calculated as follows:

* Using atomic percentage of alloy and pure Ti/Ta values

** Using ThermoCalc database

*** Estimated from absorptivity data which shows Ta absorbing higher than Ti [430, 431]

A3. Etched prior β grain structure of L-PBF single melt Ti25Ta

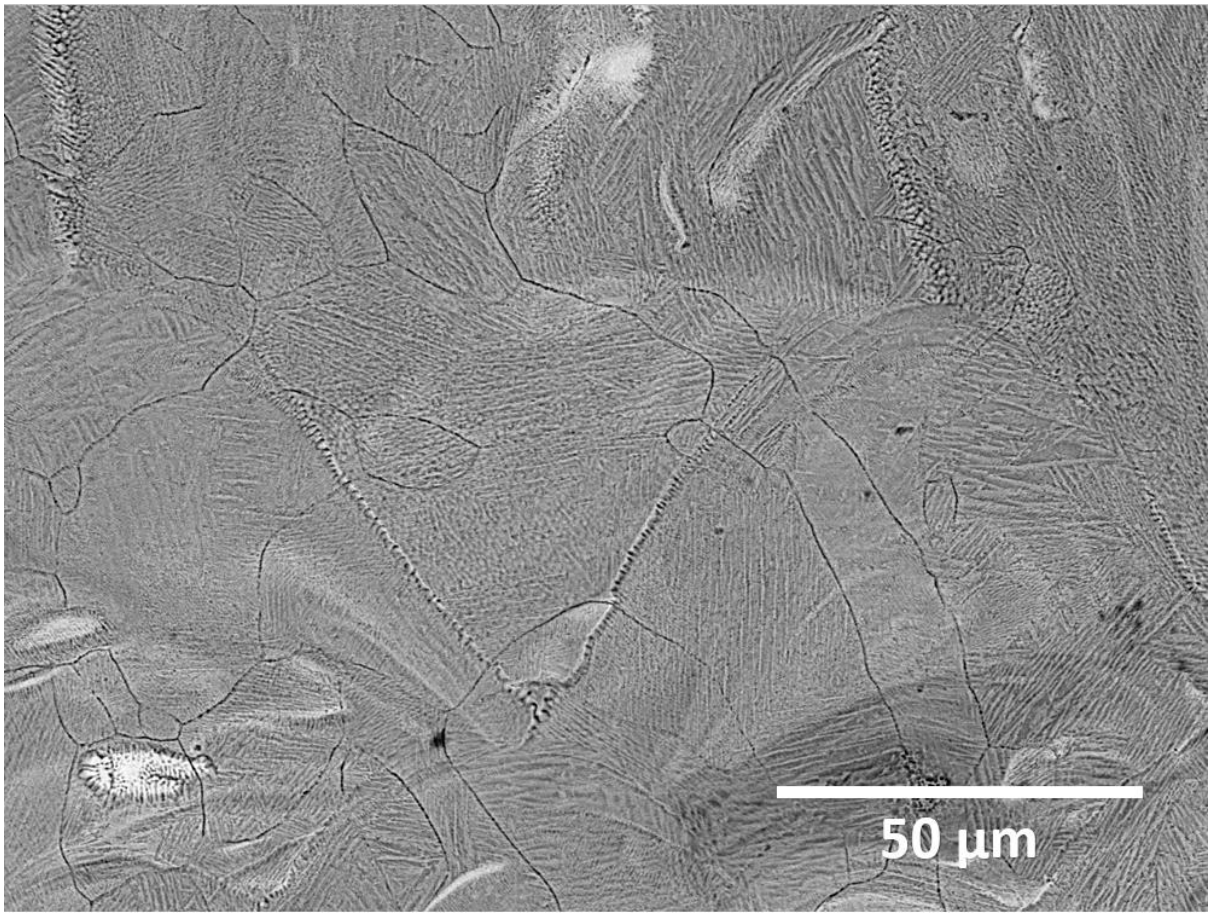

Figure 8-2: Etched L-PBF Ti25Ta single melt sample displaying non-columnar prior β grain boundaries.

A4. Repeated Parameter Laser Degradation Study

The parameter optimisation samples determined initially in Section 3.4 were printed again using the exact same process parameters, 2 years later. Figure 8-3 shows that there was a noted increase in porosity after the 2 year period, attributed to degradation of the laser. The lower density samples produced after 2 years however still showed an overall density of > 99.63 %, representative of well processed L-PBF Ti [194, 381-383]. The degradation of the laser highlights the need for improved characterisation of defects in AM parts, particularly in order to produce parts with reliable fatigue lives, as investigated by du Plessis et al. [432, 433].

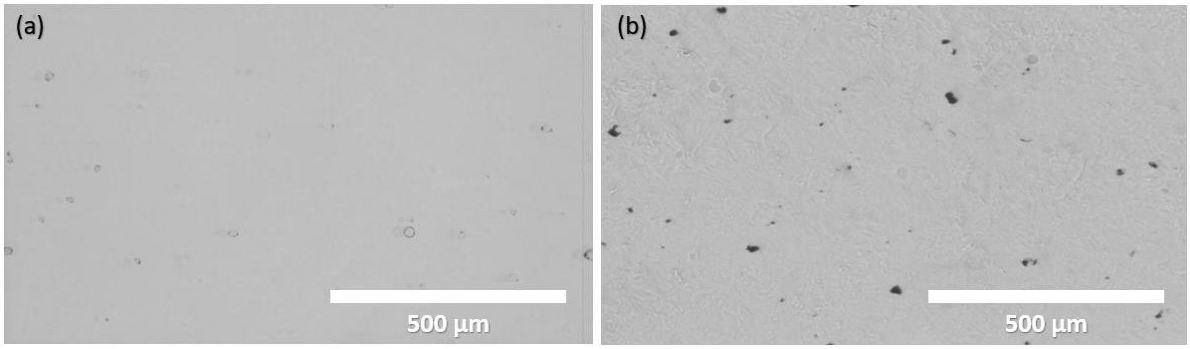

Figure 8-3: Porosity of (a) original parameter optimisation sample and (b) post 2-year reproduction of identical sample size, shape and parameters.

A5. Large area fracture surface EDX analysis

The larger area encompassing the region shown in Figure 5-6 is provided below. The shadowing caused by the uneven fracture surface makes EDX analysis at this magnification difficult, however, it can be seen over the larger area that Ta particles and pores do not correspond spatially.

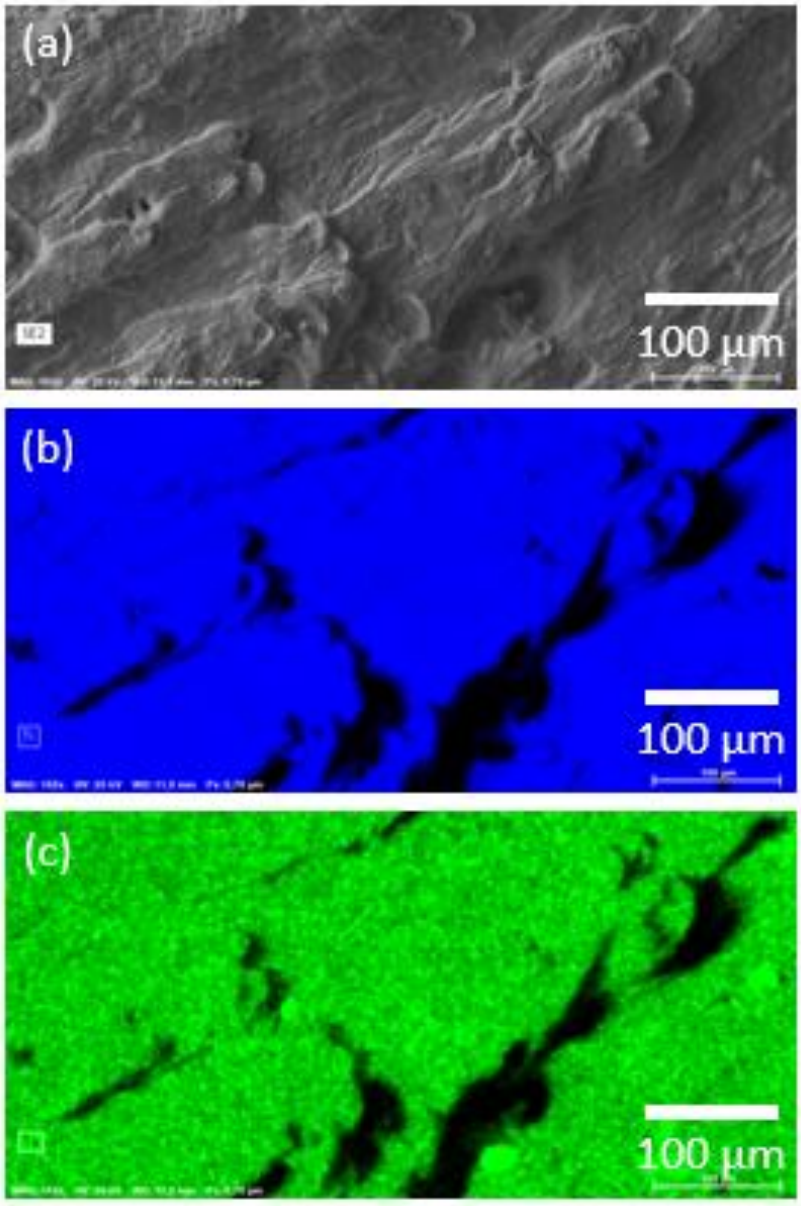

Figure 8-4: Lower magnification of EDX analysis displayed in Figure 5-6; (a) SEM image, (b) Ti mapping (c) Ta mapping.

A6. Fatigue data used to compare fatigue performance of Ti25Ta and Ti65Ta alloys

Table 8-3: Values used to create Figure 5-8.

	Test Stress (MPa)	Test Strength / Yield Strength (-)	Cycles to Failure	Yield Strength (MPa)	Elastic Modulus (GPa)
Ti25Ta Single Melt (machined) [This study]	343	-	46778	426	65
	442	-	8945		
	540	-	6373		
Ti25Ta Remelt (machined) [This study]	372	-	10390	545	77
	502	-	5896		
	694	-	1528		
Ti65Ta Single Melt (machined) [This study]	422	-	10356	381‡‡‡	81
	503	-	5356		
	629	-	2142		
Ti65Ta Remelt (machined) [This study]	497	-	10953	604‡‡‡	96
	630	-	2522		
	760	-	1051		
Ti-6Al-4V ELI (as-built) [60]	-	1	1000	-	114
	-	0.5	10000		
	-	0.25	100000		
CP Ti (as-built) [60]	-	0.8	20000	-	103
	-	0.65	60000		
	-	0.55	200000		
Ta (as-built) [60]	-	0.975	60000	-	186
	-	0.8	200000		
	-	0.6	1000000		
Ti-6Al-4V ELI (fine surface finish) [242]	400	-	66000	1015	113
	590	-	6000		
	750	-	3000		

‡‡‡ Yield strength normalised to the standard-tensile sample value by subtracting the strength increase caused by part size variation to mini-tensile samples noted in the Ti25Ta alloy.

A7. XPS Peak Fitting Data

Shirley backgrounds were used for all quantification. For high resolution scans of lower abundance/signal elements i.e. C, Al and V a 5 point average width was used to define background endpoints. Titanium high resolution peak fitting, Figure 8-5(a) was performed using several constraints. The area of the $p_{1/2}$ peaks was constrained to be half of that of the corresponding $p_{3/2}$ peak. Asymmetric line shapes (LA(1.1,5,7) were used to fit the conductive metallic peaks and GL(65) line shapes were utilised for the oxidised species. Literature splitting values were then used as a guide to fit binding energy of oxidised species [434]. High Resolution fitting was not attempted on the Ta4f region due to the overlapping elemental species limiting the production of any meaningful fit. The overlapping orbitals are indicated in Figure 8-5(b).

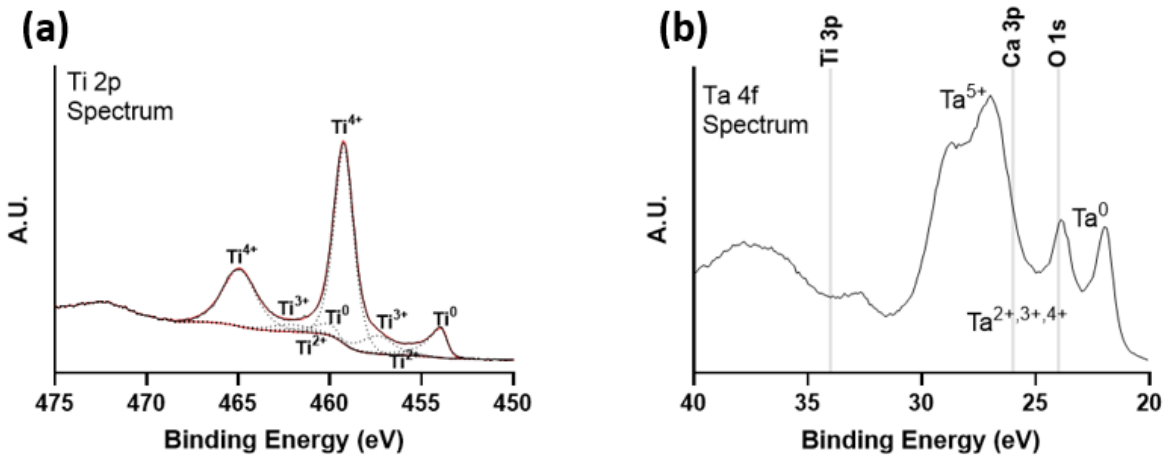

Figure 8-5: (a) High resolution fit of Ti 2p peaks for Ti-6Al-4V indicating the assigned oxidation states. (b) The high resolution scan of the Ta 4f region on Ti65Ta on which peak fitting was not attempted due to indicated overlapping species present in the study.

Based on the binding energy of Ta $4p_{1/2}$ orbital it was expected that there could be some overlap between this peak and the Ti 2p peaks used for titanium quantification. Evidence for this is shown in Figure 8-6, where following argon etching Ti65Ta deviates from samples containing lower amounts of Ta at the expected Ta $4p_{1/2}$ binding energy. This small but meaningful area was assumed to be present in the non-etched sample also, and as such, was corrected for during element quantification. Using the relative sensitivity factors for the Ta 4f and Ta $4p_{1/2}$ the Ta contribution was removed from the Ti 2p peak. It should be noted that this was a relatively minor correction ~1% surface Ti concentration. The overlap of Ta $4p_{1/2}$ with Ti 2p as well as O 1s with Ta 4f seems to be a commonly overlooked issue in the literature on TiTa alloys when performing high resolution component fitting.

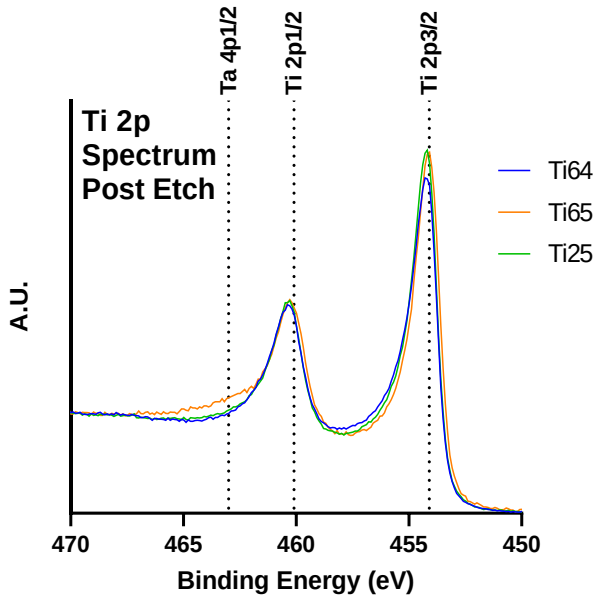

Figure 8-6: Ta 4p overlap following etching. This figure shows how the Ta 4p peak overlaps with the 2p peaks and as such has likely been included in quantification of Ti from the survey spectrum and as such this value required correction. Other smaller variations at lower binding energy are likely the result of the variation in amount of carbide present.

Table 6-3 presents the relative concentrations of metallic elements and oxygen in the oxide layer. This table has had the contributions from the adventitious carbon layer, silica and carbonate (including the oxygen contained within each) removed for ease of interpretation. A full table is presented below in Table 8-4.

Table 8-4: Relative concentrations of all detected elements in the oxide layer.

	Relative Concentration (at. %)								
	Al 2p	C 1s	Ca 2p	N 1s	O 1s	Si 2p	Ta 4d	Ti 2p	V 2p
Ti64	5.1 (1.2)	23.9 (3.3)	1.2 (0.1)	0.9 (0.3)	47.9 (1.3)	3.9 (0.2)	-	16.7 (1.4)	0.4 (0.2)
Ti25	-	10.8 (4.6)	0.8 (0.2)	-	55.1 (2.8)	3.5 (1.1)	5.3 (0.8)	23.3 (2.5)	-
Ti65	-	22.0 (4.0)	1.1 (0.1)	-	49.5 (1.7)	5.3 (1.0)	8.4 (1.2)	14.6 (1.5)	-

A8. Biological Testing Replicates over 5 hBMSC Donors

Cell Attachment

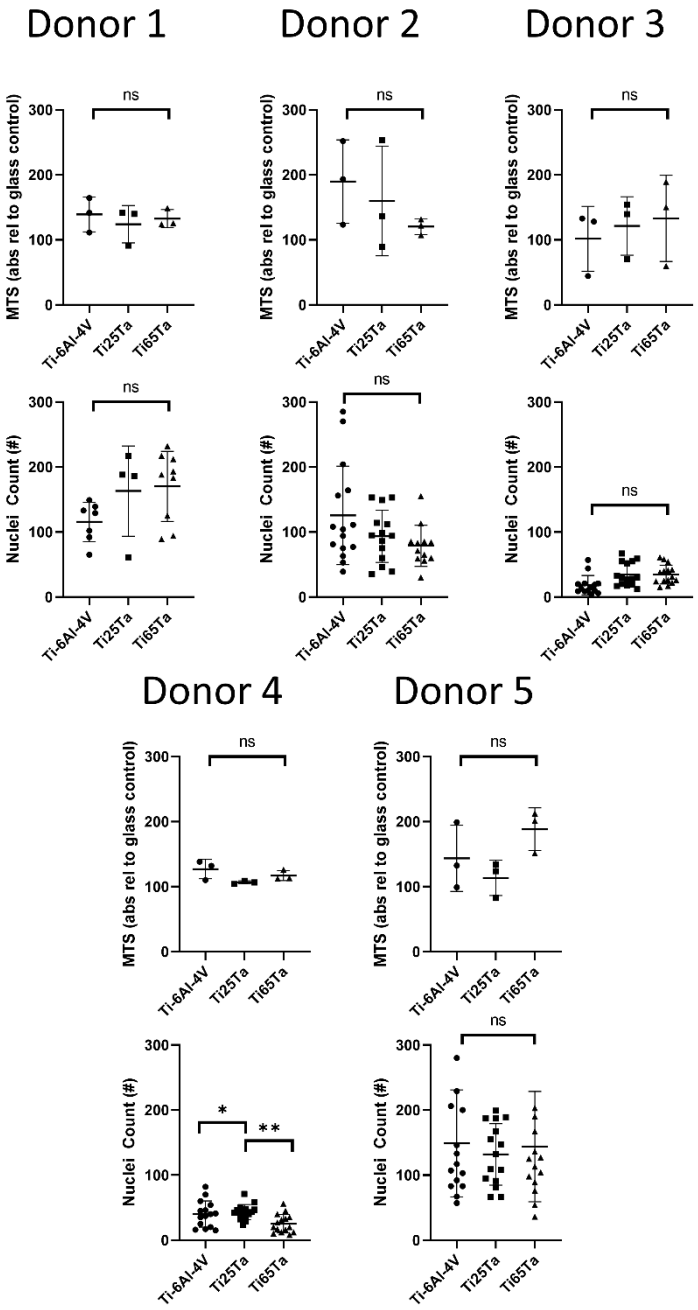

Figure 8-7: Replicate adhesion data for Figure 6-10, including supporting nuclei counting data. For the nuclei counting data, each data point represents the number of nuclei counted from one of five images taken across the surface area of each substrate.

Cell Proliferation

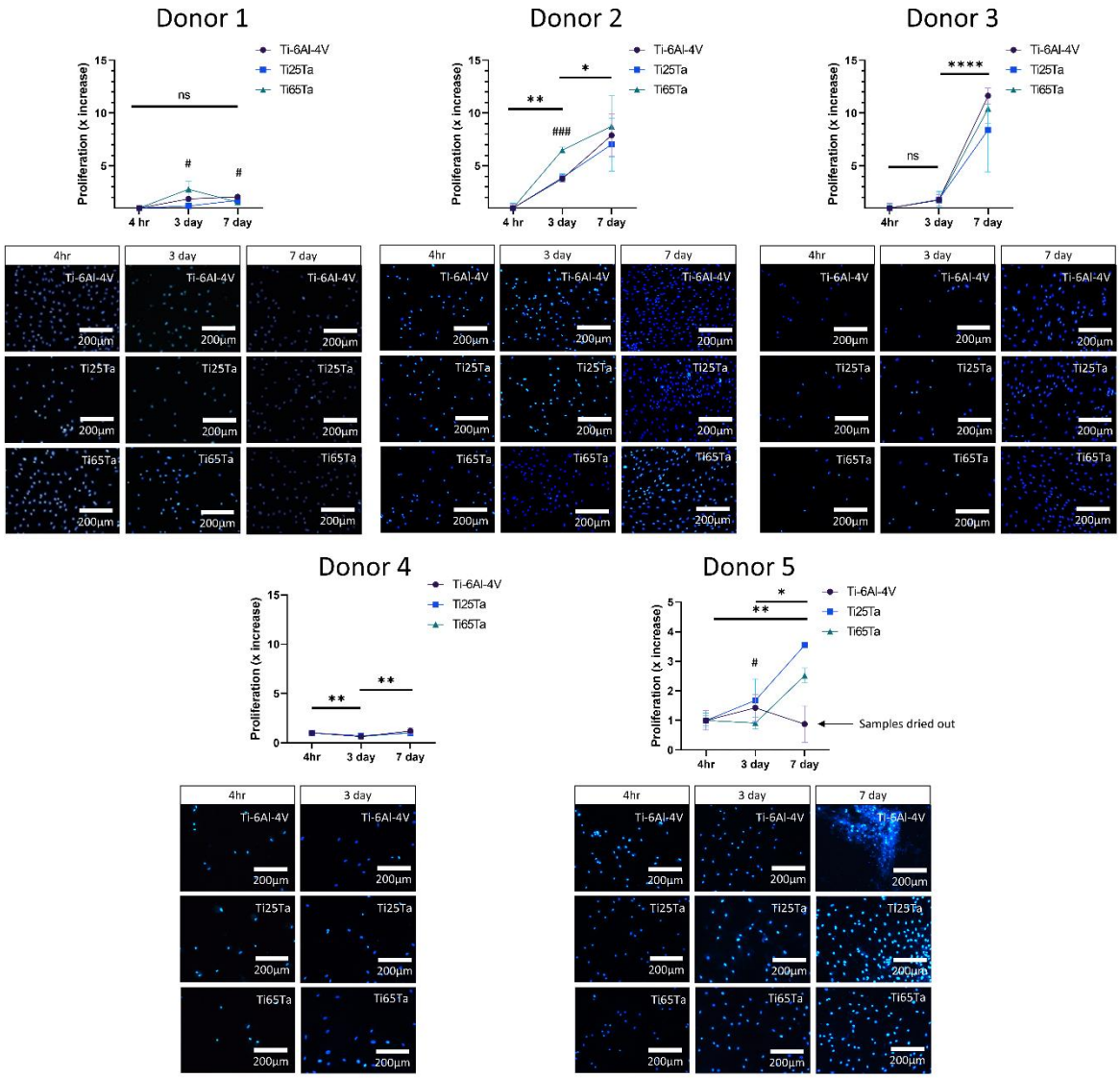

Figure 8-8: Replicate proliferation data for Figure 6-10.

Cell Morphology 4 hr Timepoint

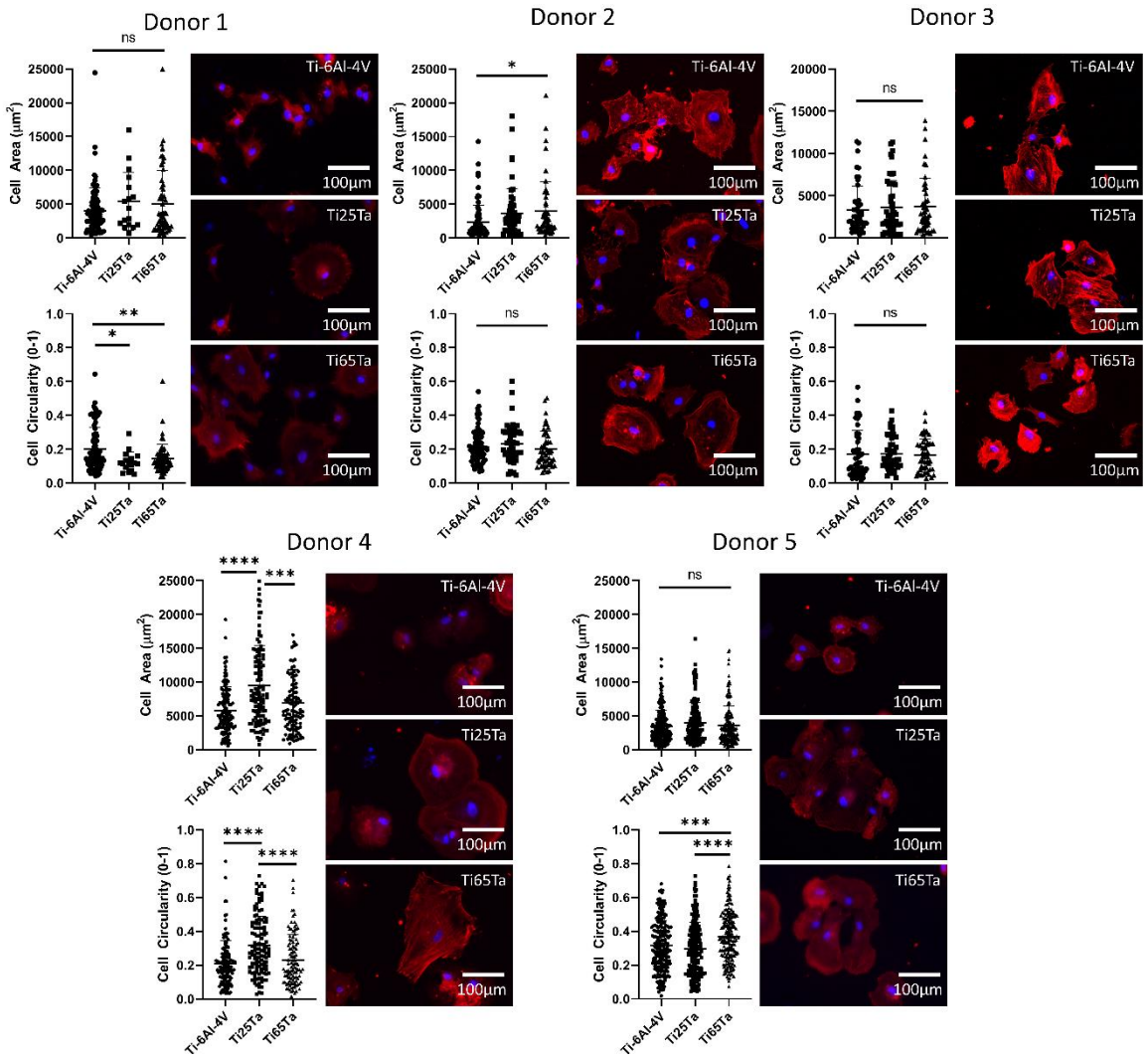

Figure 8-9: Replicate data for Figure 6-11 at 4 hr time point.

Cell Morphology 3 day Timepoint

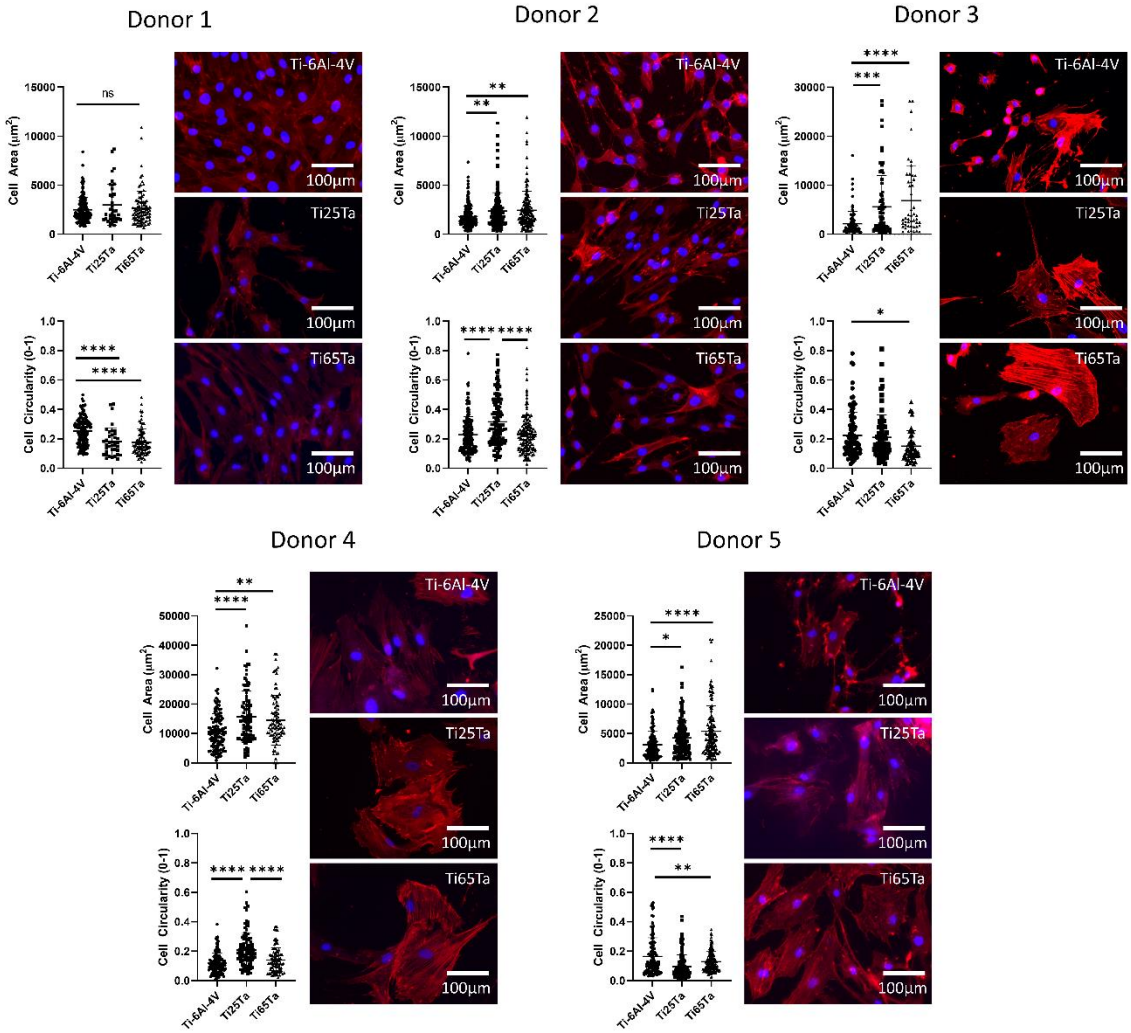

Figure 8-10: Replicate data for Figure 6-11 at 3 day time point.

ALP Activity and Mineralisation

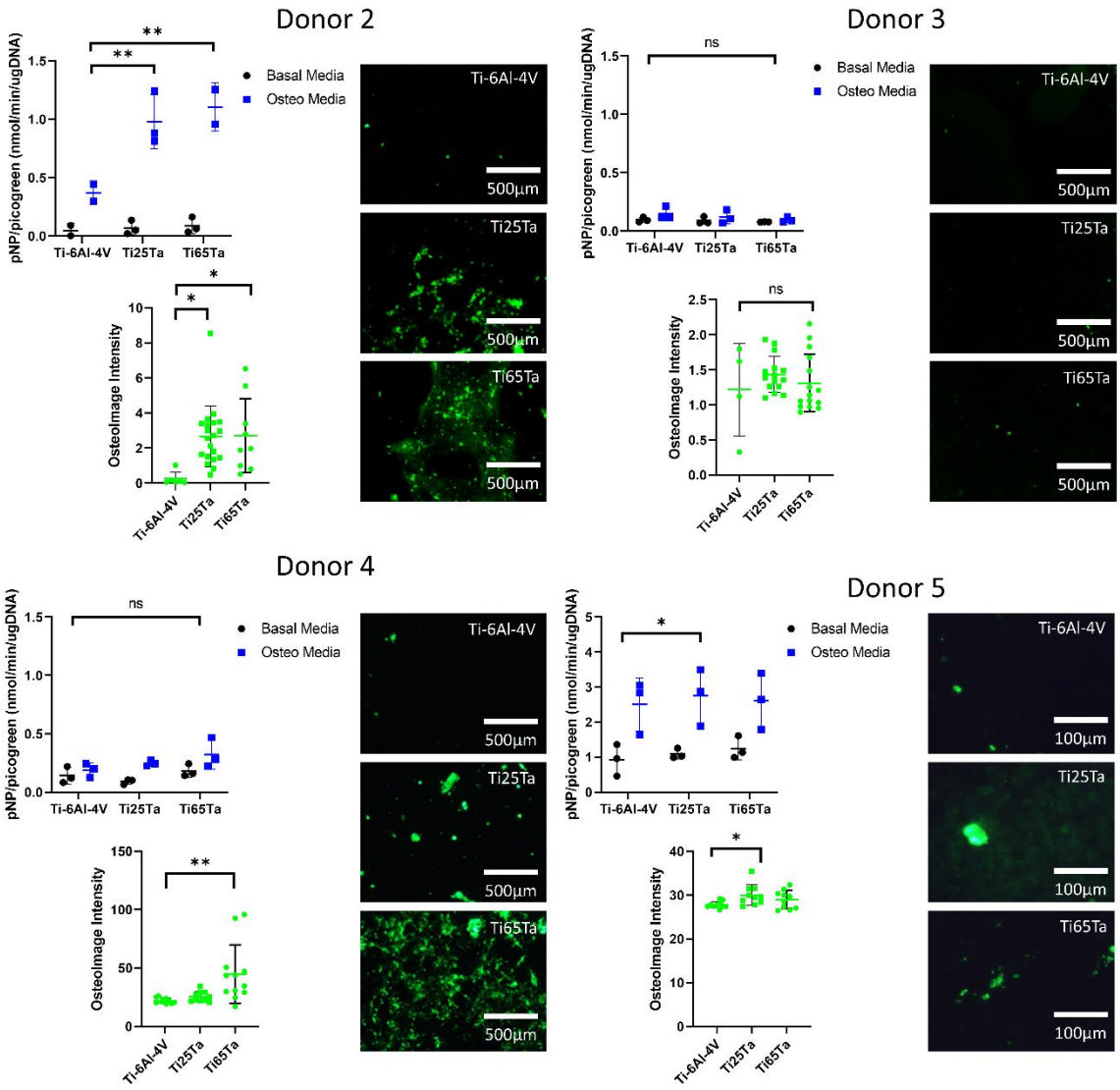

Figure 8-11: Replicate data for Figure 6-12.

The mineral study for Donor 5 was conducted at 3 weeks due to COVID lab shutdowns. As a result of the lower mineral deposition and lower fluorescence, Donor 5 mineral samples were analysed at a higher magnification. NB: Donor 3 showed no differentiation capacity so was excluded from analysis.